UNIVERSITÀ
degli STUDI
di CATANIA

DEPARTMENT OF BIOLOGICAL, GEOLOGICAL AND
ENVIRONMENTAL SCIENCES
PH.D. IN EARTH AND ENVIRONMENTAL SCIENCES
CYCLE XXXVIII

Sabrina Elettra Zafarana

DEVELOPMENT OF REINFORCED ALKALI ACTIVATED MATERIALS FOR CULTURAL HERITAGE RESTORATION

Tutor: Chiar.mo Prof. Paolo Mazzoleni

Co-Tutor: Chiar.ma Prof.ssa Germana Barone
Chiar.ma Prof.ssa Cristina Maria Belfiore
Chiar.mo Dott. Claudio Finocchiaro

Coordinators: Prof.ssa Agata Di Stefano
Prof.ssa Rosanna Maniscalco

Academic Year 2024-2025

Index

Preface 16

1 Introduction 18

1.1 Ordinary Portland Cement (OPC) vs Alkali Activated Materials (AAMs) and Geopolymers 19

1.2 Alkali-activated Materials vs Geopolymers 21

1.3 Italian Waste Management Policies and regulatory framework 25

1.4 Fiber reinforced composites 26

1.5 Geological setting of the areas of interest 28

2 Materials 34

2.1 Basalt and Granophyre sawing waste sludges 34

2.2 Metakaolin 37

2.3 Alkaline solutions 38

2.4 Synthetic and organic fibres 39

3 Methods 41

3.1 Mineralogical, chemical, molecular and morphological characterization 41

3.1.1 X-Ray Fluorescence (XRF) 41

3.1.2 X-Ray Diffraction (XRD) 42

3.1.3 Fourier-transform infrared spectroscopy (FT-IR) 42

3.1.4 Confocal Microscope 43

3.1.5 Scanning Electron Microscope and Energy Dispersive X-ray Spectroscopy (SEM-EDS) 46

3.2 Thermal Characterization 46

3.3 Rheological characterization 47

3.4 Physical-mechanical characterization 48

3.4.1 Inductively coupled plasma - optical emission spectrometry (ICP-OES) 45

3.4.2 Helium pycnometer 48

3.4.3 Freeze-thaw tests 49

3.4.4 Compressive and flexural strength resistance 50

4 Results and discussion 52

4.1 Raw powdered materials 52

4.1.1 Mineralogical, chemical and molecular characterization 52

4.1.2 Thermal characterization 57
4.2 Formulation of granophyre sludge-based AAMs 59
4.2.1 Binary mixtures design development 59
4.2.2 Mineralogical and molecular characterization 62
4.2.3 Morphological and mechanical characterization 66
4.3 Advanced characterisation of the optimal GSW-based formulation 70
4.3.1 Morphological characterization with confocal microscope 70
4.3.2 Thermal characterization 71
4.3.3 Rheological characterization 72
4.3.4 Freeze-thaw tests 75
4.4 Basalt sawing waste AAMs 77
4.4.1 Mineralogical, molecular and morphological characterization 77
4.4.2 Thermal characterization 80
4.4.3 Rheological characterization 81
4.4.4 Freeze-thaw resistance test 84
4.4.5 Mechanical characterization of FB45 85
4.5 Comparison between GSW- and BSW-based binders 86
4.6 Development of fibre-reinforced Granite Sawing Waste-based AAMs 89
4.6.1 Morphological and chemical characterization 89
4.6.2 Chemical, Physical and mechanical characterization 96
4.7 Development of fibre-reinforced Basalt Sawing Waste-based AAMs 106
4.7.1 Morphological characterization 106
4.7.2 Chemical, Physical and mechanical characterization 112
4.8 Comparison between fibre-reinforced binders 121
5 Conclusions 125
6 I Case study: Preliminary evaluation of Design of Experiments (DoE) approach for the prediction of new Alkaline-Activated Materials (AAMs) formulations 127
6.1 Introduction 127
6.2 Materials and methods 129
6.2.1 Raw materials 129

6.2.2 Design parameters 130
6.2.3 Preparation process 133
6.2.4 Analytical methods 133
6.3 Results and discussion 134
6.3.1 Mineralogical and molecular analysis 134
6.3.2 Mechanical characterization 141
6.3.3 Conductivity measurements 142
6.4 Evaluation of the statistical model 143
6.4.1 Compressive strength 143
6.4.2 Ionic conductivity 146
6.5 Prediction 149
6.6 Conclusion 151
7 II Case study: Influence of activator molarity and Waste-Glass-to-Volcanic-Ash ratios on microstructure of potassium-based alkali-activated pastes 153
7.1 Introduction 154
7.2 Materials 157
7.3 Methods 160
7.4 Results and discussion 162
7.4.1 Structural data 162
7.4.2 Physical-mechanical data 177
7.5 Conclusion 181
8 III Case study: Insight on the rheological properties of Alkali Activated Materials for 3D printing applications 183
8.1 Introduction 183
8.2 Materials and methods 186
8.2.1 Materials 186
8.2.2 Methods 187
8.3 Results and discussion 189
8.3.1 Chemical characterization 189
8.3.2 Rheological characterization 190
8.3.3 Kinetics of the consolidation reactions and thermal stability in the early stages 195
8.3.4 Characterization of 3D printed specimens 196
8.4 Conclusion 200

9 Bibliography 202

List of figures

Figure 1 - Carbon dioxide emissions, expressed in million metric tons, from the manufacture of cement worldwide from 1960 to 2023 (taken from [5]) 19
Figure 2 - Alkaline activation reaction of aluminosilicate powders (taken from [14]). 21
Figure 3 - Alkali-Activated Materials (AAMs) vs Geopolymers (taken from [18]). 23
Figure 4 - Chemical structures of geopolymers (low-calcium precursors) (a), and alkali-activated materials (high-calcium precursors) (b) (taken from [17]). 24
Figure 5 - Structural scheme of the central Mediterranean domains (taken from [44]). 29
Figure 6 - Structural scheme of Sicily (taken from [45]). 30
Figure 7 - Excerpt from the geological map of the Varese province (taken from [57]). 33
Figure 8 - Geological map of Mt. Etna. The red area indicates the volcanic building while the back circle denotes the location of the A. M. Basalti company (modified after [62]). 35
Figure 9 - Google Earth image of Varese province and Cuasso al Monte area. The red circle denotes the Bonomi Quarry. 36
Figure 10 - GSW as received before the drying process (a); and after drying while sieving (b). 36
Figure 11 - Structure modification according to increasing calcination temperature (taken from [65]). 38
Figure 12 Components of a confocal microscope (a); Scanning mirror functioning (b) (taken from [81]) 44
Figure 13 - XRD patterns of raw materials: Granophyre sawing waste sludge (GSW); Basalt sawing waste sludges (BSW); Metakaolin (MK). 54
Figure 14 - FT-IR spectra of the raw powders. 57
Figure 15 – Thermal characterization of the raw materials: TG (a) and DTA (b). 58
Figure 16 – X-Ray Diffraction patterns of the consolidated materials: activated with 8M NaOH (a) and 9.9M NaOH (b). 63
Figure 17 – FT-IR spectra of the consolidated materials activated with 8M NaOH (a) and 9.9M NaOH (b). 65
Figure 18 – SEM micrographs of specimens GSW5-40 (a), GSW6-40 (b), GSW7-40 (c), and GSW8-40 (d). Red circles indicate the points selected for EDS analysis; red arrows identify unreacted mineral relicts and efflorescence (5d). 67
Figure 19 – SEM micrographs of specimens GSW5-1H2O (a), GSW3-1H2O (b) and GSW4-1H2O (c). Red circles denote the points where EDS analysis was carried out. 68
Figure 20 - Confocal micrograph of GSW6-40 specimen. Lateral dimensions, expressed in microns (μm), are reported on the x and y axes. The total represented area is of ~1684 × 1408 μm. 71

Figure 21 - Thermal analysis of GSW6-40. 72
Figure 22 - Rheological behaviours of materials without a threshold stress (a) and with yield stress (b) (modified from [148]). Curves represent the Newtonian (1), Pseudoplastic (2), Dilatant (3), Bingham fluids (4), Casson fluids (5). 47
Figure 23 - Rheological characterization of GSW6-40: structural rebuilding test. 73
Figure 24 - Strain sweep test of GSW6-40 paste. 74
Figure 25 - Shear stress and strain curve of GSW6-40 paste. 74
Figure 26 - Flow curve of GSW6-40 paste. 75
Figure 27 – Appearance of specimens before (a) and after (b) the freeze-thaw cycles. 76
Figure 28 - X-ray diffraction pattern of consolidated FB45. 78
Figure 29 - FT-IR spectra of the consolidated AAMs based on BSW (FB45). 79
Figure 30 – Confocal microscope micrograph of specimen FB45. Lateral dimensions, expressed in microns (μm), are reported on the x and y axes. The total represented area is of ~1684 × 1408 μm. 80
Figure 31 - Thermogravimetric (TG) and differential thermal analysis (DTA) curves of FB45. 81
Figure 32 - Rheological characterization of FB45: structural rebuilding test. 82
Figure 33 - Strain sweep test of FB45 paste. 83
Figure 34 - Shear stress and strain curve of FB45 paste. 83
Figure 35 - Shear stress and shear rate curve of FB45 paste. 84
Figure 36 – Appearance of FB45 consolidated specimens before (a) and after (b) the freeze-thaw test. 85
Figure 37 – EDS compositional map of GSW consolidated materials reinforced with palm fibres. The grey image represents the BSE image, while the coloured maps show the elemental distribution of carbon (C), oxygen (O), sodium (Na), calcium (Ca), aluminium (Al), silicon (Si), and potassium (K), respectively. 90
Figure 38 - EDS compositional map of GSW consolidated materials reinforced with prickly pear fibres. The grey image represents the BSE image, while the coloured maps show the elemental distribution of carbon (C), oxygen (O), sodium (Na), calcium (Ca), aluminium (Al), silicon (Si), and potassium (K), respectively. 91
Figure 39 - EDS compositional map of GSW consolidated materials reinforced with carbon fibres. The grey image represents the BSE image, while the coloured maps show the elemental distribution of carbon (C), oxygen (O), sodium (Na), calcium (Ca), aluminium (Al), silicon (Si), and potassium (K), respectively. 92
Figure 40 - Flexural strength resistance of AAMs based on GSW reinforced with increasing percentages (0.5–2 wt.%) of palm (black), prickly pear (grey), and carbon fibres (green). 102
Figure 41 - Compressive strength of AAMs based on GSW reinforced with increasing percentages (0.5–2%) of palm (black), prickly pear (grey), and carbon fibres (green). 105
Figure 42 - EDS compositional maps of FB45 consolidated material reinforced with palm fibres. The grey image represents the BSE image, while the coloured maps

show the elemental distribution of carbon (C), oxygen (O), sodium (Na), calcium (Ca), aluminium (Al), silicon (Si), and potassium (K), respectively. 107
Figure 43 - EDS compositional maps of FB45 consolidated material reinforced with prickly pear fibres. The grey image represents the BSE image, while the coloured maps show the elemental distribution of carbon (C), oxygen (O), sodium (Na), calcium (Ca), aluminium (Al), silicon (Si), and potassium (K), respectively..... 108
Figure 44 - EDS compositional maps of FB45 consolidated material reinforced with carbon fibres. The grey image represents the BSE image, while the coloured maps show the elemental distribution of carbon (C), oxygen (O), sodium (Na), calcium (Ca), aluminium (Al), silicon (Si), and potassium (K), respectively. 109
Figure 45 - Flexural strength of AAMs based on FB45 reinforced with increasing percentages (0.5–2%) of palm (black), prickly pear (grey), and carbon fibres (green). 118
Figure 46 - Compressive strength of AAMs based on FB45 reinforced with increasing percentages (0.5–2%) of palm (black), prickly pear (grey), and carbon fibres (green). 121
Figure 47 - Flexural vs compressive strengths of reinforced and unreinforced specimens based on granite and basalt sawing wastes. 123
Figure 48 - Compressive strength vs total porosity of reinforced and unreinforced specimens based on granite and basalt sawing wastes. 124
Figure 49 - X-Ray diffraction patterns of raw materials. 135
Figure 50 - Diffractograms of consolidated samples. 136
Figure 51 - Relationship between the measured real (grey squares) and theoretical (black circles) amorphous phase contents, Na/Si (dark red triangles pointing upwards) and Al/Si (red triangles pointing downwards) molar ratios. 138
Figure 52 - DRIFT spectra of consolidated AAMs and raw materials. 139
Figure 53 - Shift of T-O band in function of Si/Al molar ratio. 140
Figure 54 - Average compressive strength of specimens in relation to the shift of stretching vibration of T-O bond, where T= Si or Al (indicated by the black squares). Error bars indicate the standard deviation for compressive strength. 142
Figure 55 - Leverage plots for each factor influencing the compressive strength: FB (a), MK (b), NaOH (c), Na2SiO3 (d). 144
Figure 56 - Leverage plots for each factor influencing the conductivity: FB (a), MK (b), NaOH (c), Na2SiO3 (d). 148
Figure 57 - Prevision profiler from JMP software. For each factor, the graphs displayed the response variation according to compositional changes (black solid line), with the 95% confidence interval (grey shaded area). The selected composition is indicated by the red dotted lines and numbers above each factor. The corresponding responses for conductivity and compressive strength, with their confidence intervals, are shown in brackets in red and blue, respectively. 150
Figure 58 - Compositional ternary diagram of the three binary mixtures VG4 (●), VG1.5 (■), and G (▲), based on the weighted contribution of Al2O3, SiO2 and alkali within the raw materials. Alkali includes: Na2O, MgO and K2O. 160

Figure 59 - XRD patterns of both precursors (V and G) and synthetized materials differentiated by the ratio of the solid mixtures: VG1.5(7) and VG1.5(9); VG4(7) and VG4(9)..... 163
Figure 60 - FT-IR spectra of both precursors and synthetized materials activated with 7M (a) and 9M (b) KOH solutions. 166
Figure 61 - SEM micrographs and EDS profiles of G(7) (a) and G(9) (b) samples. Circles, indicating the spot analysis, are distinguished as follows: red - matrix; black – glass grain. 169
Figure 62 - SEM micrographs and EDS chemical composition: a) VG1.5(7); b) VG1.5(9); c) VG4(7); d) VG4(9). Circles, indicating the spot analysis, are distinguished as follows: blue - matrix; red - volcanic ash grain; black – glass grain. 174
Figure 63 - EDS maps: a) VG1.5(9); b) VG4(9); c) VG4(7). Colours are referred to the following elements: red – Fe; green – Ca; pink – Si; blue – Al; cyan – Mg. 177
Figure 64 - Synthesis procedure..... 187
Figure 65 - CAD file design..... 189
Figure 66 - Viscosity recovery for the studied inks at 0 minutes (a); 1 hour (b) and 2 hours (c). The lines represent: black VG1.5(7); red: VG1.5(9); blue VG4(7) and green VG4(9). 191
Figure 67 - Storage Modulus (G') and Loss Modulus (G''), expressed in Pa, for each studied ink. The lines represent: black VG1.5(7); red: VG1.5(9); blue VG4(7) and green VG4(9). Solid line corresponds to G' while the dashed line stands for G''. 192
Figure 68 - Shear Stress, expressed in Pa, and Strain for each studied ink. The lines represent: black VG1.5(7); red: VG1.5(9); blue VG4(7) and green VG4(9)..... 193
Figure 69 - Flow curves for all inks. The lines represent: black VG1.5(7); red: VG1.5(9); blue VG4(7) and green VG4(9)..... 194
Figure 70 - TG (black) and DSC (red) curves of VG1.5(9)..... 196
Figure 71 - Preliminary printing trial of VG1.5(9) without the addition of PEG. 197
Figure 72 - 3D printed specimens: whole specimen (a); top view (b); side view (c). 198
Figure 73 - Morphological micrographs: cross sectional view (a); detailed morphological surface (b). 198
Figure 74 - EDS compositional map: image top left represents the whole composition..... 199
Figure 75 - Breakage behaviour. 200

List of Tables

Table 1 - Final hydration products according to the type of binder. R refers to alkali (Na, K) or alkaline-earth (Ca, Mg) elemens (taken from [17]). 23
Table 2 - Technical data of the carbon fibres, provided by the company. 39
Table 3 - XRF analysis of the raw precursors: Granophyre sawing waste (GSW), Basalt sawing waste (BSW) and Metakaolin (MK). Alkali includes: Na_2O and K_2O. Other includes: TiO_2, P_2O_5 and MnO. 53
Table 4 – Mineralogical and amorphous phase contents of the raw precursors: Granophyre sawing waste (GSW), Basalt sawing waste (BSW), and Metakaolin (MK). 55
Table 5 - Elemental release of raw materials in 8M NaOH solution. Na was not evaluated due to the high concentration of the element in the solution. Calcium detection limit (DL) is 0.49 mg/L; Ti detection limit is 0.05 mg/L. 56
Table 6 - TG analysis events. 59
Table 7 - DTA reactions. 59
Table 8 – Formulation details of the synthesized AAMs and the integrity test results after 28 days. 61
Table 9 – Measured and theoretical amorphous amount (wt. %) for the selected consolidated specimens. 64
Table 10 – Chemical composition of the specimens was determined through Energy Dispersive Spectroscopy (EDS), with elemental abundances expressed in weight percent. 69
Table 11 – Uniaxial compressive strength values, expressed in MPa and their standard deviations. 70
Table 12 - Freeze-thaw tests: initial mass (m_i); final mass after 75 cycles (m_f); mass difference (Δm) in weight percentage. 76
Table 13 - Formulation of AAMs based on basalt sawing waste. 77
Table 14 - Amorphous phase of consolidated FB45. 79
Table 15 - Freeze-thaw tests of FB45 specimens: initial mass (m_i); final mass after the 75 cycles (m_f); mass difference in weight percentage (Δm). 85
Table 16 - Mechanical performances of FB45. 86
Table 17 - Roughness data, obtained by confocal microscope, of GSW-based AAMs with different percentages of palm fibres (from 0.5 to 2%). Data of the specimen without any fibres are also reported for comparison. Used parameters: Arithmetic mean height (Sa) and Root Mean Square (RMS). 94
Table 18 - Roughness data, obtained by confocal microscope, of GSW-based AAMs with different percentages of prickly pear fibres (from 0.5 to 2%). Data of the specimen without any fibres are also reported for comparison. Used parameters: Arithmetic mean height (Sa) and Root Mean Square (RMS). 94
Table 19 - Roughness data, obtained by confocal microscope, of GSW-based AAMs with different percentages of carbon fibres (from 0.5 to 2%). Data of the specimen

without any fibres are also reported for comparison. Used parameters: Arithmetic mean height (Sa) and Root Mean Square (RMS)..... 95
Table 20 - ICP-OES results of the released elements in solutions. Elements are expressed in mg/L. DL= detection limit. Al= 0.03; Ca= 0.01; Fe= 0.02; K= 0.02; Mg= 0.02; Na= 2.1; P=0.19; Si=0.03; Ti= 0.01; B=0.023..... 97
Table 21 - Porosity values of AAMs based on GSW reinforced with palm fibres. The values of the specimen without fibres are reported for comparison. 97
Table 22 - Porosity values of AAMs based on GSW reinforced with prickly pear fibres. The values of the specimen without fibres are reported for comparison. .. 98
Table 23 - Porosity values of AAMs based on GSW reinforced with carbon fibres. The values of the specimen without fibres are reported for comparison. 99
Table 24 - Average Flexural Strength and standard deviation of GSW-based AAMs reinforced with palm fibres. Flexural strength of the specimen without fibres is reported for comparison. 100
Table 25 - Average Flexural Strength and standard deviation of GSW-based AAMs reinforced with prickly pear fibres. Flexural strength of the specimen without fibres is reported for comparison. 100
Table 26 - Average Flexural Strength and standard deviation of GSW-based AAMs reinforced with carbon fibres. Flexural strength of the specimen without fibres is reported for comparison. 101
Table 27- Average Compressive Strength and standard deviation of GSW-based AAMs reinforced with palm fibres. Compressive strength of the specimen without fibres is reported for comparison. 103
Table 28 - Average Compressive Strength and standard deviation of GSW-based AAMs reinforced with prickly pear fibres. Compressive strength of the specimen without fibres is reported for comparison. 103
Table 29 - Average Compressive Strength and standard deviation of GSW-based AAMs reinforced with carbon fibres. Compressive strength of the specimen without fibres is reported for comparison. 104
Table 30 - Roughness data, obtained by confocal microscope, of BSW-based AAMs with different percentages of palm fibres (from 0.5 to 2%). Data of the specimen without any fibres are also reported for comparison. Used parameters: Arithmetic mean height (Sa) and Root Mean Square (RMS).....110
Table 31 - Roughness data, obtained by confocal microscope, of BSW-based AAMs with different percentages of prickly pear fibres (from 0.5 to 2%). Data of the specimen without any fibres are also reported for comparison. Used parameters: Arithmetic mean height (Sa) and Root Mean Square (RMS). 111
Table 32 - Roughness data, obtained by confocal microscope, of BSW-based AAMs with different percentages of carbon fibres (from 0.5 to 2%). Data of the specimen without any fibres are also reported for comparison. Used parameters: Arithmetic mean height (Sa) and Root Mean Square (RMS).....112
Table 33 - ICP-OES results of the released elements in solutions. Elements are expressed in mg/L. DL= detection limit. Al= 0.03; Ca= 0.01; Fe= 0.02; K= 0.02; Mg= 0.02; Na= 2.1; P=0.19; Si=0.03; Ti= 0.01; B=0.023.....113

Table 34 - Porosity values of AAMs based on FB45 reinforced with palm fibres. The values of the specimen without fibres are reported for comparison. 114
Table 35 - Porosity values of AAMs based on FB45 reinforced with prickly pear fibres. The values of the specimen without fibres are reported for comparison. .114
Table 36 - Porosity values of AAMs based on FB45 reinforced with carbon fibres. The values of the specimen without fibres are reported for comparison. 115
Table 37 - Average Flexural Strength and standard deviation of FB45 AAMs reinforced with palm fibres. Flexural strength of the specimen without fibres is reported for comparison. 116
Table 38 - Average Flexural Strength and standard deviation of FB45 AAMs reinforced with prickly pear fibres. Flexural strength of the specimen without fibres is reported for comparison. 116
Table 39 - Average Flexural Strength and standard deviation of FB45 AAMs reinforced with carbon fibres. Flexural strength of the specimen without fibres is reported for comparison. 117
Table 40 - Average Compressive Strength and standard deviation of FB45 AAMs reinforced with palm fibres. Compressive strength of the specimen without fibres is reported for comparison. 119
Table 41 - Average Compressive Strength and standard deviation of FB45 AAMs reinforced with prickly pear fibres. Compressive strength of the specimen without fibres is reported for comparison. 119
Table 42 - Average Compressive Strength and standard deviation of FB45 AAMs reinforced with carbon fibres. Compressive strength of the specimen without fibres is reported for comparison. 120
Table 43 - XRF of major chemical composition of the basalt sawing sludge (FB) and metakaolin (MK) precursors. The abundances are expressed as anhydrous weight percent of the oxides, and the given standard deviation from the instrument is reported. 130
Table 44 - Low and high levels of the considered factors. 130
Table 45 - Set of experiments. L/S states for the liquid to solid ratio, calculated by dividing the sum of the alkaline solutions and the sum of the powdered raw precursors. 131
Table 46 - Calculated chemical composition of the binary mixtures expressed in wt. % of the oxides. The molar ratios are calculated based on the weight percentages of the oxides and reported as Si/Al, Na/Si, Na/Al out of simplicity. 132
Table 47 - Real measured and theoretical calculated amorphous phase of raw and consolidated materials. 137
Table 48 - Ionic conductivity of the studied specimens. 143
Table 49 - Estimate parameters, standards errors and probabilities of each term for compressive strength resistance. 145
Table 50 - Estimate parameters, standards errors and probabilities of each term for conductivity measurements. 148
Table 51 - Experimental Compressive Strength values of predicted formulations and the experimental values obtained after testing. 150

Table 52 - Experimental conductivity of predicted formulations and the obtained experimental values after measurements. 151
Table 53 - Chemical composition of the investigated waste precursors in wt.%, volcanic ash (V) and waste glass (G) obtained respectively from previous works [321,325]. The abundances are expressed as weight % of oxides. Alkali = Na2O, MgO and K_2O; Other: includes B_2O_3 (for only G), P_2O_5 and MnO (for only V). 158
Table 54 - Nomenclature and composition of the different mix design formulations. Letters “V” and “G” refers to Volcanic ash and Glass, respectively. The numbers in parentheses represent molarity of the used activating solution..... 159
Table 55 - EDS chemical composition, expressed in atomic percentages (a.t.%), of the matrix for all consolidated samples..... 175
Table 56 - Physical-Mechanical properties: weight loss after boiling test (ΔM, %); open porosity (OP, %]); total porosity (TP, %); pH; uniaxial compressive strength (σ, MPa). 180
Table 57 - ICP-OES results of the released elements in solutions. Elements are expressed in mg/L. 181
Table 58 - Chemical composition of the studied raw waste materials obtained though XRF. Oxides are expressed in weight percentage. 190

Preface

This doctoral thesis was written as part of the Ph.D. program in Earth and Environmental Sciences of the University of Catania and focuses on the development of reinforced Alkali Activated Materials (AAMs) for cultural heritage restoration. The research aims to explore the production of innovative and sustainable materials, made from industrial wastes and by-products, to reduce the carbon footprint of the conventional used materials in the construction and restoration industries.

Granophyre and basalt sludges were used as precursors for the development of AAMs. The reason behind the selection of these materials is that they represent a waste, usually landfilled, that is largely produced during stone processing (i.e., cutting, polishing). Therefore, the valorisation of these sludges is intended through alkaline activation processes, meeting the principles of circular economy and developing efficient binders.

Moreover, this study explores the incorporation of local natural and synthetic fibres to enhance the mechanical properties of the alkali activated binders. Specifically, the addition of fibres reduces the well-known brittle nature of AAMs, making them suitable for the application in seismic areas where the disastrous failure of the materials has to be avoided. The fibres were chosen according to their physical properties, availability and ~~the~~ environmental impact.

This thesis is made up of eight chapters that investigate specific areas of the research. Chapter 1 introduces the current state of art of the studied field, including a comparison between Ordinary Portland Cement (OPC) and AAMs and the regulatory framework related to waste reuse in Italy. Chapter 2 reports the selected raw materials, alkaline solutions and fibres, including providers. Chapter 3 deeply outlines the applied experimental methods. Chapter 4 deals with the presentation and discussion of the results, starting with the characterization of the raw materials (granophyre and basalt sawing sludges and metakaolin), which included chemical, mineralogical, molecular and thermal analysis to assess the feasibility of using them as precursors. The development of the formulations and subsequent characterization and testing of the consolidated and reinforced materials is then reported. The conclusions are outlined in Chapter 5.

The final part of the thesis is represented by Chapters 6 to 8 where three different case studies are reported, with the aim of widening the potential application fields of the construction and restoration materials. The first case study investigated a Design of Experiments (DoE) approach for predictive modelling of new AAMs formulations. The second case study explored the effects of different activator concentrations and waste glass-to-volcanic ash ratios on potassium-based AAMs. Both glass and volcanic ash are wastes which are generally landfilled. The case study aims to contribute to a better understanding on the influence of these variables on the development of the microstructure and on the final physical-mechanical features. The third case study focused on the investigation of the rheological behaviour of AAMs for 3D printing applications.

This thesis adopted an interdisciplinary approach, combining geosciences, chemistry and materials engineering. The research was also supported by collaboration and training carried out at the Centre for Functional and Surface Functionalized Glass (FunGlass) in Slovakia, which significantly contributed to widen the experimental phases.

This thesis aims to widen the state of the art in the field of sustainable construction materials, opening new paths for the reuse of industrial wastes for the conservation of cultural heritage. Furthermore, the development of innovative and low impact materials for application in seismic areas is explored.

1 Introduction

In recent years, the need for a sustainable development has become a crucial goal for our society. Indeed, there has been a growing awareness on how much the mankind has a negative impact on the environment and, more in general, on our planet. This is manly caused by the rapid industrialisation and ongoing urbanisation of our cities, followed by the continued demand and depletion of resources. The enhanced attention on environmental issues, is particularly observed among the younger generation and it has led to widespread protests, strikes and to the constitution of movements such as 'Fridays for Future', guided by Greta Thunberg [1].

Moreover, in 2015 the United Nations approved 17 Sustainable Development Goals (SDGs) by the creation of the 2030 Agenda for Sustainable Development [2]. The aim of this program is for society to become concretely more conscious and focused on sustainability, guiding countries towards the creation of environmentally conscious communities [3]. The need to convert key fields, including the construction sector, to more eco-friendly fields was also highlighted. In fact, the construction industry has been recognised as one of the major end users of non-renewable resources, as well as a large producer of carbon dioxide (CO_2) [4]. In particular, the cement industry has led to a significant and steady increase in carbon dioxide emissions from global cement production, as reported in Figure 1 from 1960 to 2023, with emissions up to over 1500 million metric tons [5].

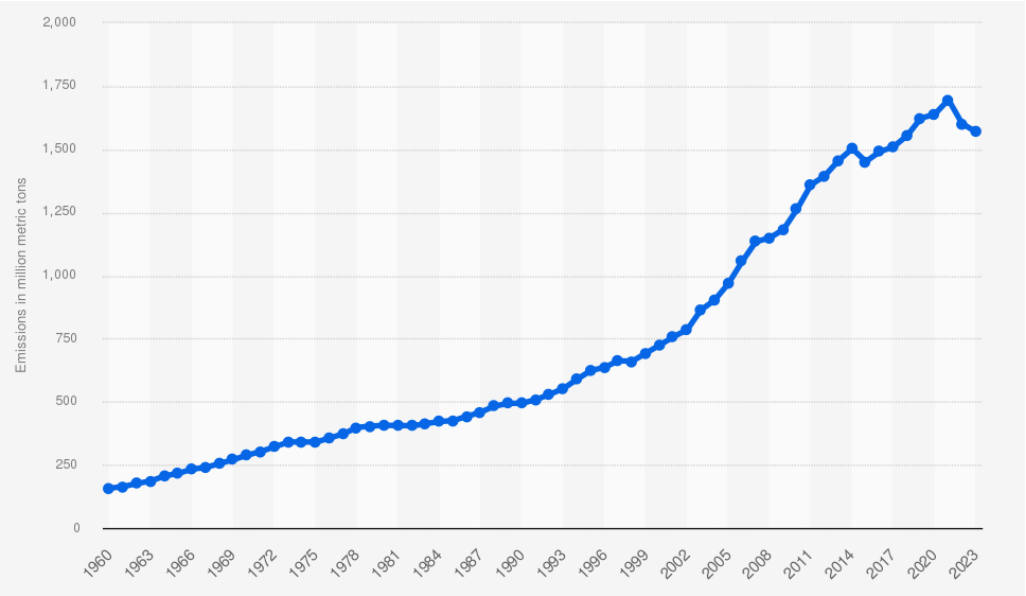

Figure 1 - Carbon dioxide emissions, expressed in million metric tons, from the manufacture of cement worldwide from 1960 to 2023 (taken from [5])

This chapter will explore the potentiality of using Alkali Activated Materials (AAMs) as new alternative binders to Ordinary Portland Cement (OPC) which is nowadays the most used binder in the construction field. Moreover, an insight on the activation reaction, properties and new frontiers in the development of these materials are investigated.

1.1 Ordinary Portland Cement (OPC) vs Alkali Activated Materials (AAMs) and Geopolymers

The construction and cement industries are responsible for about 7-8% of global anthropogenic CO_2 emissions [6]. This is related to the Portland cement production process, which involves calcining limestone at high temperatures to produce clinker [7]. In particular, it is estimated that the production of one tonne of cement leads to the emission of the same amount of CO_2 into the atmosphere. The high demand for energy, coupled with the progressive depletion of raw materials, makes this model unsustainable in the long term [8]. Considering the dual need to reduce emissions and maintain a robust infrastructure, thanks to government regulations and funding

incentives, scientists have been stimulated to conduct research to find more sustainable and low-impact alternative materials for construction purposes.
In this context, Alkali Activated Materials (AAMs) and Geopolymers have emerged as promising candidates due to their significant environmental benefits, resource use efficiency and comparable performances (i.e., mechanical properties, durability, chemical resistance in aggressive environments) to traditional cementitious systems [9]. These materials provide the possibility of being produced at room or at low temperatures and of incorporating industrial by-products such as fly ash, blast furnace slag, sawing sludge and discarded glass that can no longer be recycled, thus avoiding the problems associated with landfill disposal and promoting the principles of the circular economy [10]. Moreover, the versatility of the formulations to be tailored according to the desired final performance, makes them attractive for several applications in the construction sector [11].

In the late 1970s, Joseph Davidovits first adopted the term ‘geopolymer’, discovering that aluminosilicate sources could be activated in alkaline environments to form polymer chains of polysialates, a process known as geopolymerisation [12]. Over the years, these materials have been extensively studied, leading to an in-depth understanding of their chemical and physical behaviour, structural properties and possible applications.
The geopolymerisation reaction, described for the first time by Glukhovsky in 1967 [13], is a complex process composed of several steps, briefly summarized as follow: dissolution of aluminosilicate powders in a highly alkaline environment, followed by the condensation of the dissolved species into a three-dimensional structure ranging from amorphous to semi-crystalline [14]. The chemical mechanism typically occurs according to the following steps, as displayed in Figure 2 - Alkaline activation reaction of aluminosilicate powders (taken from [14]):

1. Dissociation and dissolution of the aluminosilicates;
2. Propagation and orientation of the free silicate and aluminosilicate species;
3. Polycondensation in oligomeric species;
4. Further polymerization to form a hardened matrix of repeated tetrahedra of -Si-O-Al-O- structural units.

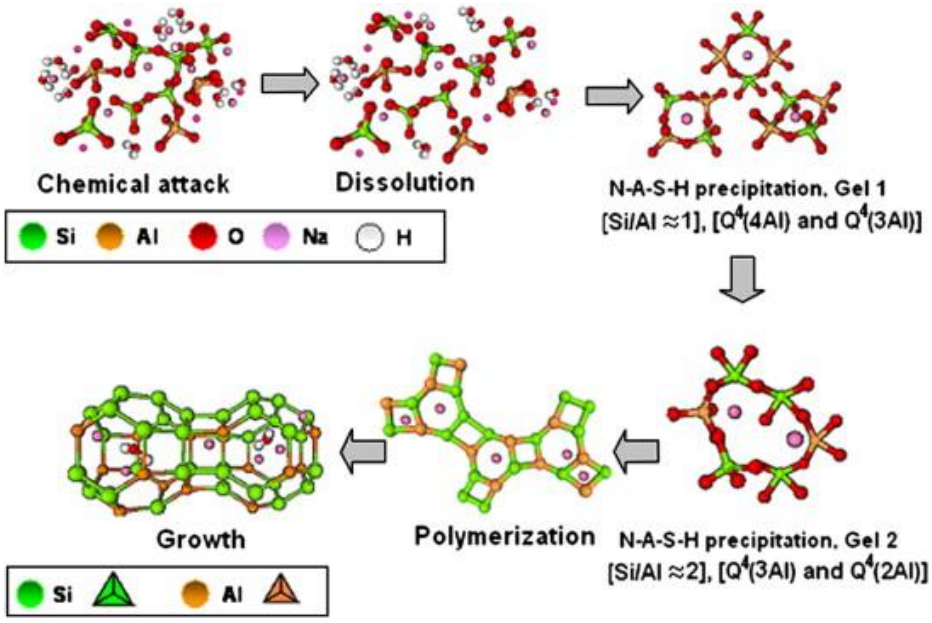

Figure 2 - Alkaline activation reaction of aluminosilicate powders (taken from [14]).

1.2 Alkali-activated Materials vs Geopolymers

Although the terms 'geopolymer' and 'alkaline-activated materials' are often used as synonyms, they refer to compositionally different final reaction products. This difference in the chemical composition has a strong influence on the chemistry, microstructure, and performances of the final consolidated materials. Even though both materials refer to the activation of aluminosilicate powders, alkaline-activated materials involve the activation of any binder in a high pH environment, including systems with a high calcium content and various types of activator solutions (sodium hydroxide, potassium hydroxide, sodium silicate, etc.). The heterogeneity in composition and the higher availability of calcium lead to the development of calcium-silicate-hydrate (C-S-H) gel as binding phase, similar to that observable in Portland Cement (with a lower Ca/Si ratio and greater incorporation of Al into the gel structure), together with the traditionally developed hydrated sodium/potassium aluminosilicate compounds (e.g., N-A-S-H) of geopolymer systems [15].

Table 1 reports the most common types of binders, the employed solid precursors and their chemical composition, related to the developed final hydration products. In particular, the chemical composition refers to calcium and alkaline metal (i.e., R_2O) oxides. Ordinary Portland Cement (OPC) is characterized by high calcium contents and very low alkali levels, which generates C-S-H (calcium hydrate silicate gel) as hydration product. OPC can also be found as Alkaline OPC or Blended OPC according to the presence of additional alkali or additional slags, respectively. These additions lead to chemical modification of the system, producing both C-S-H and N-A-S-H (hydrated sodium silica aluminate gel). Alkaline-activated binders, including materials based on slag or fly ash, exhibit variable CaO contents (up to 30 wt.%) and higher alkaline oxides levels (up to 10 wt.%), producing mainly but not exclusively N-A-S-H type. Geopolymers are obtained starting from low-Ca aluminosilicates (i.e., calcium levels below 5 wt.%) and high alkali levels (up to 20 wt.%), leading to the formation of N-A-S-H type gel only. Figure 3 displays the classification of different cementitious systems according to their calcium and aluminium contents. AAMs represent a wider class of binders, including materials with both high and low calcium contents. Specifically, high calcium systems lead to the formation of C-A-S-H gel, while low calcium contents favour the development of N-A-S-H type gel. Geopolymers represent a subcategory of alkaline-activated materials and refer only to binders consisting of aluminosilicate precursors that are characterised by an amorphous three-dimensional polymeric network of Si-O-Al bonds, similar to zeolites [16]. Portland-based and calcium sulfo-aluminate cements are binders with very high calcium content which lie outside the broader class of AAMs and are shown for comparison.

Binder Type	Solid Precursor	CaO (wt.%)	Na_2O/ K_2O (wt.%)	Hydration product	
OPC	OPC clinker	60-70	<0.6	0%	100%
Alkaline OPC	OPC clinker + R_2O	40-50	1-5	R_2O-Al_2O_3-SiO_2-H_2O (N-A-S-H)	RO-SiO_2-H_2O (C-S-H)
Blended OPC	OPC clinker + slag/Ash/basalt/red mud + R_2O	25-30	2-5		
Alkali activated slags	Metallurgical slag + R_2O	25-30	4-8		
Alkali activated fly ash	Fly ash from coal combustion + R_2O	0-25	5-10		
Geopolymers	Low-Ca aluminosilicates	0-5	10-20	100%	0%

Table 1 - Final hydration products according to the type of binder. R refers to alkali (Na, K) or alkaline-earth (Ca, Mg) elements (taken from [17]).

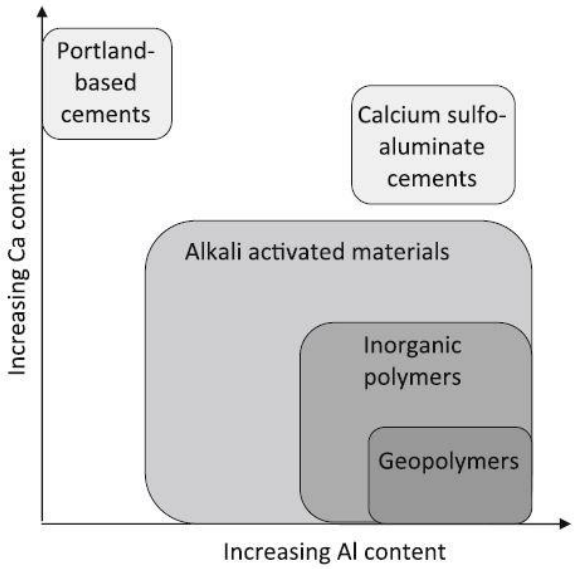

Figure 3 - Alkali-Activated Materials (AAMs) vs Geopolymers (taken from [18]).

The final materials will have different features, according to the mix design and thus the formed gel, as observed in Figure 4. For example, geopolymers usually have a denser structure, due to an extensive polymerization of $SiQ_4(nAl)$ units, which leads to highly cross-linked aluminosilicate network, resulting in an enhanced chemical resistance, lower permeability, and higher compressive strength compared to AAMs. On the contrary, AAMs are mainly characterized by less polymerized structures composed of SiQ_2 and $SiQ_2(1Al)$ units, with possible unreacted grains that produce a more heterogeneous matrix [16,19].

Furthermore, the precursor's reactivity plays a crucial role in the final performances of the materials. In geopolymers, the highly reactive precursors, such as metakaolin, easily dissolve in alkaline media thus facilitating the formation of well-developed N-A-S-H gel [20]. On the other hand, the industrial wastes or by-products have a lower reactivity, resulting in slower or partial activation. While AAMs provide rapid strength development, due to C-S-H gel formation, geopolymers have superior long-term performances due to their more stable and compact gel network [19].

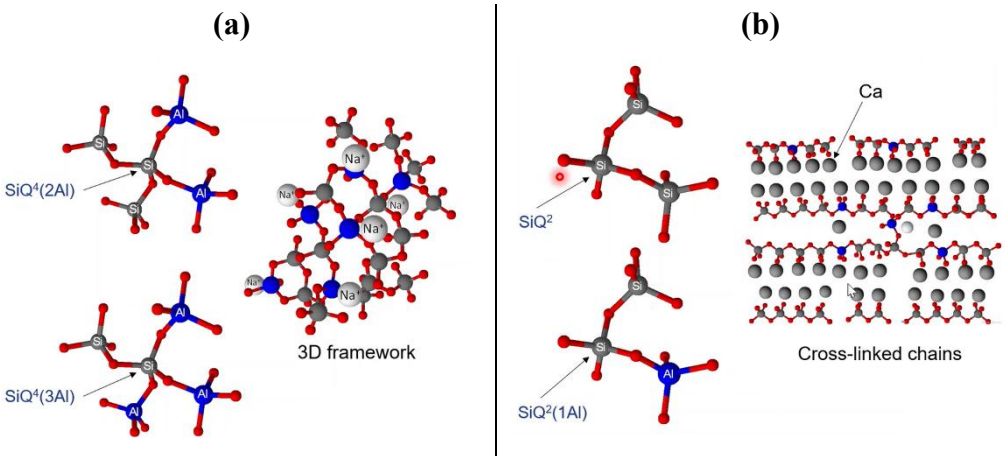

Figure 4 - Chemical structures of geopolymers (low-calcium precursors) (a), and alkali-activated materials (high-calcium precursors) (b) (taken from [17]).

Despite the differences in the final reaction products and properties, both AAMs and geopolymers offer promising alternative in the construction field. The variety

of properties make them suitable for different applications, ranging from restoration to highly aggressive or extreme environments fields.

1.3 Italian Waste Management Policies and regulatory framework

Italy is a large producer of non-hazardous wastes coming from both natural phenomena and industrial processes. Among these, the substantial amount of volcanic ash generated by the frequent eruptions of Mt. Etna (i.e., estimated to be, only for the eruptive event between the 31st of March and the 1st of April 2021, ~ 4 × 10^6 m^3, [21]) and the powders derived by the stone processing, including extraction, cutting and polishing (i.e., approximately 40% of the total stone) become waste [22]. If not properly managed, the disposal of these materials can create significative environmental problems. However, their chemical properties and large availability offer a good opportunity for their re-use [23,24].

The Italian waste management and the disposal of non-hazardous inert wastes in landfills is controlled by a complex regulatory framework. These laws changed over time in order to better fit with sustainable practices and the principles of the circular economy. One of the first innovative laws in terms of sustainability was the d. lgs. n. 22/1997, also known as "Decreto Ronchi", which aimed to promote the reduction and recovery of wastes by the recycling and enhancement of people awareness on environmental issues [25]. Afterwards, the d. lgs. n. 152/2006, also known as "Testo Unico Ambientale", introduced an improved regulation on the waste management. In the IV section, a specific ruling on the disposal of non-hazardous wastes (i.e., volcanic ash from Mt. Etna and wastes coming from the cutting processes of rocks) is outlined. In the text (article 185, comma 1, letter c), it is stated that the volcanic ash from Mt. Etna is considered as a special waste which must be subject to specific provisions for its collection, transport and re-use. In particular, if volcanic ash is reused as a replacement for raw materials within virtuous production cycles, through harmless processes for the environment and human health, it does not undergo waste treatment regulations [26,27]. Therefore, this material can be used to produce semi-processed or finished elements that meet the technical standards

required by industry regulations. The raw material must be first characterised to verify the absence of anthropogenic pollutants and assess levels of natural radioactivity [28]. This integrated approach promotes the circular economy, allowing for the aware conversion of materials, which otherwise would be disposed of, into valuable resources. Regarding the sawing sludges of rocks, such as marble, granite and basalt, the d. lgs. 152/2006 also include procedures for their processing, recovery, disposal and re-use. The main aim of the law is to reduce the environmental impact though sustainable practices involving the re-use of these raw materials in the industrial sector.

Integrating circular economy principles into the management of these special wastes not only reduces environmental impact but also promotes new economic opportunities through material recovery and reuse. Scientific research plays a crucial role in identifying effective solutions for the recovery and reuse of these materials, contributing to the promotion of the circular economy.

1.4 Fiber reinforced composites

In the last years, alkali activated materials have gained increasing attention thanks to their favourable properties and performances. Nevertheless, like other cementitious materials, AAMs suffer from brittle failure especially when subjected to flexural stress, leading to limited applications and shorter durability [4]. In this respect, in order to improve the general performances of these materials, fibres are added to the formulation. The addition of fibres is proven to reduce crack propagation (i.e., limiting the widths and expansion of cracks), resulting in enhanced physical and mechanical properties [29], such as flexural strength, fracture toughness, crack control, deformation and energy absorption [30]. The possibility to achieve these properties is due to the ability of the fibres to stop crack propagation by bearing part of the applied load even after microcracks are formed within the matrix, bridging microcracks and distributing stresses more evenly, thus improving the overall toughness of the material [31].

Moreover, some authors have demonstrated that the addition of fibres also positively affects the durability of these materials by reducing cracks and porosity

[32]. In fact, cracks can be considered as a preferential way for the transfer and mobility of external agents such as water, moisture, sulphates, chlorinates and carbonates, compromising their long-term performances [33]. Hence, the reduction of cracks is essential to increase the density of the microstructure, allowing a prolonged lifespan of the material.

The development of reinforced AAMs becomes important for the needs of the construction field, where materials with both environmental benefits and outstanding performances are required. The addition of fibres can further help scientists in designing materials with improved damage tolerance and structural safety, making these materials suitable for construction purposes in seismic regions or application that require advanced features [34]. Nowadays, many researchers are focusing on the field of reinforced AAMs, aiming to optimize the fibres' type and proportion in order to obtain improved performances. These efforts will lead to the development of a new eco-friendly and adaptable construction industry.

When talking about fibre-reinforced materials, the selection of the type of fibre plays a crucial role in the final behaviour of the material. Many fibres are currently used, including steel, carbon, glass, basalt and organic [35]. Each fibre can offer a variety of properties, according to the specific requirements and final applications. For example, steel fibres offer high splitting tensile and flexural strength, elasticity and durability, making them suitable for applications that require significant loading capacity and flexural resistance (i.e., structural elements) [36]. However, steel fibres are not recommended for aggressive environments (i.e., marine structures, bridge decks, transportation facilities, wastewater treatment plants, and coastal or salt-laden environments) as they suffer from corrosion that may end up affecting the reinforcement, eventually leading to deterioration and catastrophic failure of load-bearing elements [37,38]. In this context, glass fibres may be suitable, being resistant to corrosion and having low density, excellent flexural and shear strength [39]. In addition, polypropylene and polyvinyl fibres have also proved to be resistant to corrosion and to improve the compressive strength [40].

Moreover, carbon fibres are widely used thanks to their low density, still providing good strength and chemical stability. Although they are more expensive than other commercially available fibres, their properties make them ideal for lightweight and robust applications in both normal and extreme environments (i.e., structural,

offshore, aerospace, etc.), reducing the weight of the element while increasing the mechanical features [41]. Carbon fibres were shown to have a good influence on the drying shrinkage, brittleness and fracture toughness [42]. Recently, basalt fibres have become popular due to their high thermal stability, non-toxicity, low production cost, high resistance to chemical attack and corrosion [43]. Finally, the proper selection of the fibre is necessary to develop materials with tailored properties that satisfy the specific requirements, maximizing durability and mechanical performances of the final products.

1.5 Geological setting of the areas of interest

In this study, two Italian regions are considered of particular interest: Sicily and Lombardy. In these geographic areas, the sampling of the studied materials, extensively described in Chapter 34, occurred. This paragraph aims to provide an overall understanding on the complex geology of Italy with a focus on the geological setting and geodynamics that brought to the formation of the sampled areas.

The central Mediterranean area is made up of three structural geodynamic domains: the foreland, the orogenic, and the internal domains (Figure 5 - Structural scheme of the central Mediterranean domains (taken from [44]).

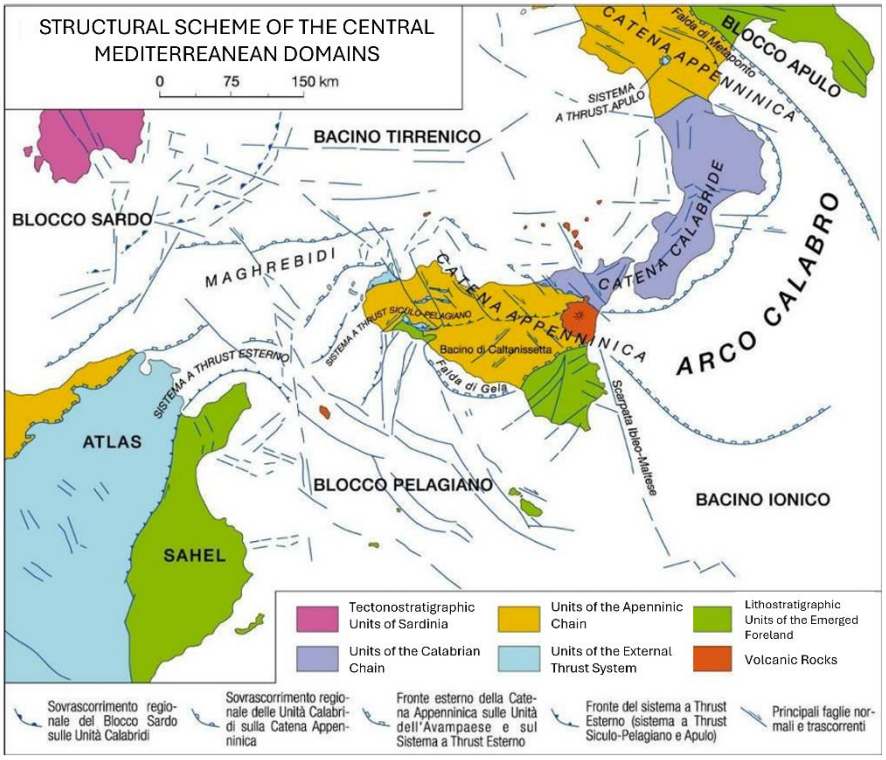

Figure 5 - Structural scheme of the central Mediterranean domains (taken from [44]).

The foreland domain includes undeformed areas such as the Pelagian block and the Ionian basin. The Orogenic domain can be divided into three overlaying structures [45]:

- The External Thrust System: it is a deep thrust system, comprising the units that belonged to the old Hybleo-Saccense foreland domain. It was formed during the late Miocene, while the Tyrrhenian Basin was opening.
- Apenninic- Maghrebian Chain: it derives from the deformation and stacking of both oceanic and continental sectors during the Miocene and Pliocene.
- Calabro-Peloritan Chain: it was formed due to the delamination of metamorphic rocks belonging to the continental European crust, starting from the late Eocene.

The internal domain is represented by the Tyrrhenian Basin and the Sardinia-Corsica Block, this latter belonging to the European crust [45].

The central Mediterranean area is highly complex, consisting of several tectonic units that originated from different geological and geodynamical domains.

Focusing on the eastern part of Sicily, its morphology is shaped by the presence of Mt. Etna Figure 6 - Structural scheme of Sicily.

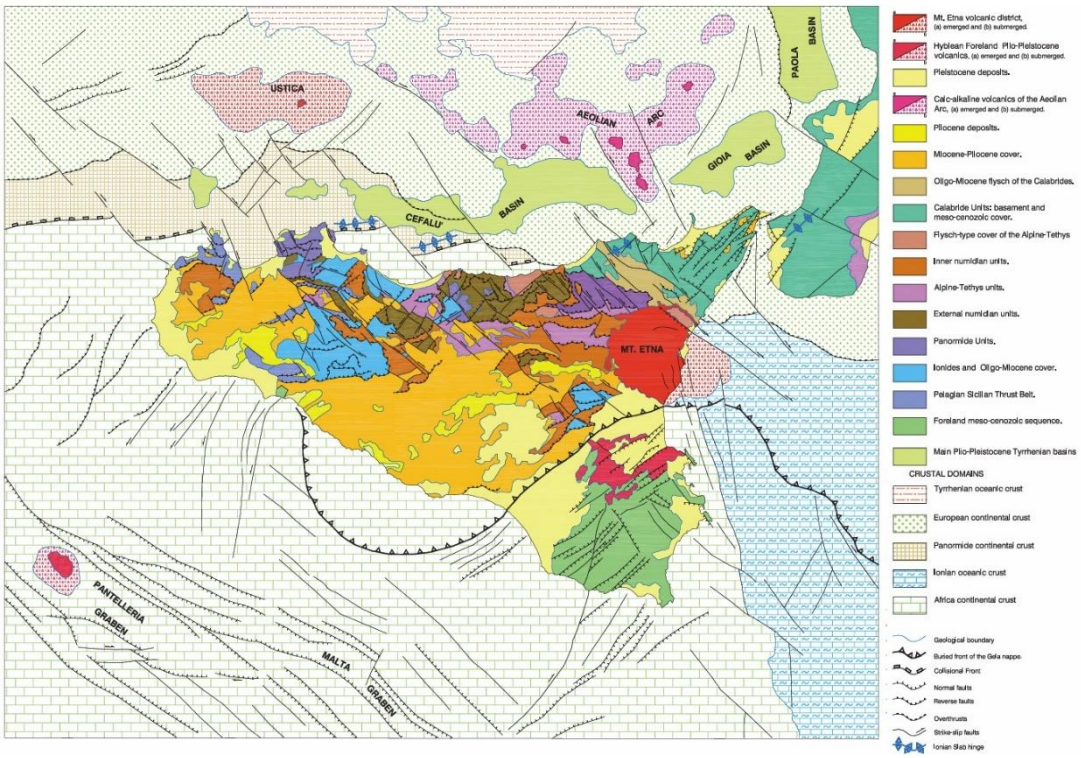

Figure 6 - Structural scheme of Sicily (taken from [45]).

Covering an area of 1200 km^2, Mt. Etna is one of the most active volcanoes in the world as well as the highest active volcano in Europe. It is located on the collision zone between the Eurasian and African plates and is characterized by the emission of mafic products. The complex evolution of Mt. Etna has been reconstructed through different studies and is divided into four phases [46–48]:

1. Tholeiitic phase: the earliest volcanic activities occurred under the sea, around 500 ka. Evidence of this can still be observed in Aci Castello and in its surrounding areas. The volcanic activity gradually shifted to subaerial eruptions due to the uplift of the eastern coast of Sicily (around 330 ka).
2. Timpe phase: starting from around 220 ka, the accumulation of numerous lava flows led to the formation of the first volcanic edifice. This phase ended around 110 ka.

3. Bove Valley phase: starting from 110 ka onward, the eruptive style began to change, shifting from fissure eruptions to central activities. During this phase, the first eruptive centres formed, with Trifoglietto being the largest. Moreover, the continuous overlapping of eruptive events led to the development of a stratovolcano structure.
4. Stratovolcano phase: the final phase began around 57 ka, when the eruptive activity migrated northwest, leading to the formation of the main edifice of Mt. Etna, known as "Ellittico". During this period, both effusive and explosive activities affected and shaped the morphology and hydrogeology of the volcano [49]. After an intense phase of eruptions, the Ellittico collapsed, forming a caldera. This caldera was subsequently filled and covered by newer volcanic products derived from the new crater. The new volcanic edifice was named "Mongibello". Mongibello experienced several consistent landslides, which contributed to the formation of the present-day Bove Valley [50].

Since the early development of the local community, Mt. Etna has influenced the social, economic, and urban landscape of the area. Even though Mongibello's activity is predominantly effusive, some particularly intense explosive eruptions, that had a significant impact on residents and infrastructures, occurred. One of the most destructive events dates back to 122 B.C., when severe damages were recorded due to the formation of the Caldera del Piano. The city of Catania was covered in ashes and lapilli, and the destruction was so extensive that the Roman government exempted the city from taxes for ten years, in order to support the economic recovery [51]. During the Middle Ages, numerous lava flows reached the low altitudes areas, posing a serious threat to towns and villages [52]. One of the most destructive episodes occurred in 1669 and is considered one of the most powerful volcanic events in the known history of Mt. Etna. The lava flow reached the coast, with a length of 17 Km and 600 million m^3 of erupted lava in only four months. Nine towns were destroyed and the lava eventually stopped against the walls of Castello Ursino, marking a crucial moment in the relationship between the volcano and the local population [53]. Moreover, the 20^{th} century is marked by an exponential growth in population within the areas surrounding Mt. Etna, leading to an increased volcanic risk. In fact, the 1928 eruption was the last highly destructive

episode which, in just 18 days, caused the complete destruction of the town of Mascali.

The geology of Lombardy region is very complex, shaped by many tectonic, sedimentary and magmatic events. The region is predominantly characterized by the presence of the Po Valley to the south, and the Southern Alps to the north. The Southern Alps are a mountain chain composed of a wide variety of rocks, ranging from the metamorphic basement of the Palaeozoic era to sedimentary sequences dating back to the Mesozoic and Cenozoic. The current structural configuration of the area is the result of the Alpine orogeny, which resulted in large folds and overthrusts, while late Palaeozoic magmatic activity led to the formation of granitic intrusions and volcanic rocks. Among the most relevant magmatic bodies in Lombardy is the Cuasso al Monte granophyre, located in the province of Varese, shown in Figure 7. It is a subvolcanic formation outcropping in the Monte San Giorgio area on the border between Italy and Switzerland. This intrusive body is linked to the Permian magmatism of the region and is closely connected with both the Permian volcanic rocks of the Piambello Series and the Variscan metamorphic basement known as Ceneri Gneiss [54].

The Cuasso al Monte area is located within the Maroggia-Brinzio Anticline, a tectonic structure with ENE-WSW orientation. At the nucleus post-Varisian intrusive rocks outcrop, among them the Cuasso granophyre. This subvolcanic body was formed as a result of silica-rich magmatism, the same process that also gave rise to granitic rocks and leucogranites with a granophyric structure. Petrographic and geochemical analyses suggest that the Cuasso granophyre is closely linked to the permo-carboniferous intrusive sequences that characterise the entire south-western Alpine region [55]. The crystallisation phases of the Cuasso al Monte pluton show an evolution from primary magmatism to advanced hydrothermal conditions [56]. The tectonic and stratigraphic context of the area suggests that the intrusion of the granophyre occurred during the Upper Permian, coinciding with marked tectonic activity that favoured the formation of sedimentary basins and volcanic structures. The Maroggia-Brinzio Anticline may have played a decisive

role in controlling magma ascent and the distribution of associated intrusive and volcanic units [55].

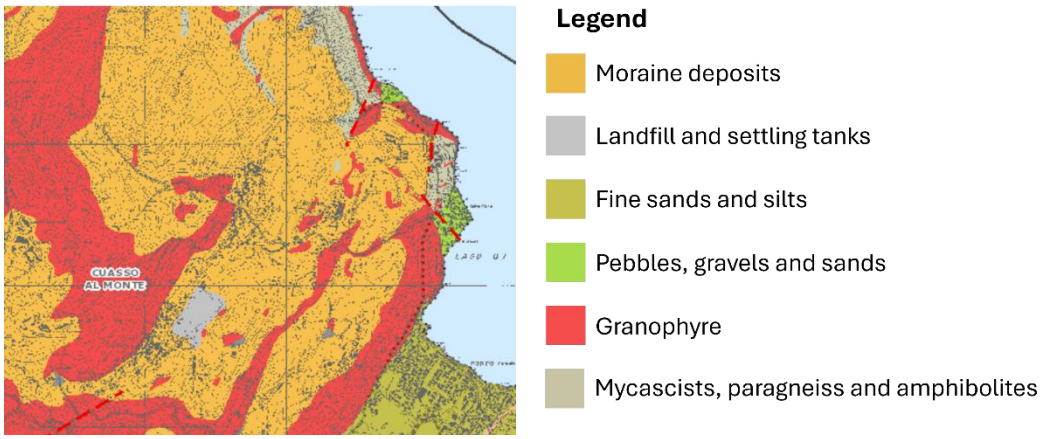

Figure 7 - Excerpt from the geological map of the Varese province (taken from [57]).

2 Materials

2.1 Basalt and Granophyre sawing waste sludges

The stone industry is responsible for the production of a large amount of waste material, deriving from the extraction, sizing, and polishing processes of rocks. The whole wastes represent about 38 wt.% of the total raw stone, while specifically the sludges consist of the 24 wt.%. It was estimated that, only from the granite market, 2.0×10^6 tons of sludges are expected to be produced annually [58]. In particular, the produced sludge is made up of rock particles, water used to cool down the saw, and potentially metallic particles coming from the latter. This sludge is mostly disposed of in landfill. After drying, the sludge appears as a powder with very small grain size [59]. Moreover, these wastes can create many problems for the human health (i.e., silicosis after inhalation of the silica-rich particles [60]), as well as land degradation, infiltration and groundwater contamination [61].

In this thesis, two sawing sludges produced from the cutting, shaping, and polishing process of different type of rocks were selected as raw materials.

Basalt sawing waste sludge (BSW), derived from the processing of local basaltic rocks, was provided by A.M. Basalti s.r.l.. The company is located in Misterbianco (Sicily, Italy; Figure 8) and deals with the manufacturing process of basaltic rocks for the production of semi-finished products, paving, coverings, and urban furniture. After sampling, the raw material was dried in oven at 105 ± 5 °C for 24 h. The dried material was then sieved in order to remove any impurities. The material didn’t need any additional treatment.

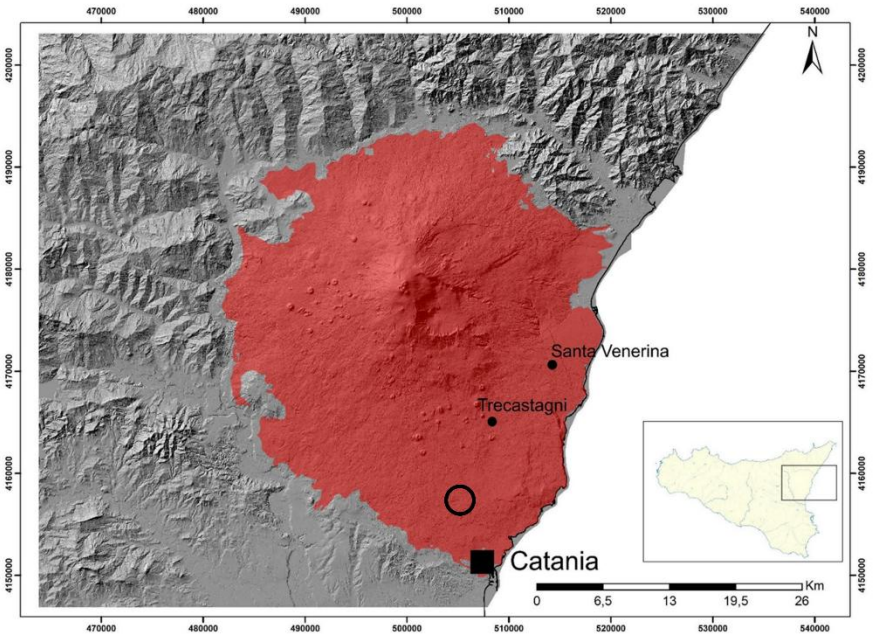

Figure 8 - Geological map of Mt. Etna. The red area indicates the volcanic building while the back circle denotes the location of the A. M. Basalti company (modified after [62]).

Granophyre sawing waste sludge (GSW) was sampled from the Bonomi quarry, located in Cuasso al Monte, a small town 10 km up from Varese (Italy) (Figure 9 - Google Earth image of Varese province and Cuasso al Monte area. The red circle denotes the Bonomi Quarry.).

Figure 9 - Google Earth image of Varese province and Cuasso al Monte area. The red circle denotes the Bonomi Quarry.

The material was provided by Prof. Danilo Bersani (University of Parma), Dott. Paolo Gentile (Piattaforma di Microscopia, Università degli Studi di Milano Bicocca) and Geom. Renato Bonomi (owner of the quarry). The material arrived still very wet (Figure 10 - GSW as received before the drying process (a); and after drying while sieving (b).) so, following the same protocol used for the BSW, it was dried in oven for 24h at 105 ± 5 °C and carefully sieved (Figure 10 - GSW as received before the drying process (a); and after drying while sieving (b).).

(a) **(b)**

Figure 10 - GSW as received before the drying process (a); and after drying while sieving (b).

2.2 Metakaolin

Metakaolin derives from the calcination process of kaolinite clays which occurs at temperatures around 500-750 °C. The high temperatures contribute to the dehydroxylation of the material, a process through which most of the hydroxyl groups (OH) are released [18]. The exothermic reactions occurring during the calcination and burning processes of kaolinite clays, leading to the formation of highly temperature-sensitive products, are reported in400−500 $°C: Al_2SiO_5(OH)_4 \rightarrow Al_2SiO_5(OH)_xO_{2-x} + \left(2 - \frac{x}{2}\right) H_2O$ (Eq. 1-3 [63].

$$400 - 500\ °C: Al_2SiO_5(OH)_4 \rightarrow Al_2SiO_5(OH)_xO_{2-x} + \left(2 - \frac{x}{2}\right) H_2O \quad \textit{(Eq. 1)}$$

$$500 - 925\ °C: Al_2O_3 \cdot 2SiO_2 \cdot 2H_2O \rightarrow Al_2O_3 \cdot 2SiO_2(MK) + 2H_2O \quad \textit{(Eq. 2)}$$

$$925\ °C - 1100\ °C: 2[Al_2O_3 \cdot 2SiO_2] \rightarrow 2Al_2O_3 \cdot 3SiO_2 + SiO_2 \quad \textit{(Eq. 3)}$$

At 500-800 °C the coordination of the alumina shifts from octahedral to tetra- and penta-coordinated units. These products are highly reactive, and the clay's structure appears to be collapsed and disarranged, as shown in Figure 11 - Structure modification according to increasing calcination temperature (taken from [65]). [64]. Moreover, it can be observed that temperatures below 400 °C and above 950 °C are not suitable for the production of materials to be used as precursor in alkali-activated reactions, due to the high cristallinity of the structures [65].

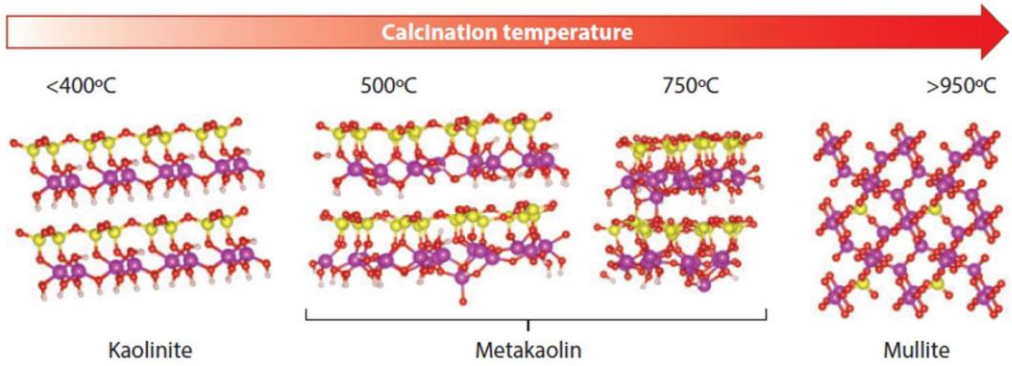

Figure 11 - Structure modification according to increasing calcination temperature (taken from [65]).

Thanks to its very high reactivity [66], chemical composition (i.e., low calcium and high silica and alumina contents), metakaolin is the most used and suitable precursor to produce geopolymers. In particular, the chemical composition of metakaolin, ranging from 55% to 62% SiO_2 and between 35% to 42% Al_2O_3, as reported in literature [67,68], leads to the formation of a well-defined microstructure with a three-dimensional network [20,69,70]. Moreover, from the environmental point of view, the use of metakaolin in the construction industry is reported to reduce up to 70% of the carbon dioxide emissions compared to conventional concrete [71].

In this study, a commercial metakaolin ARGICAL^{TM} M1000, provided by IMERYS (France), was used as an additive to enhance the reactivity of the system. The amount of added metakaolin varied according to the reactivity of the raw waste precursors and ranged from ~14% to ~27% for the selected best formulations.

2.3 Alkaline solutions

The binary powdered mixtures composed of the sawing waste sludges (i.e., basalt or granophyre) and metakaolin were activated using sodium-based solutions. In particular, a combination of sodium hydroxide and sodium silicate was employed.

Sodium hydroxide (NaOH) was mostly used with a concentration of 8M, obtained by the dilution of a commercial 9.9M solution. The activation process of GSW was also evaluated with 9.9M NaOH.

The used sodium silicate (Na_2SiO_3) was provided by Ingessil s.r.l., with a SiO_2/Na_2O molar ratio of 3.

2.4 Synthetic and organic fibres

In this study, synthetic and organic fibres were used to reinforce BSW and GSW-based composites. Commercial carbon roving 1600 Tenax (24k), provided by R&G Faserverbundwerkstoffe GmbH (Germany), was used as a synthetic fibre. The technical parameters of the carbon fibre are shown in Table 2 - Technical data of the carbon fibres, provided by the company., as reported by the company.

Parameter	**Value**	**Unit**
Density	1.78	g/cm^3
Tensile strength	4200	MPa
Tensile modulus	240	GPa
Elongation at break	1.8	%

Table 2 - Technical data of the carbon fibres, provided by the company.

The increasing attention over environmental issues and the demand for sustainable construction materials have encouraged researchers to explore alternative fibres to be used as reinforcement. In this perspective, natural fibres have gained attention due to their low density and cost-effectiveness [29]. In fact, replacing synthetic fibres with natural ones is not only environmentally beneficial but also economically advantageous, since producing synthetic fibres typically requires more energy compared to the agricultural processes used to produce natural fibres [72].

In this study, organic fibres were selected to assess their behaviour when added in the alkaline environment of the binders. Specifically, the fibres were obtained from the cortex of two local widely spread plants in Sicily. These plants are distinctive

of the Mediterranean scrub: the palm tree and the prickly pear. After natural air drying, the cortex and leaves (i.e., cortex of palm tree and leaves of prickly pear, respectively) were directly cut without requiring any additional treatment, making the preparation process simple, sustainable and environmentally friendly.

Both synthetic and organic fibres were manually cut and directly added to the slurry in different percentages ranging from 0% to 2%, with constant increments of 0.5%. Based on previous studies, all fibres were cut to a length of 10 mm, as this size has been recognized as one of the most used, balancing workability and mechanical performance in alkali-activated systems [32,40,73,74]. Moreover, for the specific used organic fibres, obtaining lengths greater than 10-20 mm proved to be both challenging and time-consuming. This was mainly due to the irregular cross-sectional morphology, roughness and presence of nodular patterns within the raw fibre which caused the breaking of the material. Therefore, the 10 mm length represented the most practical and efficient choice for processing and dispersion into the matrix.

3 Methods

3.1 Mineralogical, chemical, molecular and morphological characterization

3.1.1 X-Ray Fluorescence (XRF)

The elemental composition of the raw materials was investigated using an X-Ray Fluorescence (XRF) spectrometer, model Bruker S8 Tiger. XRF provides quantitative data by measuring the absolute amount of each element present in a sample. This is achieved through a calibration process, where raw signal intensities are converted into precise concentrations. Calibration involves the use of standards with known element concentrations, allowing the creation of a calibration curve that is then used to interpret the sample signals.

For the detection of major elements (i.e., elements present in the samples with amounts greater than 1 wt.%), samples were prepared by fusing a mixture of 0.5 g of finely ground material (i.e., particle size below 0.045 mm) with 8 g of lithium tetraborate ($Li_2B_4O_7$) to form glass beads. In contrast, for the detection of minor elements (i.e., elements with a concentration of less than 1 wt.%), the sample preparation involved pressing pellets composed of 11 g of the powdered sample combined with 1 g of wax. Moreover, boron oxide (B_2O_3) was also included to improve the accuracy of these measurements.

The XRF measurements were performed by Dr. Hana Kaňková and Dr. Jaroslava Gombárová at the Centre for Functional and Surface Functionalized Glass (FunGlass), Alexander Dubček University of Trenčín (Slovakia), where I had the opportunity to carry out part of my research during the compulsory research period abroad.

3.1.2 X-Ray Diffraction (XRD)

X-ray diffraction (XRD) analysis was performed to investigate the mineralogical composition of the samples, including both crystalline and amorphous phases. The measurements were carried out at the University of Catania (Department of Biological, Geological and Environmental Sciences) using a Miniflex Rigaku diffractometer, equipped with CuKα radiation and operating at 40 kV and 15 mA. Data were collected over a 2θ range between 5° to 75°, with a step size of 0.01° and a scanning speed of 5° per minute. In addition to phase identification, to quantify the relative amounts of crystalline and amorphous content, 5 wt.% of zinc oxide (ZnO) was added as an internal standard [75]. The acquired diffraction patterns were then processed using Profex software (version 5.2.4), in combination with the BGMN database [76,77].

The analyses were conducted not only on the raw precursors but also on the final activated materials in order to assess the occurrence of the polymerization reactions, by measuring the changes in the amorphous amount [78,79].

3.1.3 Fourier-transform infrared spectroscopy (FT-IR)

Molecular characterization of the samples was carried out through Fourier Transform Infrared Spectroscopy (FT-IR), using an Agilent Cary 630® spectrometer. This technique allowed for the identification of functional groups based on their vibrational modes. Spectral data were collected in the range of 4000 to 700 cm^{-1}, with a resolution of 4 cm^{-1}, using Agilent MicroLab software for acquisition. The obtained spectra were processed with the NGS LabSpec software, by eliminating the contribution of CO_2 present in the atmosphere consisting in signals ranging between 2400 and 2280 cm^{-1}. The measurements were carried out at the University of Catania (Department of Biological, Geological and Environmental Sciences).

3.1.4 Confocal Microscope

Confocal microscopy is a technique that allows the acquisition of images with a very high resolution, higher than that of conventional light microscopy. In the latter, a beam of photons hits the sample, and it is reflected by its surface. The objective that collects the photons is focused on a specific focal plane of the sample. Consequently, photons, reflected from areas above and below the focal plane, will result in the production of blurred images with lower resolution. Confocal microscopy overcomes the problem of out-of-focus light by introducing a pinhole that can prevent out-of-focus light from being absorbed by the detector. Thanks to this approach, high quality and blurring-free images of an object can be produced [80]. Specifically, the confocal microscope acquires several images at different subsequent focal planes and then stacks them on top of each other to obtain a complete 3D image of the sample. Figure 12 Components of a confocal microscope (a); Scanning mirror functioning (b) (taken from [81]) shows a schematic representation of the main components of a confocal microscope, according to the working principle patented by Marvin Minsky in the 1950s. The microscope consists of objective lens, detectors, pinholes, mirrors, laser illumination and filters for wavelength selection. Specifically, light is produced from a laser, and it is brought through a dichromatic mirror which reflects or transmits light depending on the specific wavelength. The selected beam is then focused on a targeted sample point thanks to the objective lens. Scanning mirrors are used to adjust the position of the beam across the sample, point by point Figure 12 Components of a confocal microscope (a); Scanning mirror functioning (b) (taken from [81]). Then, the emitted fluorescence goes back through the objective lens and the dichromatic mirror. The out-of-focus light is discarded by the pinhole, and the remaining beam is finally detected by the photomultiplier detector.

Nowadays, confocal microscopy is mainly used in the biological field for the study of cell structures, being able to provide very high-resolution images with a low background noise. However, other applications can be also found in the field of materials science [81].

(a) **(b)**

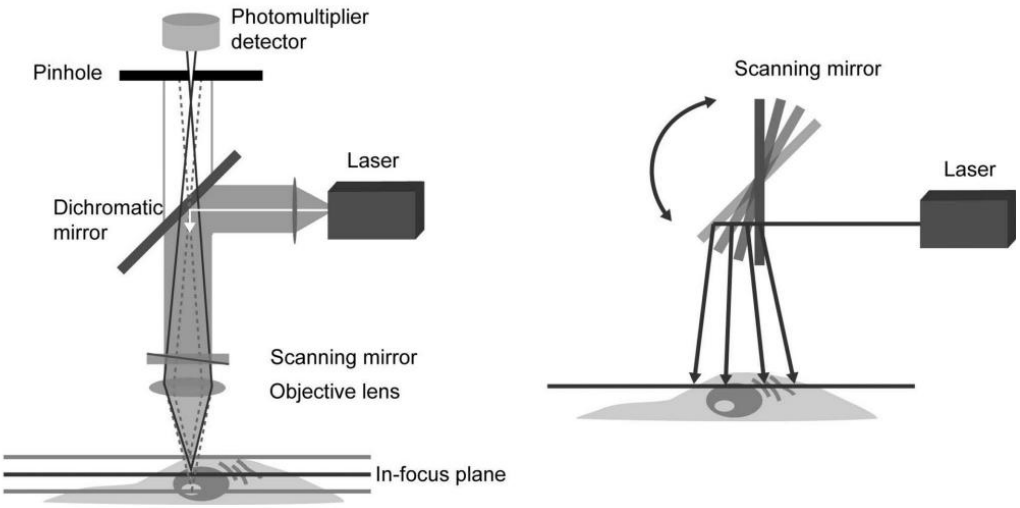

Figure 12 Components of a confocal microscope (a); Scanning mirror functioning (b) (taken from [81])

In this thesis, Sensofar Metrology S NEOX 090 Confocal microscope was used to investigate the roughness of consolidated specimens both with and without the addition of fibres. The microscope enables 2D and 3D imaging of surfaces in the bright field (BF), allowing observation of specimens at different magnification (ranging from 100x to 40 000x). The lateral resolution is of 260 nm while the Z-axis resolution is of 10 nm. Images were acquired and processed using SensoSCAN S neox (Version 7.6) and SensoVIEW (Version 2.2.2) softwares.

Arithmetic mean height (*Sa*) was computed for all samples. *Sa* is defined as the arithmetic mean height of the surface, also known as average surface roughness. Sa calculation is reported below [82]:

$$Sa = \iint_a |Z\,(x,y)|\,(dx)dy$$

Additionally, Root Mean Square (*RMS*) height was calculated. *RMS* height, also reported as *RMS* roughness takes into account the mean surface height of all data point [82]. Three points were analysed from the top part of each specimen, being the upper side very heterogeneous in terms of surface flatness. Moreover, in order to avoid any overestimation or underestimation of the roughness due to the different viscosity of the slurry caused by the fibres' content, average surface roughness

measurements were also carried on one point of the bottom side of each specimen. The measurements were carried out in FunGlass research centre, under the supervision of Dr. Branislav Hruška.

3.1.5 Inductively coupled plasma - optical emission spectrometry (ICP-OES)

Inductively Coupled Plasma Optical Emission Spectroscopy (ICP-OES) was conducted, by using an Agilent 5100 SVDV, to evaluate the occurrence of significant leaching of elements in solution from consolidated specimens, both without fibres and with the maximum fibre content (i.e., 2 wt.%), after immersion in water. ICP-OES method is suitable for detecting a wide range of elements in liquid samples and it relies on a high frequency inductively coupled plasma as the excitation source, allowing precise elemental analysis of solutions derived from either direct dissolution or decomposition of solid materials.

For this purpose, the raw powdered materials were immersed in 8M NaOH for 3 hours in order to verify the reactivity of the precursors in alkaline environment. As for the consolidated specimens, they were boiled in distilled water for three hours, simulating forced leaching condition. After cooling and before conducting the tests, the resulting leached solutions were collected and centrifuged to remove any residual solid particles, ensuring that the measurements reflected only the dissolved elements and were not affected by suspended residual particles. The leaches were then analysed to identify and quantify any elements released during the process, thus verify chemical stability. The experiments were conducted at FunGlass and ICP-OES measures were carried out by Dr. Lenka Buňová.

3.1.6 Scanning Electron Microscope and Energy Dispersive X-ray Spectroscopy (SEM-EDS)

Microstructural analysis of the consolidated specimens was carried out using Scanning Electron Microscopy coupled with Energy Dispersive X-ray Spectroscopy (SEM-EDS). This technique was employed to explore morphological features including texture, porosity, binder-fibre adhesion and the possible presence of unreacted particles belonging to the raw precursors.

A JEOL JSM-IT500 Analytical Scanning Electron Microscope, equipped with an EDS detector, was used for the acquisition of micrographs and to identify the chemical composition of selected areas within the specimens. The microscope operated at a voltage of 20 kV and a beam current of 8 nA. Prior to the analyses, the samples were coated, by using a Quorum Q150V ES plus sputter-coater, with a 10 nm layer of platinum to improve conductivity.

The analyses were performed at the FunGlass research centre, under the supervision of MSc. Mohammed Boujida and Dr. Mokhtar Mahmoud.

3.2 Thermal Characterization

The thermal behaviour of the used materials was investigated using a Netzsch STA 449 F1 Jupiter instrument, which enables Simultaneous Thermal Analysis (STA) by combining Thermogravimetric Analysis (TGA) and Differential Scanning Calorimetry (DSC) in a single measurement. The measurements were carried out in air atmosphere, with the temperature ranging from 25°C to 1300°C and a controlled heating rate of 5°C/min. This setup allowed for the evaluation of mass changes, thermal stability and energy transformations occurring within the samples across the studied temperature range. The analyses were performed on both the raw precursors and the activated specimens, in order to evaluate how the thermal properties evolved as a result of the polymerization process. The analyses were carried out at the FunGlass research centre, under the supervision of Dr. Beáta Pecušová.

3.3 Rheological characterization

The rheological behaviours of the materials can be represented by shear stress (τ) vs shear rate (γ̇) graphs, as shown in Figure 13 (a-b). The curve (1) shows the behaviour of Newtonian fluids, where the shear stress linearly increases with the shear rate. This behaviour suggests that the viscosity is always constant and does not depend on the deformation rate. For materials with pseudoplastic behaviour (2), also known as shear-thinning, the viscosity decreases with the increase in shear rate. On the contrary, an increment in viscosity is observed for materials with dilatant or shear-thickening behaviour, represented by curve (3). Figure 13 b represents the behaviour of materials which present an intrinsic resistance to flow and need a finite yield stress to start flowing. Specifically, curve (4) shows the Bingham fluid behaviour where, after overcoming an initial stress, the material starts flowing and behaving as a Newtonian fluid. The curve (5) displays the Casson behaviour of materials which, after overcoming an initial stress, behave in a shear-thinning way.

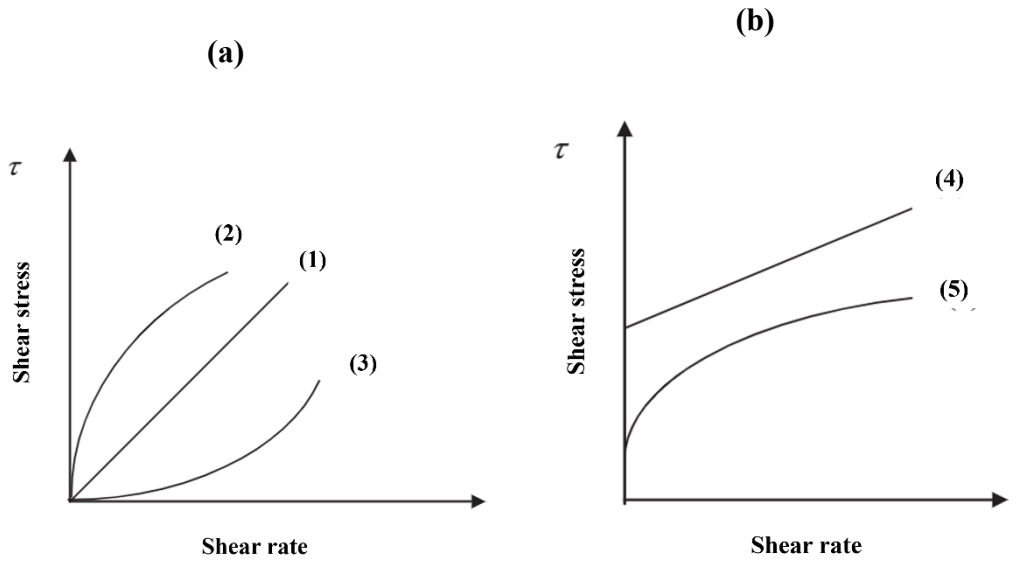

Figure 13 - Rheological behaviours of materials without a threshold stress (a) and with yield stress (b) (modified from [148]). Curves represent the Newtonian (1), Pseudoplastic (2), Dilatant (3), Bingham fluids (4), Casson fluids (5).

The rheological properties of the slurries were evaluated using a Haake Mars III rheometer, equipped with 35 mm plate in a parallel geometry. The analyses were conducted exclusively on the slurries without fibre, as the high viscosity of the fibre-reinforced mixtures made measurements impossible. Multiple test protocols were employed to gain a comprehensive understanding of the rheological behaviour and viscoelastic properties of the materials under different conditions.

Specifically, the viscosity recovery test consisted of two sequential steps in rotational mode at a constant shear rate. Initially, a shear rate of 10 s^{-1} was applied for 60 seconds to simulate the extrusion phase, followed by a much lower shear rate of 0.1 s^{-1} for another 60 seconds, representing post-extrusion conditions. This setup was designed to evaluate the slurry's ability to recover its original viscosity after being subjected to mechanical stress, being an essential property for maintaining the given shape.

Additionally, a dynamic strain sweep test was carried out in oscillatory mode under constant deformation, with strain values ranging from 0.001 to 200% with a frequency set at 1 Hz. This test provided insight into whether the material behaved predominantly in an elastic (solid-like) or viscous (liquid-like) manner under oscillatory stress conditions.

Finally, flow curve tests were conducted in rotational mode, using a shear rate range from 0.01 to 100 s^{-1}. These tests allowed to determine the shear-thinning and thixotropic behaviour of the slurries, key features for materials as they influence and control the flowability.

The tests were performed at the FunGlass research centre, after Dr. Ali Talimian delivered a training.

3.4 Physical-mechanical characterization

3.4.1 Helium pycnometer

The determination of the true density and volume of the consolidated specimens was carried out by using a Quantachrome Ultrapyc 1200e, an automatic gas pycnometer operating in a helium atmosphere, with an accuracy of ± 0.001 g/cm^3.

The pycnometer is able to provide data on the actual volume of the solid samples, by measuring the volume displaced by helium (i.e., gas capable of penetrating even the small pores, on the order of the nanometer).

The analyses were conducted on both specimens with and without the fibre reinforcement, to assess whether the addition of fibres had any influence on the internal structure of the materials in terms of density. The measurements were carried out at FunGlass research centre, under supervision of Dr. Anna Prnová.

The helium pycnometer was used to calculate the bulk and true density of the consolidated samples. The geometric density was calculated as the weight to volume ratio using an analytical balance and a caliper. Furthermore, the density of the specimens was employed to calculate the open and total porosities. The formulas for determining the open (Eq. 4; $\emptyset_{open}$) and total porosity (Eq. 5; $\emptyset_{total}$) involve the ratio of the geometric density (ρ_{geom}) to the apparent density (ρ_{app}) or to the true density (ρ_{true}) of the specimens [83,84]:

$$\emptyset_{open} = 1 - \left(\frac{\rho_{geom}}{\rho_{app}}\right) \quad \text{(Eq. 4)}$$

$$\emptyset_{total} = 1 - \left(\frac{\rho_{geom}}{\rho_{true}}\right) \quad \text{(Eq. 5)}$$

3.4.2 Freeze-thaw tests

Freeze-thaw tests were carried out using an Angelantoni Discovery DY110 climatic chamber, designed to simulate a wide range of environmental conditions, including variations in temperature and humidity. The instrument is commonly used to assess the long-term performances of materials under accelerated aging conditions.

The testing procedure followed the UNI 7087:2017 standard [85,86], which consists of 75 freeze–thaw cycles, each lasting 12 hours, conducted on 4 cubic specimens of 4 cm-edge for each formulation. Every cycle included three distinct phases:

1. Cooling phase: the temperature gradually decreases from 5°C to -20°C, with a controlled rate of 5°C/h.
2. Freezing phase: the temperature is kept constant at -20°C for 2 h.
3. Unfreezing phase: the temperature is gradually raised from -20°C to 5°C, at a rate of 5°C/h.

The initial and final mass after the 75 cycles were measured, and the mass loss was evaluated. Due to limited time and material availability, freeze–thaw resistance tests were carried out only on specimens without the addition of fibres. The aim was to evaluate the durability and the structural integrity of the consolidated materials undergoing thermal stress. The experiments were conducted in FunGlass research centre, under the supervision of Dr. Aleksandra Ewa Nowicka.

3.4.3 Compressive and flexural strength resistance

Mechanical tests are essential for the evaluation of the mechanical performances of the materials. In this study, both compressive and flexural strength tests were carried out using a 70-T1182 Controls UNIFRAME universal automatic testing machine. Specifically, four specimens of 2 cm^3 were tested for each formulation to determine the uniaxial compressive strength. The machine was equipped with a 50 kN load cell, set with a peak sensitivity of 3 kN and a loading rate of 1200 N/s. Moreover, for the flexural strength tests three prisms with dimensions of 2x2x8 cm^3 were tested using a 10 kN load cell. The measurement sensitivity of the instrument was ± 0.001 kN, ensuring high precision in data acquisition.

In the case of fibre-reinforced specimens, the six half-prisms obtained from the flexural tests were subsequently used for uniaxial compressive strength testing, in accordance with the EN 1015-11:2019 standard. This approach was necessary due to the limitations associated with testing fibre-reinforced materials in small cubic specimens. Specifically, the use of 2 cm-edge cubic specimens with 1 cm long fibres would result in a high fibre to specimen ratio, which could lead to uneven fibre distribution, increased edge effects, and non-representative failure modes. These conditions can compromise the accuracy of the mechanical response, particularly the fibre–matrix interaction [87–89].

On the other hand, the use of half-prisms, obtained from the flexural strength tests (i.e., initial specimen size of 2x2x8 cm^3), provides a more appropriate volume for testing, reducing boundary effects and allowing for a more homogeneous fibre distribution [89]. The mechanical tests were carried out at the University of Catania (Department of Biological, Geological and Environmental Sciences).

4 Results and discussion

4.1 Raw powdered materials

The following chapter will focus on the characterization of the raw granite and basalt sawing wastes, used as precursors in this study. The mineralogical, chemical and elemental compositions of the materials are to be considered as representative of the average values of the Cuasso al Monte granophyre and of the Etnean basalts. However, minor contaminations can be potentially introduced during the sawing process.

4.1.1 Mineralogical, chemical and molecular characterization

The X-ray fluorescence (XRF) chemical characterization of the raw powdered precursors is reported in Table 3 - XRF analysis of the raw precursors (values in wt.%): Granophyre sawing waste (GSW), Basalt sawing waste (BSW) and Metakaolin (MK). Granophyre sawing waste (GSW) is mainly composed of silica (76.7 wt.%) and alumina (12.9 wt.%). Moderate contents of alkali (namely, Na_2O and K_2O) were also detected (8.3 wt.%). Basalt sawing waste (BSW) analysis revealed a substantial amount of silica and alumina (i.e., 47 wt.% and 18 wt.%, respectively), along with calcium oxide (10 wt.%). Moreover, high levels of magnesium oxide and alkali were found (i.e., 5 wt.% and 5.9 wt.%, respectively). Metakaolin (MK) showed the highest amount of alumina (35 wt.%) compared to the other powdered precursors, coupled with intermediate levels of silicon oxide (61 wt.%). Very low amounts of calcium and magnesium oxides and alkali were also observed (i.e., 0.13 wt.%, 0.13 wt.%, and 0.56 wt.%, respectively). The detected iron oxide levels were very low for GSW and MK (namely, 1.3 wt.% each), while 11 wt.% was found in BSW.

Overall, the GSW and BSW exhibited suitable elemental compositions for alkali activated process. Nevertheless, the incorporation of metakaolin is essential to increase the alumina contents, thus the reactivity of the system which contributes to the formation of a more stable polymeric network [90]. However, the differences in composition of GSW and BSW make it necessary to tailor formulations based on the specific chemistry of the precursors.

ID	SiO_2	Al_2O_3	CaO	Fe_2O_3	MgO	Alkali	Other
GSW	76.7 ± 0.4	12.9 ± 0.8	0.65 ± 0.05	1.3 ± 0.1	0.09 ± 0.02	8.3 ± 0.3	-
BSW	47 ± 2	18 ± 1	10.0 ± 0.4	11 ± 1	5 ± 1	5.9 ± 0.5	3.1
MK	61 ± 1.7	35 ± 3.0	0.13 ± 0.06	1.3 ± 0.1	0.13 ± 0.07	0.56 ± 0.04	1.9

Table 3 - XRF analysis of the raw precursors (values in wt.%): Granophyre sawing waste (GSW), Basalt sawing waste (BSW) and Metakaolin (MK). Alkali includes: Na_2O and K_2O. Other includes: TiO_2, P_2O_5 and MnO.

The diffraction patterns of the studied raw materials are reported in Figure 14 - XRD patterns of raw materials: Granophyre sawing waste sludge (GSW); Basalt sawing waste sludges (BSW); Metakaolin (MK). Granophyre sawing waste sludge (GSW) is mainly composed of biotite ($K[Mg, Fe^{2+}]_3AlSi_3O_{10}(OH)_2$), microcline ($KAlSi_3O_8$), muscovite ($KAl_2[AlSi_3O_{10}](OH)_2$), plagioclase (i.e., a solid solution between two endmembers, namely anorthite ($CaAl_2Si_2O_8$) and albite ($NaAlSi_3O_8$) and quartz (SiO_2). The shown composition is typically reported for granite stones as well as Cuasso al Monte granophyre [91]. Basalt sawing waste sludge (BSW) is mainly characterized by plagioclase, pyroxene ($[Ca,Mg,Fe^{2+},Fe^{3+},Ti,Al]_2[Si,Al]_2O_6$), olivine ($[Mg,Fe]_2SiO_4$), and magnetite ($Fe_3O_4$). These minerals are representative of the typical composition of basalt rocks of Mt. Etna [21]. Metakaolin (MK) pattern indicated the presence of peaks related to anatase (TiO_2), quartz and muscovite. Moreover, for all the raw powdered precursors zincite (ZnO) was also detected, because it was added as internal standard for the quantification of the mineralogical and amorphous phases.

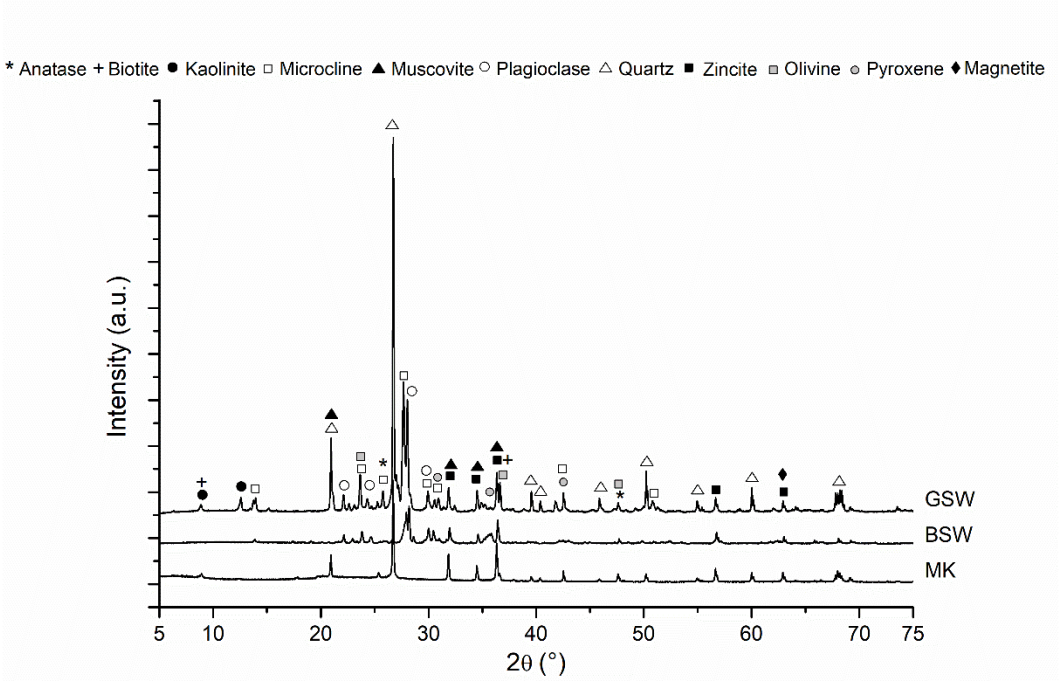

Figure 14 - XRD patterns of raw materials: Granophyre sawing waste sludge (GSW); Basalt sawing waste sludges (BSW); Metakaolin (MK).

The amount of amorphous content for each material (i.e., GSW, BSW, and MK), prior to activation process, and the mineralogical phases, determined by X-ray diffraction with Rietveld refinement, is reported in Table 4 – Mineralogical and amorphous phase contents, expressed in wt.%, of the raw precursors: Granophyre sawing waste (GSW), Basalt sawing waste (BSW), and Metakaolin (MK). The negligible amorphous content exhibited by GSW and BSW (namely, 0% and 0.6%) confirms the crystalline nature of the precursors. On the other hand, metakaolin (MK) showed a very high amorphous content (71.61 %), mainly due to the undergone thermal treatment of kaolin clays.

The presence of amorphous phases is associated with enhanced reactivity in alkaline environments, thus contributing to the improvement of AAMs properties [92]. Hence, the incorporation of metakaolin as an additive in binary mixtures alternately composed of GSW and BSW is crucial to improve the overall reactivity of the system [93].

ID	Biotite (wt.%)	Microcline (wt.%)	Muscovite (wt.%)	Plagioclase (wt.%)	Quartz (wt.%)	Olivine (wt.%)	Pyroxene (wt.%)	Anatase (wt.%)	Kaolinite (wt.%)	Amorph (wt.%)
GSW	0.24 ± 0.0010	25.16 ± 0.0061	4.09 ± 0.0022	17.72 ± 0.0066	52.79 ± 0.0064	-	-	-	-	0
BSW	0.32 ± 0.0023	-	-	58.2 ± 0.011	-	9.22 ± 0.0020	31.66 ± 0.0035	-	-	0.6 ± 0.016
MK	-	-	2.75 ± 0.0012	-	21.14 ± 0.0016	-	-	1.09 ± 0.0008	3.42 ± 0.0011	71.61 ± 0.0025

Table 4 – Mineralogical and amorphous phase contents, expressed in wt.%, of the raw precursors: Granophyre sawing waste (GSW), Basalt sawing waste (BSW), and Metakaolin (MK).

The Inductively Coupled Plasma with Optical Emission Spectroscopy (ICP-OES) was performed to assess the reactivity of the raw precursors in alkaline solution. The dissolution rate of Al and Si in alkaline environment reflects the availability of reactive species to form a stable network, thus it can be used to determine the precursor's reactivity for AAMs production [94–96]. The raw powders were immersed with a ratio of 1:10 in 8M NaOH solution for 3 hours. The solution was then filtered and analysed to quantify the amount of dissolved elements, as reported in Table 5 - Elemental release of raw materials in 8M NaOH solution. Na was not evaluated due to the high concentration of the element in the solution. Calcium detection limit (DL) is 0.49 mg/L; Ti detection limit is 0.05 mg/L.. The GSW showed the smallest Al and Si releases (i.e., ~56 and 148 mg/L, respectively), while Ca and Mg were relatively higher compared to the other raw materials, namely ~12, and ~0.6 mg/L, respectively. The high K releases (i.e., 825 mg/L) are consistent with the presence of K-feldspar, as found in the XRD pattern. The elemental releases of BSW powders appeared to be slightly higher, being the material more reactive in alkaline environment. The Al contribution was almost the double of GSW (i.e., 97 mg/L), essential during the alkaline activation reaction, while Ca content in solution was smaller, limiting the formation of C-A-S-H products. Fe content aligned with the presence of iron-rich minerals, such as olivine, pyroxene and biotite. The NaOH composition after the immersion of MK powder is mainly characterized by very high release of Al and Si, confirming its suitable role as aluminosilicate precursor for the production of N-A-S-H network [12,97]. Therefore, the addition of MK is

useful to balance Si/Al ratio, to enhance the reaction process and promote gel formation.

	mg/L							
	Al	**Si**	**Ca**	**Fe**	**K**	**Mg**	**Ti**	**Si/Al**
GSW	55.5 ± 0.7	148 ± 2	11.8 ± 0.1	3.49 ± 0.06	825 ± 29	0.571 ± 0.002	<DL	2.66
BSW	97.1 ± 0.3	162 ± 1	7.21 ± 0.06	4.10 ± 0.08	847 ± 14	0.241 ± 0.001	0.23 ± 0.03	1.66
MK	3890 ± 187	4360 ± 230	<DL	51.1 ± 0.5	702 ± 13	0.183 ± 0.001	1.29 ± 0.09	1.12

Table 5 - Elemental release of raw materials in 8M NaOH solution. Na was not evaluated due to the high concentration of the element in the solution. Calcium detection limit (DL) is 0.49 mg/L; Ti detection limit is 0.05 mg/L.

Molecular composition of the raw powders is shown in Figure 15 - FT-IR spectra of the raw powders. All FT-IR spectra exhibited a clear characteristic main band, associated to the aluminosilicate structure. This band typically ranges from 1200 to 900 cm^{-1}, according to the specific nature of the aluminosilicate precursor [98]. The peak detected at 1042 cm^{-1} is related to the vibration of Si-O/Al–O bond of aluminosilicate materials [99] , along with a shoulder at 1092 cm^{-1} attributed to the asymmetric stretching of Si-O-Si and Al-O-Si [100]. The peaks at 1042 and 1006 cm^{-1} are linked to the Si-O-Ca bonds, or to the asymmetric stretching of T-O (where T= Si or Al) [101]. The band at 973 cm^{-1} is ascribed to the Si-O stretching of Si-O-Na/K [102]. Moreover, the signal at 782 cm^{-1} is related to the symmetric stretching of Si-O-Si [100].

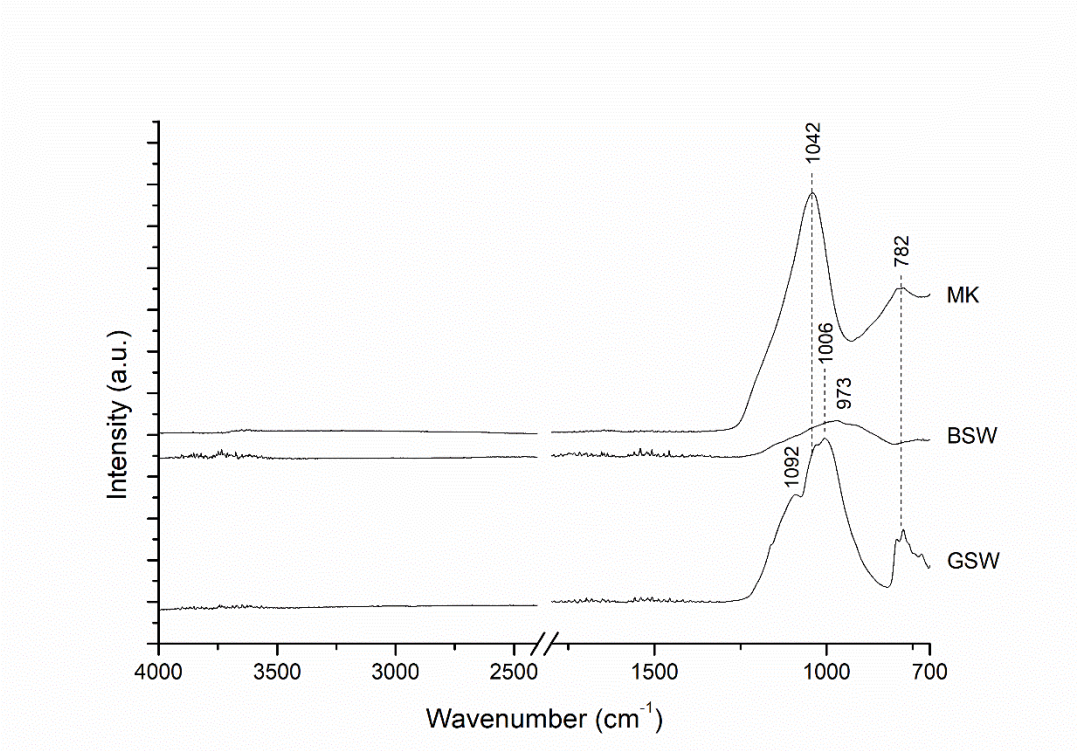

Figure 15 - FT-IR spectra of the raw powders.

4.1.2 Thermal characterization

Figure 16 – Thermal characterization of the raw materials: TG (a) and DTA (b). (a-b) display the thermogravimetric (TG) (a) and differential thermal analysis (DTA) (b) curves of the raw materials. All raw powders exhibited an initial mass loss (up to ~700°C), followed by a stabilization. GSW and BSW appeared particularly stable with a total mass loss of ~1%, indicating the thermal stability of the contained minerals, while MK displayed a more extensive mass change up to ~2.5%. The mass loss up to 300°C is mainly due to the evaporation of adsorbed water in the pores or surface of the powdered materials [103]. Between 300°C and 800 °C the dehydration of hydrate minerals can be observed, as in the case of MK, where the mass loss is attributable to the dihydroxylation of clay minerals [104]. The overall thermal events and the relative temperature ranges are summarised in Table 6.

The DTA curves revealed thermal reactions associated with phase changes (Figure 16 – Thermal characterization of the raw materials: TG (a) and DTA (b). b). GSW

displayed a slight endothermic peak due to the transformation of α to β quartz [103], located at ~550°C, followed by an endothermic event at ~1150°C due to the partial melting of the powder [105]. BSW showed an exothermic reaction between 150° and 550°C due to the oxidation of iron from Fe^{2+} to Fe^{3+} [106]. Moreover, endothermic peaks located at ~800°, 900° and 1200°C can be ascribed to the transition of olivine to hematite [103] and melting process [106], respectively. Specifically, olivine – which crystallizes at 1620°C – during annealing reacts with air and forms hematite, forsterite and amorphous silica [107], as reported in Equation 6. After that crystallization of glassy phases occurs, as demonstrated by the two sharp exothermic peaks after 1200°C [103,106]. MK exhibited a small endothermic peak at ~100°C related to evaporation of adsorbed water. The exothermic peak at 1000°C can be ascribed to the reaction of illite and quartz that produce mullite [105], while at 1150°C the endothermic peak marked the partial melting of the powder. The overall reactions are summarized in Table 7 - DTA reactions.

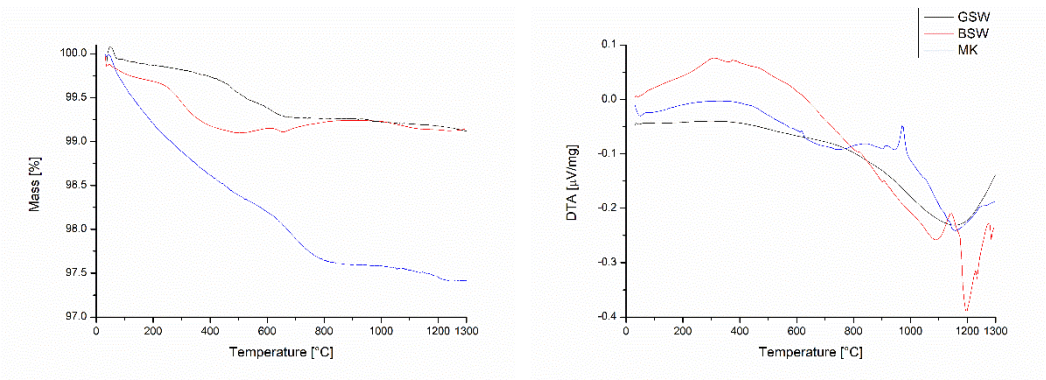

(a) (b)

Figure 16 – Thermal characterization of the raw materials: TG (a) and DTA (b).

$$(Mg,Fe)_2SiO_4 + {}^{5}/_{2}\ O_2 \rightarrow Mg_2SiO_4 + SiO_2 + Fe_2O_3 \quad \text{(Eq. 6)}$$

Temperature interval	Events
0 – 300 °C	Loss of adsorbed water
300 – 800 °C	Dehydroxylation of hydrate minerals
800 – 1000 °C	Phases stabilization

Table 6 - TG analysis events.

Temperature interval	Event	Type of event
100 °C	Evaporation	Endothermic
150 – 500 °C	Fe^{2+} to Fe^{3+} oxidation	Exothermic
500 °C	α to β quartz transformation	Endothermic
800 to 900 °C	Olivine to hematite transition	Endothermic
1000 °C	Mullite formation	Exothermic
1150 to 1200 °C	Partial melting	Endothermic
1200 °C	Crystallization	Exothermic

Table 7 - DTA reactions.

4.2 Formulation of granophyre sludge-based AAMs

The

4.2.1 Binary mixtures design development

After

The

The

The

Sample	FC (wt.%)	MK (wt.%)	NaOH	Na2SiO3	H2O	Integrity
GSW10-4.6	100	-	100	-	-	Not
GSW10-20	100	-	20	80	-	Not
GSW10-30	100	-	30	70	-	Not
GSW10-40	100	-	40	60	-	Not
GSW10-50	100	-	50	50	-	Not
GSW10-60	100	-	60	40	-	Not
GSW10-70	100	-	70	30	-	Not
GSW10-80	100	-	80	20	-	Not
GSW5-40	50	50	40	60	-	Passed
GSW6-40	60	40	40	60	-	Passed
GSW7-40	70	30	40	60	-	Passed
GSW8-40	80	20	40	60	-	Passed
GSW9-40	90	10	40	60	-	Not
GSW5-50	50	50	50	50	-	Not
GSW6-50	60	40	50	50	-	Not
GSW7-50	70	30	50	50	-	Not
GSW8-50	80	20	50	50	-	Not
GSW9-50	90	10	50	50	-	Not
GSW5-60	50	50	60	40	-	Not
GSW6-60	60	40	60	40	-	Not
GSW7-60	70	30	60	40	-	Not
GSW8-60	80	20	60	40	-	Not
GSW9-60	90	10	60	40	-	Not
NaOH 9.9M (wt.%)						
GSW5-1H2O	50	50	25	50	25	Passed
GSW3-1H2O	30	70	25	50	25	Passed
GSW4-1H2O	40	60	25	50	25	Passed
GSW4-1.5H2O	40	60	22.2	44.4	33.3	Not

Table

4.2.2 Mineralogical and molecular characterization

The

Moreover,

All

Similarly,

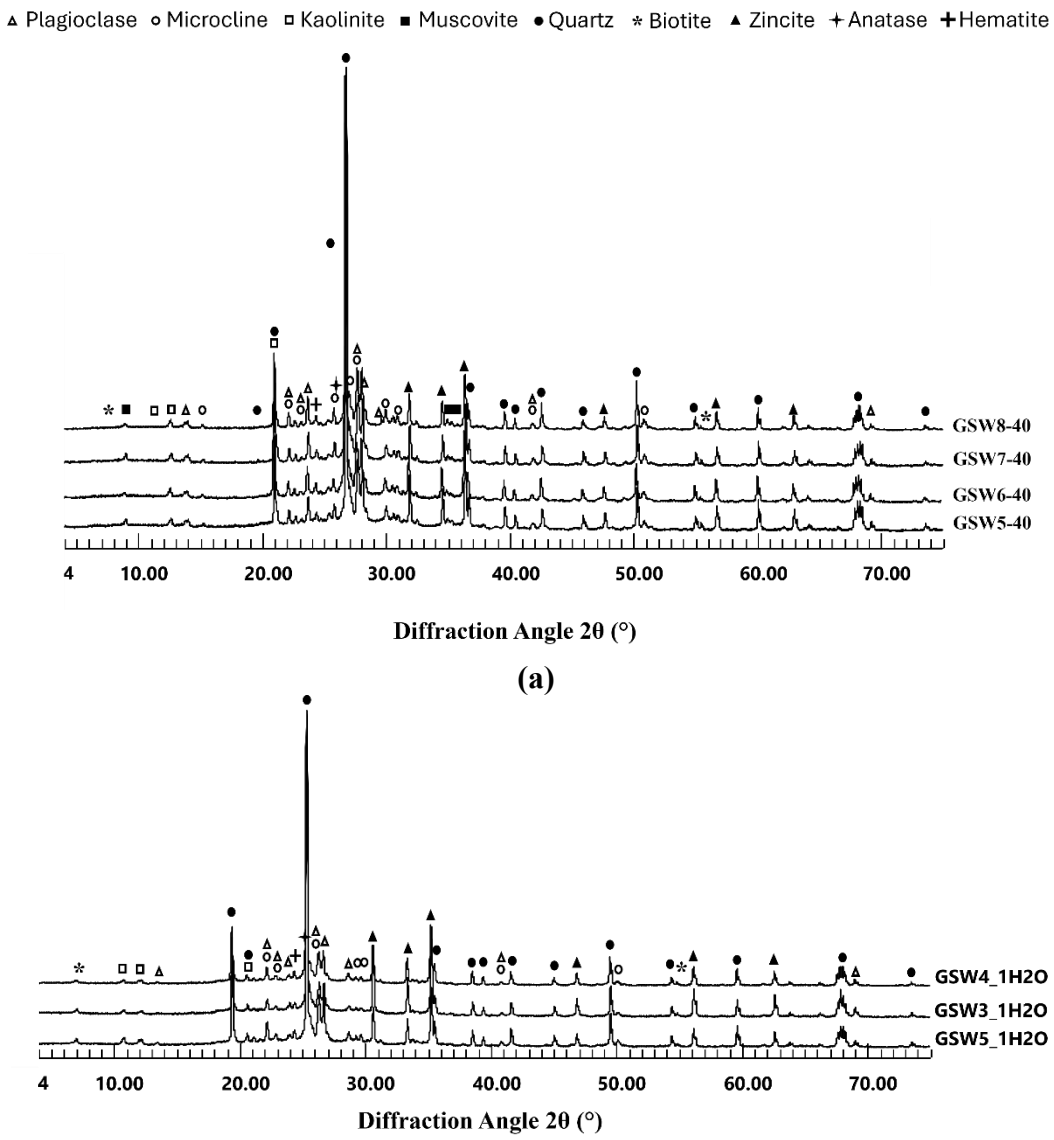

Figure

Sample ID	GSW5-	GSW6-	GSW7-	GSW8-	GSW5-	GSW3-	GSW4-
Measured	34.13	31.33	24.97	25.88	42.24	61.94	53.20
Theoretical	35.80	28.64	21.48	14.32	35.80	50.12	42.96

Table

The

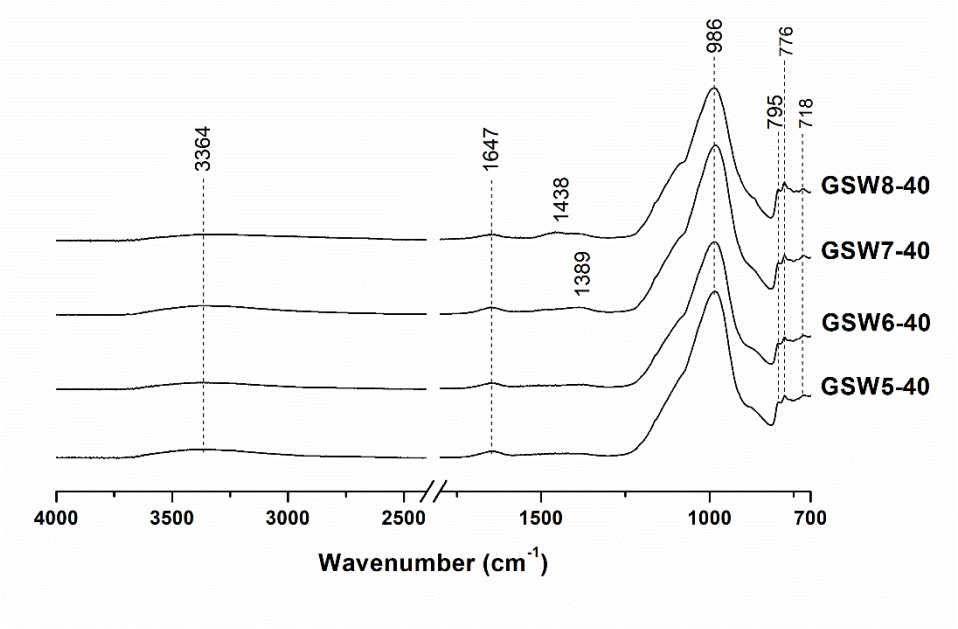

(a)

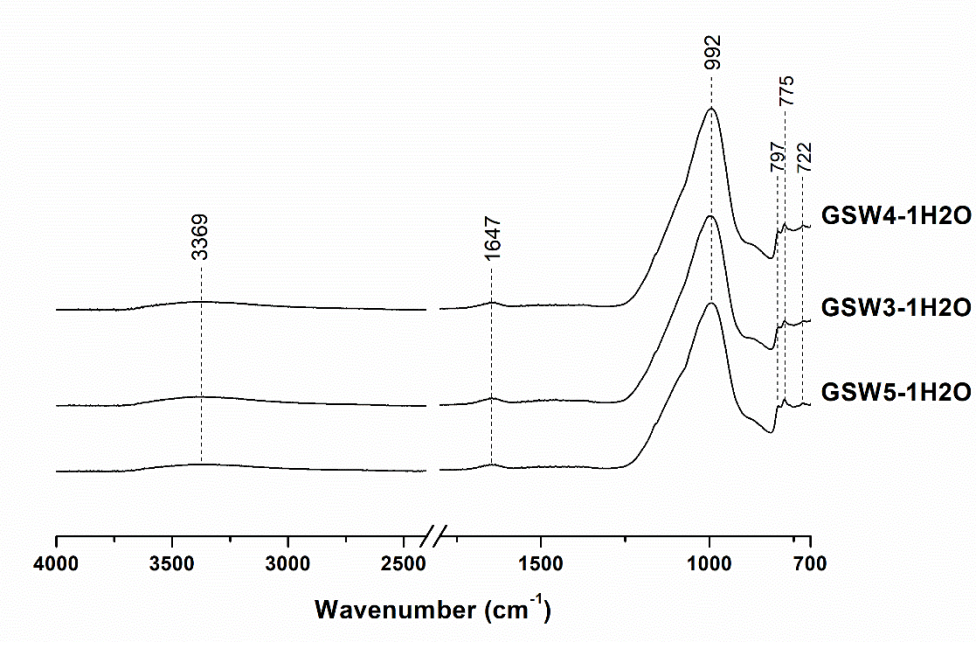

(b)

Figure

4.2.3 Morphological and mechanical characterization

Figure

Figure

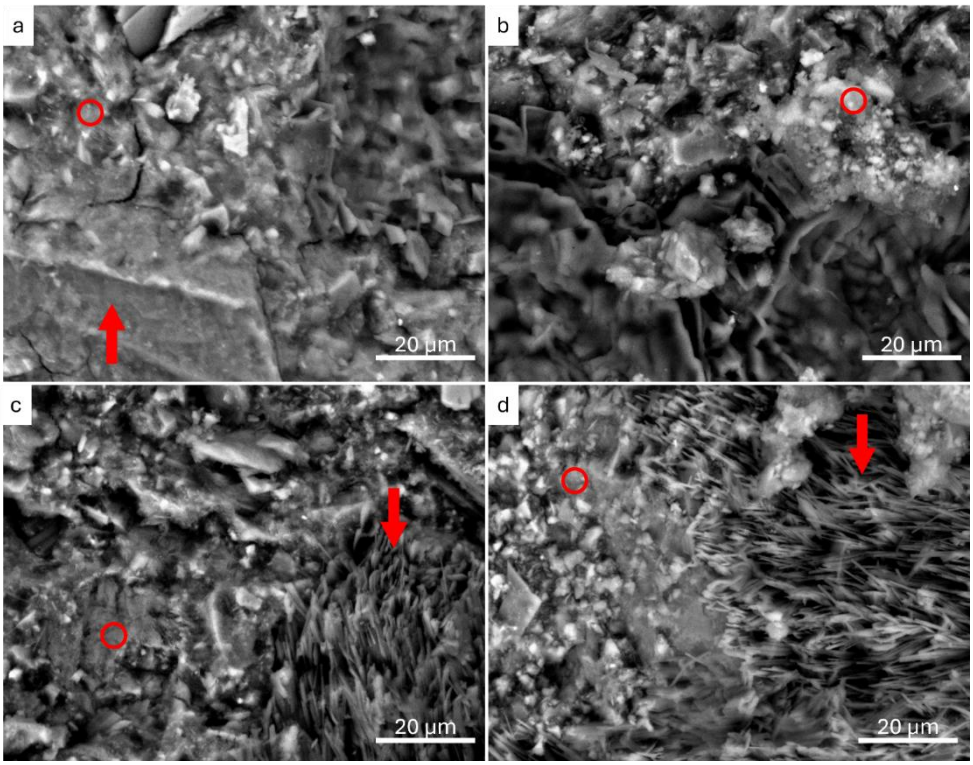

Figure

Figure

Generally,

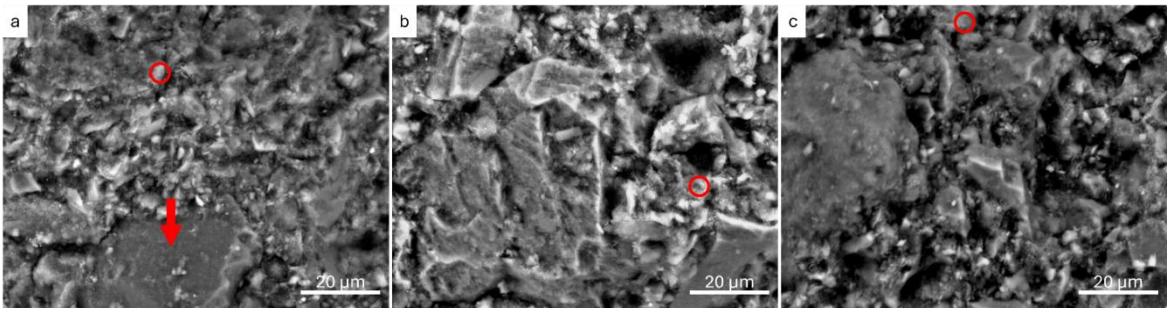

Figure

Table

Sample	wt. %										
	Na	**Si**	**Al**	**Si/Al**	**Mg**	**P**	**K**	**Ca**	**Ti**	**Mn**	**Fe**
GSW5-	6.1	62.8	25.9	2.4	0.2	0.3	2.1	0.5	0.6	0.2	1.3
GSW6-	4.4	61.7	19.5	3.1	0.1	0.05	13.3	0.3	0.2	0.07	0.4
GSW7-	4.5	64	19.3	3.3	0.1	0.4	11.5	0	0	0	0.2
GSW8-	3.3	58.2	13.7	4.2	0.2	0.1	21.4	0.6	0.7	0.3	1.5
GSW5-	8.1	74	15.5	4.7	0.2	0	1.1	0.1	0.2	0.08	0.7
GSW3-	3.1	80.1	14.7	5.4	0.2	0.05	0.6	0.1	0.4	0.09	0.7
GSW4-	4.6	56	34.8	1.6	0.3	0.2	1.1	0.3	1.1	0	1.6

Table

The

In

The

ID	Compressive [MPa]	Standard
GSW5-40	27.63	2.95
GSW6-40	29.37	2.77
GSW7-40	23.07	1.73
GSW8-40	22.23	3.52
GSW5-1H2O	18.63	2.20
GSW3-1H2O	24.87	0.95
GSW4-1H2O	22.64	2.04

Table

4.3 Advanced characterisation of the optimal GSW-based formulation

After

4.3.1 Morphological characterization with confocal microscope

Figure

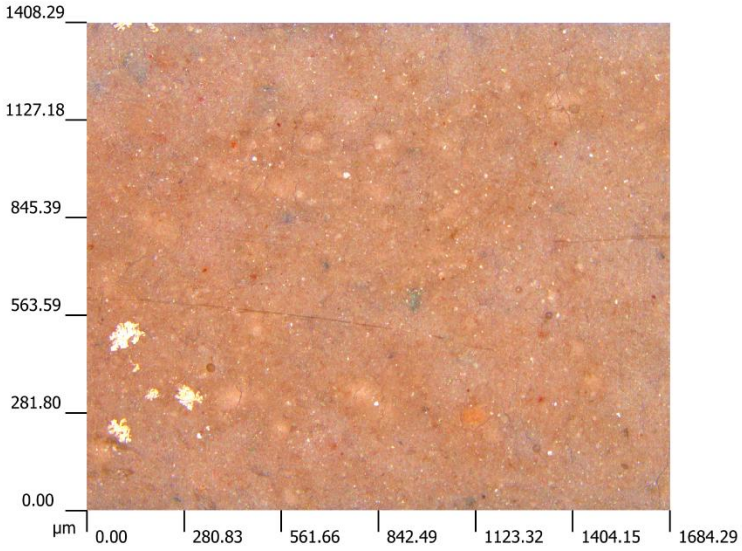

Figure

4.3.2 Thermal characterization

The

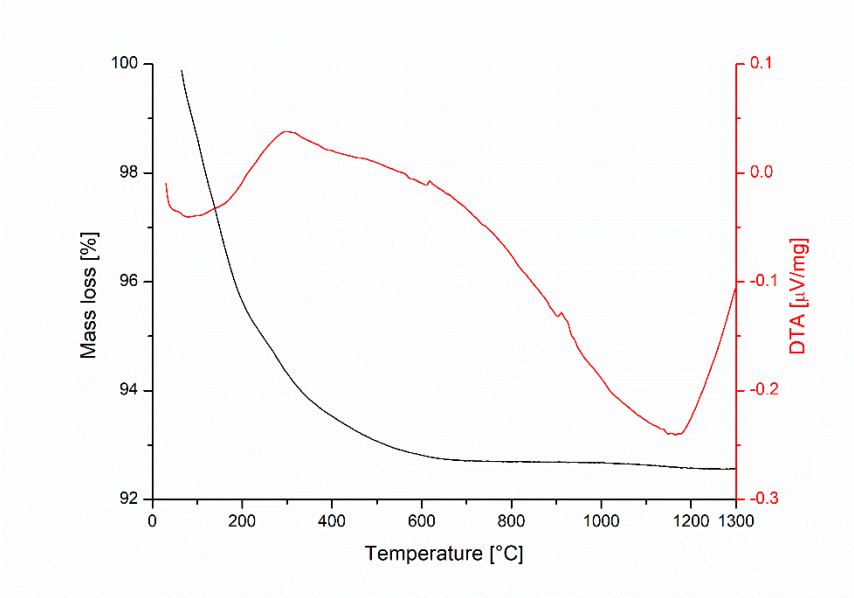

Figure 22 - Thermal analysis of GSW6-40.

4.3.3 Rheological characterization

The

Figure

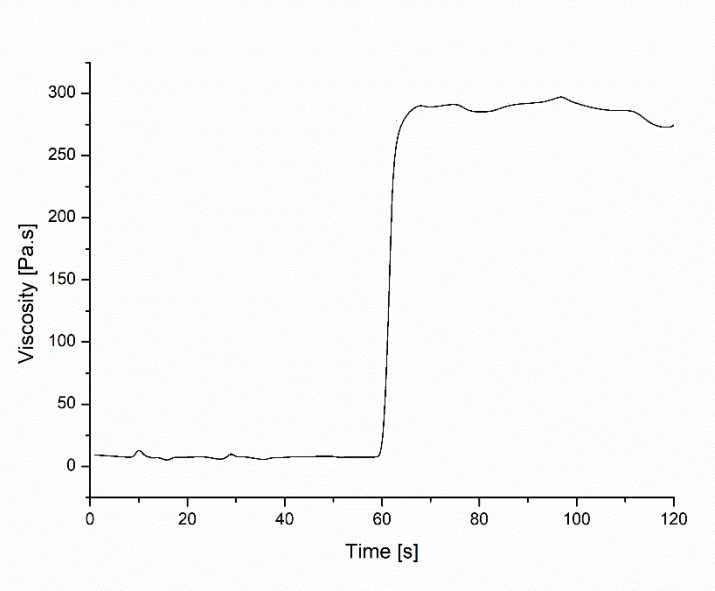

Figure 23 - Rheological characterization of GSW6-40: structural rebuilding test.

Figure

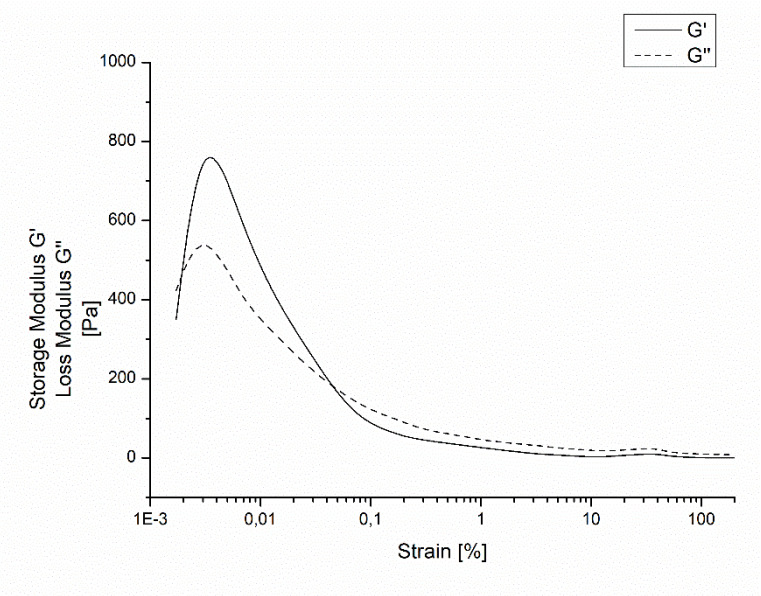

Figure 24 - Strain sweep test of GSW6-40 paste.

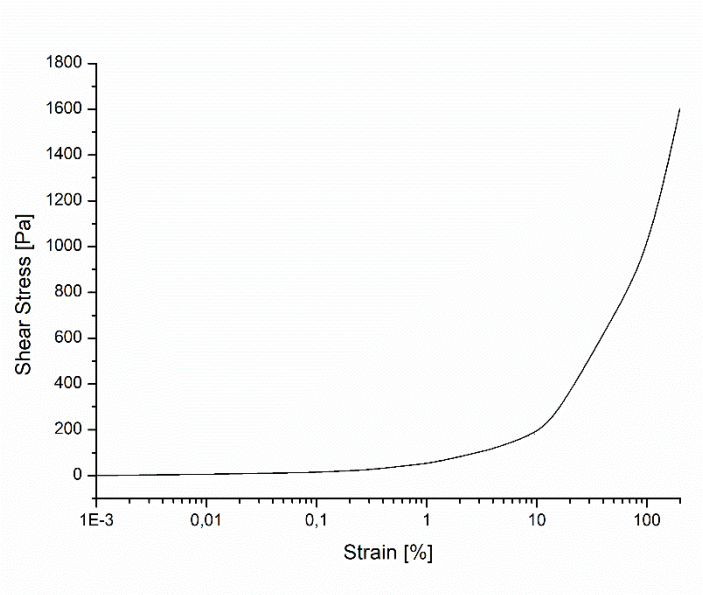

Figure 25 - Shear stress and strain curve of GSW6-40 paste.

The

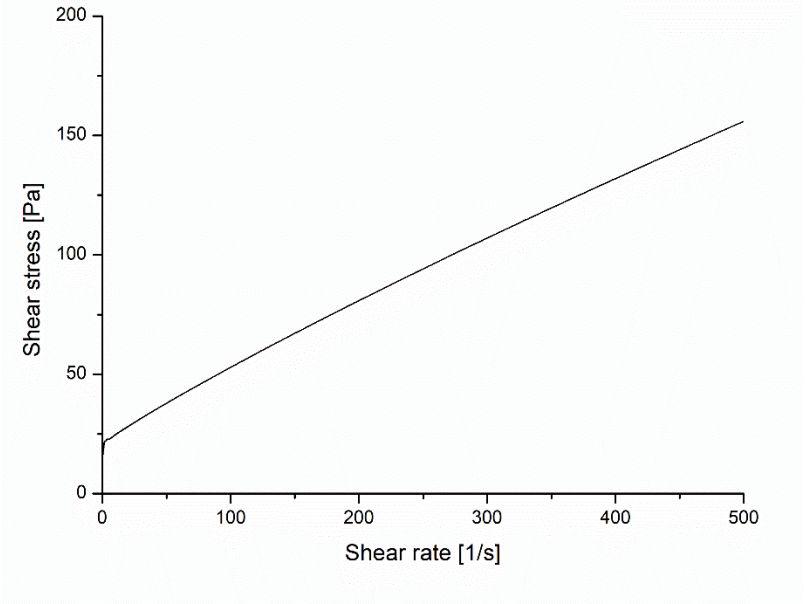

Figure 26 - Flow curve of GSW6-40 paste.

4.3.4 Freeze-thaw tests

The

This

ID	m_i [g]	m_f [g]	Δm [wt. %]	Average [wt. %]
GSW6-40_1	134.289	120.391	10.3	10.1 ± 0.3
GSW6-40_2	133.642	120.154	10.1	
GSW6-40_3	141.594	126.884	10.3	
GSW6-40_4	139.779	126.197	9.7	

Table

(a)

(b)

Figure 27 – Appearance of specimens before (a) and after (b) the freeze-thaw cycles.

4.4 Basalt sawing waste AAMs

This

ID	Basalt	Metakaolin	NaOH	Na_2SiO_3	L/S
FB45	55.17	13.79	13.96	17.08	0.45

Table 13 - Formulation of AAMs based on basalt sawing waste.

4.4.1 Mineralogical, molecular and morphological characterization

The

Kaolinite

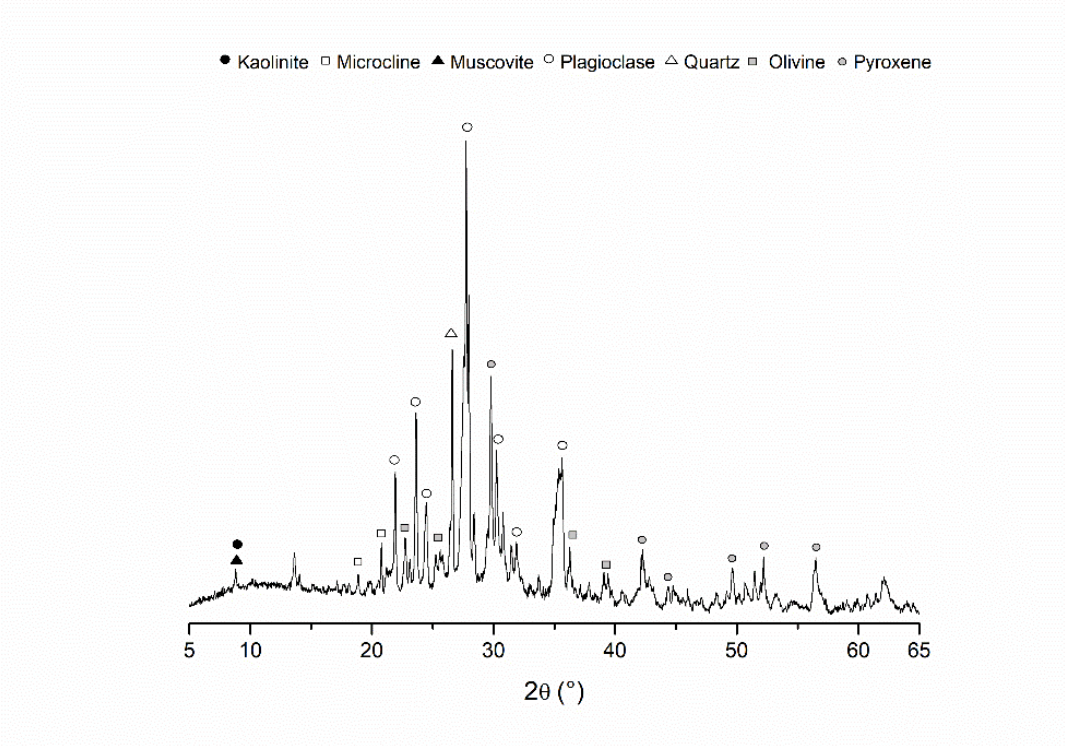

Figure 28 - X-ray diffraction pattern of consolidated FB45.

The

ID	Amorphous phase [%]

FB45	40.01 ± 0.007

Table 14 - Amorphous phase of consolidated FB45.

The

Peaks

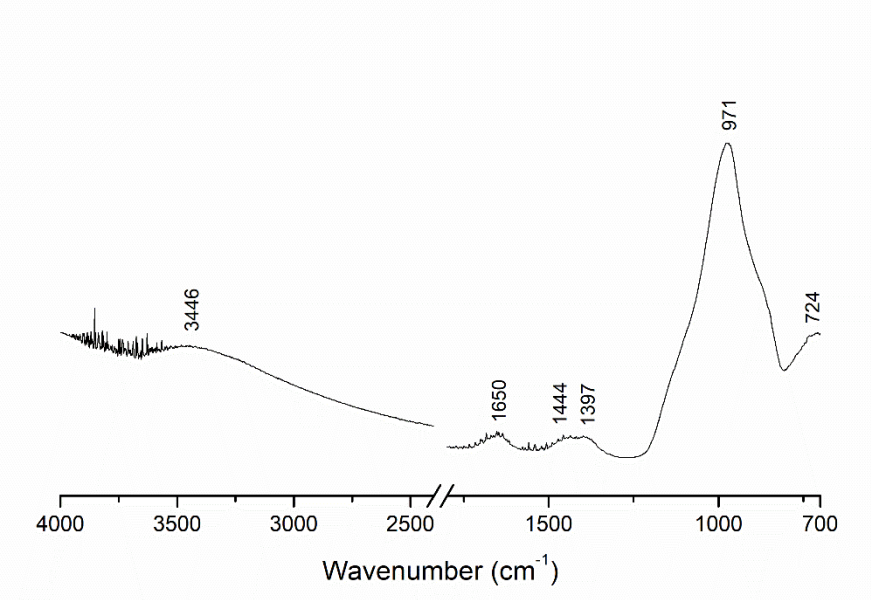

Figure 29 - FT-IR spectra of the consolidated AAMs based on BSW (FB45).

The

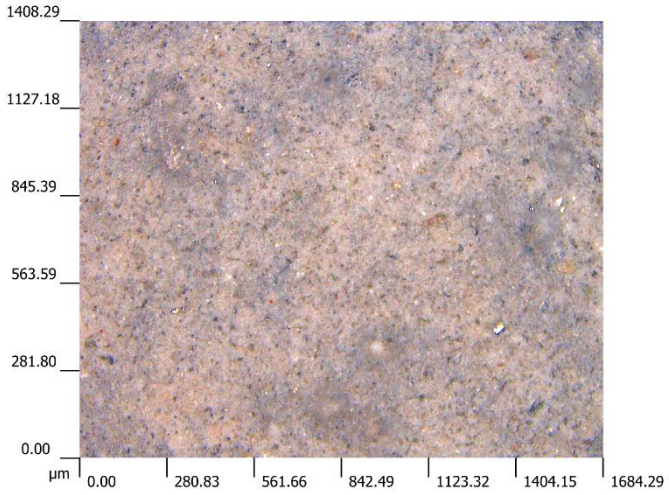

Figure

4.4.2 Thermal characterization

The

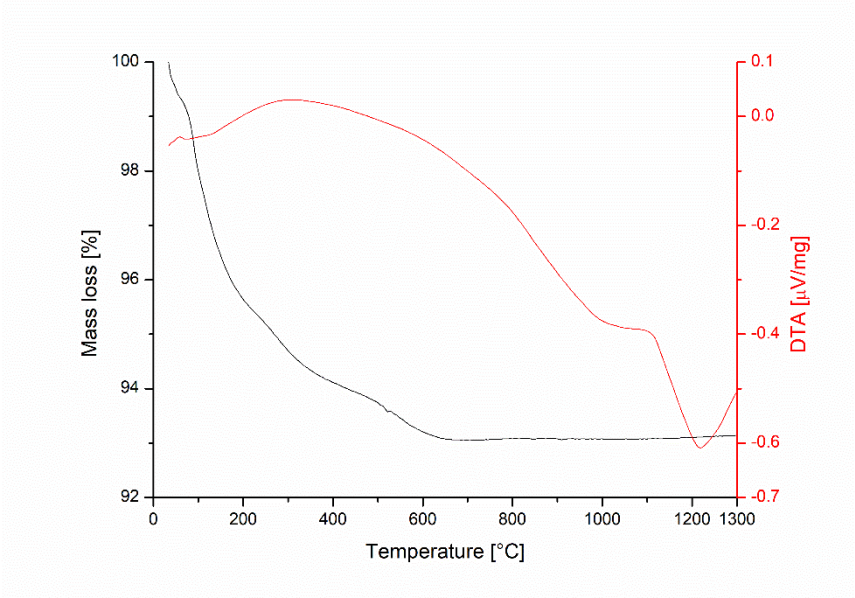

Figure

4.4.3 Rheological characterization

From

The

The

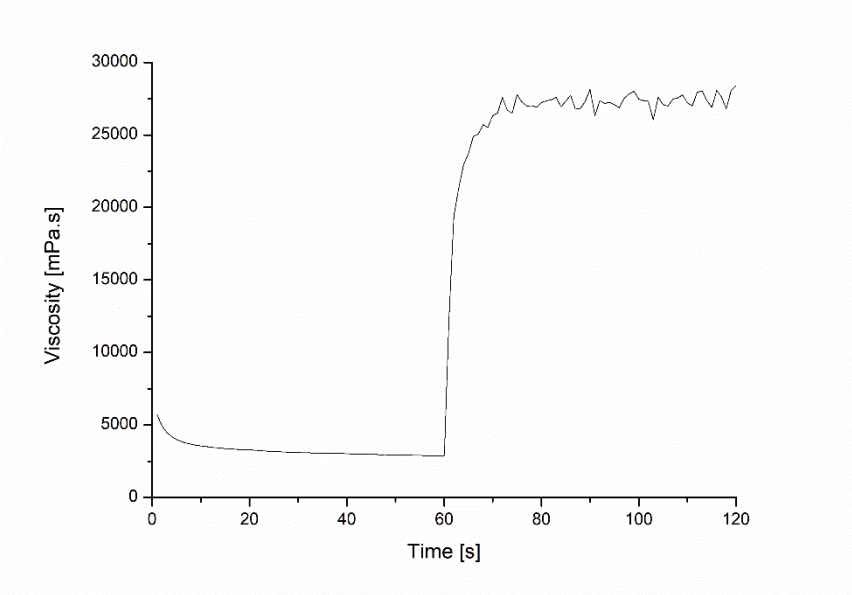

Figure 32 - Rheological characterization of FB45: structural rebuilding test.

Dynamic

Figure

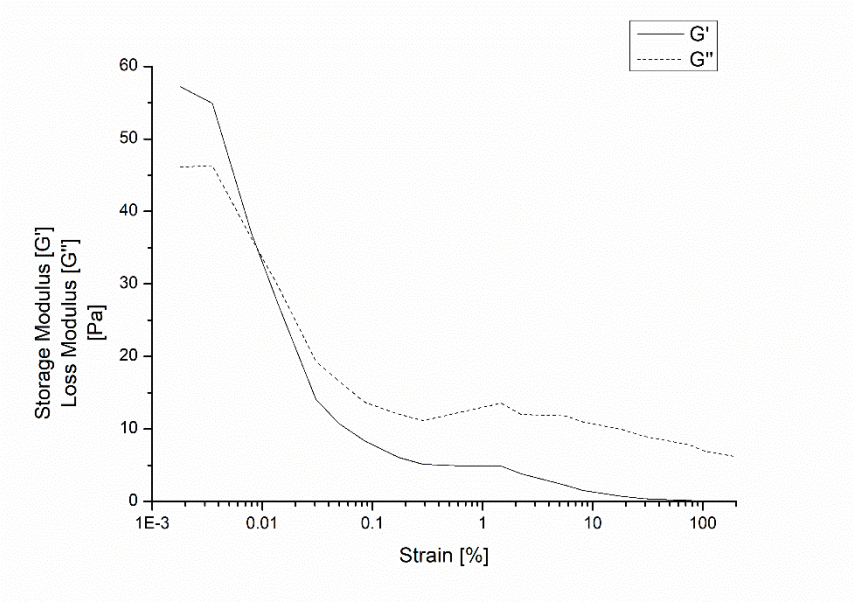

Figure 33 - Strain sweep test of FB45 paste.

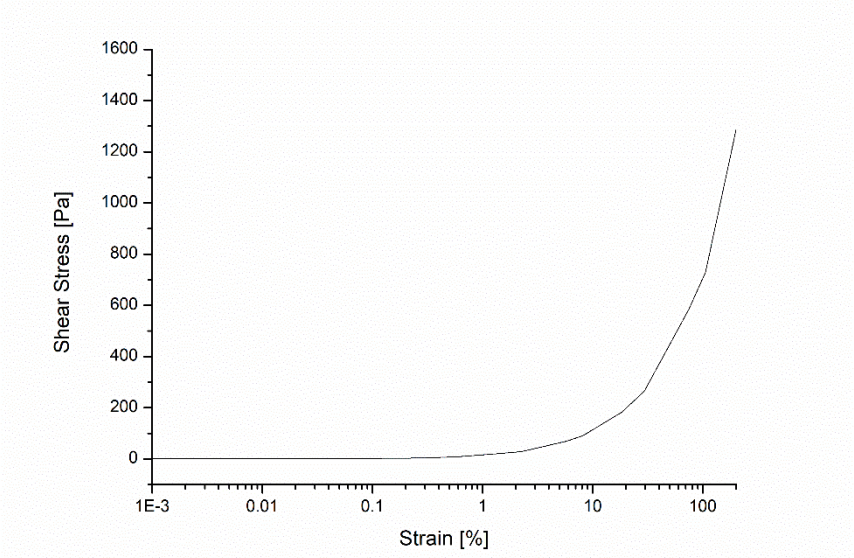

Figure 34 - Shear stress and strain curve of FB45 paste.

Figure

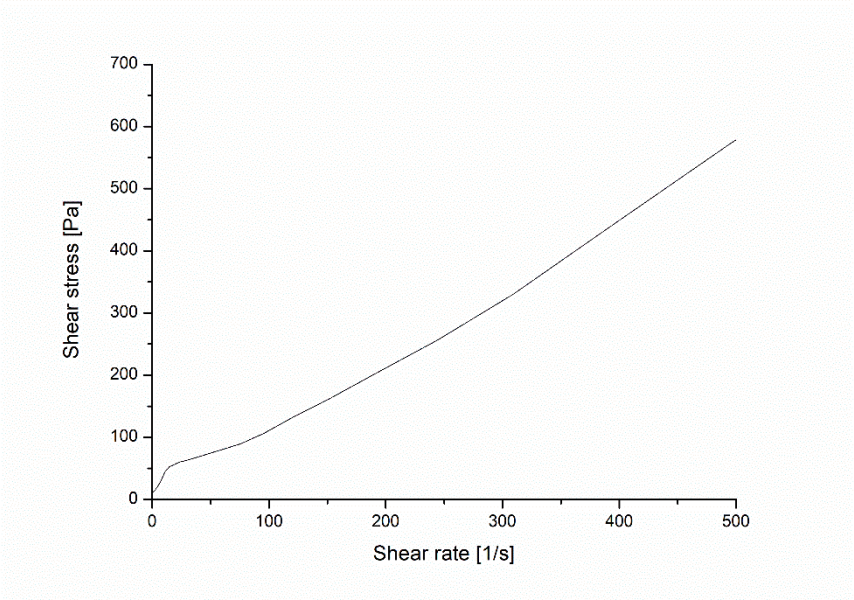

Figure 35 - Shear stress and shear rate curve of FB45 paste.

4.4.4 Freeze-thaw resistance test

The

ID	m_i [g]	m_f [g]	Δm [wt. %]	Average [wt. %]
FB45_1	143.326	128.654	10.23	10.10 ± 0.11
FB45_2	138.260	124.256	10.12	
FB45_3	139.523	125.444	10.09	
FB45_4	133.721	120.401	9.96	

Table

(a)

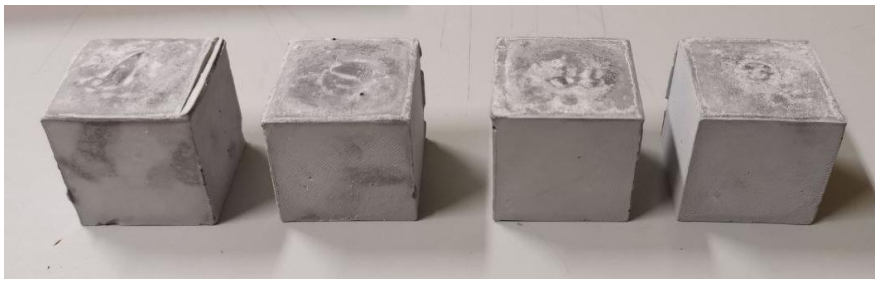

(b)

Figure

4.4.5 Mechanical characterization of FB45

Table

ID	Compressive	Flexural
FB45	28.8 ± 1.7	6.8± 1.2

Table 16 - Mechanical performances of FB45.

4.5 Comparison between GSW- and BSW-based binders

In

Both

Moreover,

Confocal

Thermal

The

The

The

In

4.6 Development of fibre-reinforced Granite Sawing Waste-based AAMs

In

4.6.1 Morphological and chemical characterization

Figure

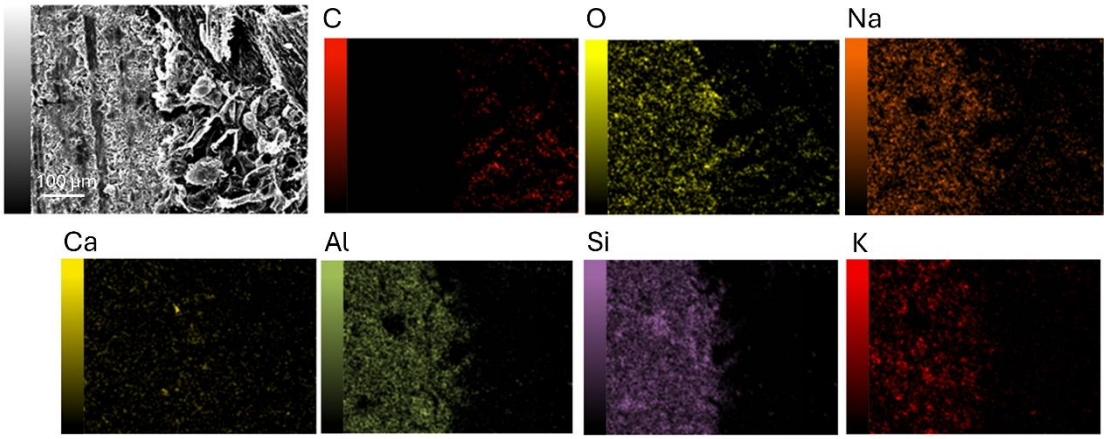

Figure

Figure

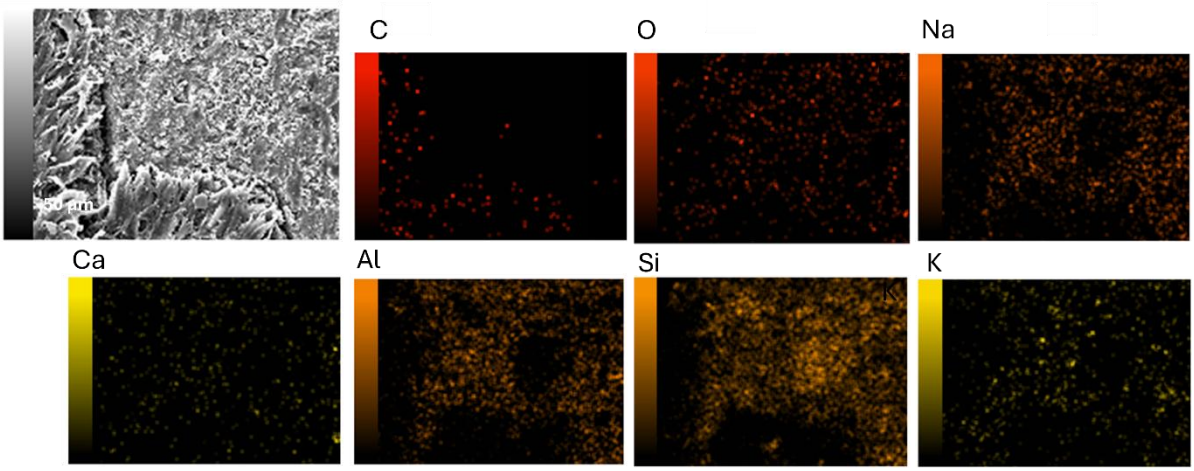

Figure

Figure

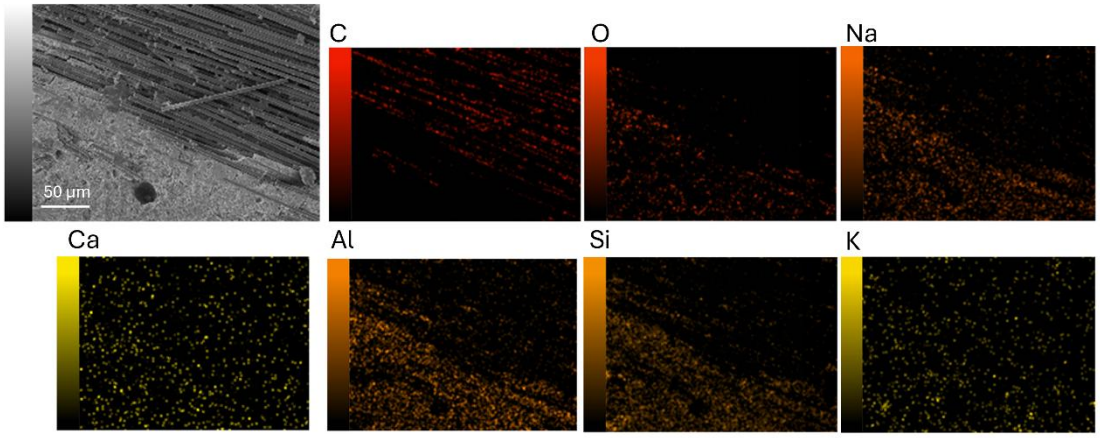

Figure

Taken

The

The

Roughness

ID	*Sa* [μm]			*RMS* [μm]		
	Top part		Bottom	Top part		Bottom
	Average	Standard	Value	Average	Standard	Value
GSW	2.73	1.55	0.60	3.42	2.02	0.77
GSW-P0.5	4.00	1.61	0.37	4.12	0.69	0.50
GSW-P1	3.76	1.15	0.75	6.15	1.84	0.95
GSW-P1.5	1.57	1.01	0.38	3.32	2.13	0.40
GSW-P2	4.50	1.75	0.46	6.26	2.65	0.48

Table

The

ID	Sa [μm]			RMS [μm]		
	Top part		Bottom	Top part		Bottom
	Average	Standard	Value	Average	Standard	Value
GSW	2.73	1.55	0.60	3.42	2.02	0.77
GSW-F0.5	2.02	0.35	0.71	2.01	1.27	0.99
GSW-F1	2.47	1.07	0.39	1.78	0.48	0.55
GSW-F1.5	2.28	0.50	0.34	3.40	1.64	0.39
GSW-F2	3.24	0.88	0.57	3.37	1.25	0.72

Table

The

Altogether,

ID	Sa [µm]			RMS [µm]		
	Top part		Bottom	Top part		Bottom
	Average	Standard	Value	Average	Standard	Value
GSW	2.73	1.55	0.60	3.42	2.02	0.77
GSW-C0.5	12.74	1.92	1.48	16.47	1.78	4.12
GSW-C1	13.69	2.75	1.04	17.11	0.27	1.34
GSW-C1.5	17.38	2.27	2.75	21.68	1.16	7.64
GSW-C2	17.41	2.35	1.89	21.34	1.59	3.04

Table

4.6.2 Chemical, Physical and mechanical characterization

Inductively

The

Despite

Overall,

ID	mg/l									
	Al	Ca	Fe	K	Mg	Na	P	Si	Ti	B
GSW-	3.18	<DL	0.32	4.36	<DL	416	0.33	6.64	<DL	0.04
GSW-	2.90	<DL	0.26	4.05	0.05	347	0.44	6.86	<DL	0.03
GSW-	3.18	<DL	0.23	3.74	<DL	368	0.42	6.37	<DL	0.046

Table

Porosity

ID	Porosity [%]		
	Open	Closed	Total
GSW no fibre	33.38	1.99	35.37
GSW-P0.5	32.00	2.02	34.02
GSW-P1	36.71	1.06	37.77
GSW-P1.5	34.18	3.73	37.91
GSW-P2	35.83	3.48	39.31

Table

Table

ID	Porosity [%]		
	Open	Closed	Total
GSW no fibre	33.38	1.99	35.37
GSW-F0.5	33.97	2.54	36.51
GSW-F1	35.50	1.93	37.43
GSW-F1.5	32.45	2.90	35.35
GSW-F2	39.64	2.31	41.95

Table

Table

Overall,

ID	Porosity [%]		
	Open	Closed	Total
GSW no fibre	33.38	1.99	35.37
GSW-C0.5	34.18	0.86	35.04
GSW-C1	34.48	0.99	35.47
GSW-C1.5	32.33	0.95	33.25
GSW-C2	30.85	1.45	32.30

Table

The

ID	Average	Standard deviation
GSW no fibre	9.7	1.1
GSW-P0.5	7.3	1.3
GSW-P1	5.3	1.7
GSW-P1.5	11.0	1.6
GSW-P2	6.1	1.6

Table

Flexural

ID	Average	Standard deviation
GSW no fibre	9.7	1.1
GSW-F0.5	8.3	1.9
GSW-F1	9.5	1.7
GSW-F1.5	16.4	1.8
GSW-F2	12.6	1.0

Table

Table

ID	Average	Standard deviation
GSW no fibre	9.7	1.1
GSW-C0.5	13.9	1.7
GSW-C1	16.0	1.5
GSW-C1.5	18.5	1.8
GSW-C2	22.0	2.0

Table

The

Across

Similarly,

Palm

Overall,

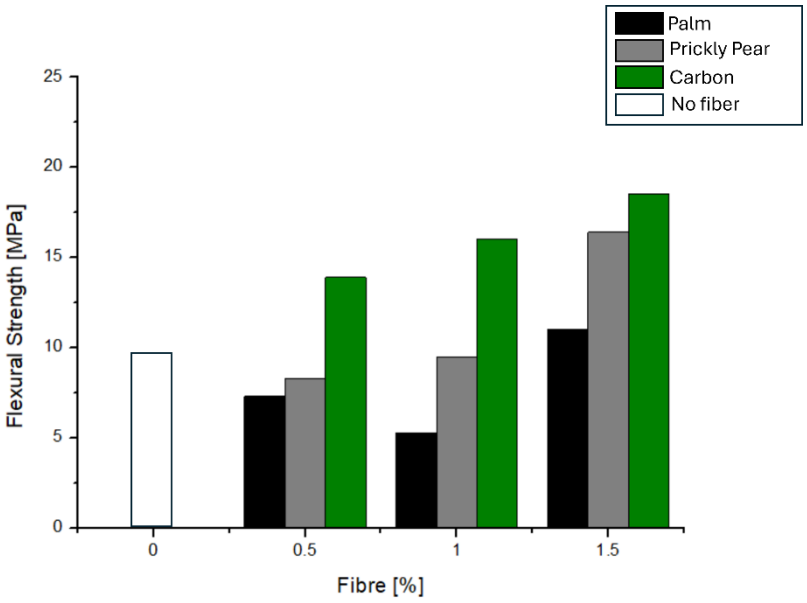

Figure

The

ID	Average	Standard deviation
GSW no fibre	29.37	2.77
GSW-P0.5	17.3	2.4
GSW-P1	24.5	1.9
GSW-P1.5	18.4	2.0
GSW-P2	13.8	1.1

Table

A

The

ID	Average	Standard deviation
GSW no fibre	29.37	2.77
GSW-F0.5	18.9	1.8

GSW-F1	18.4	2.1
GSW-F1.5	21.8	1.9
GSW-F2	17.7	2.3

Table

On

Overall,

ID	Average	Standard deviation
GSW no fibre	29.37	2.77
GSW-C0.5	41.6	1.7
GSW-C1	36.6	1.8
GSW-C1.5	46.4	2.7
GSW-C2	41.0	2.5

Table

The

Both

Taken

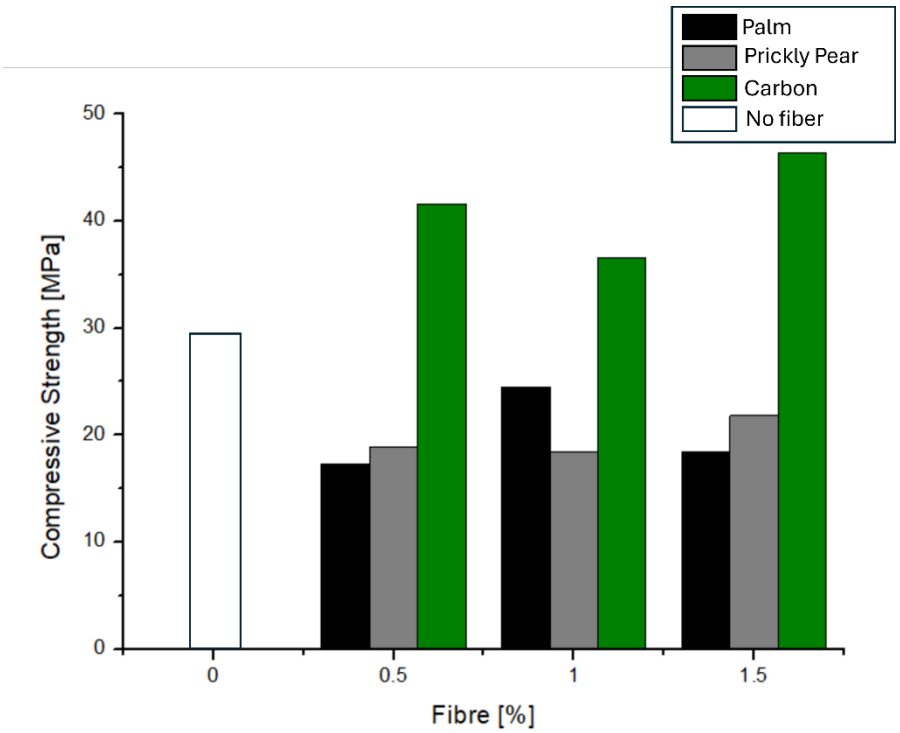

Figure

4.7 Development of fibre-reinforced Basalt Sawing Waste-based AAMs

This

4.7.1 Morphological characterization

The

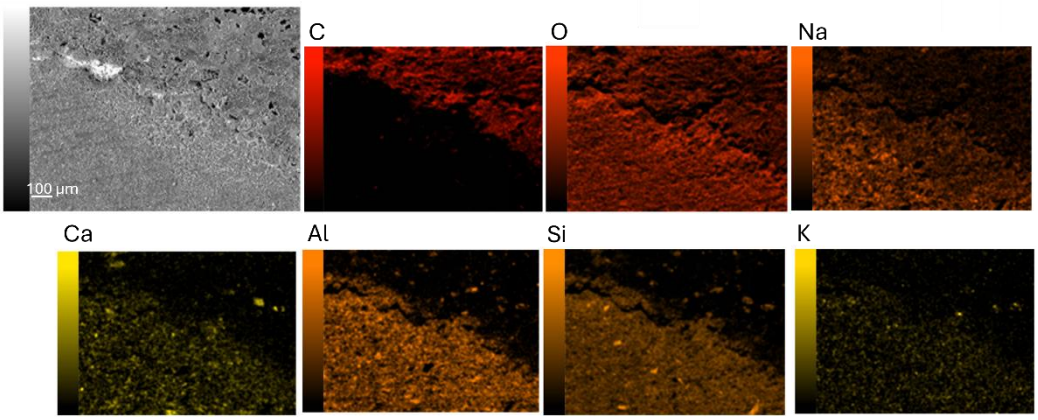

Figure

Figure

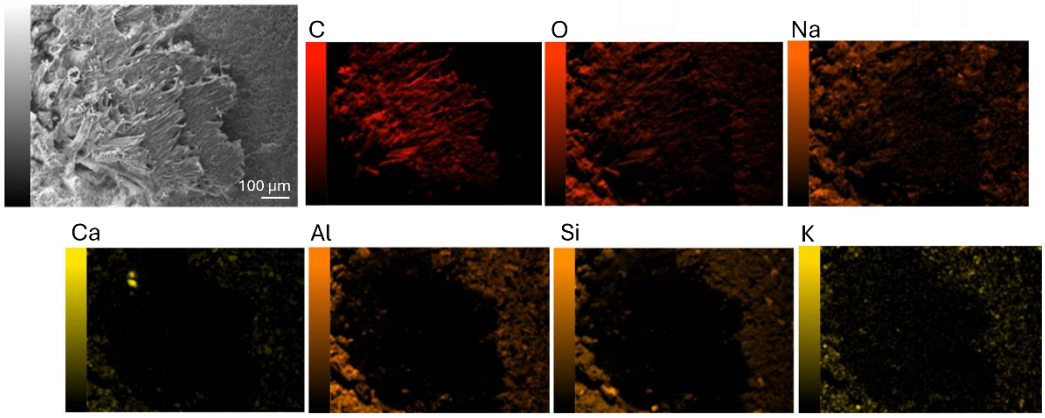

Figure

Figure

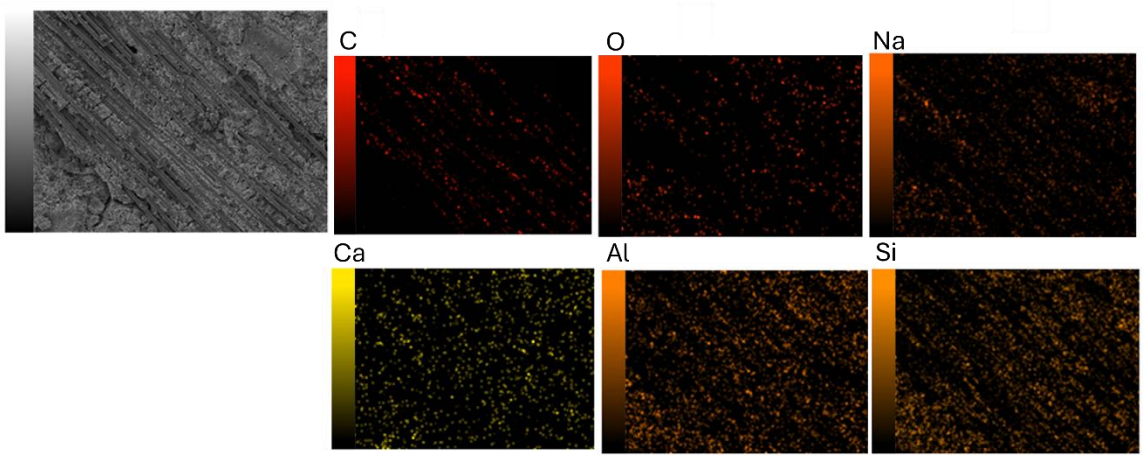

Figure

The

ID	Sa [µm]			RMS [µm]		
	Top part		Bottom	Top part		Bottom
	Average	Standard	Value	Average	Standard	Value
FB45	2.41	0.17	0.92	3.04	0.24	1.17
FB45-P0.5	1.94	0.61	0.50	1.73	0.97	1.04

FB45-P1	2.45	0.62	0.65	4.32	1.21	1.07
FB45-P1.5	3.16	0.92	0.66	6.49	0.85	1.10
FB45-P2	4.90	0.59	0.87	11.79	0.57	1.77

Table

Table

ID	Sa [μm]			RMS [μm]		
	Top part		Bottom	Top part		Bottom
	Average	Standard	Value	Average	Standard	Value
FB45	2.41	0.17	0.92	3.04	0.24	1.17
FB45-F0.5	2.02	0.46	0.64	2.74	0.32	0.91
FB45-F1	2.12	1.54	1.02	2.93	0.61	1.09
FB45-F1.5	2.21	0.45	0.56	3.55	0.74	0.78
FB45-F2	2.78	0.91	0.78	4.81	0.91	1.05

Table

The

Finally,

ID	Sa [μm]		RMS [μm]	
	Top part	Bottom	Top part	Bottom

	Average	Standard	Value	Average	Standard	Value
FB45	2.41	0.17	0.92	3.04	0.24	1.17
FB45-C0.5	7.22	2.34	1.03	9.47	2.11	1.98
FB45-C1	7.86	2.33	1.99	8.89	1.97	2.49
FB45-C1.5	9.20	1.87	3.11	10.24	1.77	3.97
FB45-C2	14.92	2.38	3.10	18.18	1.21	4.77

Table

4.7.2 Chemical, Physical and mechanical characterization

The

Finally,

ID	mg/L									
	Al	Ca	Fe	K	Mg	Na	P	Si	Ti	B
FB45-	0.70	1.36	0.29	29.8	0.13	1525	1.39	32.8	0.03	0.18
FB45-	0.62	0.77	0.16	26.7	0.11	1441	1.56	50	<DL	0.13
FB45-	0.51	0.49	0.09	25.6	<DL	1304	1.26	35	<DL	0.14

Table

The

ID	Porosity		
	Open	Closed	Total
FB45 – no fibre	28.19	2.56	30.75
FB45-P0.5	32.44	3.00	35.44
FB45-P1	30.31	5.45	35.76
FB45-P1.5	36.30	2.63	38.93
FB45-P2	38.50	1.46	39.96

Table

Table

ID	Porosity		
	Open	Closed	Total
FB45 – no fibre	28.19	2.56	30.75
FB45-F0.5	33.00	2.98	35.97
FB45-F1	35.85	1.52	37.37
FB45-F1.5	35.87	2.64	38.52
FB45-F2	36.11	5.00	41.11

Table

The

Finally,

ID	Porosity		
	Open	Closed	Total
FB45 – no fibre	28.19	2.56	30.75
FB45-C0.5	32.43	0.52	32.95
FB45-C1	33.21	0.28	33.49
FB45-C1.5	35.59	3.27	38.86
FB45-C2	36.55	0.95	37.50

Table

Table

ID	Average	Standard deviation
FB45 no fibre	6.8	1.2
FB45-P0.5	5.8	1.4
FB45-P1	6.1	1.2
FB45-P1.5	8.8	1.4
FB45-P2	6.7	1.1

Table

Table

ID	Average	Standard deviation
FB45 no fibre	6.8	1.2
FB45-F0.5	6.4	1.8
FB45-F1	7.3	1.9
FB45-F1.5	9.0	2.2
FB45-F2	6.7	2.1

Table

The

The

ID	Average	Standard deviation
FB45 no fibre	6.8	1.2
FB45-C0.5	33.6	2.1
FB45-C1	14.9	1.8
FB45-C1.5	23.3	1.0
FB45-C2	24.9	1.7

Table

Figure

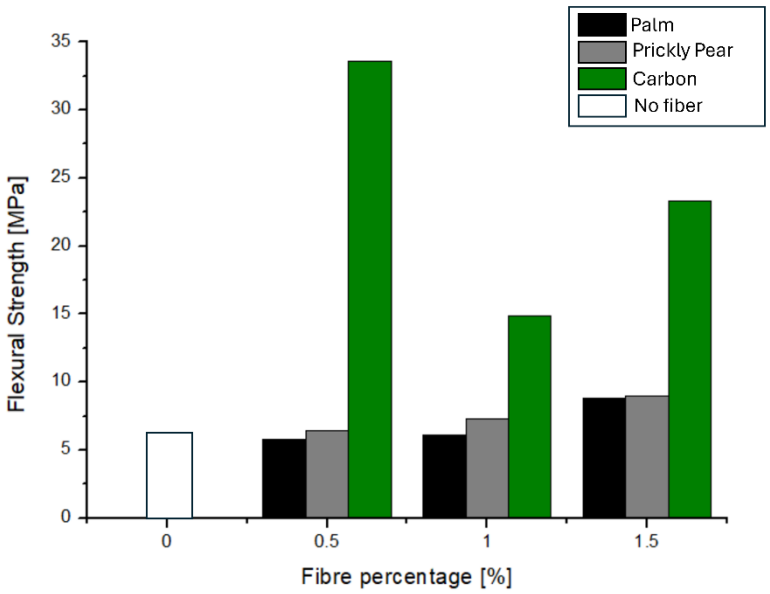

Figure

Table

ID	Average	Standard deviation
FB45 no fibre	28.8	1.7
FB45-P0.5	13.1	0.8
FB45-P1	13.4	0.9
FB45-P1.5	14.7	1.3
FB45-P2	15.1	1.1

Table

Table

ID	Average	Standard deviation
FB45 no fibre	28.8	1.7
FB45-F0.5	19.0	1.5

FB45-F1	17.6	1.2
FB45-F1.5	17.4	1.8
FB45-F2	15.7	1.4

Table

Table

ID	Average	Standard deviation
FB45 no fibre	28.8	1.7
FB45-C0.5	27.7	1.2
FB45-C1	26.9	0.9
FB45-C1.5	30.2	2.3
FB45-C2	34.7	2.7

Table

Figure

At

Finally,

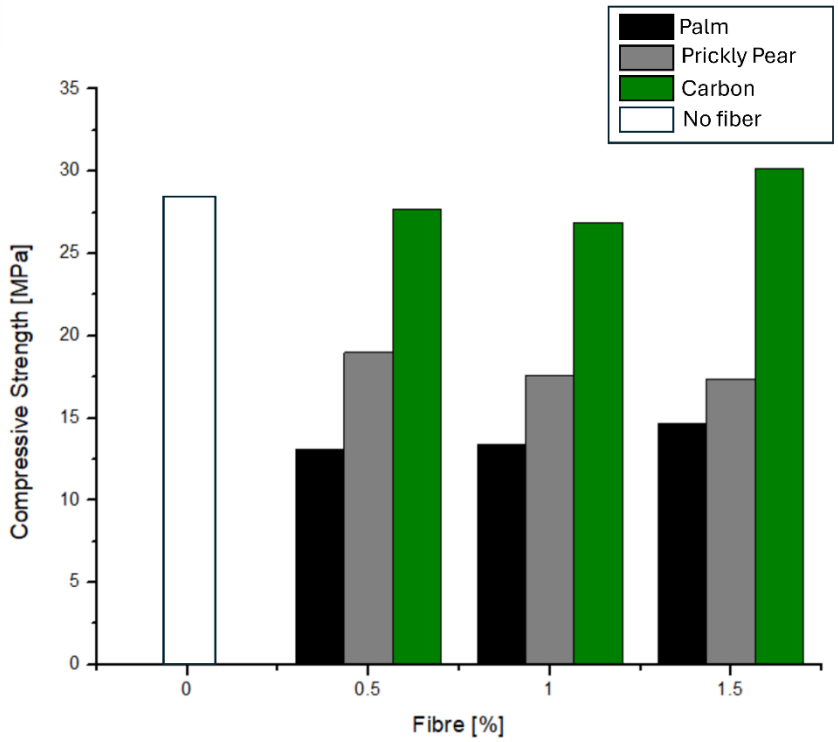

Figure

4.8 Comparison between fibre-reinforced binders

The

From

The

Porosity

Chemical

In

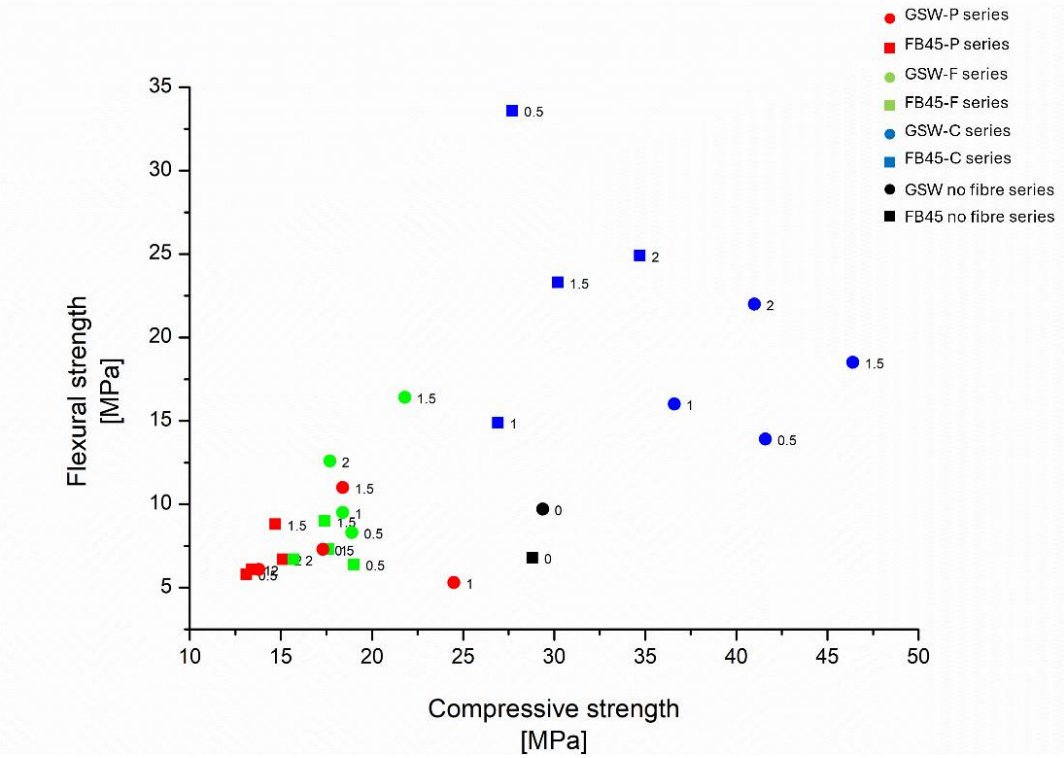

Figure

Moreover,

Finally,

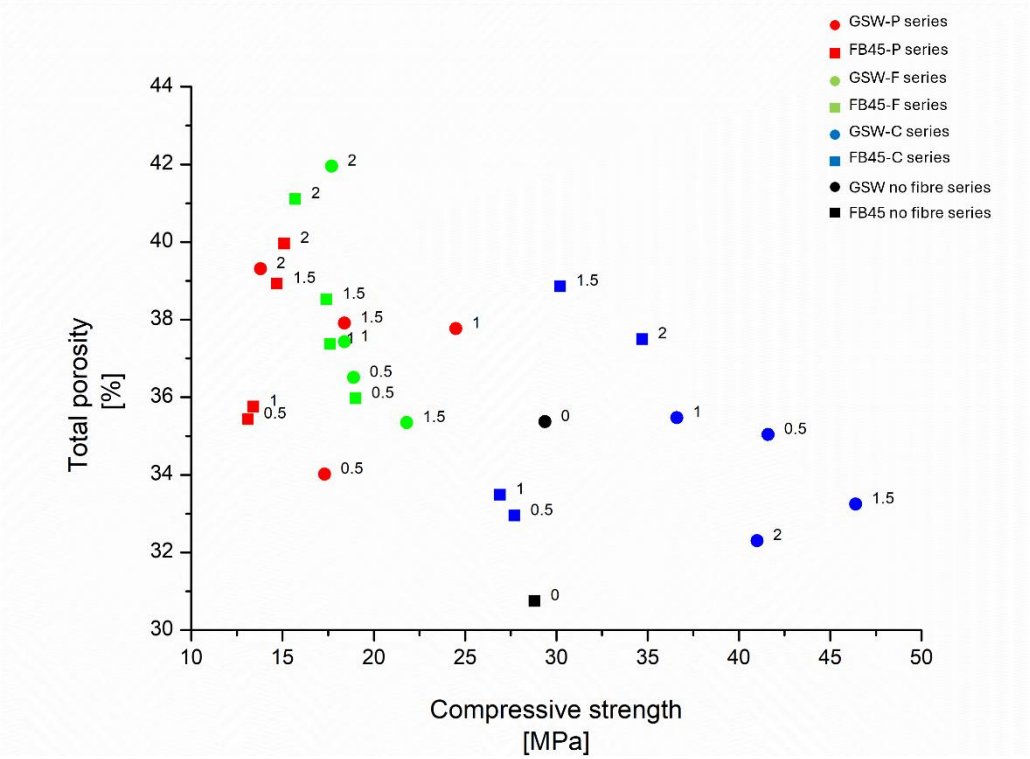

Figure

5 Conclusions

This

The

Among

Moreover,

From

In

6 I Case study: Preliminary evaluation of Design of Experiments (DoE) approach for the prediction of new Alkaline-Activated Materials (AAMs) formulations

Sabrina Elettra Zafarana[1], Germana Barone[1] & Paolo Mazzoleni[1]

1-

This

6.1 Introduction

Recently,

Traditionally,

Design

D-

6.2 Materials and methods

6.2.1 Raw materials

Sawing

Specifically,

Moreover,

FB

The

.

	SiO_2	Al_2O_3	CaO	Fe_2O_3	K_2O	MgO	Na_2O	TiO_2
FB	47 ± 2	18 ± 1	10.0 ± 0.4	11 ± 1	1.6 ± 0.1	5 ± 1	4.3 ± 0.5	1.7
MK	61	35	0.13 ± 0.06	1.3	0.52 ± 0.04	0.13 ± 0.07	0.04 ± 20	1.7

Table

6.2.2 Design parameters

The

Factor	Low Level	High level
FB	48	65
MK	10	20
NaOH	10	20
Na_2SiO_3	12	22

Table 44 - Low and high levels of the considered factors.

RUN	ID	FB (%)	MK	NaOH	Na_2SiO_3	L/S
1	FB7MK10-91	48	10	20	22	0.72
2	FB5MK20-167	48	20	20	12	0.47
3	FB7MK10-91_2	48	10	20	22	0.72
4	FB5MK10-45	58	10	10	22	0.47
5	FB5MK20-167_2	48	20	20	12	0.47
6	FB5MK20-45	48	20	10	22	0.47
7	FB5MK10-167	58	10	20	12	0.47
8	FB3MK10-67	65	10	10	15	0.33
9	FB4MK10-132	62	10	16	12	0.38
10	FB5MK20-45_2	48	20	10	22	0.47

Table

Table

ID	SiO_2	Al_2O_3	CaO	Fe_2O_3	K_2O	MgO	Na_2O	TiO_2	H_2O	Si/Al	Na/Si	Na/Al
FB7MK10-91	28.66	12.14	4.81	5.41	0.82	2.41	2.06	0.98	33.08	2.36	0.07	0.16
FB5MK20-167	34.76	15.64	4.82	5.54	0.87	2.42	2.07	1.15	24.84	2.22	0.05	0.13
FB7MK10-91_2	28.66	12.14	4.81	5.41	0.82	2.41	2.06	0.98	33.08	2.36	0.07	0.16
FB5MK10-45	33.36	13.94	5.81	6.51	0.98	2.91	2.49	1.15	26.60	2.39	0.07	0.17
FB5MK20-	34.76	15.64	4.82	5.54	0.87	2.42	2.07	1.15	24.84	2.22	0.05	0.13
FB5MK20-45	34.76	15.64	4.82	5.54	0.87	2.42	2.07	1.15	25.60	2.22	0.05	0.13
FB5MK10-167	34.76	15.64	4.82	5.54	0.87	2.42	2.07	1.15	24.84	3.19	0.07	0.13
FB3MK10-67	36.65	15.20	6.51	7.28	1.09	3.26	2.79	1.27	19.84	2.41	0.07	0.18
FB4MK10-132	35.24	14.66	6.21	6.95	1.04	3.11	2.67	1.22	21.85	2.40	0.07	0.18
FB5MK20-45_2	34.76	15.64	4.82	5.54	0.87	2.42	2.07	1.15	25.60	2.22	0.05	0.13

Table

6.2.3 Preparation process

The

6.2.4 Analytical methods

Quantitative

Additionally,

Ionic

After

6.3 Results and discussion

6.3.1 Mineralogical and molecular analysis

To

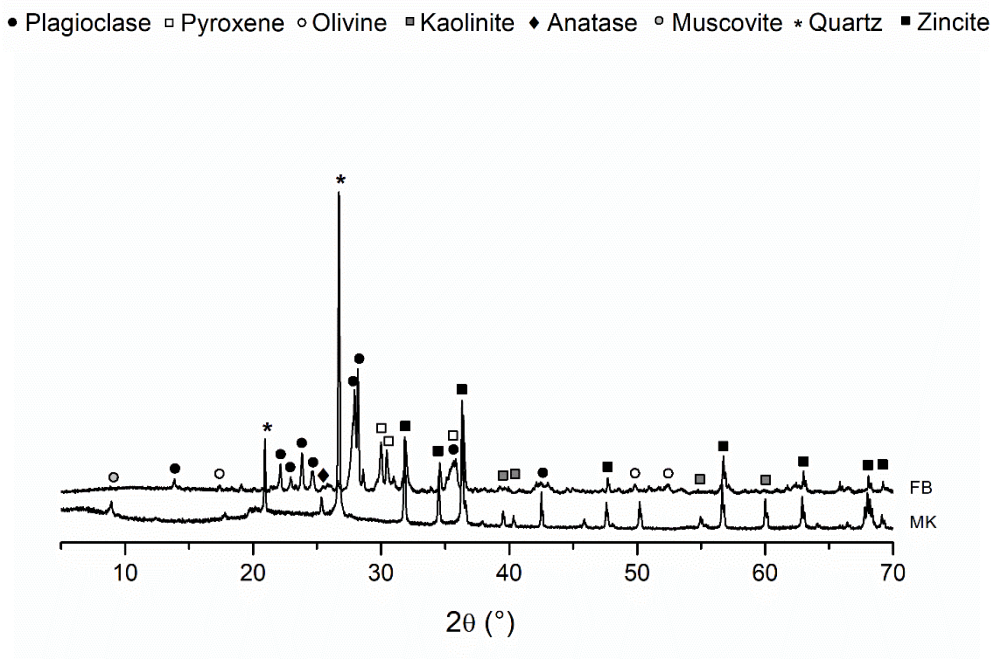

Figure 49 - X-Ray diffraction patterns of raw materials.

Figure

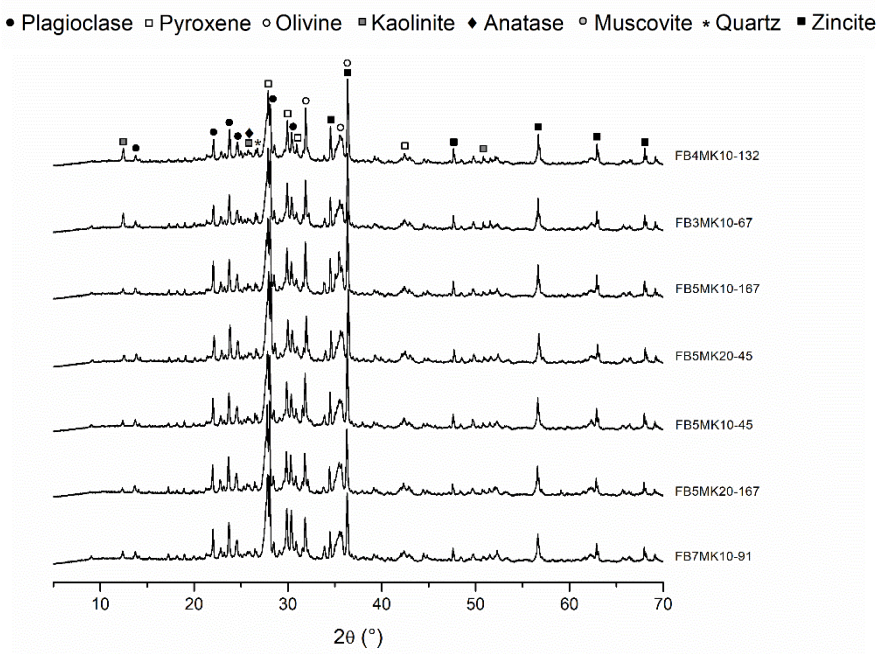

Figure 50 - Diffractograms of consolidated samples.

The

For

ID	Real	Theoretical amorp. phase (wt.%)
FB-Raw	0.63	-

MK-Raw	60.58	-
FB7MK10-91	36.32	6.36
FB5MK20-167	39.73	12.41
FB5MK10-45	21.32	6.42
FB5MK20-45	43.69	12.41
FB5MK10-167	18.55	6.42
FB3MK10-67	23.91	6.46
FB4MK10-132	31.41	6.44

Table

Figure

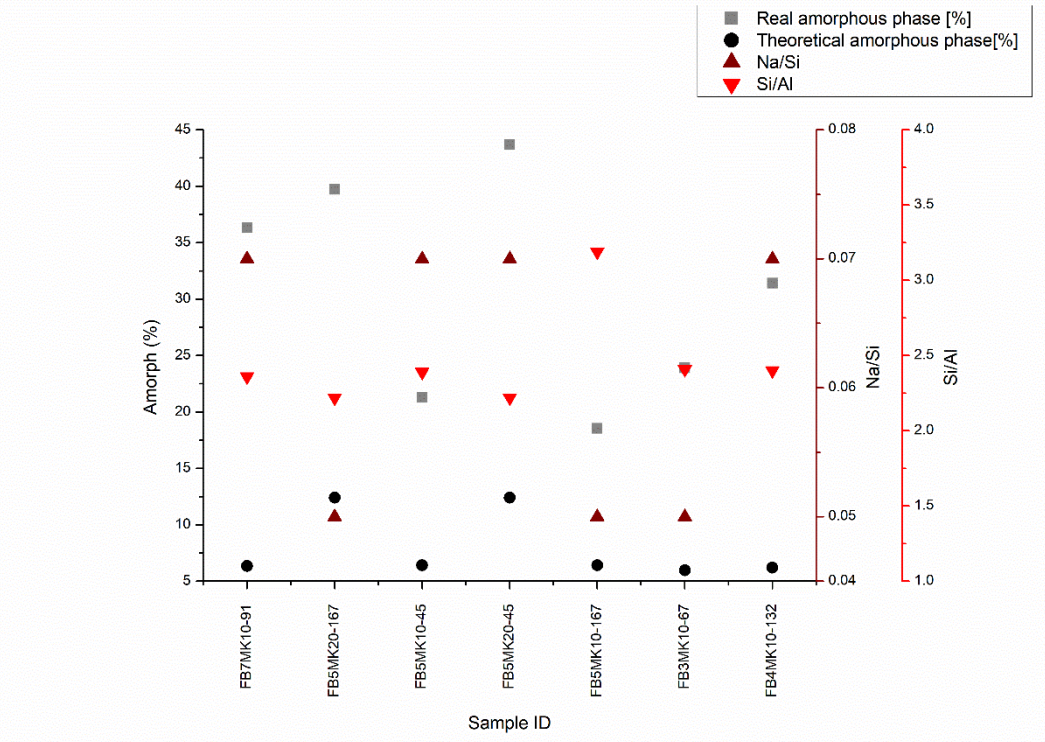

Figure

The

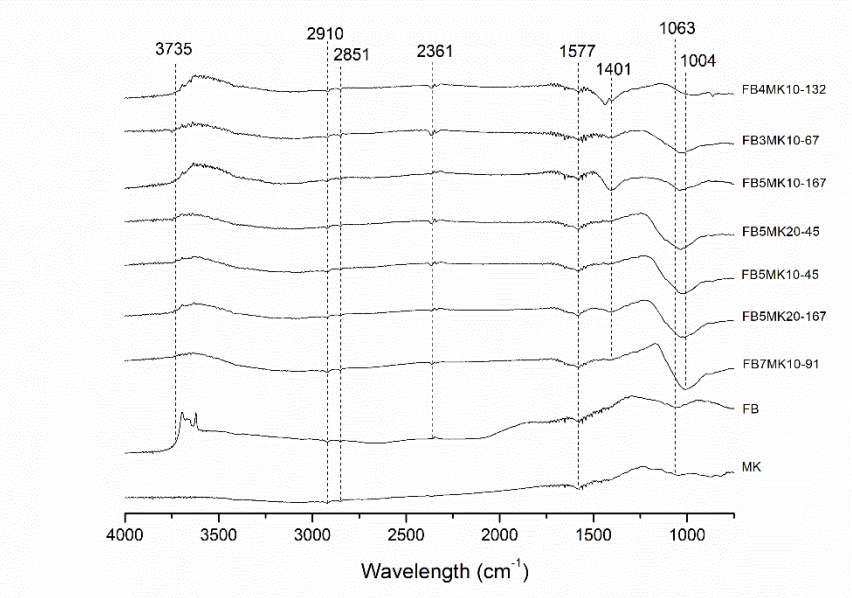

Figure 52 - DRIFT spectra of consolidated AAMs and raw materials.

Figure

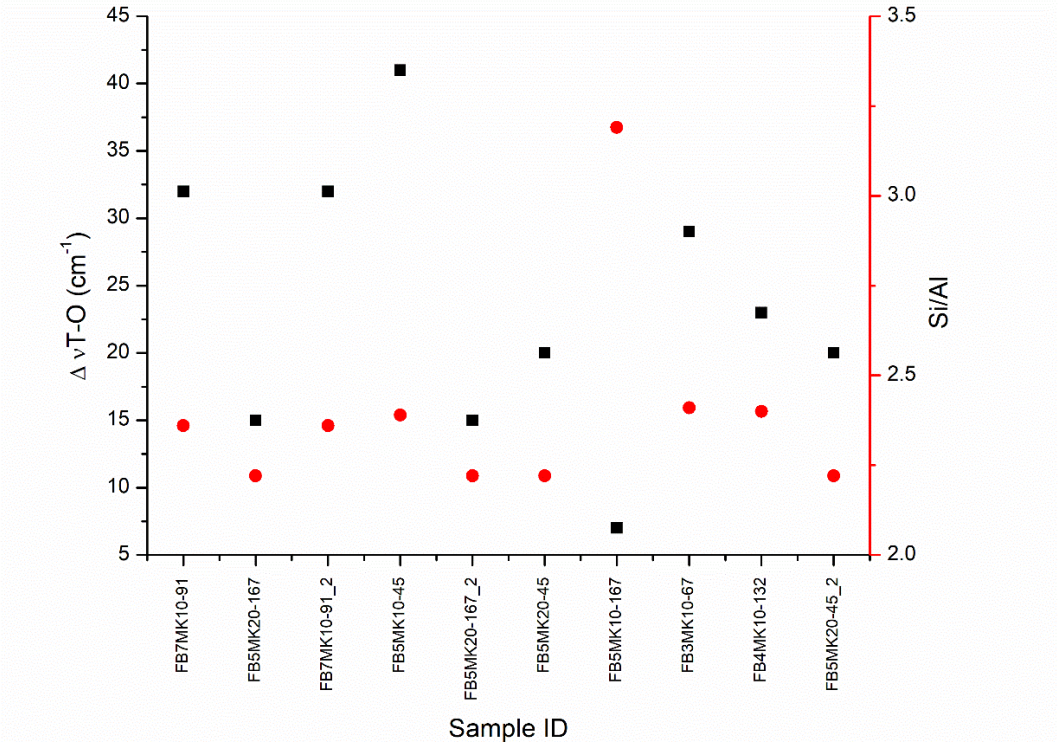

Figure 53 - Shift of T-O band in function of Si/Al molar ratio.

6.3.2 Mechanical characterization

Figure

Moreover,

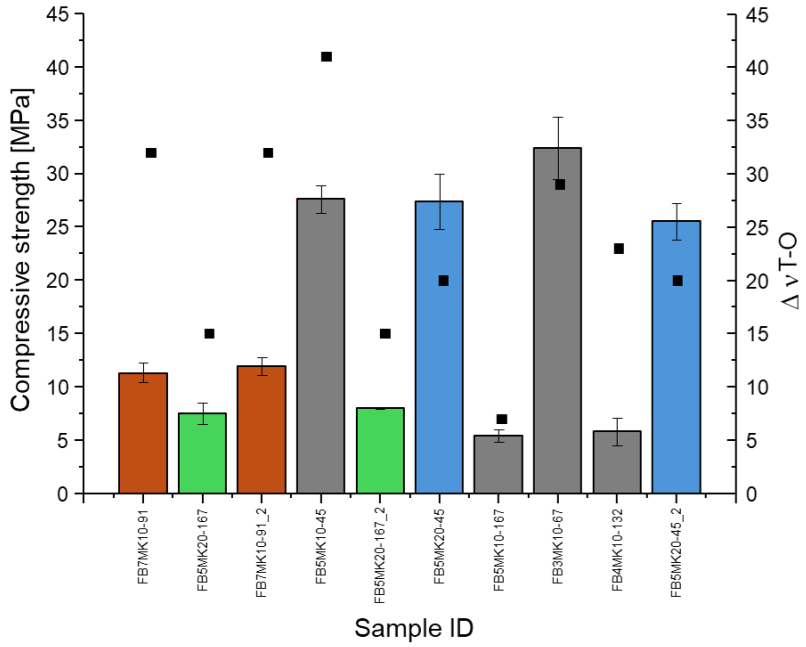

Figure

6.3.3 Conductivity measurements

Table

The

ID	Ionic Conductivity [µS/cm]
FB7MK10-91	1280
FB5MK20-167	592
FB7MK10-91_2	1396
FB5MK10-45	538
FB5MK20-167_2	574
FB5MK20-45	140
FB5MK10-167	1040
FB3MK10-67	258
FB4MK10-132	590
FB5MK20-45_2	128

Table 48 - Ionic conductivity of the studied specimens.

6.4 Evaluation of the statistical model

6.4.1 Compressive strength

Using

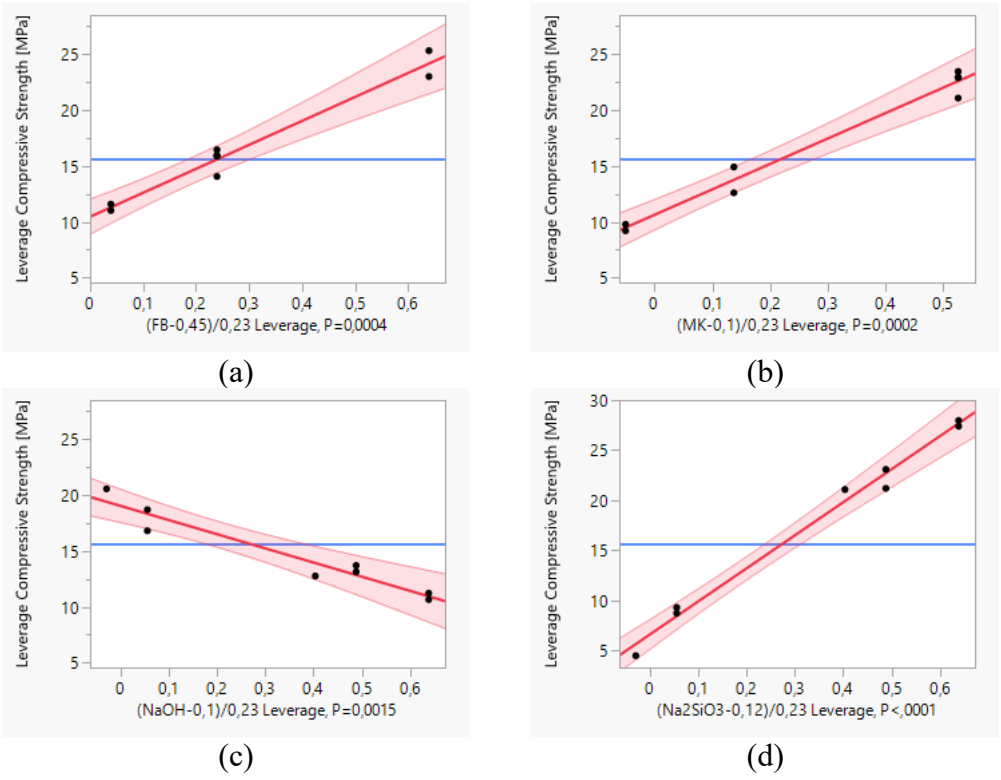

Figure

Table

In

Term	Estimate	Std Error	Probability
FB	21.435	1.956493	0.0004*
MK	22.769	1.69098	0.0002*
NaOH	-12.67017	1.647022	0.0015*
Na_2SiO_3	32.977167	1.647022	<0.0001*

Table

The

The DoE analysis collected the $Y\square compressive\square = 21.43 * \left(\frac{FB-0.45}{0.23}\right) + 22.76 * \left(\frac{MK-0.1}{0.23}\right) + \left(-12.67 * \left(\frac{NaOH-0.1}{0.23}\right)\right) + 32.97 * \left(\frac{Na_2SiO_3-0.12}{0.23}\right)$ Equation $Ycompressive=21.43 * \left(\frac{FB-0.45}{0.23}\right) + 22.76 * \left(\frac{MK-0.1}{0.23}\right) + \left(-12.67 * \left(\frac{NaOH-0.1}{0.23}\right)\right) + 32.97 * \left(\frac{Na_2SiO_3-0.12}{0.23}\right)$ Equation that draws the effects of each factor by expressing the compressive strength (Y) as a function of the coded variables. Each coefficient quantifies the factors' influence on compressive strength. In the equation, the coefficients (i.e., the estimates) are representative of the measure of the increase or decrease of the compressive strength. The central points (i.e., 0.45, 0.1 and 0.12) are reference values for the factors in the experimental design. Each factor is normalized to ensure that its effect is evaluated in relation to the central point of the experimental conditions, with the value 0.23 representing the half-range used for normalization (i.e., the middle point of the variation range of the experimental factors).

$$Y_{compressive} = 21.43 * \left(\frac{FB-0.45}{0.23}\right) + 22.76 * \left(\frac{MK-0.1}{0.23}\right) + \left(-12.67 * \left(\frac{NaOH-0.1}{0.23}\right)\right) + 32.97 * \left(\frac{Na_2SiO_3-0.12}{0.23}\right)$$

Equation 7

6.4.2 Ionic conductivity

The leverage graphs shown in Figure 56 depicted how sensitive the response is to changes in each individual component. Table 50 supported the behaviour reported in Figure 56, by quantifying the impact of each factor. Specifically, the high parameter estimate obtained by NaOH (i.e., approximately 2039) suggested how strongly this factor affected the response, with increasing NaOH resulting in a significant rise in ionic conductivity. This behaviour is due to the release of free sodium and OH^- ions in the solution, leading to higher conductivity [265]. The leverage plot (Figure 56) reflects this effect, showing a steep line as the amount of the factor increases. Moreover, the statistical significance of NaOH coefficient (i.e., $P < 0.0001$) (Table 50) confirmed its role as major contributor to the conductivity of the system. Another strong positive impact was exhibited by sodium silicate (Na_2SiO_3), with an estimated coefficient of 966.41 (Table 50). While curing occurs,

silicate species form gels and networks that retain sodium ions. The exceeding soluble ions are then released [283–285]. The behaviour of Na_2SiO_3 in the system is clearly illustrated by the leverage plot (Figure 56), showing a positive slope trend, and by the statistically significant coefficient (i.e., $P < 0.0001$), underlining its contribution to the response (Table 50). FB revealed to have a smaller positive impact on conductivity when compared to the alkaline activators, as displayed by the moderate slope reported in fig. 56, consistent with its relatively small influence on the conductivity. Basalt sludges contain oxides (including iron, calcium, and magnesium) which may partially dissolve in the alkaline environment, contributing to increase in ionic conductivity. Even though its coefficient is statistically significant ($P = 0.0269$) (Table 50), its impact is negligible compared to the alkaline solutions.

On the contrary, MK exhibited a negative coefficient (i.e., -750.15) (Table 50), suggesting that increasing its content resulted in a reduction in the ionic conductivity. This behaviour may be explained by the presence of the aluminosilicates species, contained in the MK, that react with the alkaline solutions to form a stable gel network, leading to strong bonding within the matrix and few soluble free ions [9,135,270]. MK leverage graph displayed a negative trend, supporting this opposite behaviour. Moreover, the statistical significance of MK coefficient ($P = 0.0002$), as showed in tab. 47, further supported the statistical robustness of the model.

Overall, these results aligned with the Equation 8$Y_{conductivity} = 240 * \left(\frac{FB-0.45}{0.23}\right) + \left(-747.2 * \left(\frac{MK-0.1}{0.23}\right)\right) + 2038.98 * \left(\frac{NaOH-0.1}{0.23}\right) + 966.41 * \left(\frac{Na_2SiO_3-0.12}{0.23}\right)$ Equation which models the conductivity as a function of the four factors (i.e., FB, MK, NaOH and Na_2SiO_3). As in the equation (1), according to the design, each factor is normalized by its baseline (e.g., FB = 0.45, MK = 0.1, NaOH = 0.1, Na_2SiO_3 = 0.12), in order to ensure comparison, and then multiplied by its coefficient (reported in Table 50).

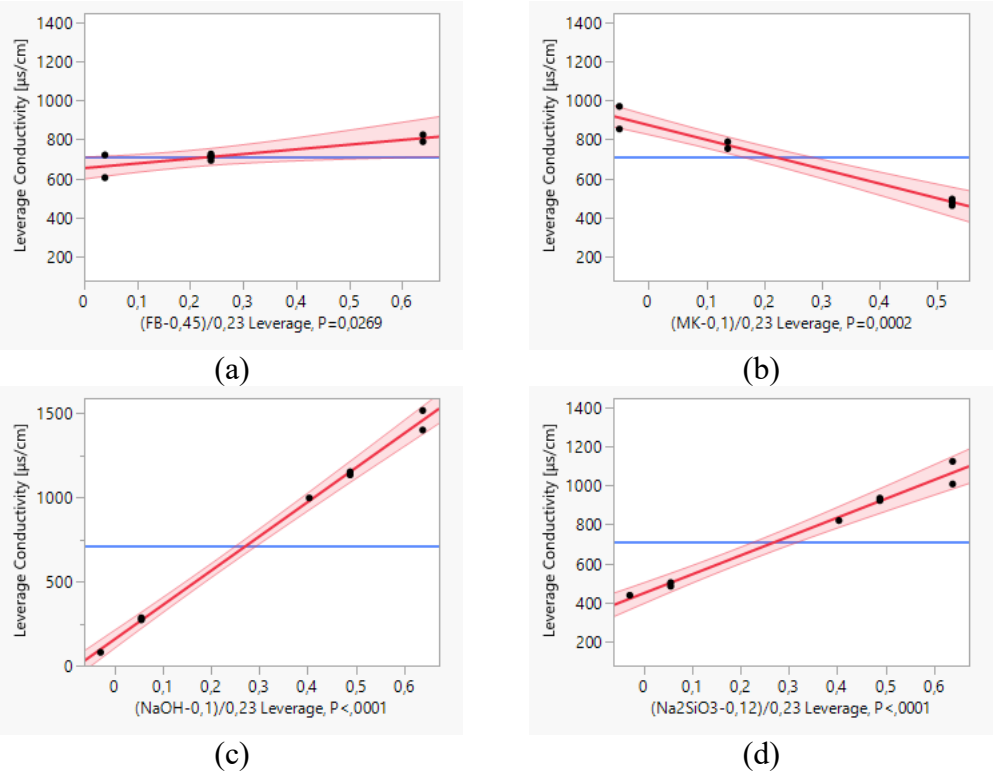

Figure 56 - Leverage plots for each factor influencing the conductivity: FB (a), MK (b), NaOH (c), Na2SiO3 (d).

Term	Estimate	Std Error	Probability > |t|
FB	240	70.25993	0.0269*
MK	-750.15	60.72507	0.0002*
NaOH	2038.9833	59.14646	<0.0001*
Na_2SiO_3	966.41	59.14646	<0.0001*

Table 50 - Estimate parameters, standard errors and probabilities of each term for conductivity measurements.

As for the ionic conductivity measurements, the model also demonstrated good predictive accuracy, with R^2 equal to 0.99515 and an RMSE of 44.436 µS/cm, indicating that the model can estimate the conductivity trends with high reliability.

$$Y_{conductivity} = 240 * \left(\frac{FB-0.45}{0.23}\right) + \left(-747.2 * \left(\frac{MK-0.1}{0.23}\right)\right) + 2038.98 * \left(\frac{NaOH-0.1}{0.23}\right) + 966.41 * \left(\frac{Na_2SiO_3-0.12}{0.23}\right)$$ *Equation 8*

6.5 Prediction

DoE approach enables to make predictions for the selected response. The prediction profiler shown in *Figure 57* is used to assess the impact of the factors on the final compressive strength and ionic conductivity. Each window allowed to understand how the changes of a single factor would affect the responses. The black lines represented the predicted regression lines for each factor, with 95% confidence intervals displayed as grey shaded areas. The red dashed lines indicate the factor levels. The suggested formulation that provided the optimal desirability, which is the improved performance [286], (i.e., 0.937525), namely PRED1, was synthetized and then tested in order to assess the reliability of the model. In addition, four other specimens were formulated to further confirm the robustness of the design.

Table 51 displayed the predicted compressive strength ranges (low, average, and high), expressed in MPa, and the experimental values obtained after testing the activated materials. All formulation fell within the predicted range of the compressive strength, with PRED2 being the only exception but having compressive strength values close to the expected range.

The mechanical performances' ranges are satisfied, demonstrating the reliability of the predictive model. The best compressive strength (i.e., 27.4 MPa) was achieved by specimen PRED1.

Furthermore, the obtained experimental values proved to be acceptable and comparable with those obtained by other authors using different materials [62,287–289].

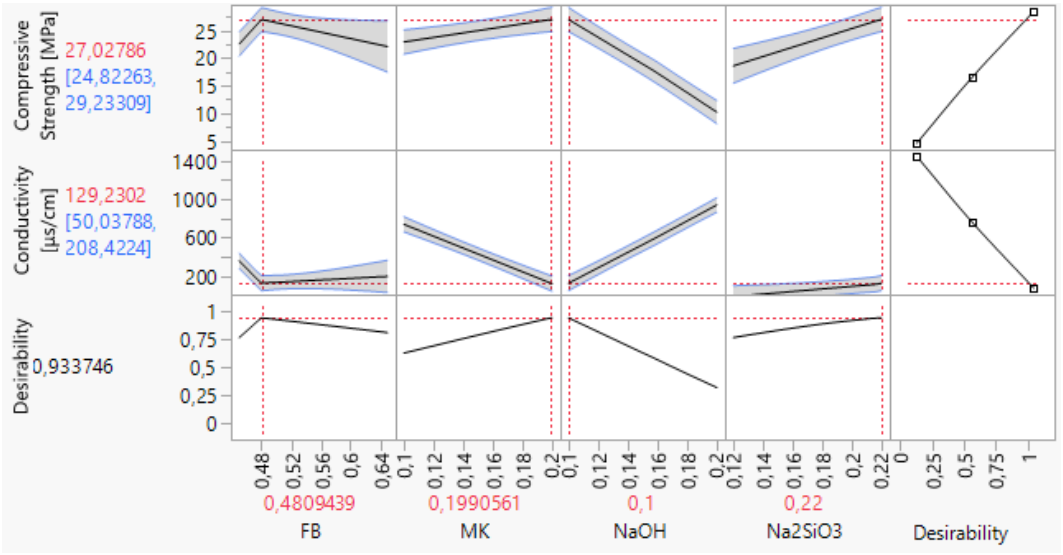

Figure 57 - Prevision profiler from JMP software. For each factor, the graphs displayed the response variation according to compositional changes (black solid line), with the 95% confidence interval (grey shaded area). The selected composition is indicated by the red dotted lines and numbers above each factor. The corresponding responses for conductivity and compressive strength, with their confidence intervals, are shown in brackets in red and blue, respectively.

ID RUN	Predicted formulation				Predicted compressive strength [MPa]			Experimental compressive strength [MPa]
	FB [%]	MK [%]	NaOH [%]	Na_2SiO_3 [%]	Low	Average	High	
PRED1	48	20	10	22	24.8	27.0	29.2	27.4 ± 1.7
PRED2	60	15	10	15	20.2	23.5	26.8	19.7 ± 1.6
PRED3	62	10	8	20	22.3	25.4	28.6	25.8 ± 2.9
PRED4	58	15	10	17	20.9	23.7	26.4	24.4 ± 1.0
PRED5	57	18	9	16	20.2	22.9	25.6	20.7 ± 2.8

Table 51 - Experimental Compressive Strength values of predicted formulations and the experimental values obtained after testing.

Table 52 displayed the predicted and the experimental conductivity values of the predicted formulations. The predictions were generated using three different levels (i.e., low, average and high). Again, all the measured data, except PRED2, fall within the predicted conductivity range, further corroborating the reliability of the model. In particular, the lowest conductivity values were exhibited by specimen PRED1 (i.e., 112). The software identified this formulation as the one with the most desirable balance between conductivity and compressive strength. On the contrary,

the highest conductivity values were achieved by PRED2 (i.e., 598), with the measurement not falling within the predicted range. These results highlighted the robustness of the model's prediction in estimating the final desired responses of the materials with acceptable accuracy.

ID RUN	Predicted formulation				Predicted conductivity [µs/cm]			Experimental conductivity [µs/cm]
	FB [%]	MK [%]	NaOH [%]	Na_2SiO_3 [%]	Low	Average	High	
PRED1	48	20	10	22	50.0	129.2	208.4	112
PRED2	60	15	10	15	19,2	138.6	258.1	598
PRED3	62	10	8	20	379.0	492.5	606.0	336
PRED4	58	15	10	17	89.4	187.6	285.7	198
PRED5	57	18	9	16	3.5	99.9	196.5	186

Table 52 - Experimental conductivity of predicted formulations and the obtained experimental values after measurements.

6.6 Conclusion

In this study the reliability of statistical methods, such as the Design of Experiments (DoE), in the prediction of responses of AAMs was assessed. The possibility to tailor selected behaviours by adjusting the starting given factors (i.e., precursors, alkaline solutions, curing time etc.) allows scientists to reduce extensive testing, consequently saving time, resources, and costs.

The DoE approach was used to understand the influence of different factors (i.e., FB, MK, NaOH and Na_2SiO_3) on the chosen final responses (i.e., compressive strength and chemical stability in water by means of ionic conductivity measurements of the eluate), verifying the accuracy of the software's predictions based on the experimental results. The seven formulations suggested in the experimental plan were first studied to assess the occurred polymerization reaction through mineralogical and compositional methods. XRD and FT-IR spectroscopy confirmed the occurred activation of the raw materials, with the formation of an aluminosilicate gel structure. The amorphous content differed among the formulations according to the percentage of MK, with higher amount leading to

greater amorphous phases and improved reactivity. Moreover, the model allowed to draw the following considerations:

- The compressive strength was positively affected when the amount of MK and Na_2SiO_3 was increased, while higher NaOH content led to a drop in the mechanical performance. Moreover, the ionic conductivity measurements also revealed a direct correlation with NaOH content, with higher amount of the solution in the formulation leading to increased conductivity. These results are considered true for the selected range only.
- The leverage plots illustrated the significance of all factors in determining compressive strength and conductivity, with the model providing accurate equations for predicting both responses, allowing for tailoring formulations with desired properties.
- The predicted formulations were synthesized and tested. Specimens fell within the predicted range, demonstrating the robustness and reliability of the design. Only one specimen slightly deviated from the predicted ranges limits.

Finally, the statistical model gave predictions that allowed for the selection of formulations with desired performances. This study underlined the importance of integrating statistical tools into material science for optimizing AAMs, speeding up the processes and improving the sustainability of the construction materials field. These results pave the way for further research to improve predictive algorithms by including more variables and trials.

7 II Case study: Influence of activator molarity and Waste-Glass-to-Volcanic-Ash ratios on microstructure of potassium-based alkali-activated pastes

Sabrina Elettra Zafarana[1], Paolo Scanferla[2], Claudio Finocchiaro[1], Germana Barone[1], Paolo Mazzoleni[1], Jozef Kraxner[2], Dusan Galusek[2,3].

[1]*Department of Biological, Geological and Environmental Sciences, University of Catania, Italy*
[2]*FunGlass, Alexander Dubcek University of Trencin, Slovakia*
[3]*Joint Glass Centre of the IIC SAS, TnUAD and FChFT STU, Trenčín, Slovakia*

This chapter has been submitted for publication in Journal of Sol-Gel Science and Technology. Initial Submission Date: 18.06.2025. Manuscript number: 4c446838-566d-4df1-93e5-dd46a55caaaf. Currently: Accepted for publication.

Keywords:
volcanic pyroclastic deposits; waste glass; structure; alkali-activation process; compressive strength.

ABSTRACT

In this study, binary alkali-activated pastes based on volcanic ash from Mount Etna (Italy) and borosilicate waste glass were synthesized for the first time using potassium hydroxide (KOH) at different molarities (i.e., 7M and 9M) and moderate temperature (60 °C). This work aims to define how the reactants involved in the mix design, specifically the solution concentration and solid proportions of the waste precursors, influence the final microstructure and subsequently their physical and mechanical properties. For this purpose, a multidisciplinary approach,

including mineralogical, molecular, chemical, and morphological investigations, was applied to elucidate these properties. The physical-mechanical parameters, including density, uniaxial compressive strengths, porosity, pH, and leaching resistance determined by boiling tests, were quantified. Increasing KOH molarity from 7M to 9M contributes to the formation of a more stable Si-O-Si/Al network, enhancing the compressive strength resistance (~ 21 to 23 MPa) and reducing both weight loss (~7 to 9%) and the open porosity (~ 20%). The combined effect of higher molarity and waste glass proportion positively influenced the mechanical response, as a result of the formation of a denser and more compact microstructure. Results confirmed that sustainable materials can be produced using potassium-based binders made from volcanic ash and waste glass.

7.1 Introduction

In recent years, the EU has made significant strides in addressing ecological and climate change issues leading to a renewed focus on the environmental impact of construction industry, which has been recognized as a major source of greenhouse gas emissions [290]. This sector is responsible for about 39% of atmospheric CO_2 emissions and over 30% of resource consumption [235,291]. Producing one tonne of Portland cement generates an equivalent amount of CO_2, highlighting the urgent need for more sustainable practices [292]. To address these challenges, the development of new alternative materials, which are still able to maintain high levels of physical-mechanical performances, becomes crucial. In this regard, alkali-activated materials (AAMs) are becoming increasingly popular due to the sustainable synthesis process (generally at room temperature) as well as the recycling of waste materials (industrial by-products or natural ones) according to the principles of the circular economy [9,293–295]. AAMs represent a class of inorganic solid materials derived by the mixing of an aluminosilicate powdered precursor and an alkaline solution. This leads to a polycondensation reaction, forming a N-A-S-H or (N, C)-A-S-H gel phase [9,294,295]. Numerous studies have demonstrated the suitability of various waste materials, including fly ash [296], ground granulated blast slag (GGBS) [297], silica fume, rice husks [298], volcanic ash [139], and waste glass [299], for use in alkaline environments. This study

examines binary mixtures composed of glass waste and volcanic ash from Mount Etna in Italy. Glass is a non-biodegradable material, and its global production reaches approximately 130 million tonnes per year [300,301]. It represents approximately 5% of the global municipal solid waste, with a recycling rate of around 80% and 30% of the total glass placed on the market in Europe and USA, respectively [302–304]. However, the fine fraction is always disposed in landfills due to possible contamination by plastics and metals [305,306], with following land occupation and potential soil or groundwater pollution [307].

Glass reportedly provides healthier storage conditions compared to plastic, leading to an increased use of glass materials. Consequently, there has been a significant rise in production of glass and a corresponding increase of the amount of glass in municipal solid waste in recent years [308]. This trend has also been confirmed by Saadatpour et al., who studied the waste glass flow of New York city and reported a correlation between the increase in the use of the glass and the costs of the municipal solid waste systems [309]. Using waste glass in building materials can decrease landfill impact, reduce emissions, and lower production costs in the construction sector [310,311]. Specifically, the inclusion of glass fiber into cement and concrete application can help the recycling of ~ 500.000 tons per year [312]. Several studies have explored the physical-mechanical properties of AAMs based only on waste glass or as a partial replacement of metakaolin or fly ashes, ascertaining that the addition of waste glass contributes positively to workability [313,314], extends the setting time [315] and aids in controlling the final density of the product [316]. Moreover, other authors have identified that variations in mechanical performance may stem from the composition of the used glass. Incorporating waste glass in the formulation of AAMs (up to approximately 20%) can enhance the mechanical strength [317,318].

Another largely available natural material is represented by volcanic pyroclastic deposits such as the ashes from Mount Etna volcano in Italy, where this material is normally considered a municipal waste and it is landfilled if not included into a sustainable production process, ensuring safe manufacturing system and an efficient material reuse (national law n.108 of 07/29/2021). It was estimated that ~4 $\times$ 10^6 m^3 of pyroclastic material erupted in the time span between February and April 2021 [319], which is a conservative evaluation considering the frequent explosive activities. Several authors reported on the use of volcanic deposits in

alkaline environments. Small amounts of metakaolin were added to overcome low reactivity of the volcanic deposits [139,289,320,321], obtaining good chemical and physical-mechanical properties both in one-part [139] and binary systems for different applications, including pastes [288], foamed materials [322] or fire-resistant materials up to 1000°C [321].

A recent development has focused on the innovative use of volcanic ash combined with soda lime glass, activated by a low-molarity NaOH solution (3M). This approach aims to produce materials with a "double life," allowing for their reuse at the end of their lifecycle. These materials can be transformed into second-generation foams designed for thermal and acoustic insulation applications. The production of these foams involves a thermal activation process, where the samples are placed in a muffle furnace at 950°C for 15 minutes, followed by rapid cooling to room temperature. This method has resulted in a significant enhancement in the compressive strength of the heat-treated specimens [323]. However, the heat treatment is an energy-intensive process with significant carbon footprint. To promote the production of more sustainable materials, it is preferable to synthesize them at low to moderate temperature (room temperature or below 60°C). The incorporation of other sources of waste glass, such as soda-lime or pharmaceutical, in alkali-activated materials has already been studied with promising results [314,324]. However, the chemical composition of the borosilicate fiberglass waste, used in this study, is different, with higher calcium and aluminium contents, which can lead to different performances of the final activated materials [325,326].

This paper for the first time explores the potential of producing AAMs based on volcanic ash from Mt. Etna and borosilicate waste glass, at moderate temperature (i.e., 60°C), and activated by potassium hydroxide solutions of different molarities as an alternative and better performing activator than common sodium-based solutions. The formulations were studied by a multi-methodological approach, evaluating microstructure, physical-mechanical properties and the chemical stability of each formulation. X-ray powder diffraction (XRD) and scanning electron microscopy with energy-dispersive X-ray spectroscopy (SEM-EDS) were used to determine the mineralogical composition of synthesized mixtures and to examine chemical and morphological features of the product. The density and porosity were quantified using a helium pycnometer. Chemical stability assessments were conducted through leaching tests on the leachates obtained after

boiling water experiments. Uniaxial compressive strength tests were performed to evaluate the mechanical properties of the formulations. This research aims to lay a robust foundation for future applications of alkali-activated materials in the construction industry, harnessing the promising potential of volcanic ash and waste glass as innovative and sustainable resources.

7.2 Materials

Pyroclastic materials (V) and waste fiberglass (G) were used as raw materials for the synthesis of binary mixtures. The volcanic ashes were sampled in a landfill of Zafferana Etnea village, located on the eastern slope of the Mt. Etna volcano (Italy), which collects the pyroclastic deposits of volcanic activities starting in 2013. After the sampling, preliminary quartering was performed to obtain a sample of representative composition. The pyroclastic material was initially wet-milled in a ball mill to achieve a grain size of less than 75 μm, followed by drying in an oven at 100 ± 5°C.

The waste glass, provided by Johns Manville Slovakia a.s. a fiber glass producer, is a by-product of industrial glass fiber production. The material is made of coarse particles, sometimes even made of large agglomerates, resulting from the cutting process during the fibers' production. Therefore, the material was first crushed in an alumina mortar with alumina crushing balls to avoid any contamination and then sieved below 120 μm. The milling process was essential to enhance the specific surface area of each glass particle in order to expose more glass to be attacked by the solution and greatly enhance its dissolution.

Chemically, volcanic ash and glass are mainly composed of silica and alumina (Table 50). Calcium oxide is also very abundant, with glass containing more than double the amount of calcium oxide than volcanic ash. A significant difference in composition can be also seen in the content of iron oxide and alkali metals (i.e., Na_2O, MgO, and K_2O), with volcanic ash containing a higher amount of iron oxide and alkalis than the waste glass. This difference reflects the presence of common volcanic minerals of basaltic composition (e.g., plagioclase $NaAlSi_3O_8$ – $CaAl_2Si_2O_8$; olivine Mg_2SiO_4 – Fe_2SiO_4; pyroxene (ABT_2O_6), (where A - Na, Ca,

Fe^{2+}, Mg, Zn, Mn^{2+}, Li; B - Al, Fe^{3+}, Mg, Sc, Ti, Cr^{3+}, V; T - Si, Al) and iron oxides such as hematite Fe_2O_3.

	SiO_2	Al_2O_3	CaO	TiO_2	Fe_2O_3	Alkali	Other
V	46.5 ± 0.5	18.4 ± 0.5	10.0 ± 0.5	1.6 ± 0.5	12.0 ± 0.5	10.6 ± 1.5	0.9 ± 0.5
G	56.4 ± 0.6	13.6 ± 0.2	23.2± 0.1	0.4 ± 0.01	0.2 ± 0.03	1.1 ± 0.1	5.1 ± 0.02

Table 53 - Chemical composition of the investigated waste precursors in wt.%, volcanic ash (V) and waste glass (G) obtained respectively from previous works [321,325]. The abundances are expressed as weight % of oxides. Alkali = Na_2O, MgO and K_2O; Other: includes B_2O_3 (for only G), P_2O_5 and MnO (for only V).

Potassium hydroxide (KOH) solutions in different concentrations, 7M and 9M, respectively, were used to activate two binary mixtures of powders with different proportions (60/40 and 80/20 wt.%, respectively, for V and G), as well as 100% waste glass as a benchmark. For ease of mixing, the liquid to solid ratio (l/s) was set at 0.42 for all formulations. The chosen concentration (i.e., 7M and 9M) represented, respectively, the minimum required molarity to effectively dissolve the precursors and the maximum upper limit to avoid fast setting of the paste [327,328]. The protocol used for preparing all formulations is as follows: preparation of the solution by dissolving hydroxide in deionized water; addition of the powders; mixing with overhead mechanical stirrer at 500 rpm for 1.5 h. The obtained paste was then poured into cylindrical silicone pots, sealed to guarantee a 100% relative humidity and kept in an oven at 60°C for 4 days.

After the consolidation, the samples were carefully demoulded and subsequently prepared for analyses. The denominations of all specimens are summarized in Table 2. Each sample was named according to the ratio between the precursors: $VG_{1.5}$ and VG_4 stand for the 60/40 and 80/20 wt.% mixtures, respectively, followed in brackets by the molarity of the used KOH solution (i.e., $VG_{1.5}(7)$ or $VG_{1.5}(9)$). The binders composed of 100% waste glass were named G(7) and G(9) (Table 51).

ID sample	V (wt.%)	G (wt.%)	Molarity of KOH solution (mol/l)
$VG_{1.5}(7)$	60	40	7
$VG_{1.5}(9)$	60	40	9
$VG_4(7)$	80	20	7
$VG_4(9)$	80	20	9
G(7)	-	100	7
G(9)	-	100	9

Table 54 - Nomenclature and composition of the different mix design formulations. Letters "V" and "G" refers to Volcanic ash and Glass, respectively. The numbers in parentheses represent molarity of the used activating solution.

The ternary diagram displaying the contribution of silica, alumina and alkali on the binary solid mixtures (i.e., $VG_{1.5}$, VG_4 and G) is displayed in Figure 58. The plot highlighted a consistent increase in SiO_2 content with the growing waste glass proportion within the mixtures (i.e., from VG_4 to G). On the other hand, the amount of Na_2O, K_2O and MgO decreases, due to the limited or absent contribution of the volcanic ash. The Al_2O_3 content remained relatively stable, being slightly higher in the VG_4 set, due to the greater contribution of alumina from volcanic ash. Despite being limited, the difference in composition may have an impact on the formation of the gel network, thus influencing the final microstructure and mechanical performances.

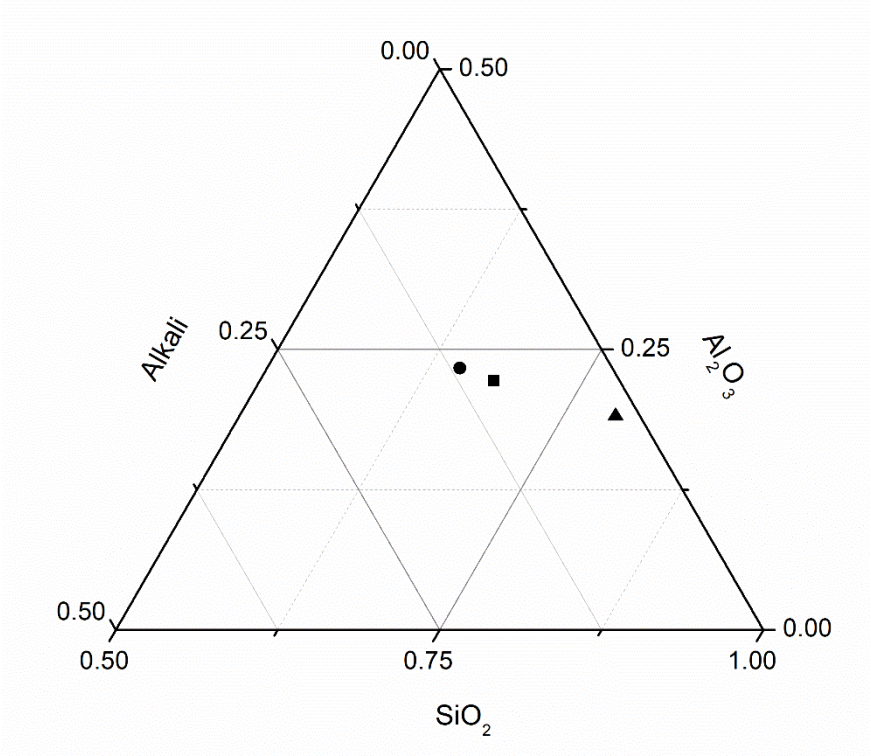

Figure 58 - Compositional ternary diagram of the three binary mixtures VG_4 (●), $VG_{1.5}$ (■), and G (▲), based on the weighted contribution of Al_2O_3, SiO_2 and alkali within the raw materials. Alkali includes: Na2O, MgO and K2O.

7.3 Methods

To verify the chemical stability of the activated materials, feasibility tests were carried out. One small piece of specimen (3g) was immersed in 120 mL of distilled water and let it boil for 3 hours. The difference in weight (compared to the starting value) was measured. Mineralogical evaluations were conducted on both raw and consolidated specimens by X-ray diffraction (XRD), using a Bruker D8 Advance diffractometer with CuKα radiation produced at 40 kV and 40 mA. The step size was set at 0.05° with a 1 s counting time, within the 2θ range of 10 – 60°. The crystalline phases were identified using Minerals and MarsMineralCompendium/Profex 5.0 software [77]. The structures of mineral phases were identified using AMCSD (American Mineralogist Crystal Structure Database) reference numbers [76].

Molecular spectroscopy investigations were conducted on raw precursors and consolidated materials using Fourier-Transform Infrared (FTIR) spectrometer

model 2000 (Perkin Elmer, Waltham, MA, USA). The patterns were recorded in the wavenumber range from 500 to 4000 cm^{-1} with 2 cm^{-1} spectra resolution and with 64 average scans. To ensure data comparability, the atmospheric CO_2 signal within the spectral range of 2400 to 1800 cm^{-1} was removed and spectra were then normalized according to a baseline [321,329].

Detailed insights into the morphological distribution of elements were carried out on consolidated materials by an Environmental Scanning Electron Microscope (ESEM) FEI Quanta 200 ESEM (Eindhoven, Netherlands) equipped with an electron dispersion microprobe (EDS). The EDS profiles were normalized with respect to the most abundant element detected (Si) to improve readability and profiles comparison.

The amount of the elements released in water after boiling the samples for 3 hours, with a solid to liquid ratio of 1:10, was determined by inductively coupled plasma optical emission spectroscopy (ICP-OES; Agilent 5100). Geometric density was calculated as the weight/volume ratio using an analytical balance and a digital calliper. Bulk and true density of the consolidated samples was measured by a helium pycnometer (Micromeritics AccuPyc 1330, Norcross, GA, USA). The densities were used to calculate the open and total porosity, using equations (4) and (5), respectively [83,84]:

$$\emptyset_{open} = 1 - \left(\frac{\rho_{geom}}{\rho_{app}}\right) \quad (4)$$

$$\emptyset_{total} = 1 - \left(\frac{\rho_{geom}}{\rho_{true}}\right) \quad (5)$$

Moreover, specimens were immersed in distilled water for 7 days and the pH of the solution was evaluated using an Edge pH (Hana Instruments, US) pH-meter, with an analysis time of 2 min to stabilise the measured value.

Mechanical performances were assessed through uniaxial compressive strength tests on consolidated cylindrical samples with an aspect ratio of 2:1 (h = 24 mm, d = 12 mm) using a universal testing machine (Quasar 25, Galdabini S.p.a., Cardano al Campo, Italy) with a crosshead speed of 0.5 mm/min and equipped with a 25 kN load cell. The average stress value of 5 specimens for each formulation was reported.

7.4 Results and discussion

7.4.1 Structural data

After consolidation, the formation of condensed water was observed on the surface of the samples, likely as byproduct of polycondensation processes in the system [330]. Several authors have studied the development of the matrix in AAMs, finding out a series of chemical reactions involving the dissolution, coagulation and condensation [9,331]. At the beginning of the reaction, the alkaline solution dissolves the precursor, breaking the bonds between Si and Al, forming monomeric species in the solution. These are then reorganized into silicate and aluminate oligomers, progressively forming an amorphous gel of the N-A-S-H (sodium-aluminate-silicate hydrate) or C-S-H (calcium-silicate hydrate) type. During this phase, the water previously involved in the dissolution process is released [97].

Fig. 59 shows the X-ray diffraction pattern of raw materials (i.e., V and G) and synthetized samples. Only an amorphous phase with no crystalline mineralogical phases were detected in the waste glass precursor. In volcanic ash and binary mixtures, several crystalline phases were identified. These included plagioclase, a solid solution of anorthite and albite as end-members ($CaAl_2Si_2O_8$ and $NaAlSi_3O_8$; amcsd_0000874 and amcsd_0016634), augite as clinopyroxene ($Ca(Mg, Fe)Si_2O_6$; amcsd_0012864), forsterite-olivine ($Mg_2(SiO)_4$; amcsd_0000171) and iron oxides and hydroxides, consisting of hematite (Fe_2O_3; amcsd_0014076) and goethite (FeO(OH); amcsd_0016645). Calcite ($CaCO_3$; asmcsd_0000984) and hillebrandite ($Ca_6Si_3O_9(OH)_6$; amcsd_0001745) were detected in the consolidated glass-only specimens. No significant differences of phase composition were recognized between the precursors and consolidated binary-mixture materials. However, an increase in the content of the amorphous phase was observed in the final consolidated materials, represented as a hump in the diffraction pattern, resulting from the addition of waste glass. A shift of the centre of the hump from $2\theta \sim 26°$ in raw waste glass to $2\theta \sim 30°$ in consolidated mixtures was detected (marked by arrows in Fig. 59). This result indicates gel formation through polycondensation

reactions, and the consequent partial dissolution of the mineralogical phases derived from the volcanic precursor as reported in previous studies [156,323]. This conclusion is further supported by the presence of hillebrandite, a hydrated calcium silicate, which is involved in the final CSH gel formation.

The final structure of the alkali-activated materials was mainly influenced by the proportion of the precursors and the concentration of the alkaline solution. The formulations with a higher glass content contained lower amounts of crystalline phases (plagioclase, augite, and olivine) compared to the precursor.

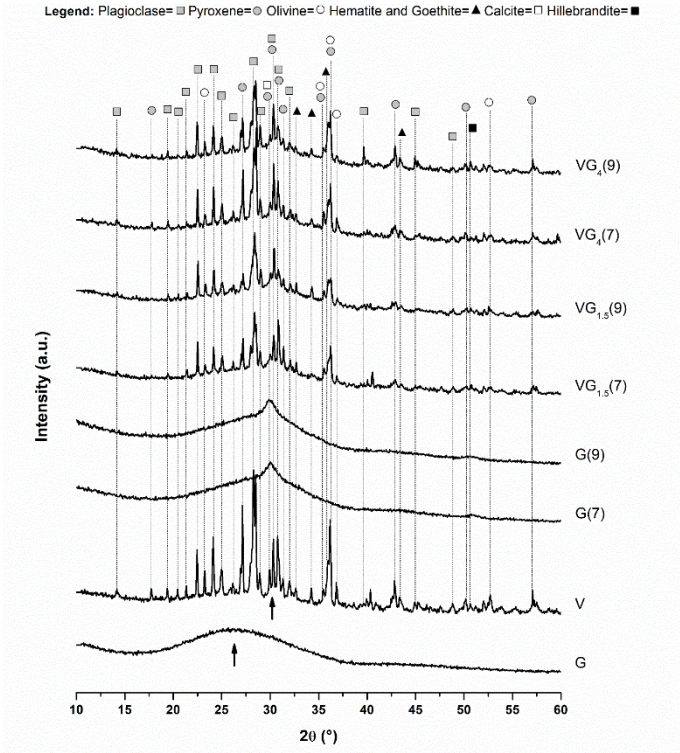

Figure 59 - XRD patterns of both precursors (V and G) and synthetized materials differentiated by the ratio of the solid mixtures: VG1.5(7) and VG1.5(9); VG4(7) and VG4(9).

Figure 60 - FT-IR spectra of both precursors and synthetized materials activated with 7M (a) and 9M (b) KOH solutions.presents the FT-IR spectra of the precursors and synthetized materials. Despite the difference in the ratio of used precursors, the resulting spectra of consolidated samples are similar. The stretching and bending vibrations of O-H bonds, which are typically associated with the formation of C-S-

H products, were observed in the synthesized materials [124]. These vibrations occurred in the range of approximately 3360 to 3380 cm^{-1}. Additionally, H-O-H bonds were detected at around 1640 cm^{-1} only in the consolidated materials, ascribable to absorbed water molecules within the alkali-activated matrix [101].

In all spectra, except for one raw powder, CO_3^{2-} species were also identified, with characteristic vibrations between 1350 and 1750 cm^{-1}. The peak at ~ 1400 cm^{-1} can be ascribed to carbonatation processes and, specifically, to the asymmetric stretching of O-C-O bonds [332]. The peak near 1740 cm^{-1} observed in the samples activated with a more concentrated solution, can be associated with the stretching and bending of the excess O-H bonds resulting from the higher molarity of the solution (Figure 60b) [160]. The observed structural differences are linked to the different molarity of the alkaline solution used to activate the mixtures. This suggests an unbalanced stoichiometric reaction between the precursors and the activating solution, leading to an excess of (OH) ions and potassium. Due to the reaction with atmospheric CO_2, free alkaline ions can form K_2CO_3 [99]. The reaction is documented by the appearance of the peaks in the range between 1350 and 1750 cm^{-1} [99]. In the samples activated with KOH 7M, the absence of the peak at 1738 cm^{-1}, attributed to carbonation processes, can be explained by the formation of a more organized and stable Si-O-Si/Al network [333,334]. A peak detected around 1200 cm^{-1} is linked to the asymmetric deformation of Si-O-Al bonds [335]. This peak is more pronounced in sample $VG_{1.5}(9)$, most likely due to the enhanced dissolution of aluminium species in highly alkaline environments (9M). Despite volcanic ash, and consequently the set VG_4, containing a higher aluminium content, as shown in Table 50, the waste glass in $VG_{1.5}(9)$ appears to be more reactive. This may be ascribed to the higher amorphous amount in the glass, rather than the volcanic ash, that facilitates a more effective release of reactive aluminium species (such as $[Al(OH)_4]^-$). This increase in the amount of aluminium appears to facilitate bonding with the Si-O- chains, resulting in more effective chemical interactions between the activator and the glass particles.

Some differences in shape and position of the characteristic main band, associated to the aluminosilicate structure and ranging from 1200 to 900 cm^{-1}, are showed among the precursors and consolidated materials (Figure 60 a-b), while no significant variations were observed among the bands of the synthetized samples, despite the differences in the molarity of the K-solution [321]. The precursors

displayed a main band with shoulders that can be attributed to the silicate structure, with the maxima at ~1000, 950/940, and 920 cm^{-1}. The peaks detected in G can be assigned to Si-O-Si asymmetric stretching vibrations, specifically to Q1 and Q2 motifs at 950 cm^{-1} and ~1000 cm^{-1}, respectively [336]. The volcanic ash (V) spectra contained the most intense peak located at ~1000 cm^{-1}, which can be ascribed to the Si-O-Ca bond [101], to the Si–O–M bonds (where M= K or Na) or to asymmetric stretching of T-O (where T= Si or Al) [102], and to the presence of Si-O-Fe bonds [337–339]. In the binary mixtures, regardless of the molarity of the solution, a narrower and a more intense peak was detected. This is probably attributed to the formation of a more organized and ordered structure with the consequent formation of an alumino-silicate matrix [340]. The shift of these peaks from lower to higher wavelengths is usually related to the specific length and bending of the Si-O bond [329], to the polycondensation reactions in particular, which leads to the increase of the intensity of the Si–O stretching vibration [128,340]. According to other authors, the shift can be linked to the increase of the amount of Si-O or Al-O tetrahedra [341].

FTIR spectra highlighted the key role of the molarity of the alkaline solution in influencing the final structure of the consolidated materials. Despite variations in the precursor's proportions, the molarity of the alkaline solution was found to be determining factor influencing the final structure of consolidated samples. Higher molarity solutions tend to promote the formation of more organised Si-O-Si/Al and Si-O-Ca networks, emphasizing the importance of optimising the concentration of the activator solution to obtain the desired structural properties. Higher KOH molarity promoted greater dissolution of Si and Al species, enhancing the polycondensation reaction and resulting in a more cross-linked aluminosilicate network. The K^+ ions balanced the negative charged AlO_4^- tetrahedra, producing a more stable network [342]. This effect is evident in the FT-IR spectra, where 9 M consolidated materials resulted in a more intense and shifted characteristic Si-O-Si/Al band, suggesting the formation of a dense and stable material.

(a)

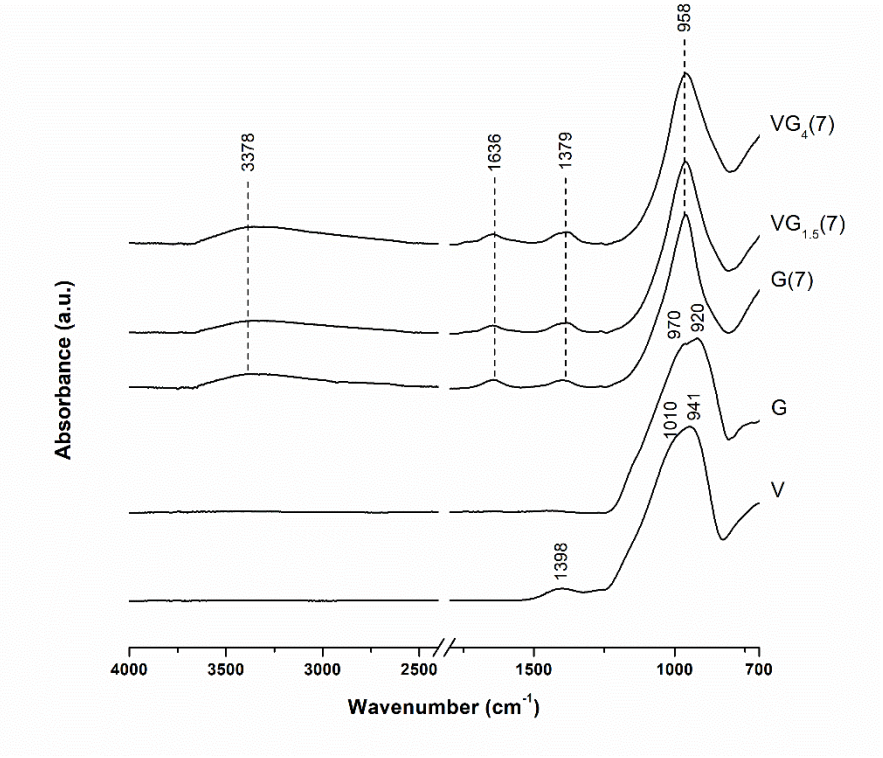

(b)

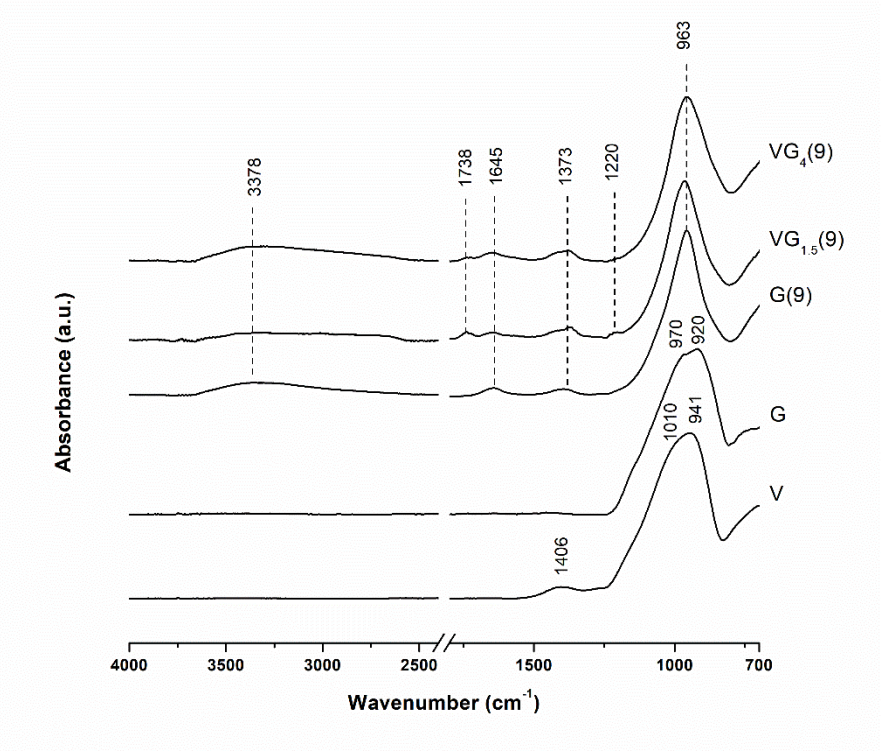

Figure 60 - FT-IR spectra of both precursors and synthetized materials activated with 7M (a) and 9M (b) KOH solutions.

Figure 61 displays the microstructure and chemical composition of the matrix and the glass grains of consolidated G-samples. In both specimens, glass particles with sub-angular shape (i.e., grains with slightly rounded edges) and polymodal size distribution (i.e., even if < 120 μm) were observed. The fragments, especially the most noticeable ones, displayed the typical conchoidal fracture of glass [343]. The structures seem to be dense and compact, with a texture consisting of glass grains and a matrix [344]. No macropores can be detected at this magnification; however, some cracks are visible and generally surrounding larger grains. It is also possible to discern important differences between the specimens activated with the solutions of different concentrations. At higher molarities, the matrix appears to be visually more compact and homogenous. At lower molarities, the grains with different sizes appear to have fewer connections with the matrix. Despite different molarity of the solutions, few differences in the chemical composition of their components can be detected in both samples. The unreacted glass grains of G(7) displayed the known composition of glass, containing Si, Al, Ca, K, Mg and Na. It has to be noted that EDS detector cannot detect boron, which is contained in the glass precursor according to XRF analysis. A distribution of elements typical of the Si-O- network, based on silica-aluminates was confirmed in the matrix, of both the G(7) and G(9) samples. The contribution of the alkaline activator on the chemical composition of the matrix is evident, as there is a consistent increase in the intensity of the K peak between the grain and the matrix.

(a)

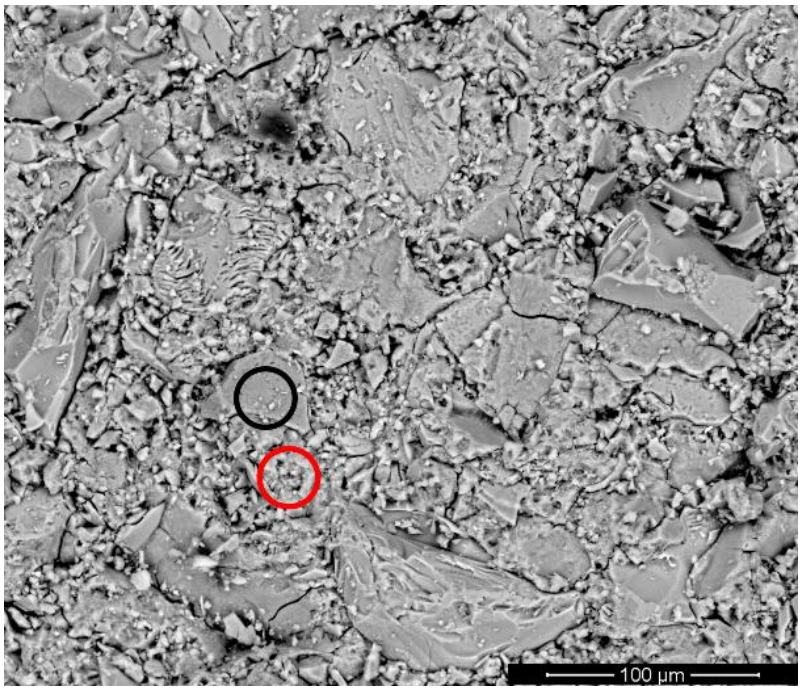
100 µm

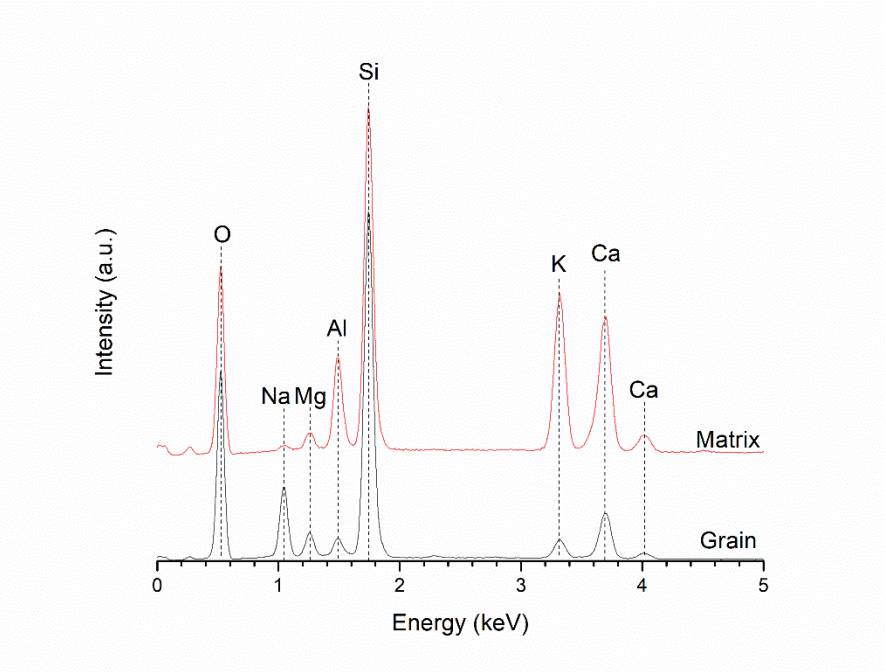
Si
O
K
Ca
Al
Na Mg
Ca
Matrix
Grain
Intensity (a.u.)
0
1
2
3
4
5
Energy (keV)

(b)

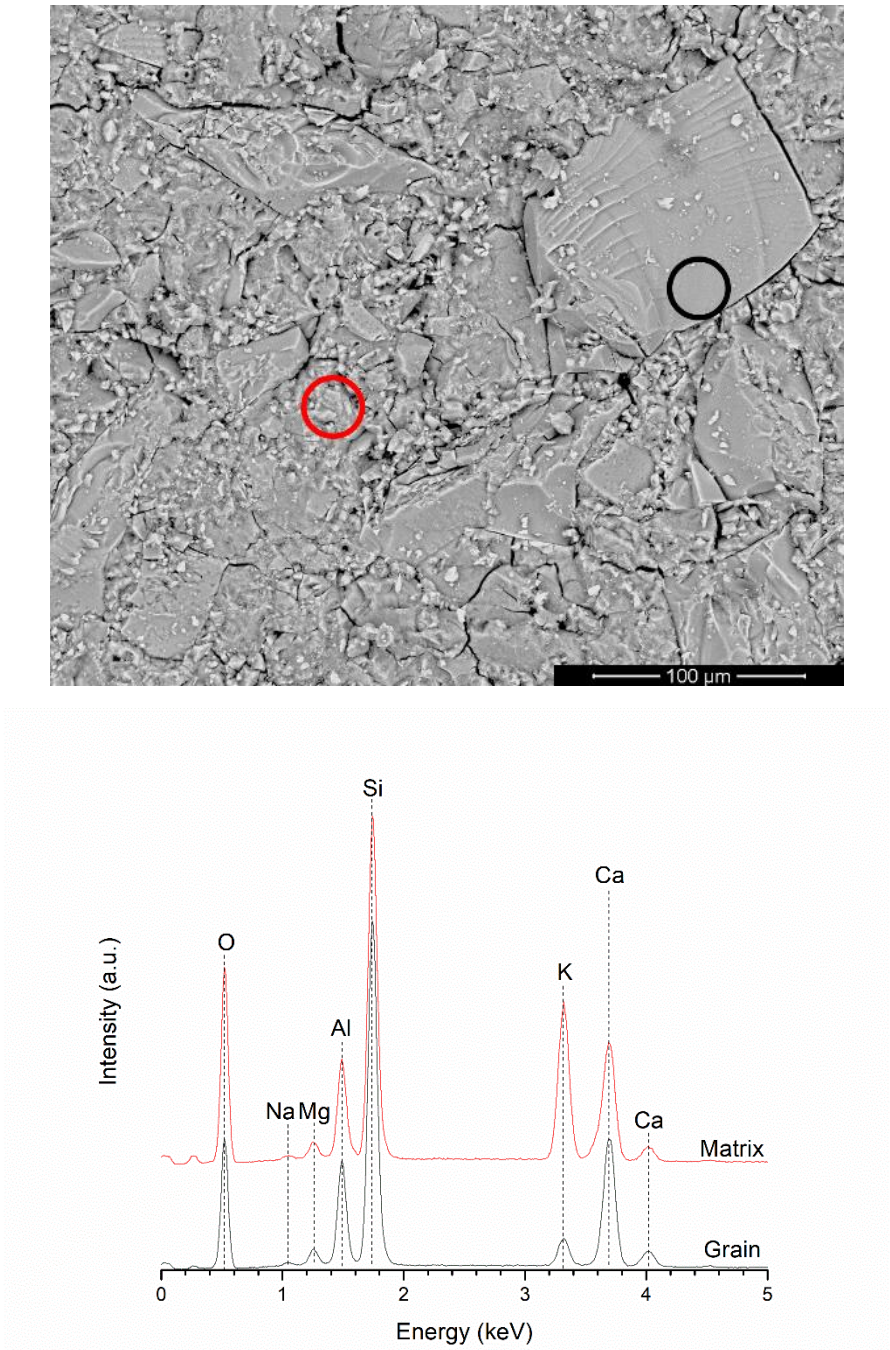

Figure 61 - SEM micrographs and EDS profiles of G(7) (a) and G(9) (b) samples. Circles, indicating the spot analysis, are distinguished as follows: red - matrix; black – glass grain.

Figure 62 (a-d) presents the SEM micrographs and EDS profiles of binary mixtures. Overall, heterogeneous structures, with grains showing irregular shapes and different particle sizes were observed. Focusing on the proportions of solid

mixtures, a stronger difference in grain size was detected, with bigger unreacted grains mainly found in the $VG_{1.5}$ set (Figure 62 a-b). The glass grains showed the typical composition, containing mainly Si, O, Al, and Ca as the predominant constituents (along with B). Other elements, present in smaller quantities (i.e., Na, Mg, and Fe), were also detected. The composition corresponds with the results of the XRF analysis of the precursors (Table 53 - Chemical composition of the investigated waste precursors in wt.%, volcanic ash (V) and waste glass (G) obtained respectively from previous works [321,325]. The abundances are expressed as weight % of oxides. Alkali = Na2O, MgO and K2O; Other: includes B2O3 (for only G), P2O5 and MnO (for only V).). The EDS spectrum of volcanic ash reflected the characteristic composition of its constituent minerals, showing the peaks of Si, Al, Ca, Na, and Mg. The intensity of the Fe peak is high, with some contribution from Ti and V. The relative increase of the content of potassium in the matrix compared to the volcanic ash and waste glass suggests successful activation of the precursors and the subsequent formation of an aluminosilicate network.

Figure 62 (c-d) shows the SEM micrographs and EDS chemical composition profiles of specimens VG4(7) and VG4(9). Unlike the samples with lower volcanic ash content (i.e., the proportion of 60/40 %wt.), a more homogeneous structure can be observed in the VG4 set, suggesting a better packing of solid particles within the matrix, probably due to the occurrence of a more extensive reaction. Despite the differences in the molarity of the solution, EDS analysis of the consolidated specimens showed a similar composition for the glass grains, volcanic ash and matrix. A small relative difference in the intensity of Mg and Fe peaks was found in the volcanic ash. The latter contains also V, which appeared to be absent in the specimens activated with KOH 7M. This is attributed to the heterogeneity of the volcanic precursor, whose chemical composition may vary within the compositional range of basalt.

The binary mixtures appeared to be more porous, albeit with a smaller pore size when compared to the samples prepared from pure glass precursor (100% G). The presence of these linear gaps can be ascribed to the development of voids, between the unreacted particles and the matrix, induced by the dissolution reaction [323]. Specifically, the visible pores can be related to the expulsion of condensation water during the dissolution process of the volcanic ash by the alkaline solution [345].

(a)

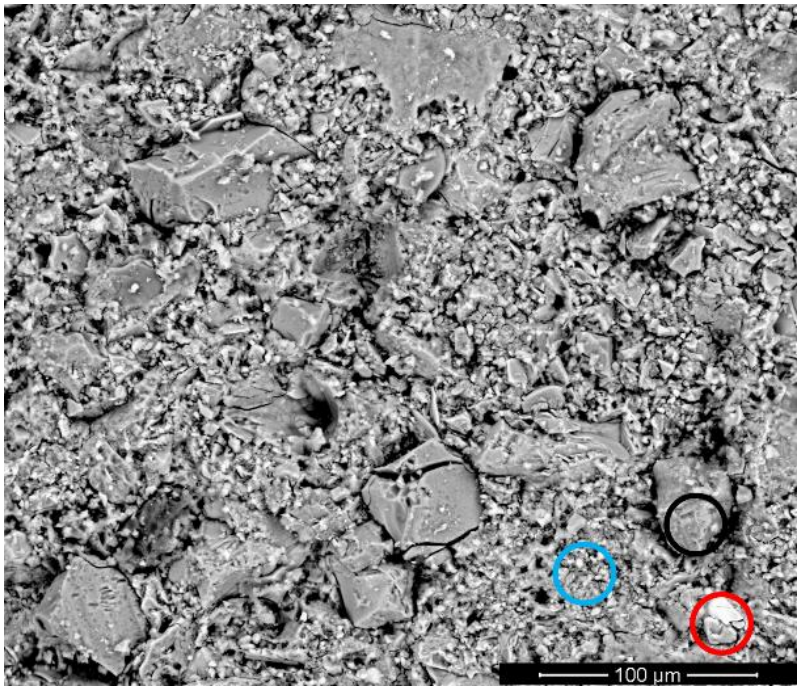
100 µm

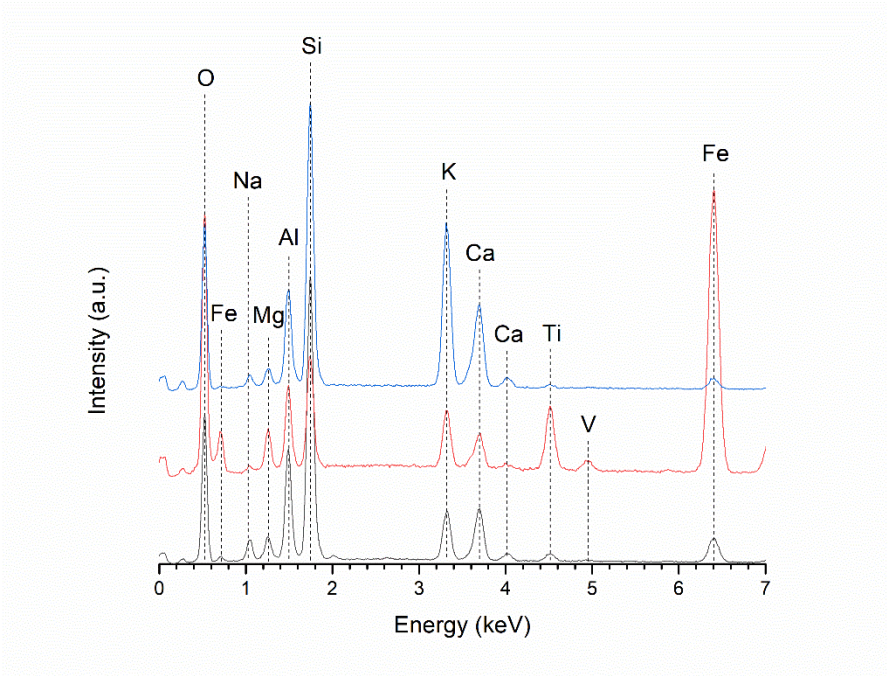
O
Si
Na
Al
Fe
Mg
K
Ca
Ca
Ti
V
Fe
Intensity (a.u.)
0
1
2
3
4
5
6
7
Energy (keV)

(b)

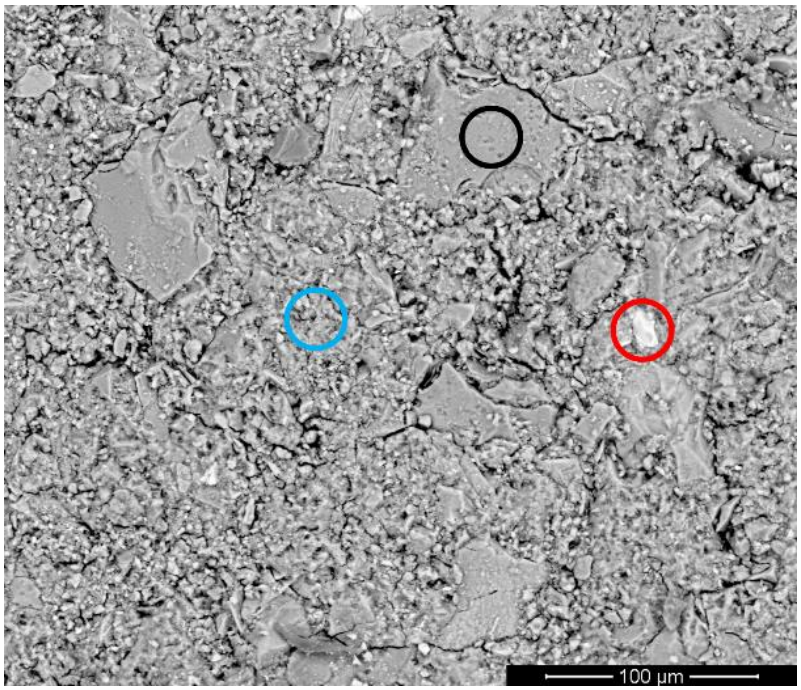
100 µm

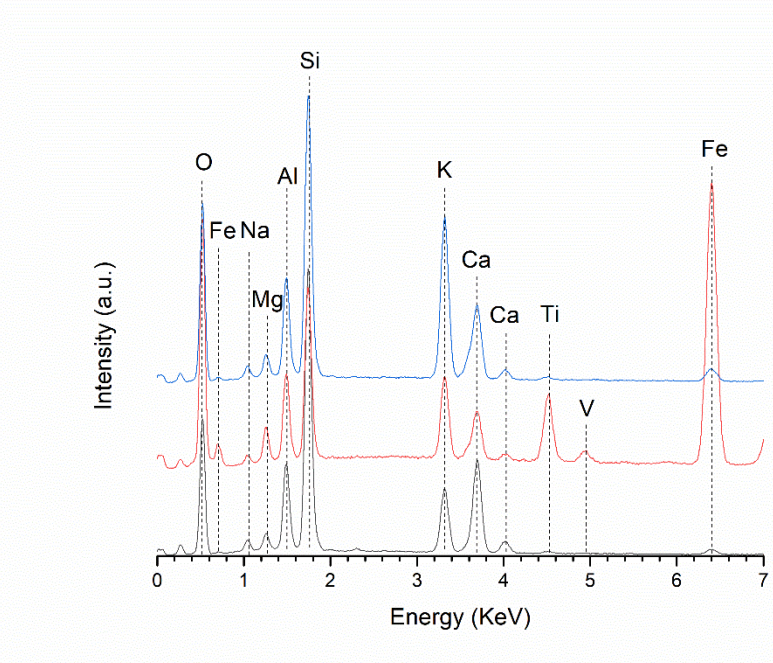
Si
O
Al
K
Fe
Fe Na
Ca
Mg
Ca
Ti
V
Intensity (a.u.)
0
1
2
3
4
5
6
7
Energy (KeV)

(c)

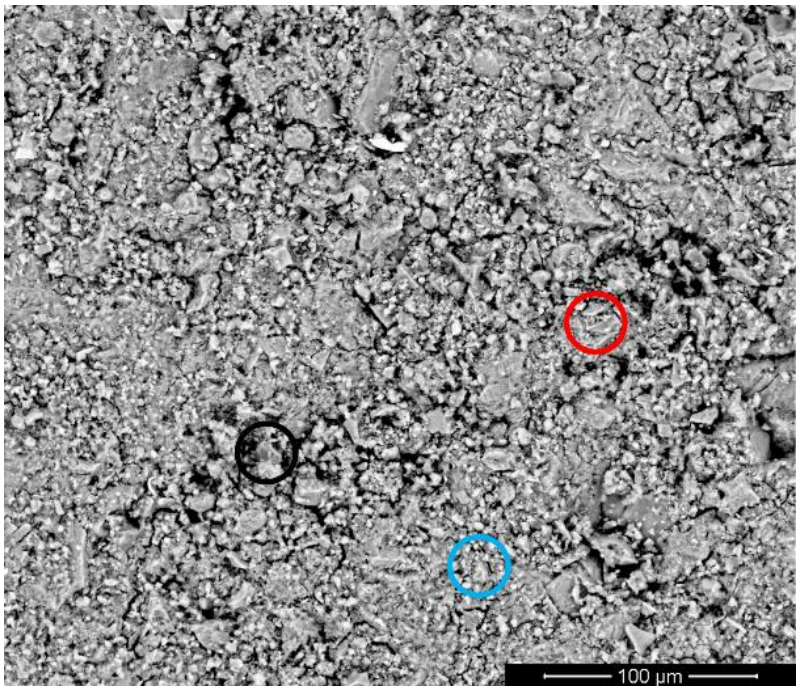
100 µm

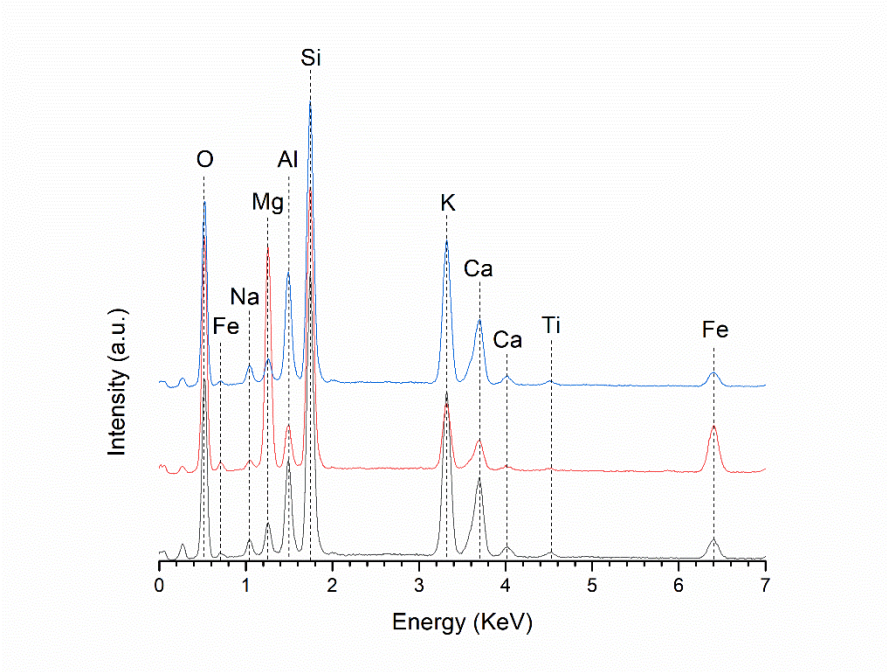
Si
O
Al
Mg
K
Ca
Na
Fe
Ca
Ti
Fe
Intensity (a.u.)
0
1
2
3
4
5
6
7
Energy (KeV)

(d)

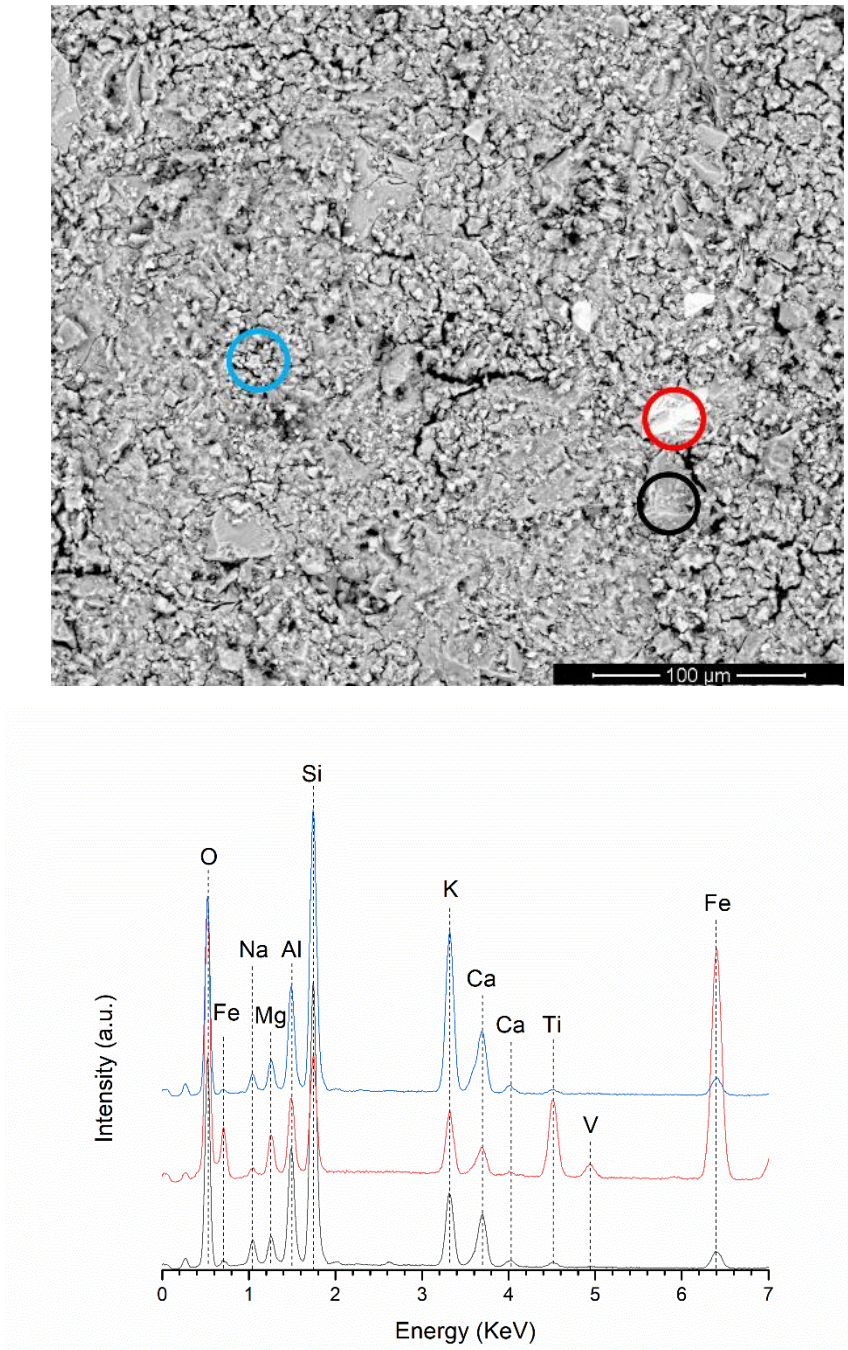

Figure 62 - SEM micrographs and EDS chemical composition: a) VG1.5(7); b) VG1.5(9); c) VG4(7); d) VG4(9). Circles, indicating the spot analysis, are distinguished as follows: blue - matrix; red - volcanic ash grain; black – glass grain.

Table 55 shows the elemental composition of the activated samples determined by EDS analysis. The samples activated with a more concentrated alkaline solution showed a higher content of K, Al and O together with a lower concentration of Ca

and Si. The samples with a higher glass content (e.g., set VG1.5) contained less Fe, Mg and Na, reflecting the contribution of the raw materials composition, as documented by the results of XRF analysis shown in Table 53.

Sample	O	Si	Al	Na	Mg	K	Ca	Fe	Ti
VG1.5(7)	46.1 ± 0.5	15.6 ± 0.2	5.3 ± 0.1	1 ± 0.1	1.1 ± 0.1	13.3 ± 0.2	8.1 ± 0.1	2.8 ± 0.1	0.5 ± 0.1
VG1.5(9)	46.9 ± 0.4	15.5 ± 0.1	5.5 ± 0.1	1.1 ± 0.1	1.4 ± 0	13.7 ± 0.1	7.1 ± 0.1	3.3 ± 0.1	0.4 ± 0
VG4(7)	44.2 ± 0.4	15.3 ± 0.1	4.7 ± 0.1	1.3 ± 0.1	1.9 ± 0.1	12.1 ± 0.1	6.7 ± 0.1	4.5 ± 0.1	0.6 ± 0
VG4(9)	46.6 ± 0.4	14.4 ± 0.1	5.4 ± 0.1	1.5 ± 0.1	1.8 ± 0.1	12.3 ± 0.1	5.5 ± 0.1	4.2 ± 0.1	0.6 ± 0
G(7)	48.7 ± 0.4	16.7 ± 0.2	4.5 ± 0.1	0.4 ± 0.1	1 ± 0	11.7 ± 0.1	12 ± 0.1	0.2 ± 0.1	0.2 ± 0
G(9)	49.9 ± 0.4	16.7 ± 0.2	4.7 ± 0.1	0.3 ± 0	0.9 ± 0	11.8 ± 0.1	10.7 ± 0.1	0.2 ± 0.1	0.2 ± 0

Table 55 - EDS chemical composition, expressed in atomic percentages (a.t.%), of the matrix for all consolidated samples.

Figure 63 showed the EDS maps of the binary mixtures VG1.5(9) (a), VG4(9) (b) and VG4(7) (c). Both the grains and the matrix showed similar overall compositions. The VG1.5(9) containing more glass than ash, showed a predominantly silica-calcic composition due to the contribution of glass (Figure 63 a). Few magnesium and iron rich spots are undissolved volcanic grains, recognisable as areas with a lighter colour within the micrographs. The sample VG4(7) appeared to be more heterogeneous, in terms of composition, with the volcanic ash being more abundant in proportion to glass. The presence of iron, magnesium, silicon, and aluminium reflects the chemical composition of the minerals that compose the volcanic ash (i.e., plagioclase, olivine, pyroxene, and iron oxides).

The EDS analysis emphasizes the critical role that the ratio of the used precursors and the molarity of the alkaline solution play in shaping the final structure and gel

formation. The increase of the proportion of volcanic ash can lead to a more heterogeneous structure, as evidenced by larger residual particles in the matrix, indicating the partial or lower reactivity of the ash. Utilizing higher molarity solutions, such as VG4(9), promotes chemical reactions between the constituents. This results in a more homogeneous and compact matrix characterized by fewer pores and cracks, ultimately enhancing the overall quality of the gel.

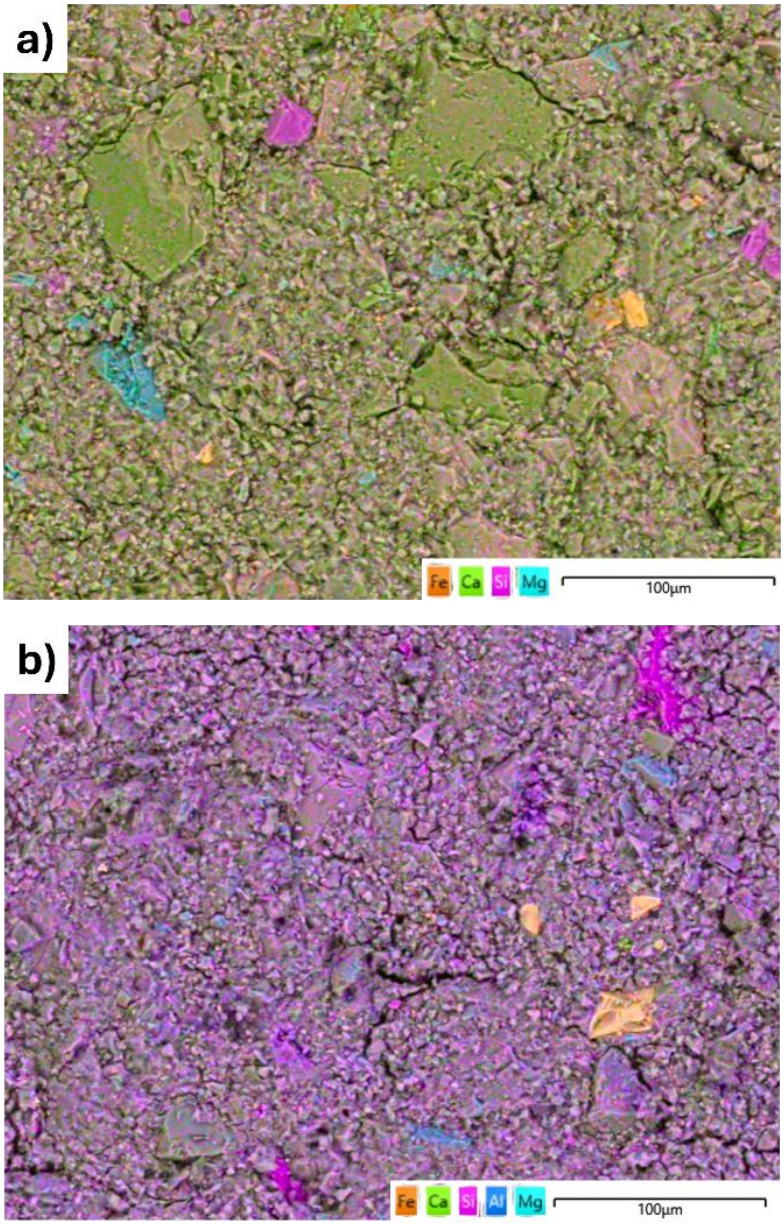

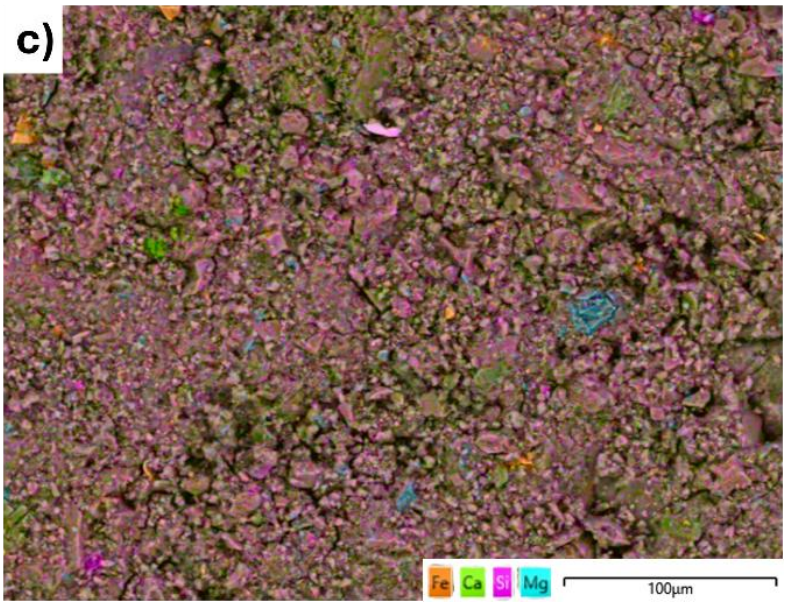

Figure 63 - EDS maps: a) VG1.5(9); b) VG4(9); c) VG4(7). Colours are referred to the following elements: red – Fe; green – Ca; pink – Si; blue – Al; cyan – Mg.

7.4.2 Physical-mechanical data

The results presented in Table 56 - Physical-Mechanical properties: weight loss after boiling test (ΔM, %); open porosity (OP, %]); total porosity (TP, %); pH; uniaxial compressive strength (σ, MPa).highlight the physical-mechanical performance of the material of different formulations. After 4 days of curing at 60°C, all formulations were consolidated. The chemical stability, assessed through boiling water experiments, showed promising results, with minimal weight loss observed for all tested samples, as reported in Table 56. Among all specimens, the binary mixtures activated with 9M KOH showed a reduced weight loss of 6.6%, 9.1%, and 4.9% for VG1.5(9), VG4(9) and G(9), respectively. On the contrary, the 7M KOH solution resulted in a higher weight loss of 10.2%, 15.2%, and 6.4% for VG1.5(9), VG4(9) and G(9), respectively. These values align with those observed by other authors [346,347]. The boiling water remained clear after the test, indicating that the samples were undamaged and with no signs of mechanical disintegration [348].A closer examination of the samples with different composition of solid mixtures but activated with the alkaline solution of the same concentration, revealed some differences. The VG4 set demonstrated a higher weight loss compared to the VG1.5 set. Considering the molarity of the solutions, the observed trend suggests

an inverse relationship between weight loss and the concentration of the activator solution; specifically, higher KOH concentrations correlate with reduced weight loss.

This analysis underscores the importance of both the ratio of solid precursors—with higher glass content producing a stronger network —and the concentration of the alkaline solution used. A higher molarity of the alkaline solution contributes to chemical stability. These findings indicate the potential for optimizing formulations for improved performance and durability. This latter behaviour was also confirmed by the results obtained in the benchmark set based on only glass, where G(9) sample showed a lower weight loss than G(7). This is probably attributable to the more concentrated solution's ability to make the precursors react more strongly, resulting in a more cohesive structure. The porosity of the specimens was also in line with the described behaviour. In the binary mixture and in the samples prepared from 100% G activated with the 7M KOH solution, the total porosity was higher compared to the samples activated with the higher-molarity solution. Increasing the concentration of the activating solution typically leads to a reduction in open porosity, which is attributed to a higher dissolution of the precursors, resulting in a denser and more uniform microstructure [349,350]. Regardless of composition, samples contained predominantly open porosity (Table 56). The closed porosity represented only about 1-2% of the total porosity for all tested samples. This result could be related to the partial dissolution of solid particles. Moreover, the porosity values align with or are even significantly lower than those previously reported by other authors [308,323,351].

More details were obtained by the ICP-OES analysis of the released elements: the measured values are reported in Table 57. For the specimens activated using KOH 7M (i.e., VG1.5(7) and VG4(7)), Ca concentrations were higher for the composition with a higher amount of glass. Na and Si contents were higher in the samples containing a lower amount of glass. The concentrations of Al and Fe were similar. The specimens obtained using 9M KOH (i.e., VG1.5(9) and VG4(9)) showed that the Ca content is higher in specimens with lower volcanic ash content, while Na levels were lower. Al, Si, and Fe concentrations were higher in samples with a greater proportion of volcanic ash. In the samples made of waste glass only, a noticeable difference was observed for Na and Si contents for G(7) and G(9) while Al and Ca levels were similar. Iron was below the detection limit (i.e., <0.1 mg/L),

in accordance with the composition of the used raw materials. The results indicate that the ash-to-glass ratio and the concentration of the alkaline solution significantly influence the hydrolytic resistance of consolidated materials, with 9M KOH activated samples typically resulting in an increased release of Al and Fe in the solutions. Calcium levels showed minimal variations for all samples. Na and Si levels were higher in samples synthetized using lower molarity alkaline solutions, suggesting that specimens activated with 9M KOH were more stable. This is consistent with the structural role of Na and K, forming the primary network (Na/K + Al and Si), while Fe contributes to the development of the secondary network. The lower release of Na and Si in highly alkali-activated samples indicates their stronger incorporation within the primary network, leading to enhanced stability [99,321]. VG4(9) was the only exception in terms of release of Si, with detected content higher than the other 9M KOH activated specimens. This may further support the conclusion that higher molarities of the solution promotes the formation of a more stable network of strong Si-O-Si bonds [311]. For all samples, Ti and Mg levels were below the detection limit. There were no significant differences in the pH of the solution. G samples exhibited a slightly lower pH compared to the binary mixtures, although there was a slight increase in the pH of samples activated with the 9M-K-solution (see Table 56).

In the uniaxial compressive test, the VG4 set exhibited lower strength values compared to the VG1.5 set, with average compressive strengths of approximately 12 MPa and 22 MPa, respectively. The samples activated with a more concentrated solution displayed higher strength values. This trend was particularly evident in the G set, where the strength of the sample G(9) was nearly three times higher than the strength of the sample G(7), increasing from 12 MPa to 36 MPa. These results indicate that both a higher glass content in the solid mixtures and a higher molarity of the alkaline solution positively influenced the compressive strength.

The addition of volcanic ash impaired the final compressive strengths of the samples. The observed weight loss during the boiling water test, along with the porosity measurements, suggests that a higher glass content and a higher molarity of the alkaline solution enhance the formation of a stronger network. This improves the chemical balance between the precursors and the alkaline solution, resulting in improved packing and bonding within the matrix. This improvement may be

attributed to the significant amounts of calcium typically found in volcanic ash, which facilitates the formation of Si-O-Ca network. This calcium-rich network is generally stronger, in terms of mechanical properties, than the Si-O-Si/Al network that predominates in samples made of 100% glass. However, the presence of modest amount of iron oxide into the raw volcanic ash may contribute to long term evolution of the aluminosilicate network, providing improvement of the mechanical performances over time. This is due to the possible partial substitution of Al^{3+} by Fe^{3+} within the gel networks, along with the oxidation of Fe^{2+} to Fe^{3+} over time [339,352].

In all alkali-activated systems, the calcium-based networks develops faster than the Si-O-Si networks. This difference can be explained by the high reactivity of calcium in alkaline environments, which promotes immediate formation of calcium silicate hydrates (C-S-H) and other calcium-rich phases. These calcium-rich phases contribute to the early strength and the development of the material's microstructure. The formation of Si-O-Si bonds involves more complex polymerization processes, leading to the creation of a more stable network, very resistant to chemical attacks, that take longer time to develop [353,354].

Sample	ΔM [%]	OP [%]	TP [%]	pH	σ [MPa]
VG1.5(7)	10.2	24	24.7	12.6	21 ± 1
VG1.5(9)	6.6	20	21	12.7	23 ± 2
VG4(7)	15.2	21.5	24.7	12.6	10 ± 2
VG4(9)	9.1	20.2	21.8	12.8	13 ± 2
G(7)	6.4	17.1	18	12.2	12 ± 1
G(9)	4.9	14.5	16	12.1	36 ± 3

Table 56 - Physical-Mechanical properties: weight loss after boiling test (ΔM, %); open porosity (OP, %]); total porosity (TP, %); pH; uniaxial compressive strength (σ, MPa).

Sample	mg/l					
	Al	Ca	Fe	K	Na	Si
VG1.5(7)	0.5 ± 0.1	0.08 ± 0.007	0.01 ± 0.001	86.4 ± 0.3	5.1 ± 0.04	7.9 ± 0.04
VG1.5(9)	1.2 ± 0.02	0.1 ± 0.005	0.01 ± 0.001	86.5 ± 0.4	5.1 ± 0.04	7.0 ± 0.06
VG4(7)	0.6 ± 0.01	0.04 ± 0.005	0.02 ± 0.001	87.1 ± 0.3	7.0 ± 0.05	5.2 ± 0.04
VG4(9)	1.4 ± 0.01	0.05 ± 0.005	0.02 ± 0.001	85.3 ± 0.2	6.7 ± 0.05	6.5 ± 0.04
G(7)	0.4 ± 0.01	0.1 ± 0.008	<DL	90.2 ± 0.4	3.2 ± 0.03	5.9 ± 0.02
G(9)	0.7 ± 0.02	0.1 ± 0.008	<DL	90.7 ± 0.5	2.6 ± 0.02	5.9 ± 0.03

Table 57 - ICP-OES results of the released elements in solutions. Elements are expressed in mg/L.

7.5 Conclusion

The reaction mixture composition and properties especially the concentration of the KOH activator and the solid faction of waste precursors (volcanic ash and waste borosilicate glass), significantly affected the microstructure and, consequently, the physical and mechanical properties of the consolidated binary mixtures. The occurrence of polycondensation reactions was assumed in all sample sets, regardless of the mix design. The key conclusions from this study are summarized as follows:

- The higher molarity of the activating solution promotes the formation of a more stable Si-O-Si/Al network. Specifically, 9 M KOH solution produced a higher degree of network polymerization, that resulted in materials with a denser microstructure. This is attributable to the presence of potassium ions that contributed to the stabilization of the aluminosilicate network by balancing the negative charges of AlO_4^- tetrahedra.
- SEM micrographs revealed an irregular distribution of precursor grains in the $VG_{1.5}$ set, while the VG_4 set exhibited a more homogeneous distribution (better packing of solid particles). EDS maps indicated a predominantly

silica-calcic composition in the $VG_{1.5}$ set, attributed to a higher amount of glass in the reaction mixture. In the VG_4 set, with a higher amount of volcanic ash, greater heterogeneity of the composition was observed.

- Both the higher molarity of the activating solution and a higher fraction of waste glass positively influenced the uniaxial compressive strengths. Higher variations in weight loss and open porosity were observed in the samples activated with the less concentrated KOH solution and containing a higher fraction of volcanic ash.

The study outlines the potential for producing alkali-activated materials from glass and volcanic ash wastes through the activation process using potassium hydroxide solutions with various molarities. This brings new opportunities for sustainable production of construction materials. Future studies will focus on the exploration of a wider experimental plan, including a larger number of samples along with the investigation of the effects of other variables (i.e., different molarities and curing temperatures) on long-term performances and durability.

8 III Case study: Insight on the rheological properties of Alkali Activated Materials for 3D printing applications

Sabrina Elettra Zafarana[1], Claudio Finocchiaro[1], Abel Woldu Ourgessa[2], Paolo Scanferla[2], Akansha Mehta[2], Jozef Kraxner[2], Dušan Galusek[2,3], Germana Barone[1], Paolo Mazzoleni[1]

[1]Department of Biological, Geological and Environmental Sciences, University of Catania, Italy

[2]FunGlass, Alexander Dubcek University of Trencin, Slovakia

[3]Joint Glass Centre of the IIC SAS, TnUAD and FChFT STU, Trenčín, Slovakia

8.1 Introduction

The increasing awareness of environmental issues has led to reconsidering the impact of the construction industry, which is responsible for approximately 7-8% of the total anthropogenic emissions [355]. However, in a rapidly growing society, developing eco-sustainable materials is essential. In this perspective, Alkali-Activated Materials (AAMs) have emerged [356], thanks to the possibility of incorporating industrial wastes and by-products, leading to reduced carbon footprint [9]. These materials result from the activation reaction of aluminosilicate powders by alkaline solution [12,137], through several steps that lead to the formation of a polymeric network [357].

Volcanic deposits are widespread around the world and some active areas (e.g., Mt. Etna volcano, Italy) offer a large volume [358]. The deposits, once erupted, are considered waste if not properly valorised (i.e., according to the Italian national

legislation) [359]. Moreover, they can negatively influence the daily city life (e.g., transports and mobility) [360]. In this scenario, in the last years, they were used as precursor in alkaline activation process (in two and one-part systems) [139] thanks to their aluminosilicate and mainly amorphous compositions, to produce alkaline-activated pastes for different applications (e.g., fire-resistant foams) [288,321].
However, volcanic glass is less reactive than other precursors like metakaolin and fly ash, requiring small addition of metakaolin to improve setting time and final properties [361]. Therefore, the binary mixtures produced in previous studies have exhibited good mechanical properties, durability and resistance to atmospheric exposure and salt spray [362], making them suitable for construction and restoration [288].
Furthermore, with the advancement of technology, new and revolutionary progress has been made in the field of additive manufacturing (AM), also known as 3D printing (3DP), of construction materials. Additive manufacturing allows for an efficient use of resources, reducing waste of material and time [363]. While traditional construction methods involve cutting and shaping processes, leading to material loss, AM allows the deposition of the material only where needed, optimising its use [364]. This lowers costs and reduces environmental impact, meeting the principles of sustainability and driving a revolutionary approach in the construction industry [365]. Whereas in the traditional construction industry shapes are constrained, the production of layer-by-layer materials allows the development of structures and elements with greater flexibility in design (i.e., from scaffolds for biomedical application and tissue engineering to house construction) [366–369]. Another advantage of AM lies in the speed of the construction process. 3DP allows for much shorter construction times, sometimes resulting in small structures to be completed in short time (i.e., ~37 m^2 house printed in less than two days) [370,371]. This is beneficial in cases of natural disasters, such as earthquakes, where fast reconstruction times are required [372].
AM comprises several techniques that can be used for the 3D printing of AAMs [373,374]. Binder Jetting (BJ) involves the deposition of a liquid, called binder, into a powder bed surface to create the final desired shape [375]. This method meets several drawbacks as the final material tends to have high porosity and low strength compared to the traditionally casted AAMs. Moreover, the starting materials often require specific properties in terms of grain size, flowability and wettability of the

powders [376]. Post-printing treatments such as infiltration or sintering are additionally often needed [377–379]. Photopolymerization techniques, such as stereolithography (SLA) and digital light processing (DLP), are based on the incorporation of a photocurable agent in the AAMs formulation which is selectively cured through the exposure to a UV light source [380,381]. However, these agents are very expensive, and they could affect the final activation reaction of the system, leading to a decrease in mechanical strength and durability of the final material [382].

Direct Ink Writing (DIW) is a method based on extruding a viscous paste through a nozzle. The so-called ink is deposited layer by layer, allowing complex shape building and minimal waste of material [383]. However, the need of strict control on the rheological properties, to ensure proper extrusion, and the necessity to have strong adhesion between layers, to avoid delamination, are crucial challenges [384]. Among all these techniques, DIW does not require any additional post-printing treatments. Although DIW requires tight control over rheological behaviour, it remains the most suitable method thanks to its reduced energy consumption compared to high temperature AM techniques, making the process more environmentally sustainable, thus contributing to the reduction of the overall energy footprint of additive manufacturing.

However, DIW suffers from limitations, e.g., setting time and structural integrity, to ensure extrudability and structural stability during the printing process [385]. Formulations have to balance workability, printability and mechanical features, making the process of design and optimisation of formulations more complex. Indeed, rheology plays a crucial role when it comes to 3D printing applications as fresh-state properties (including viscosity, yield stress and thixotropy) significantly influence the printability and the final mechanical performances [387,388]. Unlike conventional cement pastes, AAMs exhibit distinctive time-dependent viscoelastic properties, which are influenced by the type and concentration of activators, precursor composition and curing conditions. The control over these parameters is crucial for ensuring extrudability, shape stability and interlayer bonding of the printed structures [389]. Furthermore, recent studies have explored the use of rheology modifier additives (i.e., such as polysaccharides, polycarboxylated ethers and nanoclays) to improve printability while maintaining good mechanical performance [390,391]. In addition, optimisation of activator concentration and

binder-to-aggregate ratio can further refine the printability of the AAMs, making them a viable alternative to conventional materials [392].

This study aims to explore for the first time how the rheological properties of waste-based AAMs are affected by changes on the proportions of the precursors and of the molarity of the activator solution. Specifically, binary mixtures of volcanic ash and waste glass (i.e., 60:40 and 80:20, respectively) activated with potassium hydroxide at different molarities (7M and 9M) were used. These formulations were already validated in a previous work (see II case study), which proved that the addition of waste glass in the system contributes to the formation of a stable aluminosilicate network with reduced porosity, resulting in improved mechanical performance. In addition, preliminary printing tests of the best ink by DIW method were carried out to confirm its suitable rheology.

8.2 Materials and methods

8.2.1 Materials

Waste fiberglass (G), industrial waste provided by Johns Manville Slovakia a.s., was firstly crushed and then sieved to ensure a grain size < 40 μm. Volcanic ash (V) from Mt. Etna (Italy) was taken from a landfill located in Zafferana Etnea, in the eastern flank of the volcano. After a wet-milling, the material was dried at 100 ± 5°C and sieved below 40 μm to match the glass powder's grain size, thus guaranteeing a better homogeneity. Combined binary mixtures of V and G with ratios of 80:20 and 60:40, respectively, and activated with KOH in different molarities (i.e., 7M and 9M) (see II case study) were studied to assess their suitability for 3D printing processes. Regardless of the molarity of the KOH solution, the liquid to solid ratio was always kept constant (namely, L/S= 0.46). Samples were labelled using the powdered precursors letters followed by their ratio in the subscript (i.e., 4 and 1.5 when the ratio was 80:20 and 60:40, respectively). The molarity of the solution was reported in brackets.

The raw powders were mixed with alkaline KOH solution and stirred at 500 rpm for 2h. Afterwards, the obtained inks were tested for the rheological and kinetic characterization. Only for the printing process, the addition of a rheology modifier

was essential. In particular, 4 wt.% of Polyethylene Glycol (PEG) was added to the slurry after mixing the precursors for 1.5 h, followed by additional 30 min of homogenization. The addition of PEG was necessary as the printed inks tended to collapse. The printed scaffolds with the addition of PEG were then cured for 48h at 60 °C in a close box to ensure proper consolidation (Figure 64).

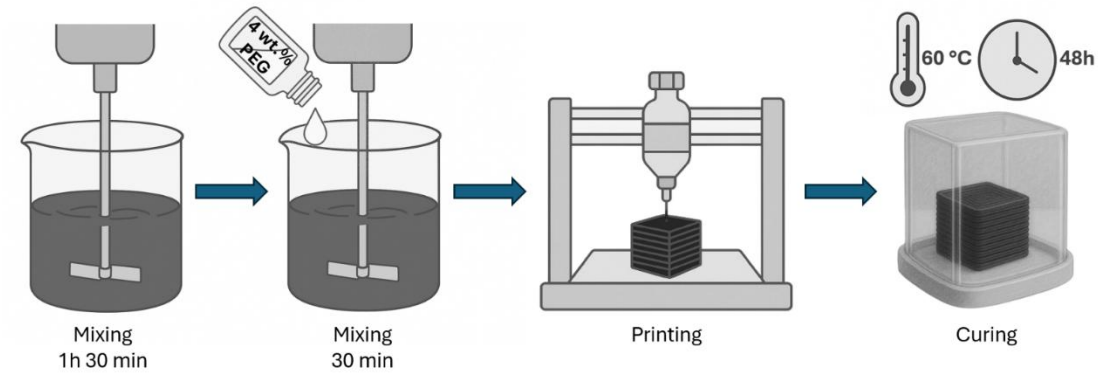

Figure 64 - Synthesis procedure.

8.2.2 Methods

Firstly, the chemical composition of the raw precursors was obtained by using a Bruker S8 Tiger X-Ray Fluorescence (XRF) spectrometer. The rheological characterization of the inks was performed over time (i.e., 0 min, 1 h and 2 h after the mixing process) using a rotational rheometer (Rheometer-viscometer-Haake Mars III), equipped with 35 mm plates with parallel geometry; measurements were performed with 1 mm gap with controlled temperature of 20 °C. Inks were tested without the addition of any rheology modifiers. The instrument was set to evaluate the rheological behaviour of the studied inks under different conditions to assess their stability performance for printing. In particular, the viscosity rebuilding rate test involved two consecutive steps in rotational mode under a constant rate (CR). Firstly, a shear rate of 10 1/s was applied for 60 s, followed by a lower shear rate of 0.1 1/s for 60 s. The used shear rates are selected in order to simulate the extrusion and post-printing conditions, respectively. The described setup allows the evaluation of the inks' ability to recover their viscosity after shearing (i.e., keep their shape after the printing process), as reported by other authors [393,394]. Specifically, the structure rebuilding rate of the inks was calculated by considering

the total relative recovered viscosity at 90s as a reference point of maximum structural rebuilding. The increase in viscosity over time was then evaluated. This approach allowed for a consistent comparison of the inks' thixotropic behaviour.

Moreover, the dynamic strain sweep test was conducted in oscillation mode under constant deformation (CD), with applied strain values ranging from 0.001 to 200 and a frequency of 1 Hz. The test allows to assess whether the inks were behaving in an elastic or viscous way under oscillatory stress. Consequently, flow curve tests were carried out in rotational mode with shear rates ranging from 0.01 to 100 1/s with the aim of determining shear-thinning and thixotropic behaviours of the inks.

For the ink which showed the best rheological features (i.e., highest structural rebuilding rate and enhanced thixotropic behaviour), the consolidation reactions and thermal stability of the slurry in the early curing stages were investigated for a better understanding of the kinetic reaction and the required curing time. Isothermal calorimetry was performed with a Netzsch STA 449 F1 Jupiter that allowed the Simultaneous Thermal Analysis (STA) through the acquisition of both Thermogravimetric Analysis (TGA) and Differential Scanning Calorimetry (DSC) signals. Right after the 2h mixing process, a small amount of slurry was dripped into a Pt-crucible and kept at the constant temperature of 60 °C for 24 h, to study the thermodynamics and kinetics of the consolidation reaction. The first 100 minutes of the test, corresponding to the complete stabilization and consolidation of the specimen, were reported.

An Original Prusa i3Mk3S 3D printer was upgraded into a DIW setup for the printing of the selected slurry. The ink was embedded into a conical plastic syringe (30 cm^3) connected with a nozzle of 4 mm diameter. A non-captive stepper motor with a shaft wound with piston cap was attached on top of the syringe and screwed tightly. The torque of the stepper motor was controlled by a module to produce a smooth extrusion. The printing took place at room temperature with a speed maintained at 6.5 mm/seconds. The CAD file of the 3D structure was designed to have a 3 mm layer height and 6 mm spacing between filaments, to ensure better adhesion between layers. The file was then sliced using UltiMaker Cura software, with 0.90° orientation. The final dimensions of the printed samples measured 40 x 40 x 25 mm (Figure 65). The printed structures were cured at 60°C for 48 h, ensuring proper consolidation and structural stability.

Compressive strength was assessed by Uniaxial Compressive Strength (UCS) tests on 4 printed samples (40 x 40 x 25 mm). A Controls UNIFRAME automatic compression testing machine, equipped with a 50 kN load cell and operated with a speed of 1 mm/min, was used.

Scanning electron microscopy coupled with energy-dispersive X-ray spectroscopy (SEM-EDS) analysis, performed using a JEOL JSM-IT500 analytical microscope, were used to investigate the microstructural and compositional features of the samples.

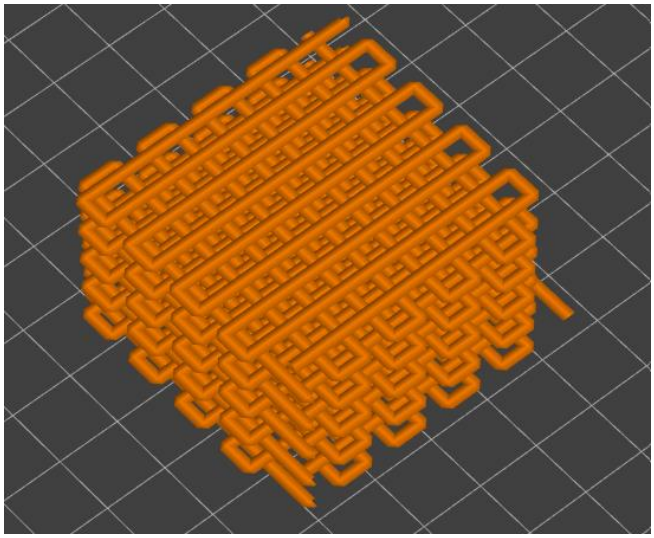

Figure 65 - CAD file design.

8.3 Results and discussion

8.3.1 Chemical characterization

The chemical composition of both waste glass and volcanic ash is reported in Table 58. Waste glass (G) is mainly composed by a high silica content and significant presence of calcium oxide (i.e., 57 and 22.5 wt.%, respectively), together with moderate amounts of alumina. Very low concentrations of alkaline metals and MgO are displayed, along with boron. In comparison, volcanic ash (V) is characterized by lower levels of silica and calcium oxides (i.e., 48 and 10.4 wt.%, respectively). Significant content of alumina (17 wt.%), alkali metals (5.5 wt.%) and iron (10.8

wt.%) were reported. Moreover, a small amount of titanium was identified. The high silica and alumina contents in both materials make them suitable for alkaline activation processes [9].

	Wt.%							
	SiO_2	**Al_2O_3**	**CaO**	**Na_2O + K_2O**	**MgO**	**B_2O_3**	**Fe_2O_3**	**TiO_2**
G	57 ± 1	14.1 ± 0.2	22.5 ± 0.8	0.71 ± 0.05	2.2 ± 0.05	1.8 ± 0.1	-	-
V	48 ± 4	17 ± 1	10.4 ± 0.1	5.5 ± 0.51	5.2 ± 0.7	-	10.8 ± 0.8	1.8 ± 0.3

Table 58 - Chemical composition of the studied raw waste materials obtained though XRF. Oxides are expressed in weight percentage.

8.3.2 Rheological characterization

Figure 66 shows the viscosity rebuilding of the four different inks at three different times following the end of mixing. All inks displayed a substantial increase in viscosity after the first step of the test which concurred with the reduction in shear rate from 10 1/s to 0.1 1/s. The exhibited behaviour is also known as thixotropic, which implies a reduction in viscosity, following the application of a high shear, and a subsequent recovery of viscosity when the shear is reduced, due to the reconstruction of the internal structure [149]. Moreover, a progressive increase in viscosity is observed over time. This finding is in line with other studies on AAMs, that highlighted how the bonding between aluminosilicate species is enhanced over time [395]. For each tested time and applied shear rate, the same behaviour is observed with $VG_4(7)$ being the ink which showed the lowest viscosity and $VG_{1.5}(9)$ showing the highest values. Furthermore, the structural rebuilding rate percentages at 90 s of testing were calculated. It was found out that the highest rebuilding rate was reached by ink $VG_{1.5}(9)$ (i.e., 93%) while the lowest (i.e., 87%) was obtained by $VG_4(7)$. Intermediate values of 89% and 90% were achieved by $VG_4(7)$ and $VG_{1.5}(7)$, respectively.

Regardless, the rapid increase in the system's rigidity suggested that the slurry may exhibit suitable rheological properties for printing processes, helping to minimize the deformation of the printed structures. These results aligned with the behaviours

reported for alkali-activated systems, based on different precursors, subjected to viscosity recovery testing [363,393].

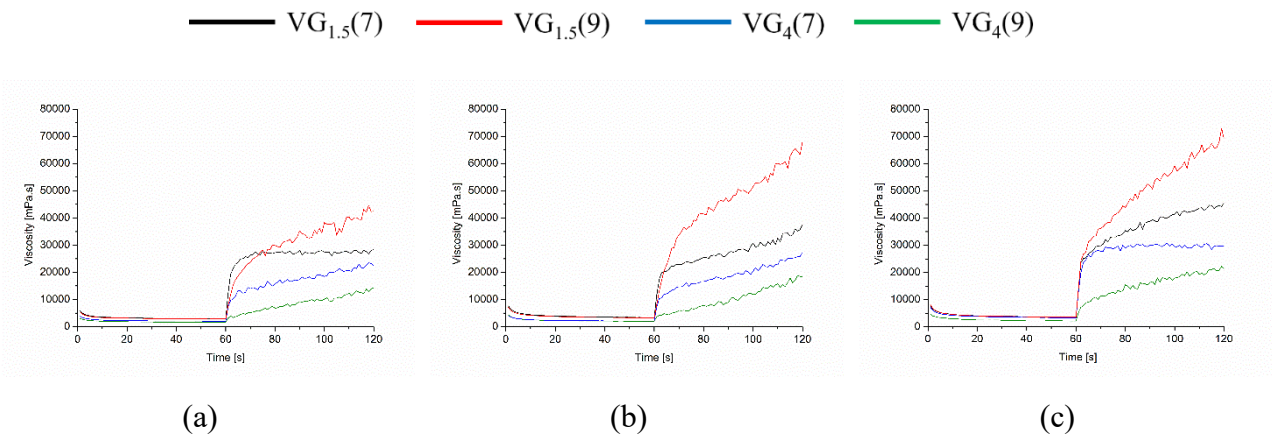

Figure 66 - Viscosity recovery for the studied inks at 0 min (a); 1 h (b) and 2 h (c). The lines represent: black VG1.5(7); red: VG1.5(9); blue VG4(7) and green VG4(9).

Figure 67 displays the dynamic strain sweep test, involving the evolution of both storage modulus (G') and loss modulus (G''), represented by solid and dashed lines, respectively, as functions of strain for the four investigated inks at 0 min, 1 h, and 2 h after mixing. The storage modulus (G') is a measure of the amount of energy stored in the material while the dissipated energy is represented by the loss modulus (G'') [396]. For Direct Ink Writing (DIW) purposes a material with higher storage modulus is preferred, ensuring shape stability after printing. Anyhow, a good balance between G' and G'' is also required, as the storage modulus promotes the solid-like behaviour, making it harder to extrude throughout the nozzle [397].

In particular, at low strain levels, the inks mostly showed an initial increase in both G′ and G″, with G′ having always higher values than G''. This behaviour highlighted a predominantly elastic response [152,398], also observed in Figure 68 (a-c). Specifically, for all specimens when the applied strain was small, the shear stress remained very low, indicating an elastic-like behaviour of the inks. As strain increased, both moduli decreased and then intersected at a crossover value, also known as "gel point". At these points, G' and G'' are balanced, and the transition from the solid state to the fluid state starts occurring [399,400]. Beyond the

crossover point both moduli began to decrease, with G''>G', marking a shift in the material's behaviour. In fact, the reduction in G′ with increasing strain reflects structural weakening, often referred to as strain softening, where the internal alumino-silicate bonds are progressively broken under rising stress, making the material act like a fluid [152,153].

The crossover points and the change from solid to viscous-like material corresponded to the inversion in the slope of the curve [153], as depicted in Figure 67.

Inks $VG_{1.5}(7)$ and $VG_4(9)$ displayed intermediate behaviours. Over time, the crossover points moved to higher strain levels, reflecting a gradual reinforcement of the microstructural network of the material. This likely occurs due to the ongoing formation and strengthening of the aluminosilicate bonds, which contribute to enhanced structural hardening.

Finally, for all inks the transition from solid-like to liquid-like behaviour under growing strain was observed, which is essential for extrusion purposes. Specifically, the crossover point was observed at lower strain levels for inks with higher volcanic ash contents and lower KOH molarity, underlining that both the volcanic ash to glass ratio and the alkaline concentration governed the rheological performance, with higher glass contents and molarity of the solution facilitating rapid crosslinking of the aluminosilicate species.

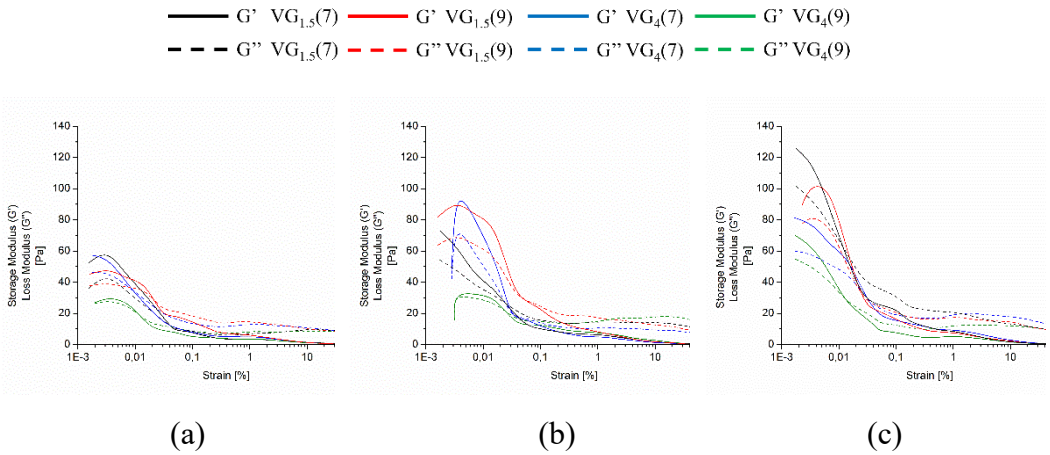

Figure 67 - Storage Modulus (G') and Loss Modulus (G''), expressed in Pa, for each studied ink as function of strain. The lines represent: black VG1.5(7); red: VG1.5(9); blue VG4(7) and green VG4(9). Solid line corresponds to G' while the dashed line stands for G''.

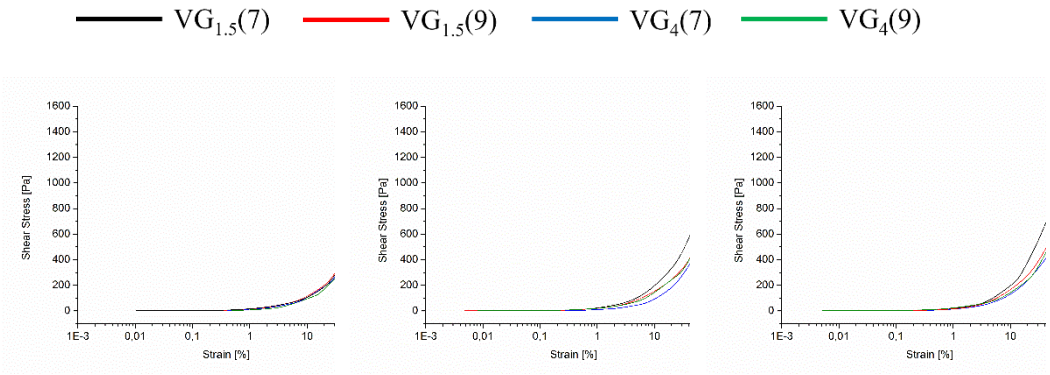

Figure 68 - Shear Stress, expressed in Pa, and Strain for each studied ink. The lines represent: black VG1.5(7); red: VG1.5(9); blue VG4(7) and green VG4(9).

Figure 69 (a-b) displayed the evolution of the shear stress with the increasing shear rate, also known as flow curves, for the studied inks measured over time. Shear-thinning behaviour was exhibited by all specimens, observed by the reduction in viscosity when low shear rates were applied. Right after mixing (Figure 69 a), specimen $VG_{1.5}(9)$ mostly exhibited the highest shear stress over shear rate, suggesting a less fluid behaviour due to strong interaction and aggregation between particles [401]. On the contrary, lowest shear stress values were detected for ink $VG_4(9)$, highlighting its ease to flow which may lead to deformation after printing. Intermediate behaviours were observed for $VG_{1.5}(7)$ and $VG_4(7)$, with moderate shear stress values across the provided shear rates.

Changes in the flow curves were determined by both the precursor ratios and the molarity of the alkali-activating solution, which play a crucial role in reaction kinetics [402]. During shear deformation, these inks undergo mechanical interactions and particle rearrangement [403]. A higher solution concentration leads to increased shear stress, primarily due to the development of inter-particle forces [389]. This process is driven by water consumption and the formation of gel reaction products, resulting in a significant rise in yield stress [404,405].

After letting the inks settle for 1h (Figure 69 b), the same trend was observed with shear stress remaining relatively small at low shear rates. Figure 69 c displays the inks 2 h after mixing. Again, higher yield stress values were shown for $VG_{1.5}(9)$, providing good structural stability. A well-defined shear-thinning behaviour was also demonstrated by $VG_{1.5}(7)$ and $VG_4(7)$, while $VG_4(9)$ revealed to still have a very low shear stress that may lead to excessive flowability and further instability in printed structures.

Overall, the rheological behaviours over time were demonstrated. The optimal shear-thinning property displayed by $VG_{1.5}(9)$ and $VG_{1.5}(7)$ ensures suitable features for DIW making them flow under intermediate stress and maintain their structural shape after printing. $VG_4(9)$ and VG4(7) exhibited lower values, being too fluid and facing potential collapse problems. The trends are consistent with the one reported in literature [406,407].

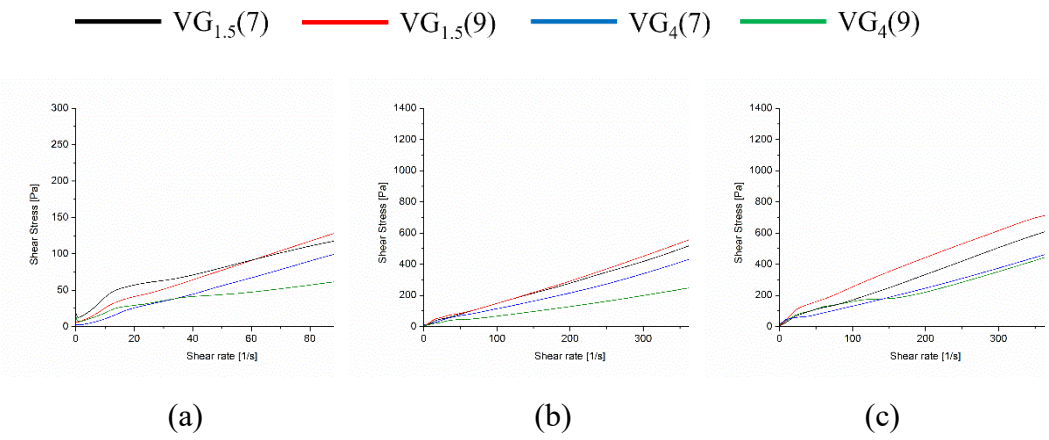

Figure 69 - Flow curves for all inks. The lines represent: black VG1.5(7); red: VG1.5(9); blue VG4(7) and green VG4(9).

Overall, the observed rheological behaviours of the studied inks can be explained by considering the combined effects of precursor composition and alkaline KOH concentration. Inks with higher glass content and more concentrated KOH solution (i.e., $VG_{1.5}(9)$) exhibited enhanced structural rebuilding rate, after the removal of the applied shear, and higher viscosity. This behaviour is likely ascribable to the ability of the system to promote a more rapid reorganization of the bonding between

the aluminosilicate species [153]. On the contrary, inks with higher volcanic ash content and lower molarity (i.e., $VG_4(7)$) showed lower viscosity and relative recovery, indicating a less intense polymerization process that leads to the formation of a less rigid gel network. The observed behaviour may be linked to the increased amount of calcium in the $VG_{1.5}$ set which is known to affect the rheological properties, by producing an increase in viscosity [408]. This is due to the fast formation of C-A-S-H type gel which produces internal friction [401].

The rheological findings are consistent with FTIR results reported in a previous study (see II case study), where it was observed that inks activated with 9M KOH exhibited a more intense and faster formation of aluminosilicate bonds, leading to a denser, stronger and more compact gel network.

8.3.3 Kinetics of the consolidation reactions and thermal stability in the early stages

After the rheological characterization of all inks, $VG_{1.5}(9)$ was chosen for preliminary study on the kinetics of the consolidation reaction, thanks to its favourable properties and the higher mechanical features, as already investigated in a previous study (see II case study).

The thermogravimetric (TG) and differential scanning calorimetry (DSC) curves of the VG1.5(9) ink, displayed in Figure 70, provided important insights into the behaviour of the material during the consolidation process. The mass loss is ascribed to both the release of moisture and the activation reaction [409]. Specifically, the loss of hydroxyl groups in the early stages of the polymerisation reaction, due to condensation processes, could be the responsible for the rapid weight loss during the first 30 min (about 11%) [410]. Subsequently, a gradual decrease in the TG curve is observed, leading to the subsequent formation of a plateau, reaching ~84%. This decrease may be related to further decomposition of compounds due to structural stabilization, suggesting the formation of a stable aluminosilicate network in the consolidated material [411].

The DSC curve revealed both endothermic and exothermic reactions. In particular, the occurrence of an important endothermic event is observed in the first 5 min, which is consistent with the dissolution of the precursors and water evaporation [412–414], as already confirmed by the rapid mass loss observed in the TG curve.

Moreover, a subsequent exothermic peak is reported, which can be attributed to the polymerisation reaction [415–417]. After about 50 min, a complete stabilisation of the DSC curve was observable, suggesting the end of consolidation reactions and the achievement of a stable structure in the consolidated material [418]. Overall, the TG and DSC curves provided important information regarding thermal stability and kinetics of reaction during the early stages of material consolidation. Specifically, the rapid mass loss and the occurred network formation within the first 100 min significantly influence the rheological behaviour of the material, being responsible for the hardening through time. The occurred network formation was also proven in the previous study though FT-IR analysis (see II case study). The considerable total weight loss (~16%) is likely due to the high exposed specific surface area.

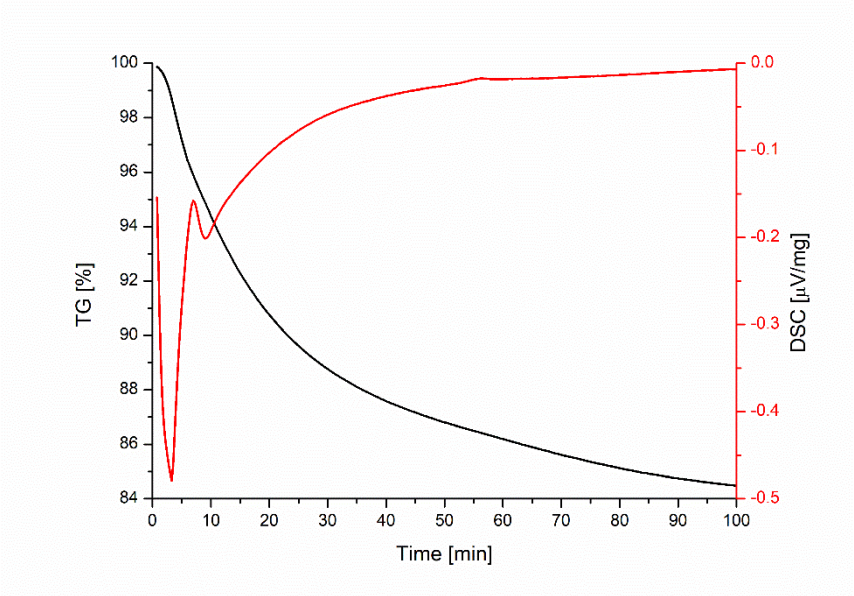

Figure 70 - TG (black) and DSC (red) curves of VG1.5(9).

8.3.4 Characterization of 3D printed specimens

Although the rheological characterization of the fresh alkali-activated paste suggested promising behaviour for extrusion-based 3D printing, the preliminary printing tests of the ink $VG_{1.5}(9)$ revealed several critical issues. As shown in Figure

71, the extruded layers displayed significant spreading upon deposition, resulting in poor shape retention. The printed geometry could not keep vertical build-up, and the material showed the tendency to flatten after extrusion. Consequently, no clear distinction between individual layers or interlayer spacing was observed, indicating insufficient buildability. Further optimization of the paste formulation through the addition of rheology modifiers was necessary to improve shape retention and maintain the printing geometry.

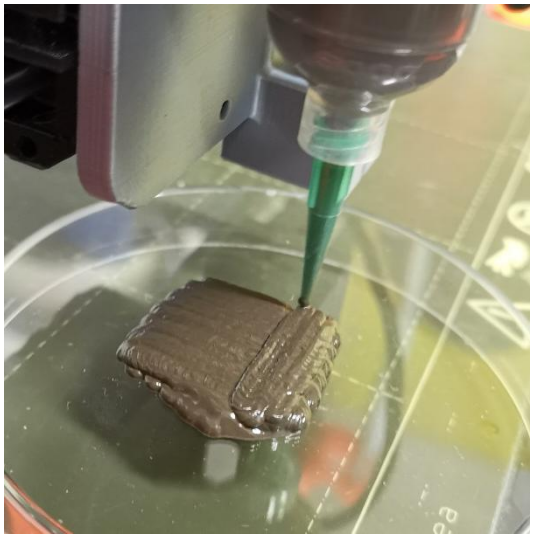

Figure 71 - Preliminary printing trial of VG1.5(9) without the addition of PEG.

Figure 72 (a-c) showed the 3D printed specimens with the addition of 4 wt.% of PEG after curing. From the macroscopic point of view, they exhibited a well-defined geometry, good shape retention without any signs of delamination between layers. The side image (Figure 72 c) showed the presence of distinguishable printed layers with good adhesion. Some small surface irregularities are visible, due to interruption of the printing process. SEM micrographs displayed in Figure 73 (a-b) revealed a homogeneous microstructure, with the presence of amorphous phase. No unreacted particles were detected, while the structure appeared to be porous at both lower and higher magnification. No signs of layer detachment were observed at lower magnification (Figure 73 a).

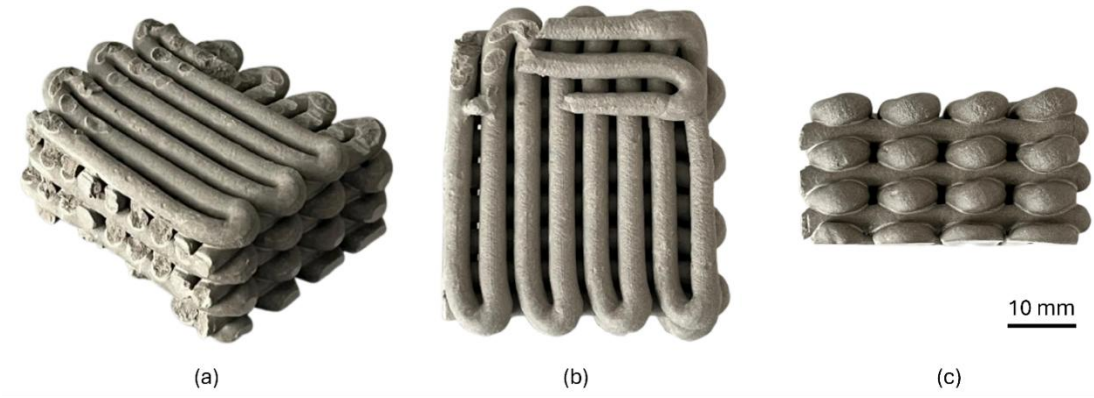

Figure 72 - 3D printed specimens: whole specimen (a); top view (b); side view (c).

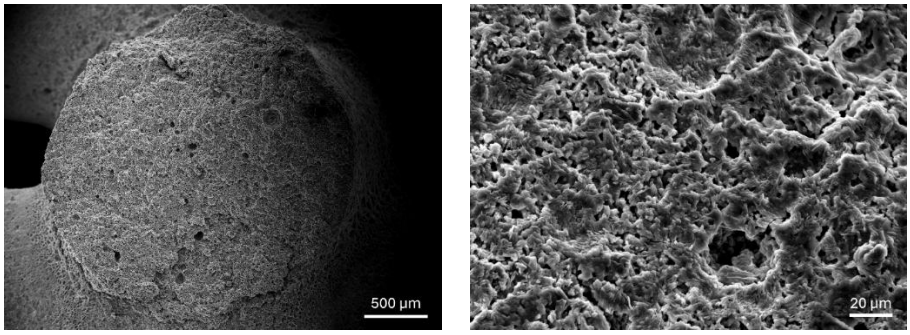

Figure 73 - Morphological micrographs: cross sectional view (a); detailed morphological surface (b).

EDS compositional map revealed a Si- and Al-rich matrix consistent with alkali-activated gel formation (Figure 74). The distribution of potassium is also very high and consistent with the activation of the raw powders with KOH solution. The presence of high levels of calcium and sodium suggested the possible development of reaction products such as C-A-S-H or N-A-S-H-type phases. Fe- and Ti-rich domains are coherent with the chemical composition of the raw volcanic ash, as reported in Table 58.

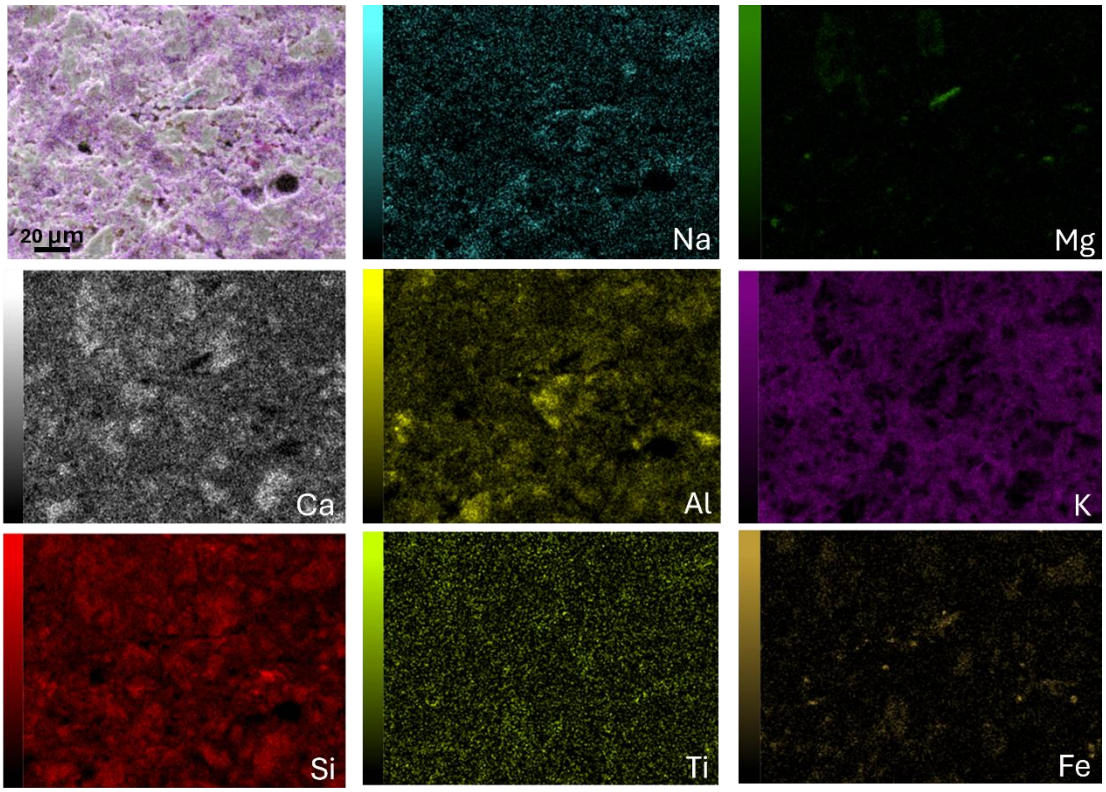

Figure 74 - EDS compositional map: the top left image represents the whole composition.

The mechanical characterization of the 3D printed specimens revealed a predominantly brittle failure mode, with cracks propagating along weak interfaces (Figure 75). Compression testing of the printed specimens achieved a maximum compressive strength of 5.87 ± 1.5 MPa, confirming moderate mechanical performance consistent with the observed microstructure. Nevertheless, these values fell within the expected range for 3D printed alkali-activated materials based on metakaolin [153,419], supporting their potential for low-strength, sustainable construction applications. These results are promising for applications where moderate mechanical performance is acceptable, and where the use of waste-derived materials can offer environmental and economic benefits.

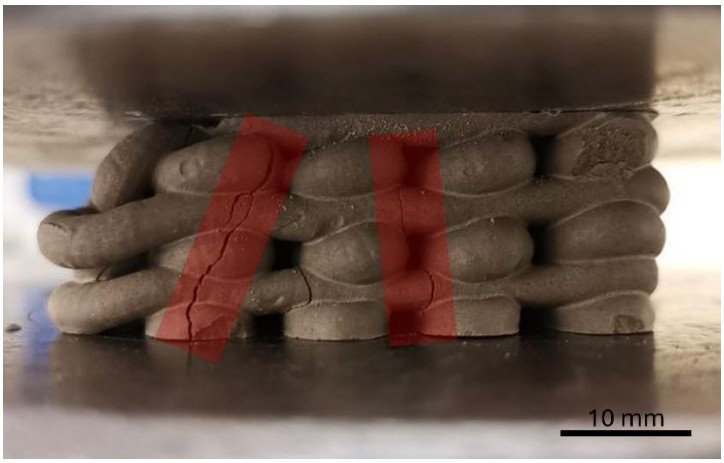

Figure 75 - Breakage behaviour.

8.4 Conclusion

This study demonstrated the feasibility of using volcanic ash and waste glass-based alkali activated inks for Direct Ink Writing (DIW) applications. The successful use of these industrial and natural waste materials aligns with the principles of circular economy and environmental sustainability.

- Among the different compositions investigated, $VG_{1.5}(9)$ exhibited the best rheological behaviour. Specifically, high structural rebuilding and storage modulus (G'), indicated fast recovery after shear stress was applied and stability after printing, ensuring extrudability and shape retention.
- The TG-DSC analysis of $VG_{1.5}(9)$ confirmed the occurrence of the consolidation reaction in the early 100 min.
- Despite the good rheological behaviour, the addition of 4 wt.% PEG as a rheology modifier was necessary to guarantee the structural stability of the printed specimens. The 3D printed samples showed good layer cohesion and reduced spreading during deposition. The mechanical characterization of the printed samples revealed a compressive strength of 5.87 ± 1.5 MPa, which is consistent with other low-strength alkali-activated inks used for non-structural construction applications.

Overall, the results highlighted for the first time the potential of using waste glass and volcanic ash-derived alkali-activated inks in additive manufacturing processes,

such as DIW. The ability to tailor the rheological properties through formulation modification and additives (i.e., rheology modifiers) offers a promising solution to produce sustainable and low-impact materials for the development of non-structural elements. Future work will explore further optimization of the formulation for increased mechanical performance and long-term durability assessment.

9 Bibliography

[1] H. Wallis, L.S. Loy, What drives pro-environmental activism of young people? A survey study on the Fridays For Future movement, J Environ Psychol 74 (2021) 101581. https://doi.org/10.1016/J.JENVP.2021.101581.

[2] W. Colglazier, Sustainable development agenda: 2030, Science (1979) 349 (2015) 1048–1050. https://doi.org/10.1126/SCIENCE.AAD2333.

[3] B. Soergel, E. Kriegler, I. Weindl, S. Rauner, A. Dirnaichner, C. Ruhe, M. Hofmann, N. Bauer, C. Bertram, B.L. Bodirsky, M. Leimbach, J. Leininger, A. Levesque, G. Luderer, M. Pehl, C. Wingens, L. Baumstark, F. Beier, J.P. Dietrich, F. Humpenöder, P. von Jeetze, D. Klein, J. Koch, R. Pietzcker, J. Strefler, H. Lotze-Campen, A. Popp, A sustainable development pathway for climate action within the UN 2030 Agenda, Nature Climate Change 2021 11:8 11 (2021) 656–664. https://doi.org/10.1038/s41558-021-01098-3.

[4] M. Nawaz, A. Heitor, M. Sivakumar, Geopolymers in construction - recent developments, Constr Build Mater 260 (2020) 120472. https://doi.org/10.1016/J.CONBUILDMAT.2020.120472.

[5] Global cement CO_2 emissions 1960-2023 | Statista, (n.d.). https://www.statista.com/statistics/1299532/carbon-dioxide-emissions-worldwide-cement-manufacturing/ (accessed March 6, 2025).

[6] A. Balaguer Pascual, M. Tohoue Tognonvi, A. Tagnit-Hamou, Waste glass powder-based alkali-activated mortar, Int J Res Eng Technol 03 (2014) 32–36. https://doi.org/10.15623/IJRET.2014.0325006.

[7] P. Duxson, J.L. Provis, G.C. Lukey, J.S.J. van Deventer, The role of inorganic polymer technology in the development of 'green concrete,' Cem Concr Res 37 (2007) 1590–1597. https://doi.org/10.1016/J.CEMCONRES.2007.08.018.

[8] A.J. Moseson, D.E. Moseson, M.W. Barsoum, High volume limestone alkali-activated cement developed by design of experiment, Cem Concr Compos 34 (2012) 328–336. https://doi.org/10.1016/J.CEMCONCOMP.2011.11.004.

[9] J.L. Provis, Alkali-activated materials, Cem Concr Res 114 (2018) 40–48. https://doi.org/10.1016/J.CEMCONRES.2017.02.009.

[10] G.L.F. Benachio, M. do C.D. Freitas, S.F. Tavares, Circular economy in the construction industry: A systematic literature review, J Clean Prod 260 (2020) 121046. https://doi.org/10.1016/J.JCLEPRO.2020.121046.

[11] J.L. Provis, S.A. Bernal, Geopolymers and related alkali-activated materials, Annu Rev Mater Res 44 (2014) 299–327. https://doi.org/10.1146/ANNUREV-MATSCI-070813-113515/CITE/REFWORKS.

[12] J. Davidovits, Geopolymers - Inorganic polymeric new materials, Journal of Thermal Analysis 37 (1991) 1633–1656. https://doi.org/10.1007/BF01912193/METRICS.

[13] V.D. Glukhovsky, Soil silicate articles and structures, Kiev , 1967. https://scholar.google.com/scholar?hl=it&as_sdt=0%2C5&q=+Glukhovsky+V.D.+%281967%29%2C+Soil+Silicate+Articles+and+Structure+%28Gruntosilikatnye+

vyroby+I++konstruktsii%29%2C+Ed.+Budivelnyk+Publisher%2C+Kiev.&btnG= (accessed February 24, 2025).

[14] C. Shi, A.F. Jiménez, A. Palomo, New cements for the 21st century: The pursuit of an alternative to Portland cement, Cem Concr Res 41 (2011) 750–763. https://doi.org/10.1016/J.CEMCONRES.2011.03.016.

[15] C.K. Yip, G.C. Lukey, J.S.J. Van Deventer, The coexistence of geopolymeric gel and calcium silicate hydrate at the early stage of alkaline activation, Cem Concr Res 35 (2005) 1688–1697. https://doi.org/10.1016/J.CEMCONRES.2004.10.042.

[16] I. Lecomte, C. Henrist, M. Liégeois, F. Maseri, A. Rulmont, R. Cloots, (Micro)-structural comparison between geopolymers, alkali-activated slag cement and Portland cement, J Eur Ceram Soc 26 (2006) 3789–3797. https://doi.org/10.1016/J.JEURCERAMSOC.2005.12.021.

[17] T. Luukkonen, Alkali-Activated Materials in Environmental Technology Applications, 2022. https://books.google.it/books?hl=it&lr=&id=lGJjEAAAQBAJ&oi=fnd&pg=PP1&dq=alkali-activated+materials+in+environmental+technology+applications+woodhead+publishing&ots=fHWl2iYyVZ&sig=hvUciZCbPWsCib6xu9LxiPNYu3w&redir_esc=y#v=onepage&q=alkali-activated%20materials%20in%20environmental%20technology%20applications%20woodhead%20publishing&f=false (accessed February 25, 2025).

[18] J.L. Provis, van Deventer Jannie S.J., Alkali Activated Materials: State-of-the-Art Report, 2014. https://books.google.it/books?hl=it&lr=&id=fvXHBAAAQBAJ&oi=fnd&pg=PR5&dq=van+deventer&ots=k6RU1_GyBH&sig=JalFFFf9C0IhUaK6ojWw10-Je38&redir_esc=y#v=onepage&q&f=false (accessed February 13, 2025).

[19] F. Pacheco-Torgal, J.A. Labrincha, C. Leonelli, A. Palomo, P. Chindaprasirt, Handbook of Alkali-Activated Cements, Mortars and Concretes, Handbook of Alkali-Activated Cements, Mortars and Concretes (2014) 1–830. https://doi.org/10.1016/C2013-0-16511-7.

[20] M.L. Granizo, M.T. Blanco-Varela, S. Martínez-Ramírez, Alkali activation of metakaolins: Parameters affecting mechanical, structural and microstructural properties, J Mater Sci 42 (2007) 2934–2943. https://doi.org/10.1007/S10853-006-0565-Y/FIGURES/6.

[21] M. Giuffrida, M. Cardone, F. Zuccarello, M. Viccaro, Etna 2011–2022: Discoveries from a decade of activity at the volcano, Earth Sci Rev 245 (2023) 104563. https://doi.org/10.1016/J.EARSCIREV.2023.104563.

[22] L. Zichella, R. Bellopede, S. Spriano, P. Marini, Preliminary investigations on stone cutting sludge processing for a future recovery, J Clean Prod 178 (2018) 866–876. https://doi.org/10.1016/J.JCLEPRO.2017.12.226.

[23] M. Cavalieri, P.L. Ferrara, C. Finocchiaro, M.F. Martorana, An Economic Analysis of the Use of Local Natural Waste: Volcanic Ash of Mt. Etna Volcano (Italy) for Geopolymer Production, Sustainability 2024, Vol. 16, Page 740 16 (2024) 740. https://doi.org/10.3390/SU16020740.

[24] N. Careddu, G.A. Dino, Reuse of residual sludge from stone processing: differences and similarities between sludge coming from carbonate and silicate stones—Italian experiences, Environ Earth Sci 75 (2016) 1–9. https://doi.org/10.1007/S12665-016-5865-1/TABLES/2.

[25] Rifiuti Decreto Ronchi Decreto Legislativo 1997 n.22, (n.d.). https://www.ambientediritto.it/Legislazione/Rifiuti/2002/Decreto%20Ronchi%201997%20n.%2022.htm (accessed March 4, 2025).

[26] d.lgs. n. 152/2006 (T.U. ambiente), (n.d.). https://www.bosettiegatti.eu/info/norme/statali/2006_0152.htm#177 (accessed March 4, 2025).

[27] DECRETO-LEGGE 31 maggio 2021, n. 77 - Normattiva, (n.d.). https://www.normattiva.it/uri-res/N2Ls?urn:nir:stato:decreto.legge:2021;77~art8 (accessed June 10, 2025).

[28] LINEE GUIDA PER LA RACCOLTA, LA DETENZIONE E L'UTILIZZO DELLE CENERI VULCANICHE | Regione Siciliana, (n.d.). https://www.regione.sicilia.it/istituzioni/servizi-informativi/decreti-e-direttive/linee-guida-raccolta-detenzione-l-utilizzo-ceneri-vulcaniche (accessed March 4, 2025).

[29] K. Korniejenko, E. Frączek, E. Pytlak, M. Adamski, Mechanical Properties of Geopolymer Composites Reinforced with Natural Fibers, Procedia Eng 151 (2016) 388–393. https://doi.org/10.1016/J.PROENG.2016.07.395.

[30] D. Jia, P. He, M. Wang, S. Yan, Geopolymer and Geopolymer Matrix Composites, 311 (2020). https://doi.org/10.1007/978-981-15-9536-3.

[31] A. Abubakr, A. Soliman, Impact Behaviour of Steel-Fibre-Reinforced Alkali-Activated Slag Concrete Exposed to Elevated Temperatures, Materials 2023, Vol. 16, Page 4096 16 (2023) 4096. https://doi.org/10.3390/MA16114096.

[32] S. Nazar, J. Yang, M.N. Amin, M. Husnain, F. Ahmad, H. Alabduljabbar, A.F. Deifalla, Investigating the influence of PVA and PP fibers on the mechanical, durability, and microstructural properties of one-part alkali-activated mortar: An experimental study, Journal of Materials Research and Technology 25 (2023) 3482–3495. https://doi.org/10.1016/J.JMRT.2023.06.115.

[33] A. Poonguzhali, H. Shaikh, R.K. Dayal, H.S. Khatak, A review on degradation mechanism and life estimation of civil structures, Corrosion Reviews 26 (2008) 215–294. https://doi.org/10.1515/CORRREV.2008.215/MACHINEREADABLECITATION/RIS.

[34] P. Serna, A. Llano-Torre, J. Martì-Vargas, J. Navarro-Gregori, Fibre Reinforced Concrete: Improvements and Innovations II, Springer International Publishing, 2022. https://doi.org/10.1007/978-3-030-83719-8.

[35] A.R.G. de Azevedo, A.S.A. Cruz, M.T. Marvila, L.B. de Oliveira, S.N. Monteiro, C.M.F. Vieira, R. Fediuk, R. Timokhin, N. Vatin, M. Daironas, Natural Fibers as an Alternative to Synthetic Fibers in Reinforcement of Geopolymer Matrices: A Comparative Review, Polymers 2021, Vol. 13, Page 2493 13 (2021) 2493. https://doi.org/10.3390/POLYM13152493.

[36] I.Y. Hakeem, O. Zaid, M.M. Arbili, M. Alyami, A. Alhamami, M. Alharthai, A state-of-the-art review of the physical and durability characteristics and microstructure behavior of ultra-high-performance geopolymer concrete, Heliyon 10 (2024) e24263. https://doi.org/10.1016/J.HELIYON.2024.E24263.

[37] J.P. Broomfield, Corrosion of Steel in Concrete : Understanding, Investigation and Repair, CRC Press, London, 2023. https://doi.org/10.1201/9781003223016.

[38] J. Provete Vincler, T. Sanchez, V. Turgeon, D. Conciatori, L. Sorelli, A modified accelerated chloride migration tests for UHPC and UHPFRC with PVA and steel fibers, Cem Concr Res 117 (2019) 38–44. https://doi.org/10.1016/J.CEMCONRES.2018.12.006.

[39] S.T. Tassew, A.S. Lubell, Mechanical properties of glass fiber reinforced ceramic concrete, Constr Build Mater 51 (2014) 215–224. https://doi.org/10.1016/J.CONBUILDMAT.2013.10.046.

[40] M. Ziada, S. Erdem, R. Alonso González-Lezcano, Y. Tammam, İ. Unkar, Influence of various fibers on the physico-mechanical properties of a sustainable geopolymer mortar-based on metakaolin and slag, Engineering Science and Technology, an International Journal 46 (2023) 101501. https://doi.org/10.1016/J.JESTCH.2023.101501.

[41] M. Kumar Gupta, N. Singh Rajput, V. Singhal, Applications and Challenges of Carbon-fibres reinforced Composites: A Review, International EVERGREENJoint Journal of Novel Carbon Resource Sciences & Green Asia Strategy 9 (2022) 682–693. https://doi.org/10.5109/4843099.

[42] D. Zhang, Y. Wang, T. Zhang, Q. Yang, Engineering and microstructural properties of carbon-fiber-reinforced fly-ash-based geopolymer composites, Journal of Building Engineering 79 (2023) 107883. https://doi.org/10.1016/J.JOBE.2023.107883.

[43] J. Sim, C. Park, D.Y. Moon, Characteristics of basalt fiber as a strengthening material for concrete structures, Compos B Eng 36 (2005) 504–512. https://doi.org/10.1016/J.COMPOSITESB.2005.02.002.

[44] F. Lentini, S. Carbone, S. Catalano, Main structural domains of the central Mediterranean region and their Neogene tectonic evolution, Bollettino Di Geofisica Teorica Ed Applicata 36 (1994) 103–125. https://pascal-francis.inist.fr/vibad/index.php?action=getRecordDetail&idt=3675634 (accessed March 5, 2025).

[45] F. Lentini, S. Carbone, P. Guarnieri, Collisional and postcollisional tectonics of the Apenninic-Maghrebian orogen (southern Italy), Special Paper of the Geological Society of America 409 (2006) 57–81. https://doi.org/10.1130/2006.2409(04).

[46] S. Branca, M. Coltelli, G. Groppelli, F. Lentini, Geological map of Etna volcano, 1:50,000 scale, Italian Journal of Geosciences 130 (2011) 265–291. https://doi.org/10.3301/IJG.2011.15.

[47] S. Branca, M. Coltelli, G. Groppelli, Geological evolution of a complex basaltic stratovolcano: Mount Etna, Italy, ITALIAN JOURNAL OF GEOSCIENCES 130 (2011) f.3 (2011) 306–317. https://doi.org/10.3301/IJG.2011.13.

[48] E. De Beni, S. Branca, M. Coltelli, G. Groppelli, J.R. Wijbrans, 40Ar/39Ar isotopic dating of Etna volcanic succession, ITALIAN JOURNAL OF GEOSCIENCES 130 (2011) f.3 (2011) 292–305. https://doi.org/10.3301/IJG.2011.14.

[49] S. Branca, Geological and geomorphological evolution of the Etna volcano NE flank and relationships between lava flow invasions and erosional processes in the Alcantara Valley (Italy), Geomorphology 53 (2003) 247–261. https://doi.org/10.1016/S0169-555X(02)00315-X.

[50] S. Calvari, L.H. Tanner, G. Groppelli, G. Norini, Valle del bove, eastern flank of etna volcano: A comprehensive model for the opening of the depression and implications for future hazards, Geophysical Monograph Series 143 (2004) 65–75. https://doi.org/10.1029/143GM05.

[51] E. Boschi, E. Guidoboni, E. Boschi, E. Guidoboni, Catania terremoti e lave dal mondo antico alla fine del Novecento, (2001).

[52] Tanguy, Jean-Claude, New archeomagnetic and 226Ra-230Th dating of recent lavas for the Geological map of Etna volcano, Italian Journal of Geosciences (2012) 241–257. https://doi.org/10.3301/IJG.2012.01).

[53] S. Branca, E. De Beni, C. Proietti, The large and destructive 1669 AD eruption at Etna volcano: Reconstruction of the lava flow field evolution and effusion rate trend, Bull Volcanol 75 (2013) 1–16. https://doi.org/10.1007/S00445-013-0694-5.

[54] D. Schiunnach, M. Gaetani, G. Roghi, LA SUCCESSIONE TERRIGENA PRE-LADINICA TRA LUGANO E VARESE (CANTON TICINO, SVIZZERA; LOMBARDIA, ITALIA), Geol. Insubr. (2015). https://www.researchgate.net/publication/287968104 (accessed March 6, 2025).

[55] L.U. de Sitter, C. de Sitter-Koomans, The Geology of the Bergamasc Alps Lombardia Italy, Leidse Geologische Mededelingen 14 (1949) 1–257.

[56] F. Pezzotta, V. Diella, A. Guastoni, Chemical and paragenetic data on gadolinite-group minerals from Baveno and Cuasso al Monte, southern Alps, Italy, American Mineralogist 84 (1999) 782–789. https://doi.org/10.2138/AM-1999-5-613.

[57] Cartografia, (n.d.). https://cartografia.provincia.va.it/maps/mapindex.html?project=conf_gcartogeo&view=Litologica (accessed March 14, 2025).

[58] E. Surra, J. Sousa, M. Correia, J. Carvalheiras, J.A. Labrincha, J.C. Marques, N. Lapa, C. Delerue-Matos, Technical, Environmental, and Cost Assessment of Granite Sludge Valorisation, Applied Sciences (Switzerland) 13 (2023). https://doi.org/10.3390/APP13074513.

[59] A.J. Souza, B.C.A. Pinheiro, J.N.F. Holanda, Processing of floor tiles bearing ornamental rock-cutting waste, J Mater Process Technol 210 (2010) 1898–1904. https://doi.org/10.1016/J.JMATPROTEC.2010.07.001.

[60] R. Sivacoumar, R. Jayabalou, S. Swarnalatha, K. Balakrishnan, Particulate Matter from Stone Crushing Industry: Size Distribution and Health Effects, Journal of Environmental Engineering 132 (2006) 405–414. https://doi.org/10.1061/(ASCE)0733-9372(2006)132:3(405).

[61] G. Rizzo, F. D'Agostino, L. Ercoli, Problems of soil and groundwater pollution in the disposal of "marble" slurries in NW Sicily, Environmental Geology 55 (2008) 929–935. https://doi.org/10.1007/S00254-007-1043-9/FIGURES/6.

[62] G. Barone, C. Finocchiaro, I. Lancellotti, C. Leonelli, P. Mazzoleni, C. Sgarlata, A. Stroscio, Potentiality of the Use of Pyroclastic Volcanic Residues in the Production of Alkali Activated Material, Waste Biomass Valorization 12 (2021) 1075–1094. https://doi.org/10.1007/S12649-020-01004-6.

[63] P. min Zhan, Z. hai He, Z. ming Ma, C. feng Liang, X. xiang Zhang, A.A. Abreham, J. yan Shi, Utilization of nano-metakaolin in concrete: A review, Journal of Building Engineering 30 (2020) 101259. https://doi.org/10.1016/J.JOBE.2020.101259.

[64] B. Sabir, S. Wild, J. Bai, Metakaolin and calcined clays as pozzolans for concrete: a review, Cem Concr Compos 23 (2001) 441–454. https://doi.org/10.1016/S0958-9465(00)00092-5.

[65] M.T. Marvila, A.R.G. de Azevedo, C.M.F. Vieira, Reaction mechanisms of alkali-activated materials, Revista IBRACON de Estruturas e Materiais 14 (2021) e14309. https://doi.org/10.1590/S1983-41952021000300009.

[66] A. Elimbi, H.K. Tchakoute, D. Njopwouo, Effects of calcination temperature of kaolinite clays on the properties of geopolymer cements, Constr Build Mater 25 (2011) 2805–2812. https://doi.org/10.1016/J.CONBUILDMAT.2010.12.055.

[67] A. Fernández-Jiménez, M. Monzó, M. Vicent, A. Barba, A. Palomo, Alkaline activation of metakaolin–fly ash mixtures: Obtain of Zeoceramics and Zeocements, Microporous and Mesoporous Materials 108 (2008) 41–49. https://doi.org/10.1016/J.MICROMESO.2007.03.024.

[68] J. Cai, X. Li, J. Tan, B. Vandevyvere, Thermal and compressive behaviors of fly ash and metakaolin-based geopolymer, Journal of Building Engineering 30 (2020) 101307. https://doi.org/10.1016/J.JOBE.2020.101307.

[69] J. Zeng, K. Zhang, W. Sun, Y. Zeng, Z. Zou, Mechanics and microstructure analysis of geopolymer utilizing ilmenite tailing and metakaolin powder as alkali-activated materials, Case Studies in Construction Materials 21 (2024) e03567. https://doi.org/10.1016/J.CSCM.2024.E03567.

[70] J.L. Provis, Geopolymers and other alkali activated materials: Why, how, and what?, Materials and Structures/Materiaux et Constructions 47 (2014) 11–25. https://doi.org/10.1617/S11527-013-0211-5/FIGURES/6.

[71] Y.O. Abiodun, O.A. Olanrewaju, O.P. Gbenebor, E.F. Ochulor, D.V. Obasa, S.O. Adeosun, Cutting Cement Industry CO2 Emissions through Metakaolin Use in Construction, Atmosphere 2022, Vol. 13, Page 1494 13 (2022) 1494. https://doi.org/10.3390/ATMOS13091494.

[72] F. Pacheco-Torgal, S. Jalali, Cementitious building materials reinforced with vegetable fibres: A review, Constr Build Mater 25 (2011) 575–581. https://doi.org/10.1016/J.CONBUILDMAT.2010.07.024.

[73] N. Gaibor, D. Leitão, T. Miranda, N. Cristelo, E.N.B. Pereira, V.M.C.F. Cunha, Effect of polyacrylonitrile fiber on the properties of alkali-activated ceramic/slag-based mortar, Journal of Building Engineering 44 (2021) 103367. https://doi.org/10.1016/J.JOBE.2021.103367.

[74] C. Wang, X. Zhao, X. Zhang, Y. Zhao, Y. Wang, J. Zhao, Effects of alkali equivalent and polypropylene fibres on performance of alkali-activated municipal waste incineration bottom ash-slag mortar, Journal of Building Engineering 84 (2024) 108496. https://doi.org/10.1016/J.JOBE.2024.108496.

[75] X. Zhou, D. Liu, H. Bu, L. Deng, H. Liu, P. Yuan, P. Du, H. Song, XRD-based quantitative analysis of clay minerals using reference intensity ratios, mineral intensity factors, Rietveld, and full pattern summation methods: A critical review, Solid Earth Sciences 3 (2018) 16–29. https://doi.org/10.1016/J.SESCI.2017.12.002.

[76] BGMN Home, (n.d.). http://www.bgmn.de/index.html (accessed December 18, 2024).

[77] N. Doebelin, R. Kleeberg, Profex: a graphical user interface for the Rietveld refinement program BGMN, Urn:Issn:1600-5767 48 (2015) 1573–1580. https://doi.org/10.1107/S1600576715014685.

[78] A.F. Gualtieri, M. Zanni, Quantitative determination of crystalline and amorphous phase in traditional ceramics by combined Rietveld-RIR method, Materials Science Forum 278–281 (1998) 834–839. https://doi.org/10.4028/WWW.SCIENTIFIC.NET/MSF.278-281.834.

[79] S. Portale, C. Finocchiaro, R. Occhipinti, P. Mazzoleni, G. Barone, Feasibility study about the use of basalt sawing sludge in building and restoration, Mater Lett 333 (2023) 133624. https://doi.org/10.1016/J.MATLET.2022.133624.

[80] A. Baliyan, H. Imai, V. Kumar, Microscopy, Data Processing Handbook for Complex Biological Data Sources (2019) 97–117. https://doi.org/10.1016/B978-0-12-816548-5.00007-1.

[81] A.D. Elliott, Confocal Microscopy: Principles and Modern Practices, Curr Protoc Cytom 92 (2020) e68. https://doi.org/10.1002/CPCY.68.

[82] J.P.B. van Dam, S.T. Abrahami, A. Yilmaz, Y. Gonzalez-Garcia, H. Terryn, J.M.C. Mol, Effect of surface roughness and chemistry on the adhesion and durability of a steel-epoxy adhesive interface, Int J Adhes Adhes 96 (2020) 102450. https://doi.org/10.1016/J.IJADHADH.2019.102450.

[83] N. Bagdassarov, Density and Porosity, Fundamentals of Rock Physics (2021) 28–65. https://doi.org/10.1017/9781108380713.003.

[84] R.E. Danielson, P.L. Sutherland, Porosity, Methods of Soil Analysis, Part 1: Physical and Mineralogical Methods (2018) 443–461. https://doi.org/10.2136/SSSABOOKSER5.1.2ED.C18.

[85] UNI 7087-2017; Concrete-Determination of the Resistance to the Degrade Due to Freeze-Thaw Cycles. , UNI: Milan, Italy (2017).

[86] R. Penna, L. Feo, E. Martinelli, M. Pepe, Theoretical Modelling of the Degradation Processes Induced by Freeze-Thaw Cycles on Bond-Slip Laws of Fibres in High-Performance Fibre-Reinforced Concrete, Materials (Basel) 15 (2022). https://doi.org/10.3390/MA15176122.

[87] C. Zhang, Z. Wu, C. Luo, X. Hu, K. Li, C. Shi, N. Banthia, Size effect of ultra-high-performance concrete under compression: effects of steel fiber characteristics and

water-to-binder ratio, Constr Build Mater 330 (2022) 127170. https://doi.org/10.1016/J.CONBUILDMAT.2022.127170.

[88] K. Maryamh, K. Hauch, C. Redenbach, J. Schnell, Influence of specimen size on the fibre geometry and tensile strength of ultra-high-performance fibre-reinforced concrete, Structural Concrete 23 (2022) 1239–1252. https://doi.org/10.1002/SUCO.202000753.

[89] M.R. Wisnom, Size effects in the testing of fibre-composite materials, Compos Sci Technol 59 (1999) 1937–1957. https://doi.org/10.1016/S0266-3538(99)00053-6.

[90] F. Ameri, P. Shoaei, S.A. Zareei, B. Behforouz, Geopolymers vs. alkali-activated materials (AAMs): A comparative study on durability, microstructure, and resistance to elevated temperatures of lightweight mortars, Constr Build Mater 222 (2019) 49–63. https://doi.org/10.1016/J.CONBUILDMAT.2019.06.079.

[91] C.M. Gramaccioli, F. Demartin, P. Orlandi, CESIAN BAZZITE AND THORTVEITITE FROM CUASSO AL MONTE, VARESE, ITALY: A COMPARISON WITH THE MATERIAL FROM BAVENO, AND INFERRED ORIGIN, The Canadian Mineralogist 38 (2000) 1409–1418.

[92] L.M. Costa, N.G.S. Almeida, M. Houmard, P.R. Cetlin, G.J.B. Silva, M.T.P. Aguilar, Influence of the addition of amorphous and crystalline silica on the structural properties of metakaolin-based geopolymers, Appl Clay Sci 215 (2021) 106312. https://doi.org/10.1016/J.CLAY.2021.106312.

[93] K. Komnitsas, D. Vathi, E. Steiakakis, G. Bartzas, V. Perdikatsis, Insights on stabilization of marly soils through alkali activation with the use of slag and metakaolin as additives, Case Studies in Chemical and Environmental Engineering 8 (2023) 100400. https://doi.org/10.1016/J.CSCEE.2023.100400.

[94] J. Liu, J.H. Doh, D.E.L. Ong, Z. Liu, M.N.S. Hadi, Methods to evaluate and quantify the geopolymerization reactivity of waste-derived aluminosilicate precursor in alkali-activated material: A state-of-the-art review, Constr Build Mater 362 (2023). https://doi.org/10.1016/J.CONBUILDMAT.2022.129784.

[95] K.U. Ambikakumari Sanalkumar, M. Lahoti, E.H. Yang, Investigating the potential reactivity of fly ash for geopolymerization, Constr Build Mater 225 (2019) 283–291. https://doi.org/10.1016/J.CONBUILDMAT.2019.07.140.

[96] Y. Deng, Z. Zhang, J. Hu, Q. Yu, C. Shi, Fundamental study on reactive components and leaching kinetics of ceramic waste for geopolymer production, Compos B Eng 295 (2025) 112211. https://doi.org/10.1016/J.COMPOSITESB.2025.112211.

[97] P. Duxson, A. Fernández-Jiménez, J.L. Provis, G.C. Lukey, A. Palomo, J.S.J. Van Deventer, Geopolymer technology: The current state of the art, J Mater Sci 42 (2007) 2917–2933. https://doi.org/10.1007/s10853-006-0637-z.

[98] S. Puligilla, P. Mondal, Co-existence of aluminosilicate and calcium silicate gel characterized through selective dissolution and FTIR spectral subtraction, Cem Concr Res 70 (2015) 39–49. https://doi.org/10.1016/J.CEMCONRES.2015.01.006.

[99] C. Finocchiaro, G. Barone, P. Mazzoleni, C. Leonelli, A. Gharzouni, S. Rossignol, FT-IR study of early stages of alkali activated materials based on pyroclastic deposits (Mt. Etna, Sicily, Italy) using two different alkaline solutions, Constr Build Mater 262 (2020). https://doi.org/10.1016/J.CONBUILDMAT.2020.120095.

[100] W.K.W. Lee, J.S.J. Van Deventer, Use of Infrared Spectroscopy to Study Geopolymerization of Heterogeneous Amorphous Aluminosilicates, Langmuir 19 (2003) 8726–8734. https://doi.org/10.1021/LA026127E.

[101] A. Gharzouni, L. Ouamara, I. Sobrados, S. Rossignol, Alkali-activated materials from different aluminosilicate sources: Effect of aluminum and calcium availability, J Non Cryst Solids 484 (2018) 14–25. https://doi.org/10.1016/J.JNONCRYSOL.2018.01.014.

[102] R. Andres Robayo-Salazar, F. Puertas, R. Andrés Robayo-Salazar, R. Mejía de Gutiérrez, Effect of metakaolin on natural volcanic pozzolan-based geopolymer cement, (2016). https://doi.org/10.1016/j.clay.2016.07.020.

[103] J. Liu, Z. Chang, L. Wang, J. Xu, R. Kuang, Z. Wu, Exploration of Basalt Glasses as High-Temperature Sensible Heat Storage Materials, ACS Omega 5 (2020) 19236–19246. https://doi.org/10.1021/ACSOMEGA.0C02773.

[104] B.R. Ilić, A.A. Mitrović, L.R. Miličić, THERMAL TREATMENT OF KAOLIN CLAY TO OBTAIN METAKAOLIN, (n.d.). https://doi.org/10.2298/HEMIND100322014I.

[105] X. Shang, Z. Zhang, X. Xu, T. Liu, Y. Xing, Mineral Composition, Pore Structure, and Mechanical Characteristics of Pyroxene Granite Exposed to Heat Treatments, Minerals 2019, Vol. 9, Page 553 9 (2019) 553. https://doi.org/10.3390/MIN9090553.

[106] L.F. Lima, P.Q. Mantas, A.M. Segadães, R.C.D. Cruz, Processing and characterization of sinter-crystallized basalt glass-ceramics, J Non Cryst Solids 538 (2020) 120019. https://doi.org/10.1016/J.JNONCRYSOL.2020.120019.

[107] T. Nahhas, X. Py, N. Sadiki, Experimental investigation of basalt rocks as storage material for high-temperature concentrated solar power plants, Renewable and Sustainable Energy Reviews 110 (2019) 226–235. https://doi.org/10.1016/J.RSER.2019.04.060.

[108] F. Pacheco-Torgal, J.P. Castro-Gomes, S. Jalali, Investigations of tungsten mine waste geopolymeric binder: Strength and microstructure, Constr Build Mater 22 (2008) 2212–2219. https://doi.org/10.1016/J.CONBUILDMAT.2007.08.003.

[109] J. Yang, L. Xu, H. Wu, J. Jin, L. Liu, Microstructure and mechanical properties of metakaolin-based geopolymer composites containing high volume of spodumene tailings, Appl Clay Sci 218 (2022) 106412. https://doi.org/10.1016/J.CLAY.2022.106412.

[110] P. Palmero, A. Formia, J.M. Tulliani, P. Antonaci, Valorisation of alumino-silicate stone muds: From wastes to source materials for innovative alkali-activated materials, Cem Concr Compos 83 (2017) 251–262. https://doi.org/10.1016/J.CEMCONCOMP.2017.07.011.

[111] I.P. Segura, P.A. Jensen, A.J. Damø, N. Ranjbar, L.S. Jensen, M. Canut, Influence of sodium-based activators and water content on the fresh and hardened properties of metakaolin geopolymers, SN Appl Sci 4 (2022) 1–16. https://doi.org/10.1007/S42452-022-05167-W/FIGURES/10.

[112] I. Pundienė, J. Pranckevičienė, C. Zhu, M. Kligys, The role of temperature and activator solution molarity on the viscosity and hard structure formation of

geopolymer pastes, Constr Build Mater 272 (2021) 121661. https://doi.org/10.1016/J.CONBUILDMAT.2020.121661.

[113] C.: Al-Qutaifi, S.; K. Hanan, A.; Hamza, S. Al-Qutaifi, A.K. Hanan, A.J. Hamza, The Influence of Molarity Activity on the Green and Mechanical Properties of Geopolymer Concrete, Construction Materials 2025, Vol. 5, Page 16 5 (2025) 16. https://doi.org/10.3390/CONSTRMATER5010016.

[114] I. Lancellotti, M. Catauro, C. Ponzoni, F. Bollino, C. Leonelli, Inorganic polymers from alkali activation of metakaolin: Effect of setting and curing on structure, J Solid State Chem 200 (2013) 341–348. https://doi.org/10.1016/J.JSSC.2013.02.003.

[115] S. Ghorbani, L. Stefanini, Y. Sun, B. Walkley, J.L. Provis, G. De Schutter, S. Matthys, Characterisation of alkali-activated stainless steel slag and blast-furnace slag cements, Cem Concr Compos 143 (2023) 105230. https://doi.org/10.1016/J.CEMCONCOMP.2023.105230.

[116] S. Onutai, T. Osugi, T. Sone, Alumino-Silicate Structural Formation during Alkali-Activation of Metakaolin: In-Situ and Ex-Situ ATR-FTIR Studies, Materials 2023, Vol. 16, Page 985 16 (2023) 985. https://doi.org/10.3390/MA16030985.

[117] D.W. Zhang, K. fei Zhao, D. min Wang, H. Li, Relationship of amorphous gel-microstructure-elastoviscosity properties of alkali-activated materials fresh pastes with different Ms waterglass, Constr Build Mater 287 (2021) 123023. https://doi.org/10.1016/J.CONBUILDMAT.2021.123023.

[118] D.W. Zhang, K.F. Zhao, F. zhu Xie, H. Li, D. min Wang, Effect of water-binding ability of amorphous gel on the rheology of geopolymer fresh pastes with the different NaOH content at the early age, Constr Build Mater 261 (2020) 120529. https://doi.org/10.1016/J.CONBUILDMAT.2020.120529.

[119] A.B. Pascual, T.M. Tognonvi, A. Tagnit-Hamou, Optimization study of waste glass powder-based alkali activated materials incorporating metakaolin: Activation and curing conditions, J Clean Prod 308 (2021) 127435. https://doi.org/10.1016/J.JCLEPRO.2021.127435.

[120] M.C. Bignozzi, S. Manzi, I. Lancellotti, E. Kamseu, L. Barbieri, C. Leonelli, Mix-design and characterization of alkali activated materials based on metakaolin and ladle slag, Appl Clay Sci 73 (2013) 78–85. https://doi.org/10.1016/J.CLAY.2012.09.015.

[121] C. Kuenzel, T.P. Neville, S. Donatello, L. Vandeperre, A.R. Boccaccini, C.R. Cheeseman, Influence of metakaolin characteristics on the mechanical properties of geopolymers, Appl Clay Sci 83–84 (2013) 308–314. https://doi.org/10.1016/J.CLAY.2013.08.023.

[122] O. Vogt, N. Ukrainczyk, C. Ballschmiede, E. Koenders, Reactivity and Microstructure of Metakaolin Based Geopolymers: Effect of Fly Ash and Liquid/Solid Contents, Materials 2019, Vol. 12, Page 3485 12 (2019) 3485. https://doi.org/10.3390/MA12213485.

[123] L. Li, J. Xie, B. Zhang, Y. Feng, J. Yang, A state-of-the-art review on the setting behaviours of ground granulated blast furnace slag- and metakaolin-based alkali-

activated materials, Constr Build Mater 368 (2023) 130389. https://doi.org/10.1016/J.CONBUILDMAT.2023.130389.

[124] D.D. Ramteke, M. Hujova, J. Kraxner, D. Galusek, A.R. Romero, R. Falcone, E. Bernardo, Up-cycling of 'unrecyclable' glasses in glass-based foams by weak alkali-activation, gel casting and low-temperature sintering, J Clean Prod 278 (2021) 123985. https://doi.org/10.1016/J.JCLEPRO.2020.123985.

[125] I. Ben Messaoud, N. Hamdi, E. Srasra, Physicochemical Characterization of Geopolymer Binders and Foams Made from Tunisian Clay, Advances in Materials Science and Engineering 2018 (2018). https://doi.org/10.1155/2018/9392743.

[126] S. Yusan, A. Bampaiti, S. Aytas, S. Erenturk, M.A.A. Aslani, Synthesis and structural properties of ZnO and diatomite-supported ZnO nanostructures, Ceram Int 42 (2016) 2158–2163. https://doi.org/10.1016/J.CERAMINT.2015.09.169.

[127] N.S.D.M. Azhar, F.F. Zainal, M.M.A.B. Abdullah, Bonding and Phases Analysis of Geopolymer Materials, IOP Conf Ser Mater Sci Eng 957 (2020). https://doi.org/10.1088/1757-899X/957/1/012052.

[128] M.I. Khan, K. Azizli, S. Sufian, A.A. Siyal, Z. Man, Sodium Silicate Free Geopolymer As Coating Material: Adhesion To Steel, (2014) b016. https://doi.org/10.3390/ECM-1-B016.

[129] C.A. Rees, J.L. Provis, G.C. Lukey, J.S.J. Van Deventer, In situ ATR-FTIR study of the early stages of fly ash geopolymer gel formation, Langmuir 23 (2007) 9076–9082. https://doi.org/10.1021/LA701185G/SUPPL_FILE/LA701185G.PDF.

[130] C.A. Rees, J.L. Provis, G.C. Lukey, J.S.J. Van Deventer, Attenuated total reflectance fourier transform infrared analysis of fly ash geopolymer gel aging, Langmuir 23 (2007) 8170–8179. https://doi.org/10.1021/LA700713G/SUPPL_FILE/LA700713G-FILE002.PDF.

[131] A. Hajimohammadi, J.L. Provis, J.S.J. van Deventer, Time-resolved and spatially-resolved infrared spectroscopic observation of seeded nucleation controlling geopolymer gel formation, J Colloid Interface Sci 357 (2011) 384–392. https://doi.org/10.1016/J.JCIS.2011.02.045.

[132] M.P. Christophliemk, A.T. Pikkarainen, A. Heponiemi, S. Tuomikoski, H. Runtti, T. Hu, A.M. Kantola, U. Lassi, Preparation and characterization of porous and stable sodium- and potassium-based alkali activated material (AAM), Appl Clay Sci 230 (2022) 106697. https://doi.org/10.1016/J.CLAY.2022.106697.

[133] I. Pundienė, J. Pranckevičienė, C. Zhu, M. Kligys, The role of temperature and activator solution molarity on the viscosity and hard structure formation of geopolymer pastes, Constr Build Mater 272 (2021) 121661. https://doi.org/10.1016/J.CONBUILDMAT.2020.121661.

[134] M. Shariati, A. Shariati, N.T. Trung, P. Shoaei, F. Ameri, N. Bahrami, S.N. Zamanabadi, Alkali-activated slag (AAS) paste: Correlation between durability and microstructural characteristics, Constr Build Mater 267 (2021) 120886. https://doi.org/10.1016/J.CONBUILDMAT.2020.120886.

[135] C. Kuenzel, T.P. Neville, S. Donatello, L. Vandeperre, A.R. Boccaccini, C.R. Cheeseman, Influence of metakaolin characteristics on the mechanical properties of

geopolymers, Appl Clay Sci 83–84 (2013) 308–314. https://doi.org/10.1016/J.CLAY.2013.08.023.

[136] P. Duxson, J.L. Provis, G.C. Lukey, S.W. Mallicoat, W.M. Kriven, J.S.J. Van Deventer, Understanding the relationship between geopolymer composition, microstructure and mechanical properties, Colloids Surf A Physicochem Eng Asp 269 (2005) 47–58. https://doi.org/10.1016/J.COLSURFA.2005.06.060.

[137] J. Davidovits, J. Davidovits, Geopolymers: Ceramic-like inorganic polymers, Article in Journal of Ceramic Science and Technology (2017) 8–11. https://doi.org/10.4416/JCST2017-00038.

[138] R. Occhipinti, M.C. Caggiani, L. de Ferri, Z. Xu, C.C. Steindal, N. Razavi, F. Andriulo, P. Mazzoleni, G. Barone, Structural properties of volcanic precursors-based geopolymers before and after natural weathering, Ceram Int 49 (2023) 21892–21902. https://doi.org/10.1016/J.CERAMINT.2023.04.013.

[139] C. Finocchiaro, G. Barone, P. Mazzoleni, G. Cultrone, Insight on physical–mechanical properties of one-part alkali-activated materials based on volcanic deposits of Mt. Etna (Italy) and their durability against ageing tests, Materials and Structures/Materiaux et Constructions 57 (2024) 1–13. https://doi.org/10.1617/S11527-024-02471-2/FIGURES/6.

[140] S. Portale, P. Mazzoleni, G. Barone, Alkali activated binders based on rock sawing sludges: Synthesis, characterization and future perspectives, Constr Build Mater 450 (2024) 138669. https://doi.org/10.1016/J.CONBUILDMAT.2024.138669.

[141] M.S. Norsuzailina, H. Sinin, Efflorescence phenomenon on concrete structures, Adv Mat Res 626 (2013) 747–750. https://doi.org/10.4028/WWW.SCIENTIFIC.NET/AMR.626.747.

[142] C. Liu, Z. Li, G. Ye, Mechanisms of efflorescence of alkali-activated slag, (2024). https://doi.org/10.1016/j.cemconcomp.2024.105811.

[143] P. Zhang, X. Han, S. Hu, J. Wang, T. Wang, High-temperature behavior of polyvinyl alcohol fiber-reinforced metakaolin/fly ash-based geopolymer mortar, Compos B Eng 244 (2022) 110171. https://doi.org/10.1016/J.COMPOSITESB.2022.110171.

[144] de Lima, L. Miranda, D. Schutter, Y. Sun, L. Miranda de Lima, L. Rossi, D. Jiao, Z. Li, G. Ye, G. De Schutter, Interpretation of the early stiffening process in alkali-activated slag pastes Green Open Access added to TU Delft Institutional Repository Interpretation of the early stiffening process in alkali-activated slag pastes, Cem Concr Res 167 (2023) 107118. https://doi.org/10.1016/j.cemconres.2023.107118.

[145] P. Scanferla, A. Conte, A. Sin, G. Franchin, P. Colombo, The effect of fillers on the fresh and hardened properties of 3D printed geopolymer lattices, (2021). https://doi.org/10.1016/j.oceram.2021.100134.

[146] D. Shi, J. Ye, W. Zhang, W. Shen, Properties, mineralogy and microstructure evolution of 4-year calcium silicate slag-based alkali-activated materials, Cem Concr Compos 136 (2023) 104857. https://doi.org/10.1016/J.CEMCONCOMP.2022.104857.

[147] E. Tajuelo Rodriguez, K. Garbev, D. Merz, L. Black, I.G. Richardson, Thermal stability of C-S-H phases and applicability of Richardson and Groves' and

Richardson C-(A)-S-H(I) models to synthetic C-S-H, Cem Concr Res 93 (2017) 45–56. https://doi.org/10.1016/J.CEMCONRES.2016.12.005.

[148] D. Djafari, Rheology of materials, 2024. https://www.researchgate.net/publication/386323952_Rheology_of_materials (accessed June 12, 2025).

[149] H.A. Barnes, Thixotropy—a review, J Nonnewton Fluid Mech 70 (1997) 1–33. https://doi.org/10.1016/S0377-0257(97)00004-9.

[150] Y. Sun, S. Zhang, A. V. Rahul, Y. Tao, F. Van Bockstaele, K. Dewettinck, G. Ye, G. De Schutter, Rheology of alkali-activated slag pastes: New insight from microstructural investigations by cryo-SEM, Cem Concr Res 157 (2022) 106806. https://doi.org/10.1016/J.CEMCONRES.2022.106806.

[151] X. Dai, S. Aydin, M. Yücel Yardimci, R.E.N. Qiang, K. Lesage, G. De Schutter, Rheology, early-age hydration and microstructure of alkali-activated GGBFS-Fly ash-limestone mixtures, Cem Concr Compos 124 (2021) 104244. https://doi.org/10.1016/J.CEMCONCOMP.2021.104244.

[152] G. Stojkov, Z. Niyazov, F. Picchioni, R.K. Bose, Relationship between Structure and Rheology of Hydrogels for Various Applications, Gels 7 (2021) 255. https://doi.org/10.3390/GELS7040255.

[153] G. Franchin, P. Scanferla, L. Zeffiro, H. Elsayed, A. Baliello, G. Giacomello, M. Pasetto, P. Colombo, Direct ink writing of geopolymeric inks, J Eur Ceram Soc 37 (2017) 2481–2489. https://doi.org/10.1016/J.JEURCERAMSOC.2017.01.030.

[154] C. Lu, Z. Zhang, C. Shi, N. Li, D. Jiao, Q. Yuan, Rheology of alkali-activated materials: A review, Cem Concr Compos 121 (2021) 104061. https://doi.org/10.1016/J.CEMCONCOMP.2021.104061.

[155] T.A. Aiken, J. Kwasny, W. Sha, K.T. Tong, Mechanical and durability properties of alkali-activated fly ash concrete with increasing slag content, Constr Build Mater 301 (2021) 124330. https://doi.org/10.1016/J.CONBUILDMAT.2021.124330.

[156] P.N. Lemougna, U.F. Chinje Melo, M.P. Delplancke, H. Rahier, Influence of the chemical and mineralogical composition on the reactivity of volcanic ashes during alkali activation, Ceram Int 40 (2014) 811–820. https://doi.org/10.1016/J.CERAMINT.2013.06.072.

[157] K. Gong, C.E. White, Time-dependent phase quantification and local structure analysis of hydroxide-activated slag via X-ray total scattering and molecular modeling, Cem Concr Res 151 (2022) 106642. https://doi.org/10.1016/J.CEMCONRES.2021.106642.

[158] L. Srinivasamurthy, V.S. Chevali, Z. Zhang, M.A. Longhi, T.W. Loh, H. Wang, Mechanical property and microstructure development in alkali activated fly ash slag blends due to efflorescence, Constr Build Mater 332 (2022) 127273. https://doi.org/10.1016/J.CONBUILDMAT.2022.127273.

[159] D. Panias, I.P. Giannopoulou, T. Perraki, Effect of synthesis parameters on the mechanical properties of fly ash-based geopolymers, Colloids Surf A Physicochem Eng Asp 301 (2007) 246–254. https://doi.org/10.1016/J.COLSURFA.2006.12.064.

[160] C. Rahmawati, S. Aprilia, T. Saidi, T.B. Aulia, Mineralogical, Microstructural and Compressive Strength Characterization of Fly Ash as Materials in Geopolymer Cement, Elkawnie 7 (2021) 1. https://doi.org/10.22373/EKW.V7I1.7787.

[161] H. Kamarudin, A.M.M. Al Bakri, M. Binhussain, C.M. Ruzaidi, M. Luqman, C.Y. Heah, Y.M. Liew, Preliminary Study on Effect of NaOH Concentration on Early Age Compressive Strength of Kaolin-Based Green Cement, (n.d.).

[162] W.-H. Lee, Y.-C. Ding, K.-L. Lin, C.-Y. Lin, T.-A. Chen, Effects of Composition Type and Activator on Fly Ash-Based Alkali Activated Materials, Polymers 2022, Vol. 14, Page 63 14 (2021) 63. https://doi.org/10.3390/POLYM14010063.

[163] T. Tracz, T. Zdeb, I. Hager, B. Kozub, K. Miernik, S.G.˛ Adek, A Study of Fly Ash-Based Geopolymers with Basalt Flour Addition, Materials Proceedings 2023, Vol. 13, Page 3 13 (2023) 3. https://doi.org/10.3390/MATERPROC2023013003.

[164] D. Mrozek, M. Mrozek, R. Krzywoń, Mechanical properties of geopolymers synthesized using basalt powder as a partial substitute for metakaolin, Sci Rep 15 (2025) 1–15. https://doi.org/10.1038/S41598-025-96447-Z;SUBJMETA=1023,166,301,303,639,986;KWRD=CIVIL+ENGINEERING,MECHANICAL+PROPERTIES.

[165] I. Garcia-Lodeiro, A. Palomo, A. Fernández-Jiménez, An overview of the chemistry of alkali-activated cement-based binders, Handbook of Alkali-Activated Cements, Mortars and Concretes (2015) 19–47. https://doi.org/10.1533/9781782422884.1.19.

[166] Z. Zhang, J.L. Provis, A. Reid, H. Wang, Geopolymer foam concrete: An emerging material for sustainable construction, Constr Build Mater 56 (2014) 113–127. https://doi.org/10.1016/J.CONBUILDMAT.2014.01.081.

[167] F. Nazário Santos, S. Raquel Gomes de Sousa, A. José Faria Bombard, S. Lopes Vieira, Rheological study of cement paste with metakaolin and/or limestone filler using Mixture Design of Experiments, Constr Build Mater 143 (2017) 92–103. https://doi.org/10.1016/J.CONBUILDMAT.2017.03.001.

[168] B. Chen, B. Xu, Z. Sun, Rheological properties of cement paste with in-situ polymerization of sodium acrylate: Roles of polymerization and hydration, Constr Build Mater 457 (2024) 139381. https://doi.org/10.1016/J.CONBUILDMAT.2024.139381.

[169] D.K. Lee, M.S. Choi, Standard Reference Materials for Cement Paste: Part II-Determination of Mixing Ratios, Materials 11 (2018) 861. https://doi.org/10.3390/MA11050861.

[170] D. Jiao, R. De Schryver, C. Shi, G. De Schutter, Thixotropic structural build-up of cement-based materials: A state-of-the-art review, Cem Concr Compos 122 (2021) 104152. https://doi.org/10.1016/J.CEMCONCOMP.2021.104152.

[171] A.A. Siyal, R.M.S. Radin Mohamed, R. Shamsuddin, M.B. Ridzuan, A comprehensive review of synthesis kinetics and formation mechanism of geopolymers, RSC Adv 14 (2024) 446. https://doi.org/10.1039/D3RA06205H.

[172] M. Alshaaer, O. Alqahtani, M.M.S. Alharbi, A.O.S. Alanazi, K.A. Aldhafeeri, M.T. Ahmed, T. Alomayri, Synthesis and Characterization of Date Palm Fiber-Reinforced Geopolymer Composite, Arab J Sci Eng 47 (2022) 12323–12332. https://doi.org/10.1007/S13369-021-06378-W/FIGURES/9.

[173] C. Lv, D. Wu, G. Guo, Y. Zhang, S. Liu, E. Qu, J. Liu, Effect of Plant Fiber on Early Properties of Geopolymer, Molecules 2023, Vol. 28, Page 4710 28 (2023) 4710. https://doi.org/10.3390/MOLECULES28124710.

[174] P. Perez-Cortes, J.I. Escalante-Garcia, Gel composition and molecular structure of alkali-activated metakaolin-limestone cements, Cem Concr Res 137 (2020) 106211. https://doi.org/10.1016/J.CEMCONRES.2020.106211.

[175] V. Růžek, A.M. Dostayeva, J. Walter, T. Grab, K. Korniejenko, Carbon Fiber-Reinforced Geopolymer Composites: A Review, Fibers 2023, Vol. 11, Page 17 11 (2023) 17. https://doi.org/10.3390/FIB11020017.

[176] M. Amran, R. Fediuk, H.S. Abdelgader, G. Murali, T. Ozbakkaloglu, Y.H. Lee, Y.Y. Lee, Fiber-reinforced alkali-activated concrete: A review, Journal of Building Engineering 45 (2022). https://doi.org/10.1016/J.JOBE.2021.103638.

[177] T. Bezabih, D. Sinkhonde, D. Mirindi, Using bearing ratio curves to quantify the surface roughness parameters of fly ash-teff straw ash-based geopolymer mortars, Results in Surfaces and Interfaces 17 (2024) 100344. https://doi.org/10.1016/J.RSURFI.2024.100344.

[178] J. Castellano, M.D. Marrero, Z. Ortega, Opuntia Fiber and Its Potential to Obtain Sustainable Materials in the Composites Field: A Review, Journal of Natural Fibers 19 (2022) 10053–10067. https://doi.org/10.1080/15440478.2021.1993479;PAGE:STRING:ARTICLE/CHAPTER.

[179] Y. Du, S. Lu, J. Xu, W. Xia, T. Wang, Z. Wang, Experimental study of impact mechanical and microstructural properties of modified carbon fiber reinforced concrete, Sci Rep 12 (2022) 1–14. https://doi.org/10.1038/S41598-022-17092-4;SUBJMETA=166,301,639;KWRD=ENGINEERING,MATERIALS+SCIENCE.

[180] V. Růžek, A.M. Dostayeva, J. Walter, T. Grab, K. Korniejenko, Carbon Fiber-Reinforced Geopolymer Composites: A Review, Fibers 2023, Vol. 11, Page 17 11 (2023) 17. https://doi.org/10.3390/FIB11020017.

[181] A. Trabelsi, Z. Kammoun, Mechanical properties and impact resistance of a high-strength lightweight concrete incorporating prickly pear fibres, Constr Build Mater 262 (2020) 119972. https://doi.org/10.1016/J.CONBUILDMAT.2020.119972.

[182] M.H. Yassin, R.E. Lakys, Z.E. Merouani, A. Jumah, M.H. Farhat, Performance analysis of palm tree microfibers in concrete, Sci Rep 15 (2025) 1–32. https://doi.org/10.1038/S41598-024-84111-X;SUBJMETA=1023,166,301,639,986;KWRD=CIVIL+ENGINEERING,ENGINEERING,MATERIALS+SCIENCE,STRUCTURAL+MATERIALS.

[183] F.A. Al-Sulaiman, Date palm fibre reinforced composite as a new insulating material, Int J Energy Res 27 (2003) 1293–1297. https://doi.org/10.1002/ER.957;WGROUP:STRING:PUBLICATION.

[184] Y. Du, S. Lu, J. Xu, W. Xia, T. Wang, Z. Wang, Experimental study of impact mechanical and microstructural properties of modified carbon fiber reinforced concrete, Sci Rep 12 (2022) 1–14. https://doi.org/10.1038/S41598-022-17092-4;SUBJMETA=166,301,639;KWRD=ENGINEERING,MATERIALS+SCIENCE.

[185] J. Zhao, M. Liebscher, K. Schneider, D. Junger, V. Mechtcherine, Effect of surface profiling on the mechanical properties and bond behaviour of mineral-impregnated, carbon-fibre (MCF) reinforcement based on geopolymer, Constr Build Mater 367 (2023) 130199. https://doi.org/10.1016/J.CONBUILDMAT.2022.130199.

[186] C.; Liu, X.; Liang, Y.; Chen, Z.; Li, Ye, Guang, Degradation of alkali-activated slag subjected to water immersion, Cem Concr Compos 142 (2023) 105157. https://doi.org/10.1016/j.cemconcomp.2023.105157.

[187] M. Babaee, A. Castel, A Performance-Based Test for Mitigating the Risk of Geopolymer Concrete Surface Efflorescence Due to Alkali Leaching, Materials 2024, Vol. 17, Page 3647 17 (2024) 3647. https://doi.org/10.3390/MA17153647.

[188] S. Wang, L. Yu, L. Xu, K. Wu, Z. Yang, The Failure Mechanisms of Precast Geopolymer after Water Immersion, Materials 2021, Vol. 14, Page 5299 14 (2021) 5299. https://doi.org/10.3390/MA14185299.

[189] I. Lancellotti, F. Piccolo, K. Traven, M. Češnovar, V. Ducman, C. Leonelli, Alkali Activation of Metallurgical Slags: Reactivity, Chemical Behavior, and Environmental Assessment, Materials 2021, Vol. 14, Page 639 14 (2021) 639. https://doi.org/10.3390/MA14030639.

[190] A.A.S. Tigue, R.A.J. Malenab, J.R. Dungca, D.E.C. Yu, M.A.B. Promentilla, Chemical Stability and Leaching Behavior of One-Part Geopolymer from Soil and Coal Fly Ash Mixtures, Minerals 2018, Vol. 8, Page 411 8 (2018) 411. https://doi.org/10.3390/MIN8090411.

[191] J.A. Abdalla, R.A. Hawileh, A. Bahurudeen, G. Jyothsna, A. Sofi, V. Shanmugam, B.S. Thomas, A comprehensive review on the use of natural fibers in cement/geopolymer concrete: A step towards sustainability, Case Studies in Construction Materials 19 (2023) e02244. https://doi.org/10.1016/J.CSCM.2023.E02244.

[192] N.; Ranjbar, Zhang, General rights Fiber-reinforced geopolymer composites: A review, (n.d.). https://doi.org/10.1016/j.cemconcomp.2019.103498.

[193] X. Shang, S. Wang, B. Gong, Y. Wang, Y. Li, R. Zhong, Improved carbon fibers dispersion in geopolymer composites, Case Studies in Construction Materials 21 (2024) e03480. https://doi.org/10.1016/J.CSCM.2024.E03480.

[194] W. Zhang, B. Yin, A. Akbar, W.-W. Li, Y. Dai, K.M. Liew, Nano-micro pore structure characteristics of carbon black and recycled carbon fiber reinforced alkali-activated materials, Npj Materials Sustainability 2024 2:1 2 (2024) 1–14. https://doi.org/10.1038/s44296-024-00033-9.

[195] K. Vegere, L. Vitola, P.P. Argalis, D. Bajare, A.E. Krauklis, Alkali-Activated Metakaolin as a Zeolite-Like Binder for the Production of Adsorbents, Inorganics 2019, Vol. 7, Page 141 7 (2019) 141. https://doi.org/10.3390/INORGANICS7120141.

[196] C. Oliviero Rossi, P. Calandra, P. Caputo, B. Teltayev, V. Loise, M. Porto, J. Zhan, B. Fu, Z. Cheng, Macroscopic Properties and Pore Structure Fractal Characteristics of Alkali-Activated Metakaolin–Slag Composite Cementitious Materials, Polymers 2022, Vol. 14, Page 5217 14 (2022) 5217. https://doi.org/10.3390/POLYM14235217.

[197] J. Zhao, M. Liebscher, L. Tzounis, V. Mechtcherine, Role of sizing agent on the microstructure morphology and mechanical properties of mineral-impregnated carbon-fiber (MCF) reinforcement made with geopolymers, Appl Surf Sci 567 (2021) 150740. https://doi.org/10.1016/J.APSUSC.2021.150740.

[198] F.U.A. Shaikh, Deflection hardening behaviour of short fibre reinforced fly ash based geopolymer composites, Mater Des 50 (2013) 674–682. https://doi.org/10.1016/J.MATDES.2013.03.063.

[199] T. Lin, D. Jia, P. He, M. Wang, D. Liang, Effects of fiber length on mechanical properties and fracture behavior of short carbon fiber reinforced geopolymer matrix composites, Materials Science and Engineering: A 497 (2008) 181–185. https://doi.org/10.1016/J.MSEA.2008.06.040.

[200] T. Lin, D. Jia, P. He, M. Wang, In situ crack growth observation and fracture behavior of short carbon fiber reinforced geopolymer matrix composites, Materials Science and Engineering: A 527 (2010) 2404–2407. https://doi.org/10.1016/J.MSEA.2009.12.004.

[201] S. Yan, P. He, D. Jia, Z. Yang, X. Duan, S. Wang, Y. Zhou, Effect of fiber content on the microstructure and mechanical properties of carbon fiber felt reinforced geopolymer composites, Ceram Int 42 (2016) 7837–7843. https://doi.org/10.1016/J.CERAMINT.2016.01.197.

[202] P. He, L. Jia, G. Ma, R. Wang, J. Yuan, X. Duan, Z. Yang, D. Jia, Effects of fiber contents on the mechanical and microwave absorbent properties of carbon fiber felt reinforced geopolymer composites, Ceram Int 44 (2018) 10726–10734. https://doi.org/10.1016/J.CERAMINT.2018.03.107.

[203] Z. Kammoun, A. Trabelsi, Development of lightweight concrete using prickly pear fibres, Constr Build Mater 210 (2019) 269–277. https://doi.org/10.1016/J.CONBUILDMAT.2019.03.167.

[204] A. Trabelsi, Z. Kammoun, Mechanical properties and impact resistance of a high-strength lightweight concrete incorporating prickly pear fibres, Constr Build Mater 262 (2020) 119972. https://doi.org/10.1016/J.CONBUILDMAT.2020.119972.

[205] A.E. Bekele, H.G. Lemu, M.G. Jiru, Study of the Effects of Alkali Treatment and Fiber Orientation on Mechanical Properties of Enset/Sisal Polymer Hybrid Composite, Journal of Composites Science 2023, Vol. 7, Page 37 7 (2023) 37. https://doi.org/10.3390/JCS7010037.

[206] W. Kroehong, C. Jaturapitakkul, T. Pothisiri, P. Chindaprasirt, Effect of Oil Palm Fiber Content on the Physical and Mechanical Properties and Microstructure of High-Calcium Fly Ash Geopolymer Paste, Arab J Sci Eng 43 (2018) 5215–5224. https://doi.org/10.1007/S13369-017-3059-0/METRICS.

[207] M. Alshaaer, O. Alqahtani, M.M.S. Alharbi, A.O.S. Alanazi, K.A. Aldhafeeri, M.T. Ahmed, T. Alomayri, Synthesis and Characterization of Date Palm Fiber-Reinforced Geopolymer Composite, Arab J Sci Eng 47 (2022) 12323–12332. https://doi.org/10.1007/S13369-021-06378-W/FIGURES/9.

[208] S.F. Abrha, H.N. Shiferaw, T. Kanakubo, Bridging Behavior of Palm Fiber in Cementitious Composite, Journal of Composites Science 8 (2024) 361. https://doi.org/10.3390/JCS8090361/S1.

[209] C.I. Madueke, O.M. Mbah, R. Umunakwe, A review on the limitations of natural fibres and natural fibre composites with emphasis on tensile strength using coir as a case study, Polymer Bulletin 80 (2023) 3489–3506. https://doi.org/10.1007/S00289-022-04241-Y/FIGURES/10.

[210] T. Wang, X. Fan, C. Gao, C. Qu, J. Liu, G. Yu, The Influence of Fiber on the Mechanical Properties of Geopolymer Concrete: A Review, Polymers 2023, Vol. 15, Page 827 15 (2023) 827. https://doi.org/10.3390/POLYM15040827.

[211] J.A. Abdalla, R.A. Hawileh, A. Bahurudeen, G. Jyothsna, A. Sofi, V. Shanmugam, B.S. Thomas, A comprehensive review on the use of natural fibers in cement/geopolymer concrete: A step towards sustainability, Case Studies in Construction Materials 19 (2023) e02244. https://doi.org/10.1016/J.CSCM.2023.E02244.

[212] N. Ranjbar, M. Zhang, Fiber-reinforced geopolymer composites: A review, Cem Concr Compos 107 (2020) 103498. https://doi.org/10.1016/J.CEMCONCOMP.2019.103498.

[213] A. Beglarigale, S. Aydın, C. Kızılırmak, Fiber-Matrix Bond Characteristics of Alkali-Activated Slag Cement–Based Composites, Journal of Materials in Civil Engineering 28 (2016) 04016133. https://doi.org/10.1061/(ASCE)MT.1943-5533.0001642.

[214] S. Zidi, I. Miraoui, Enhancing Opuntia ficus-indica Fibers Properties through Alkaline Treatment: Mechanical, Thermal, and Chemical Characterization, Chemistry Africa 7 (2024) 799–811. https://doi.org/10.1007/S42250-023-00801-5/TABLES/5.

[215] S. Aydin, B. Baradan, The effect of fiber properties on high performance alkali-activated slag/silica fume mortars, Compos B Eng 45 (2013) 63–69. https://doi.org/10.1016/J.COMPOSITESB.2012.09.080.

[216] T. Lin, D. Jia, P. He, M. Wang, D. Liang, Effects of fiber length on mechanical properties and fracture behavior of short carbon fiber reinforced geopolymer matrix composites, Materials Science and Engineering: A 497 (2008) 181–185. https://doi.org/10.1016/J.MSEA.2008.06.040.

[217] Z. Wang, X. Rong, L. Zhao, X. Xing, H. Ma, Effects of Substrate Surface Characteristics on the Adhesion Properties of Geopolymer Coatings, ACS Omega 7 (2022) 11988–11994. https://doi.org/10.1021/ACSOMEGA.2C00170,.

[218] J. Wei, C. Meyer, Degradation mechanisms of natural fiber in the matrix of cement composites, Cem Concr Res 73 (2015) 1–16. https://doi.org/10.1016/J.CEMCONRES.2015.02.019.

[219] C. Lv, J. Liu, Alkaline Degradation of Plant Fiber Reinforcements in Geopolymer: A Review, Molecules 2023, Vol. 28, Page 1868 28 (2023) 1868. https://doi.org/10.3390/MOLECULES28041868.

[220] K. Korniejenko, B. Figiela, K. Miernik, C. Ziejewska, J. Marczyk, M. Hebda, A. Cheng, W.T. Lin, Mechanical and Fracture Properties of Long Fiber Reinforced Geopolymer Composites, Materials 2021, Vol. 14, Page 5183 14 (2021) 5183. https://doi.org/10.3390/MA14185183.

[221] P. Payakaniti, S. Pinitsoonthorn, P. Thongbai, V. Amornkitbamrung, P. Chindaprasirt, Effects of carbon fiber on mechanical and electrical properties of fly ash geopolymer composite, Mater Today Proc 5 (2018) 14017–14025. https://doi.org/10.1016/J.MATPR.2018.02.054.

[222] J.S. Alcaide, E.G. Alcocel, F. Puertas, R. Lapuente, P. Garcés, Carbon fibre-reinforced, alkali-activated slag mortars, Materiales de Construcción 57 (2007) 33–48. https://doi.org/10.3989/MC.2007.V57.I288.63.

[223] X. Li, L.G. Tabil, S. Panigrahi, Chemical treatments of natural fiber for use in natural fiber-reinforced composites: A review, J Polym Environ 15 (2007) 25–33. https://doi.org/10.1007/S10924-006-0042-3/FIGURES/3.

[224] D.L. Rocha, L.U.D.T. Júnior, M.T. Marvila, E.C. Pereira, D. Souza, A.R.G. de Azevedo, A Review of the Use of Natural Fibers in Cement Composites: Concepts, Applications and Brazilian History, Polymers (Basel) 14 (2022). https://doi.org/10.3390/POLYM14102043.

[225] F.D.A. Silva, B. Mobasher, C. Soranakom, R.D.T. Filho, Effect of fiber shape and morphology on interfacial bond and cracking behaviors of sisal fiber cement based composites, Cem Concr Compos 33 (2011) 814–823. https://doi.org/10.1016/J.CEMCONCOMP.2011.05.003.

[226] M. Łach, B. Kluska, D. Janus, D. Kabat, K. Pławecka, K. Korniejenko, M.D. Guigou, M. Choińska, Effect of Fiber Reinforcement on the Compression and Flexural Strength of Fiber-Reinforced Geopolymers, Applied Sciences 2021, Vol. 11, Page 10443 11 (2021) 10443. https://doi.org/10.3390/APP112110443.

[227] V. Lakshmi Narayana, L. Bhaskara Rao, A brief review on the effect of alkali treatment on mechanical properties of various natural fiber reinforced polymer composites, Mater Today Proc 44 (2021) 1988–1994. https://doi.org/10.1016/J.MATPR.2020.12.117.

[228] R. Tokonami, K. Aoki, T. Goto, T. Takahashi, Surface Modification of Carbon Fiber for Enhancing the Mechanical Strength of Composites, Polymers 2022, Vol. 14, Page 3999 14 (2022) 3999. https://doi.org/10.3390/POLYM14193999.

[229] X. Peng, Y. Wu, Z. Wei, Research progress on the surface modification of carbon fiber, RSC Adv 14 (2024) 4043–4064. https://doi.org/10.1039/D3RA08577E.

[230] C. Lv, J. Liu, Alkaline Degradation of Plant Fiber Reinforcements in Geopolymer: A Review, Molecules 2023, Vol. 28, Page 1868 28 (2023) 1868. https://doi.org/10.3390/MOLECULES28041868.

[231] N.K. Arora, I. Mishra, United Nations Sustainable Development Goals 2030 and environmental sustainability: race against time, Environmental Sustainability 2 (2019) 339–342. https://doi.org/10.1007/s42398-019-00092-y.

[232] S. Geisendorf, F. Pietrulla, The circular economy and circular economic concepts—a literature analysis and redefinition, Thunderbird International Business Review 60 (2018) 771–782. https://doi.org/10.1002/TIE.21924.

[233] E. Worrell, L. Price, N. Martin, C. Hendriks, L.O. Meida, Carbon dioxide emissions from the global cement industry, Annual Review of Energy and the Environment 26 (2001) 303–329. https://doi.org/10.1146/ANNUREV.ENERGY.26.1.303/CITE/REFWORKS.

[234] E. Benhelal, G. Zahedi, E. Shamsaei, A. Bahadori, Global strategies and potentials to curb CO2 emissions in cement industry, J Clean Prod 51 (2013) 142–161. https://doi.org/10.1016/J.JCLEPRO.2012.10.049.

[235] I. Ramón-Álvarez, E. Batuecas, S. Sánchez-Delgado, M. Torres-Carrasco, Mechanical performance after high-temperature exposure and Life Cycle Assessment (LCA) according to unit of stored energy of alternative mortars to Portland cement, Constr Build Mater 365 (2023) 130082. https://doi.org/10.1016/J.CONBUILDMAT.2022.130082.

[236] M. Nikravan, R. Firdous, D. Stephan, Life cycle assessment of alkali-activated materials: a systematic literature review, Low-Carbon Materials and Green Construction 1 (2023). https://doi.org/10.1007/S44242-023-00014-6.

[237] W.M. Kriven, C. Leonelli, J.L. Provis, A.R. Boccaccini, C. Attwell, V.S. Ducman, C. Ferone, S. Rossignol, T. Luukkonen, J.S.J. van Deventer, J. V. Emiliano, J.E. Lombardi, Why geopolymers and alkali-activated materials are key components of a sustainable world: A perspective contribution, Journal of the American Ceramic Society (2024). https://doi.org/10.1111/JACE.19828.

[238] J. Provis, J.S.J. Van Deventer, Geopolymers: Structures, processing, properties and industrial applications, n.d. https://www.researchgate.net/publication/287830381_Geopolymers_Structures_processing_properties_and_industrial_applications (accessed May 20, 2024).

[239] B. Singh, G. Ishwarya, M. Gupta, S.K. Bhattacharyya, Geopolymer concrete: A review of some recent developments, Constr Build Mater 85 (2015) 78–90. https://doi.org/10.1016/J.CONBUILDMAT.2015.03.036.

[240] W.K. Part, M. Ramli, C.B. Cheah, An overview on the influence of various factors on the properties of geopolymer concrete derived from industrial by-products, Constr Build Mater 77 (2015) 370–395. https://doi.org/10.1016/J.CONBUILDMAT.2014.12.065.

[241] S.A. Bernal, J.L. Provis, Durability of alkali-activated materials: Progress and perspectives, Journal of the American Ceramic Society 97 (2014) 997–1008. https://doi.org/10.1111/JACE.12831.

[242] Z. Tang, W. Li, Y. Hu, J.L. Zhou, V.W.Y. Tam, Review on designs and properties of multifunctional alkali-activated materials (AAMs), Constr Build Mater 200 (2019) 474–489. https://doi.org/10.1016/J.CONBUILDMAT.2018.12.157.

[243] F. Triefenbach, Design of Experiments: The D-Optimal Approach and Its Implementation As a Computer Algorithm, (2008).

[244] Bradley. Jones, Peter. Goos, Optimal design of experiments : a case study approach, (2013). https://books.google.com/books/about/Optimal_Design_of_Experiments.html?hl=it&id=EMWYkYd3sPoC (accessed August 28, 2024).

[245] D.D. Frey, F. Engelhardt, E.M. Greitzer, A role for "one-factor-at-a-time" experimentation in parameter design, Res Eng Des 14 (2003) 65–74. https://doi.org/10.1007/S00163-002-0026-9/TABLES/7.

[246] N. Delgarm, B. Sajadi, K. Azarbad, S. Delgarm, Sensitivity analysis of building energy performance: A simulation-based approach using OFAT and variance-based

sensitivity analysis methods, Journal of Building Engineering 15 (2018) 181–193. https://doi.org/10.1016/J.JOBE.2017.11.020.

[247] A. Arce, A. Komkova, J. Van De Sande, C.G. Papanicolaou, T.C. Triantafillou, Optimal Design of Ferronickel Slag Alkali-Activated Material for High Thermal Load Applications Developed by Design of Experiment, Materials 2022, Vol. 15, Page 4379 15 (2022) 4379. https://doi.org/10.3390/MA15134379.

[248] A.J. Moseson, D.E. Moseson, M.W. Barsoum, High volume limestone alkali-activated cement developed by design of experiment, Cem Concr Compos 34 (2012) 328–336. https://doi.org/10.1016/J.CEMCONCOMP.2011.11.004.

[249] Jacques. Goupy, Lee. Creighton, Introduction to design of experiments with JMP examples, third edition, (2005).

[250] M. Venkatesan, Q. Zaib, I.H. Shah, H.S. Park, Optimum utilization of waste foundry sand and fly ash for geopolymer concrete synthesis using D-optimal mixture design of experiments, Resour Conserv Recycl 148 (2019) 114–123. https://doi.org/10.1016/J.RESCONREC.2019.05.008.

[251] P.F. de Aguiar, B. Bourguignon, M.S. Khots, D.L. Massart, R. Phan-Than-Luu, D-optimal designs, Chemometrics and Intelligent Laboratory Systems 30 (1995) 199–210. https://doi.org/10.1016/0169-7439(94)00076-X.

[252] B. Jones, K. Allen-Moyer, P. Goos, A-optimal versus D-optimal design of screening experiments, Journal of Quality Technology 53 (2021) 369–382. https://doi.org/10.1080/00224065.2020.1757391.

[253] L. Piccini, T. Di Lorenzo, P. Costagliola, D.M.P. Galassi, Marble Slurry's Impact on Groundwater: The Case Study of the Apuan Alps Karst Aquifers, Water 2019, Vol. 11, Page 2462 11 (2019) 2462. https://doi.org/10.3390/W11122462.

[254] B. Coppola, P. Palmero, L. Montanaro, J.M. Tulliani, Alkali-activation of marble sludge: Influence of curing conditions and waste glass addition, J Eur Ceram Soc 40 (2020) 3776–3787. https://doi.org/10.1016/J.JEURCERAMSOC.2019.11.068.

[255] R. Clocchiatti, M. Condomines, N. Guénot, J.C. Tanguy, Magma changes at Mount Etna: the 2001 and 2002–2003 eruptions, Earth Planet Sci Lett 226 (2004) 397–414. https://doi.org/10.1016/J.EPSL.2004.07.039.

[256] R. Brooks, M. Bahadory, F. Tovia, H. Rostami, Properties of alkali-activated fly ash: high performance to lightweight, International Journal of Sustainable Engineering 3 (2010) 211–218. https://doi.org/10.1080/19397038.2010.487162.

[257] M.C. Caggiani, R. Occhipinti, C. Finocchiaro, M. Fugazzotto, A. Stroscio, P. Mazzoleni, G. Barone, Diffuse Reflectance Infrared Fourier Transform Spectroscopy (DRIFTS) as a potential on site tool to test geopolymerization reaction, Talanta 250 (2022) 123721. https://doi.org/10.1016/J.TALANTA.2022.123721.

[258] C. Belver, C. Breen, F. Clegg, C.E. Fernandes, M.A. Vicente, A variable-temperature diffuse reflectance infrared fourier transform spectroscopy study of the binding of water and pyridine to the surface of acid-activated metakaolin, Langmuir 21 (2005) 2129–2136. https://doi.org/10.1021/LA048323M/ASSET/IMAGES/MEDIUM/LA048323MN00001.GIF.

[259] M. Nasar, N. Salisu, Investigation of Effect of KBr Matrix on Drift Infrared Spectra of Some Minerals, ChemSearch Journal 5 (2014) 14–19. https://www.ajol.info/index.php/csj/article/view/114402 (accessed January 11, 2025).

[260] Z. Aly, E.R. Vance, D.S. Perera, J. V. Hanna, C.S. Griffith, J. Davis, D. Durce, Aqueous leachability of metakaolin-based geopolymers with molar ratios of Si/Al = 1.5–4, Journal of Nuclear Materials 378 (2008) 172–179. https://doi.org/10.1016/J.JNUCMAT.2008.06.015.

[261] R.L. Frost, M. Dickfos, Hydrated double carbonates - A Raman and infrared spectroscopic study, Polyhedron 26 (2007) 4503–4508. https://doi.org/10.1016/J.POLY.2007.06.003.

[262] J. Madejová, FTIR techniques in clay mineral studies, Vib Spectrosc 31 (2003) 1–10. https://doi.org/10.1016/S0924-2031(02)00065-6.

[263] A. Autef, E. Joussein, G. Gasgnier, S. Rossignol, Role of the silica source on the geopolymerization rate, J Non Cryst Solids 358 (2012) 2886–2893. https://doi.org/10.1016/J.JNONCRYSOL.2012.07.015.

[264] M. Heikal, M.Y. Nassar, G. El-Sayed, S.M. Ibrahim, Physico-chemical, mechanical, microstructure and durability characteristics of alkali activated Egyptian slag, Constr Build Mater 69 (2014) 60–72. https://doi.org/10.1016/J.CONBUILDMAT.2014.07.026.

[265] A. Tesovnik, B. Horvat, Rapid Immobilisation of Chemical Reactions in Alkali-Activated Materials Using Solely Microwave Irradiation, Minerals 14 (2024) 1219. https://doi.org/10.3390/MIN14121219/S1.

[266] J. Sall, Leverage Plots for General Linear Hypotheses, Am Stat 44 (1990) 308–315. https://doi.org/10.1080/00031305.1990.10475750.

[267] S.C. Callai, P. Tataranni, C. Sangiorgi, Preliminary evaluation of geopolymer mix design applying the design of experiments method, Infrastructures (Basel) 6 (2021). https://doi.org/10.3390/INFRASTRUCTURES6030035.

[268] N.R. Rakhimova, R.Z. Rakhimov, Reaction products, structure and properties of alkali-activated metakaolin cements incorporated with supplementary materials – a review, Journal of Materials Research and Technology 8 (2019) 1522–1531. https://doi.org/10.1016/J.JMRT.2018.07.006.

[269] J. Rocha, J. Klinowski, Solid-State NMR Studies of the Structure and Reactivity of Metakaolinite, Angewandte Chemie International Edition in English 29 (1990) 553–554. https://doi.org/10.1002/ANIE.199005531.

[270] A.M. Rashad, Alkali-activated metakaolin: A short guide for civil Engineer – An overview, Constr Build Mater 41 (2013) 751–765. https://doi.org/10.1016/J.CONBUILDMAT.2012.12.030.

[271] M.I. Rasuli, Y. Tajunnisa, A. Yamamura, M. Shigeishi, A consideration on the one-part mixing method of alkali-activated material: problems of sodium silicate solubility and quick setting, Heliyon 8 (2022) e08783. https://doi.org/10.1016/J.HELIYON.2022.E08783/ASSET/28A46155-63C6-462D-8F38-9D17480E2875/MAIN.ASSETS/GR6.JPG.

[272] A. Palomo, M.W. Grutzeck, M.T. Blanco, Alkali-activated fly ashes: A cement for the future, Cem Concr Res 29 (1999) 1323–1329. https://doi.org/10.1016/S0008-8846(98)00243-9.

[273] H. Xu, J.S.J. Van Deventer, The geopolymerisation of alumino-silicate minerals, Int J Miner Process 59 (2000) 247–266. https://doi.org/10.1016/S0301-7516(99)00074-5.

[274] G. Ishwarya, B. Singh, S. Deshwal, S.K. Bhattacharyya, Effect of sodium carbonate/sodium silicate activator on the rheology, geopolymerization and strength of fly ash/slag geopolymer pastes, Cem Concr Compos 97 (2019) 226–238. https://doi.org/10.1016/J.CEMCONCOMP.2018.12.007.

[275] A.M. Mustafa Al Bakri, H. Kamarudin, I. Khairul Nizar, M. Bnhussain, Y. Zarina, A.R. Rafiza, Correlation between Na2SiO3/NaOH ratio and fly ash/alkaline activator ratio to the strength of geopolymer, Adv Mat Res 341–342 (2012) 189–193. https://doi.org/10.4028/WWW.SCIENTIFIC.NET/AMR.341-342.189.

[276] H. Castillo, H. Collado, T. Droguett, S. Sánchez, M. Vesely, P. Garrido, S. Palma, Factors Affecting the Compressive Strength of Geopolymers: A Review, Minerals 2021, Vol. 11, Page 1317 11 (2021) 1317. https://doi.org/10.3390/MIN11121317.

[277] K.A. Klise, B.L. Nicholson, A. Staid, D.L. Woodruff, Parmest: Parameter Estimation Via Pyomo, Computer Aided Chemical Engineering 47 (2019) 41–46. https://doi.org/10.1016/B978-0-12-818597-1.50007-2.

[278] A. Játiva, E. Ruales, M. Etxeberria, Volcanic Ash as a Sustainable Binder Material: An Extensive Review, Materials 2021, Vol. 14, Page 1302 14 (2021) 1302. https://doi.org/10.3390/MA14051302.

[279] F. Hong, S. Yu, D. Hou, Z. Li, H. Sun, P. Wang, M. Wang, Study on the mechanical properties, gelling products and alkalization process of alkali-activated metakaolin: From experiment to molecular dynamics simulation, Journal of Building Engineering 79 (2023) 107705. https://doi.org/10.1016/J.JOBE.2023.107705.

[280] K.-H. Yang, J.-K. Song, Workability Loss and Compressive Strength Development of Cementless Mortars Activated by Combination of Sodium Silicate and Sodium Hydroxide, Journal of Materials in Civil Engineering 21 (2009) 119–127. https://doi.org/10.1061/(ASCE)0899-1561(2009)21:3(119)/ASSET/7F14B3EC-078E-4D32-A56A-5DB337E3C5F8/ASSETS/IMAGES/LARGE/8.JPG.

[281] D. Chicco, M.J. Warrens, G. Jurman, The coefficient of determination R-squared is more informative than SMAPE, MAE, MAPE, MSE and RMSE in regression analysis evaluation, PeerJ Comput Sci 7 (2021) 1–24. https://doi.org/10.7717/PEERJ-CS.623/SUPP-1.

[282] A.O. Aptula, N.G. Jeliazkova, T.W. Schultz, M.T.D. Cronin, The better predictive model: High q2 for the training set or low root mean square error of prediction for the test set?, QSAR Comb Sci 24 (2005) 385–396. https://doi.org/10.1002/QSAR.200430909.

[283] T. Dong, T. Sun, F. Xu, G. Ouyang, H. Wang, F. Yang, Z. Wang, Effect of Solid Sodium Silicate on Workability, Hydration and Strength of Alkali-Activated GGBS/Fly Ash Paste, Coatings 2023, Vol. 13, Page 696 13 (2023) 696. https://doi.org/10.3390/COATINGS13040696.

[284] C. Vlachakis, M. Perry, L. Biondi, Self-Sensing Alkali-Activated Materials: A Review, Minerals 2020, Vol. 10, Page 885 10 (2020) 885. https://doi.org/10.3390/MIN10100885.

[285] A. Meyer, J. Horbach, W. Kob, F. Kargl, H. Schober, Channel formation and intermediate range order in sodium silicate melts and glasses, Phys Rev Lett 93 (2004) 027801. https://doi.org/10.1103/PHYSREVLETT.93.027801/FIGURES/4/MEDIUM.

[286] J. Polson, B.A. Fette, Cognitive Techniques: Position Awareness, Cognitive Radio Technology (2009) 265–288. https://doi.org/10.1016/B978-0-12-374535-4.00008-4.

[287] A. Niş, Compressive strength variation of alkali activated fly ash/slag concrete with different NaOH concentrations and sodium silicate to sodium hydroxide ratios, Journal of Sustainable Construction Materials and Technologies 4 (2019) 351–360. https://doi.org/10.29187/JSCMT.2019.39.

[288] C. Finocchiaro, R. Occhipinti, G. Barone, P. Mazzoleni, F. Andreola, M. Romagnoli, C. Leonelli, Effects of the addition of slaked lime to alkali-activated pastes based on volcanic ashes from Mt. Etna volcano (Italy), Ceram Int 50 (2024) 24479–24486. https://doi.org/10.1016/J.CERAMINT.2024.04.181.

[289] R. Occhipinti, M.C. Caggiani, F. Andriulo, G. Barone, L. de Ferri, P. Mazzoleni, Effect of atmospheric exposure on alkali activated binders and mortars from Mt. Etna volcanic precursors, Mater Lett 315 (2022). https://doi.org/10.1016/J.MATLET.2022.131940.

[290] C. Karakosta, J. Papathanasiou, Decarbonizing the Construction Sector: Strategies and Pathways for Greenhouse Gas Emissions Reduction, Energies 2025, Vol. 18, Page 1285 18 (2025) 1285. https://doi.org/10.3390/EN18051285.

[291] G. Del Serrone, G. Riccio, L. Moretti, Cradle-to-cradle life cycle assessment of railway prestressed concrete sleepers: A state-of-the-art review and strategies for reducing environmental impacts, Resour Conserv Recycl 214 (2025) 108020. https://doi.org/10.1016/J.RESCONREC.2024.108020.

[292] P. Spencer, H. Li, S. Hocknull, G. Chalmers, T. Wang, Exploring mineral–organic interactions for eco-friendly concrete alternatives: a radical concept, RSC Sustainability 3 (2025) 2064–2078. https://doi.org/10.1039/D4SU00696H.

[293] D.N. Qader, A.S. Jamil, A. Bahrami, M. Ali, K.P. Arunachalam, A systematic review of metakaolin-based alkali-activated and geopolymer concrete: A step toward green concrete, Reviews on Advanced Materials Science 64 (2025). https://doi.org/10.1515/RAMS-2024-0076.

[294] L. Wang, H. Chen, Y. Zhang, Study on Mechanical Properties and Hydration Characteristics of Bauxite-GGBFS Alkali-Activated Materials, Based on Composite Alkali Activator and Response Surface Method, Materials 2025, Vol. 18, Page 1466 18 (2025) 1466. https://doi.org/10.3390/MA18071466.

[295] C. Liu, W. Li, J. Pang, Z. Liu, G. Mei, A. Bezuijen, P. Cachim, Engineering properties and applicability of a novel alkali-activated industrial waste-based backfilling grouts in shield tunnels, J Sustain Cem Based Mater (2025). https://doi.org/10.1080/21650373.2025.2515500.

[296] B. Zhang, Z. Ma, J. Yan, Y. Zhang, Y. Wang, Effects of fly ash vitrified slag (FVS) dosage and alkali content on the reaction of alkali-activated material (AAM), Mater Today Commun 46 (2025) 112507. https://doi.org/10.1016/J.MTCOMM.2025.112507.

[297] X. Zhang, Y. Tan, Z. Liu, F. Wang, S. Hu, Kinetics and mechanism of ground granulated blast furnace slag alkali-activated material activated by red mud and calcium carbide slag, Constr Build Mater 489 (2025) 142328. https://doi.org/10.1016/J.CONBUILDMAT.2025.142328.

[298] A. Muñoz-Castillo, P.J. Sánchez-Soto, D. Eliche-Quesada, Valorisation of rice husk ash as an activator in the preparation of alkali-activated cements based on electric arc furnace slag, Archives of Civil and Mechanical Engineering 2025 25:3 25 (2025) 1–26. https://doi.org/10.1007/S43452-025-01209-3.

[299] F. Carollo, E. De Rienzo, A. D'Angelo, P. Sgarbossa, L. Barbieri, C. Leonelli, I. Lancellotti, M. Catauro, E. Bernardo, Cold Consolidation of Waste Glass by Alkali Activation and Curing by Traditional and Microwave Heating, Materials 2025, Vol. 18, Page 2628 18 (2025) 2628. https://doi.org/10.3390/MA18112628.

[300] Glass recycling – Current market trends - recovery, (n.d.). https://www.recovery-worldwide.com/en/artikel/glass-recycling-current-market-trends-3248774.html (accessed December 18, 2024).

[301] W. Ferdous, A. Manalo, R. Siddique, P. Mendis, Y. Zhuge, H.S. Wong, W. Lokuge, T. Aravinthan, P. Schubel, Recycling of landfill wastes (tyres, plastics and glass) in construction – A review on global waste generation, performance, application and future opportunities, Resour Conserv Recycl 173 (2021) 105745. https://doi.org/10.1016/J.RESCONREC.2021.105745.

[302] S. Dadsetan, H. Siad, M. Lachemi, O. Mahmoodi, M. Sahmaran, Sodium glass liquid from glass waste as a user-friendly hardener in structural geopolymer systems, Cem Concr Compos 130 (2022) 104525. https://doi.org/10.1016/J.CEMCONCOMP.2022.104525.

[303] R. Xiao, B. Huang, H. Zhou, Y. Ma, X. Jiang, A state-of-the-art review of crushed urban waste glass used in OPC and AAMs (geopolymer): Progress and challenges, Cleaner Materials 4 (2022). https://doi.org/10.1016/J.CLEMA.2022.100083.

[304] A. Mohajerani, J. Vajna, T.H.H. Cheung, H. Kurmus, A. Arulrajah, S. Horpibulsuk, Practical recycling applications of crushed waste glass in construction materials: A review, Constr Build Mater 156 (2017) 443–467. https://doi.org/10.1016/J.CONBUILDMAT.2017.09.005.

[305] P. Larionau, M. Hujova, M. Michalková, M. Mahmoud, A. Švančárková, D. Galusková, M. Parchoviansky, E. Bernardo, D. Galusek, J. Kraxner, Low-alkali borosilicate glass microspheres from waste cullet prepared by flame synthesis, Int J Appl Glass Sci 12 (2021) 562–569. https://doi.org/10.1111/IJAG.16144.

[306] S. Kumari, S. Agarwal, S. Khan, Micro/nano glass pollution as an emerging pollutant in near future, Journal of Hazardous Materials Advances 6 (2022) 100063. https://doi.org/10.1016/J.HAZADV.2022.100063.

[307] P. Yuan, X. Cao, L. Zhao, X. Xu, A. Romero-Freire, H. Qiu, Overlooked yet critical pathways for microplastics input to soil and groundwater system: Transport

mechanisms and simulation predictions in landfill environments, Water Res 284 (2025) 124041. https://doi.org/10.1016/J.WATRES.2025.124041.

[308] A. Mehta, K. Karbouche, J. Kraxner, H. Elsayed, D. Galusek, E. Bernardo, Upcycling of Pharmaceutical Glass into Highly Porous Ceramics: From Foams to Membranes, Materials 15 (2022). https://doi.org/10.3390/ma15113784.

[309] D. Saadatpour, M. Lake, G. Gaustad, C.J. Wilkinson, Modeling the Flow of Waste Glass in New York State, Npj Materials Sustainability 2025 3:1 3 (2025) 1–7. https://doi.org/10.1038/s44296-025-00054-y.

[310] P. Manikandan, L. Natrayan, S. Duraimurugan, V. Vasugi, Influence of Waste Glass Powder as an Aluminosilicate Precursor in Synthesizing Ternary Blended Alkali-Activated Binder, Silicon (2022). https://doi.org/10.1007/S12633-021-01533-2.

[311] M.H. Samarakoon, P.G. Ranjith, W. Hui Duan, A. Haque, B.K. Chen, Extensive use of waste glass in one-part alkali-activated materials: Towards sustainable construction practices, Waste Management 130 (2021) 1–11. https://doi.org/10.1016/J.WASMAN.2021.04.060.

[312] R.T. Hemmings, Process for Converting Waste Glass Fiber into Value Added Products, Final Report, (2005). https://doi.org/10.2172/889402.

[313] R. Si, S. Guo, Q. Dai, J. Wang, Atomic-structure, microstructure and mechanical properties of glass powder modified metakaolin-based geopolymer, Constr Build Mater 254 (2020) 119303. https://doi.org/10.1016/J.CONBUILDMAT.2020.119303.

[314] M.H. Samarakoon, P.G. Ranjith, V.R.S. De Silva, Effect of soda-lime glass powder on alkali-activated binders: Rheology, strength and microstructure characterization, Constr Build Mater 241 (2020) 118013. https://doi.org/10.1016/J.CONBUILDMAT.2020.118013.

[315] G.F. Huseien, H.K. Hamzah, A.R. Mohd Sam, N.H.A. Khalid, K.W. Shah, D.P. Deogrescu, J. Mirza, Alkali-activated mortars blended with glass bottle waste nano powder: Environmental benefit and sustainability, J Clean Prod 243 (2020) 118636. https://doi.org/10.1016/J.JCLEPRO.2019.118636.

[316] P. Shoaei, F. Ameri, H. Reza Musaeei, T. Ghasemi, C.B. Cheah, Glass powder as a partial precursor in Portland cement and alkali-activated slag mortar: A comprehensive comparative study, Constr Build Mater 251 (2020) 118991. https://doi.org/10.1016/J.CONBUILDMAT.2020.118991.

[317] X. Jiang, R. Xiao, Y. Ma, M. Zhang, Y. Bai, B. Huang, Influence of waste glass powder on the physico-mechanical properties and microstructures of fly ash-based geopolymer paste after exposure to high temperatures, Constr Build Mater 262 (2020) 120579. https://doi.org/10.1016/J.CONBUILDMAT.2020.120579.

[318] G. Liang, H. Li, H. Zhu, T. Liu, Q. Chen, H. Guo, Reuse of waste glass powder in alkali-activated metakaolin/fly ash pastes: Physical properties, reaction kinetics and microstructure, Resour Conserv Recycl 173 (2021) 105721. https://doi.org/10.1016/J.RESCONREC.2021.105721.

[319] M. Giuffrida, M. Cardone, F. Zuccarello, M. Viccaro, Etna 2011–2022: Discoveries from a decade of activity at the volcano, Earth Sci Rev 245 (2023) 104563. https://doi.org/10.1016/J.EARSCIREV.2023.104563.

[320] H. Tchakoute Kouamo, J.A. Mbey, A. Elimbi, B.B. Kenne Diffo, D. Njopwouo, Synthesis of volcanic ash-based geopolymer mortars by fusion method: Effects of adding metakaolin to fused volcanic ash, Ceram Int 39 (2013) 1613–1621. https://doi.org/10.1016/J.CERAMINT.2012.08.003.

[321] P. Scanferla, C. Finocchiaro, A. Gharzouni, G. Barone, P. Mazzoleni, S. Rossignol, High temperature behavior of sodium and potassium volcanic ashes-based alkali-activated materials (Mt. Etna, Italy), Constr Build Mater 408 (2023). https://doi.org/10.1016/J.CONBUILDMAT.2023.133702.

[322] R. Occhipinti, G. Lanzafame, A. Lluveras Tenorio, C. Finocchiaro, L. Gigli, M.R. Tinè, P. Mazzoleni, G. Barone, Design of alkali activated foamy binders from Sicilian volcanic precursors, Ceram Int 49 (2023) 38835–38846. https://doi.org/10.1016/J.CERAMINT.2023.09.220.

[323] E. Bernardo, H. Elsayed, A. Mazzi, G. Tameni, S. Gazzo, L. Contrafatto, Double-life sustainable construction materials from alkali activation of volcanic ash/discarded glass mixture, Constr Build Mater 359 (2022) 129540. https://doi.org/10.1016/J.CONBUILDMAT.2022.129540.

[324] D. Lago, J. Kraxner, D. Galusek, E. Bernardo, Novel glass-based membranes for Cu adsorption: From alkali activation to sintering, Heliyon 9 (2023) e18221. https://doi.org/10.1016/J.HELIYON.2023.E18221/ASSET/F7C93A51-B12E-4DE2-9507-577EC41E2E96/MAIN.ASSETS/GR7.JPG.

[325] M. Mahmoud, J. Kraxner, A. Mehta, H. Elsayed, D. Galusek, E. Bernardo, Alkali activation-induced cold consolidation of waste glass: Application in organic-free direct ink writing of photocatalytic dye destructors, J Eur Ceram Soc 44 (2024) 5449–5459. https://doi.org/10.1016/J.JEURCERAMSOC.2023.12.023.

[326] D.D. Ramteke, M. Hujova, J. Kraxner, D. Galusek, A.R. Romero, R. Falcone, E. Bernardo, Up-cycling of 'unrecyclable' glasses in glass-based foams by weak alkali-activation, gel casting and low-temperature sintering, J Clean Prod 278 (2021) 123985. https://doi.org/10.1016/J.JCLEPRO.2020.123985.

[327] M. Mahmoud, J. Kraxner, H. Kaňková, M. Hujová, S. Chen, D. Galusek, E. Bernardo, Porous Glass Microspheres from Alkali-Activated Fiber Glass Waste, Materials 2022, Vol. 15, Page 1043 15 (2022) 1043. https://doi.org/10.3390/MA15031043.

[328] G. Dal Poggetto, P. Douwe, A. Stroscio, E. Kamseu, I. Lancellotti, A. Elimbi, C. Leonelli, Dissolution of Volcanic Ash in Alkaline Environment for Cold Consolidation of Inorganic Binders, Materials 17 (2024) 5068. https://doi.org/10.3390/MA17205068/S1.

[329] E. Prud'Homme, P. Michaud, E. Joussein, J.M. Clacens, S. Rossignol, Role of alkaline cations and water content on geomaterial foams: Monitoring during formation, J Non Cryst Solids 357 (2011) 1270–1278. https://doi.org/10.1016/J.JNONCRYSOL.2010.12.030.

[330] B. Ghiassi, Effect of curing conditions on the pore solution and carbonation resistance of alkali-activated fly ash and slag pastes, Cem Concr Res (2019). https://www.academia.edu/89850282/Effect_of_curing_conditions_on_the_pore_solution_and_carbonation_resistance_of_alkali_activated_fly_ash_and_slag_pastes (accessed March 11, 2025).

[331] A. Ślosarczyk, J. Fořt, I. Klapiszewska, M. Thomas, Ł. Klapiszewski, R. Černý, A literature review of the latest trends and perspectives regarding alkali-activated materials in terms of sustainable development, Journal of Materials Research and Technology 25 (2023) 5394–5425. https://doi.org/10.1016/J.JMRT.2023.07.038.

[332] H. El-Hassan, N. Ismail, S. Al Hinaii, A. Alshehhi, N. Al Ashkar, Effect of GGBS and curing temperature on microstructure characteristics of lightweight geopolymer concrete, MATEC Web of Conferences 120 (2017) 03004. https://doi.org/10.1051/MATECCONF/201712003004.

[333] A. Rincón, D. Desideri, E. Bernardo, Functional glass-ceramic foams from 'inorganic gel casting' and sintering of glass/slag mixtures, J Clean Prod 187 (2018) 250–256. https://doi.org/10.1016/J.JCLEPRO.2018.03.065.

[334] A. Mehta, E. Colusso, J. Kraxner, D. Galusek, E. Bernardo, Waste-derived glass as a precursor for inorganic polymers: From foams to photocatalytic destructors for dye removal, Ceram Int 48 (2022) 27631–27636. https://doi.org/10.1016/J.CERAMINT.2022.06.059.

[335] B.A. Ionescu, A.M. Barbu, A.V. Lăzărescu, S. Rada, T. Gabor, C. Florean, The Influence of Substitution of Fly Ash with Marble Dust or Blast Furnace Slag on the Properties of the Alkali-Activated Geopolymer Paste, Coatings 2023, Vol. 13, Page 403 13 (2023) 403. https://doi.org/10.3390/COATINGS13020403.

[336] P. Scanferla, A. Gharzouni, N. Texier-Mandoki, X. Bourbon, I.S. de la Plaza, S. Rossignol, Polycondensation reaction effect on the thermal behavior of metakaolin-based potassium geopolymers, J Solgel Sci Technol (2023) 1–14. https://doi.org/10.1007/S10971-023-06080-3/FIGURES/10.

[337] R. ThanigaiSelvan, M. Muthusamy, V. Nandhiraman, J. Ramaswamy, Influence of Iron-Rich Copper Slag on Structure and Properties of Alkali-Activated Fly Ash Geopolymerisation, Iranian Journal of Science and Technology - Transactions of Civil Engineering (2025) 1–18. https://doi.org/10.1007/S40996-025-01798-2/FIGURES/8.

[338] M. Zhang, E. Bernard, M.H.N. Yio, C.R. Cheeseman, R.J. Myers, Further Reduction of CO2-Emissions and Circularity in the Cement and Concrete Industry, (n.d.).

[339] C.R. Kaze, S. Tome, G.L. Lecomte-Nana, A. Adesina, H. Essaedi, S.K. Das, T. Alomayri, E. Kamseu, U.C. Melo, Development of alkali-activated composites from calcined iron-rich laterite soil, Materialia (Oxf) 15 (2021) 101032. https://doi.org/10.1016/J.MTLA.2021.101032.

[340] N. Toniolo, A. Rincón, J.A. Roether, P. Ercole, E. Bernardo, A.R. Boccaccini, Extensive reuse of soda-lime waste glass in fly ash-based geopolymers, Constr Build Mater 188 (2018) 1077–1084. https://doi.org/10.1016/J.CONBUILDMAT.2018.08.096.

[341] M. Torres-Carrasco, F. Puertas, Waste glass in the geopolymer preparation. Mechanical and microstructural characterisation, J Clean Prod 90 (2015) 397–408. https://doi.org/10.1016/J.JCLEPRO.2014.11.074.

[342] N. Amin, S. Gul, S. Sultana, S. Alam, A. Naveed, Impact of Synthetic Parameters on the Compressive Strength of Bagasse Ash-Clay Geopolymer, Crystals 2021, Vol. 11, Page 937 11 (2021) 937. https://doi.org/10.3390/CRYST11080937.

[343] A.Z. Juri, X.F. Song, Y. Nakanishi, J. Dudley, L. Jamieson, L. Yin, Surface fractures in pre-crystallized and crystallized zirconia-containing lithium silicate glass-ceramics generated in ultrasonic vibration-assisted machining, J Mech Behav Biomed Mater 147 (2023) 106132. https://doi.org/10.1016/J.JMBBM.2023.106132.

[344] N. Toniolo, A. Rincón, Y.S. Avadhut, M. Hartmann, E. Bernardo, A.R. Boccaccini, Novel geopolymers incorporating red mud and waste glass cullet, Mater Lett 219 (2018) 152–154. https://doi.org/10.1016/J.MATLET.2018.02.061.

[345] M. Li, G. Huang, Y. Cui, B. Wang, S. Zhang, Q. Wang, J. Feng, Improvement of Mechanical Properties and Condensation Behavior for Alkali-Activated Materials by Sodium Silicate, Crystals (Basel) 12 (2022). https://doi.org/10.3390/CRYST12081018.

[346] C.R. Kaze, S. Tome, G.L. Lecomte-Nana, A. Adesina, H. Essaedi, S.K. Das, T. Alomayri, E. Kamseu, U.C. Melo, Development of alkali-activated composites from calcined iron-rich laterite soil, Materialia (Oxf) 15 (2021) 101032. https://doi.org/10.1016/J.MTLA.2021.101032.

[347] C. Pelosi, R. Occhipinti, C. Finocchiaro, G. Lanzafame, E. Pulidori, M. Lezzerini, G. Barone, P. Mazzoleni, M. Rosaria Tiné, Thermal and morphological investigations of alkali activated materials based on Sicilian volcanic precursors (Italy), Mater Lett 335 (2023) 133773. https://doi.org/10.1016/J.MATLET.2022.133773.

[348] A.W. Ourgessa, J. Kraxner, H. Elsayed, D. Galusek, E. Bernardo, Sustainable construction materials from alkali-activated waste fiberglass and waste refractory, Open Ceramics 20 (2024) 100678. https://doi.org/10.1016/J.OCERAM.2024.100678.

[349] Z. Zhang, H. Wang, Analysing the relation between pore structure and permeability of alkali-activated concrete binders, Handbook of Alkali-Activated Cements, Mortars and Concretes (2015) 235–264. https://doi.org/10.1533/9781782422884.2.235.

[350] M. Sirotti, J. Carette, S. Staquet, New Insights into Pore Structure and Hydraulic Conductivity of Sodium Hydroxide Alkali-Activated Slag through Advanced Modelling, Materials 17 (2024). https://doi.org/10.3390/MA17020363.

[351] J. Xing, Y. Zhao, J. Qiu, X. Sun, Microstructural and Mechanical Properties of Alkali Activated Materials from Two Types of Blast Furnace Slags, Materials 12 (2019). https://doi.org/10.3390/MA12132089.

[352] Z. Yu, A.P. Douvalis, R. de Oliveira-Silva, Q. Shu, Y. Pontikes, D. Sakellariou, Unravelling the role of iron oxidation states in alkali-activated slags: A multinuclear solid-state NMR study on polymerization and structural evolution, Cem Concr Res 195 (2025) 107897. https://doi.org/10.1016/J.CEMCONRES.2025.107897.

[353] G. Lamaa, A.P.C. Duarte, R.V. Silva, J. de Brito, Carbonation of Alkali-Activated Materials: A Review, Materials 2023, Vol. 16, Page 3086 16 (2023) 3086. https://doi.org/10.3390/MA16083086.

[354] I.G. Richardson, The calcium silicate hydrates, Cem Concr Res 38 (2008) 137–158. https://doi.org/10.1016/J.CEMCONRES.2007.11.005.

[355] M.J. Bassan de Moraes, E.Y. Nagata, A.J. Felício Peres Duran, J.A. Rossignolo, Alkali activated materials applied in 3D printing construction: A review, Heliyon 10 (2024) e26696. https://doi.org/10.1016/J.HELIYON.2024.E26696.

[356] D. Sood, K.M.A. Hossain, Fresh State, Rheological and Microstructural Characteristics of Alkali-Activated Mortars Developed Using Novel Dry Mixing Technique under Ambient Conditions, Applied Sciences 2021, Vol. 11, Page 8920 11 (2021) 8920. https://doi.org/10.3390/APP11198920.

[357] W.M. Kriven, Inorganic polysialates or "geopolymers," American Ceramic Society Bulletin 89 (n.d.).

[358] M. Bisson, C. Spinetti, D. Andronico, M. Palaseanu-Lovejoy, M. Fabrizia Buongiorno, O. Alexandrov, T. Cecere, Ten years of volcanic activity at Mt Etna: High-resolution mapping and accurate quantification of the morphological changes by Pleiades and Lidar data, International Journal of Applied Earth Observation and Geoinformation 102 (2021) 102369. https://doi.org/10.1016/J.JAG.2021.102369.

[359] M. Cavalieri, P.L. Ferrara, C. Finocchiaro, M.F. Martorana, An Economic Analysis of the Use of Local Natural Waste: Volcanic Ash of Mt. Etna Volcano (Italy) for Geopolymer Production, Sustainability 2024, Vol. 16, Page 740 16 (2024) 740. https://doi.org/10.3390/SU16020740.

[360] D. Kusumawardani, Y. Rahmawati, M.N. Cahyadi, M. Rusli, A. Martina, An analysis of the socio-economic impacts of the 2021 mountain Semeru Eruption on household level using PLS-SEM, Lett Spat Resour Sci 16 (2023) 1–23. https://doi.org/10.1007/S12076-023-00351-X/FIGURES/3.

[361] C. Finocchiaro, G. Barone, P. Mazzoleni, C. Sgarlata, I. Lancellotti, C. Leonelli, M. Romagnoli, Artificial neural networks test for the prediction of chemical stability of pyroclastic deposits-based AAMs and comparison with conventional mathematical approach (MLR), J Mater Sci 56 (2021) 513–527. https://doi.org/10.1007/S10853-020-05250-W/TABLES/6.

[362] C. Finocchiaro, C.M. Belfiore, G. Barone, P. Mazzoleni, IR-Thermography as a non-destructive tool to derive indirect information on the physical-mechanical behaviour of alkali activated materials, Ceram Int 48 (2022) 36178–36185. https://doi.org/10.1016/J.CERAMINT.2022.08.174.

[363] P. Sahoo, S. Gupta, 3D printable earth-based alkali activated "ink": Effect of alkali concentration and binder-to-aggregate ratio, Journal of Building Engineering 98 (2024). https://doi.org/10.1016/J.JOBE.2024.111208.

[364] O. Zaid, M.H. El Ouni, Advancements in 3D printing of cementitious materials: A review of mineral additives, properties, and systematic developments, Constr Build Mater 427 (2024) 136254. https://doi.org/10.1016/J.CONBUILDMAT.2024.136254.

[365] T. de Rubeis, A. Ciccozzi, L. Giusti, D. Ambrosini, On the use of 3D printing to enhance the thermal performance of building envelope – A review, Journal of Building Engineering 95 (2024) 110284. https://doi.org/10.1016/J.JOBE.2024.110284.

[366] M. Amran, H.S. Abdelgader, A.M. Onaizi, R. Fediuk, T. Ozbakkaloglu, R.S.M. Rashid, G. Murali, 3D-printable alkali-activated concretes for building applications: A critical review, Constr Build Mater 319 (2022) 126126. https://doi.org/10.1016/J.CONBUILDMAT.2021.126126.

[367] A. Gleadall, D. Visscher, J. Yang, D. Thomas, J. Segal, Review of additive manufactured tissue engineering scaffolds: relationship between geometry and performance, Burns Trauma 6 (2018). https://doi.org/10.1186/S41038-018-0121-4/36112385/BURNS_V6_1_121.PDF.

[368] X. Lan, A. Adesida, Y. Boluk, K. Fetah, P. Tebon, M.J. Goudie, F. Marga, K. Jakab, C. Khatiwala, B. Shepherd, S. Dorfman, B. Hubbard, S. Colbert, G. Forgacs, Toward engineering functional organ modules by additive manufacturing, Biofabrication 4 (2012) 022001. https://doi.org/10.1088/1758-5082/4/2/022001.

[369] First Geopolymer 3D Printed Building In The World - YouTube, (n.d.). https://www.youtube.com/watch?v=C-tnpkcXTuc (accessed February 20, 2025).

[370] M. Sakin, Y.C. Kiroglu, 3D Printing of Buildings: Construction of the Sustainable Houses of the Future by BIM, Energy Procedia 134 (2017) 702–711. https://doi.org/10.1016/J.EGYPRO.2017.09.562.

[371] StrongPrint3D – 3D-printing your concrete structures, (n.d.). https://strongprint3d.com/ (accessed February 20, 2025).

[372] M. Bazli, H. Ashrafi, A. Rajabipour, C. Kutay, 3D printing for remote housing: Benefits and challenges, Autom Constr 148 (2023) 104772. https://doi.org/10.1016/J.AUTCON.2023.104772.

[373] G. Lazorenko, A. Kasprzhitskii, Geopolymer additive manufacturing: A review, Addit Manuf 55 (2022) 102782. https://doi.org/10.1016/J.ADDMA.2022.102782.

[374] Y.A. Al-Noaimat, S.H. Ghaffar, M. Chougan, M.J. Al-Kheetan, A review of 3D printing low-carbon concrete with one-part geopolymer: Engineering, environmental and economic feasibility, Case Studies in Construction Materials 18 (2023) e01818. https://doi.org/10.1016/J.CSCM.2022.E01818.

[375] M. Xia, J. Sanjayan, Method of formulating geopolymer for 3D printing for construction applications, Mater Des 110 (2016) 382–390. https://doi.org/10.1016/J.MATDES.2016.07.136.

[376] M. Xia, J.G. Sanjayan, Methods of enhancing strength of geopolymer produced from powder-based 3D printing process, Mater Lett 227 (2018) 281–283. https://doi.org/10.1016/J.MATLET.2018.05.100.

[377] B. Nematollahi, M. Xia, J. Sanjayan, Post-processing methods to improve strength of particle-bed 3d printed geopolymer for digital construction applications, Front Mater 6 (2019) 452804. https://doi.org/10.3389/FMATS.2019.00160/BIBTEX.

[378] P. Odaglia, M. Posani, V. Voney, G. Habert, B. Dillenburger, Geopolymer Binder Jetting with Recycled Aggregates: Testing and Validation for Construction Applications, (2023). https://doi.org/10.2139/SSRN.4594048.

[379] F.; ; Gobbin, A.; Barci, E.; Bernardo, P. Colombo, H. Elsayed, F. Gobbin, A. Barci, E. Bernardo, P. Colombo, Cold Consolidation of Pharmaceutical Waste Glass Powders Through Alkali Activation and Binder Jet 3D Printing, Materials 2024, Vol. 17, Page 5164 17 (2024) 5164. https://doi.org/10.3390/MA17215164.

[380] C. Schmidleithner, D.M. Kalaskar, Stereolithography, 3D Printing (2018). https://doi.org/10.5772/INTECHOPEN.78147.

[381] Paulo. Bártolo, Innovative developments in virtual and physical prototyping, (2012) 851. https://books.google.com/books/about/Innovative_Developments_in_Virtual_and_P.html?hl=it&id=Q002_TiMJ6kC (accessed February 12, 2025).

[382] D.C. Aduba, E.D. Margaretta, A.E.C. Marnot, K. V. Heifferon, W.R. Surbey, N.A. Chartrain, A.R. Whittington, T.E. Long, C.B. Williams, Vat photopolymerization 3D printing of acid-cleavable PEG-methacrylate networks for biomaterial applications, Mater Today Commun 19 (2019) 204–211. https://doi.org/10.1016/J.MTCOMM.2019.01.003.

[383] S.B. Balani, S.H. Ghaffar, M. Chougan, E. Pei, E. Şahin, Processes and materials used for direct writing technologies: A review, Results in Engineering 11 (2021) 100257. https://doi.org/10.1016/J.RINENG.2021.100257.

[384] S. Bakrani, S. Hamidreza, Processes and materials used for direct writing technologies, (2021). https://doi.org/10.1016/j.rineng.2021.100257.

[385] Y. Sun, M.K. Mohan, X. Dai, Y. Zhang, G. Ye, G. De Schutter, Effects of mixing conditions and activator anionic species on the rheology of silicate-activated slag concrete, Cem Concr Compos 150 (2024) 105556. https://doi.org/10.1016/J.CEMCONCOMP.2024.105556.

[386] Y. Alrefaei, Y.S. Wang, Y. Qian, J.G. Dai, Effects of Solid Activator and Fly Ash on Rheology and Thixotropy of One-Part Alkali-Activated Pastes, Journal of Advanced Concrete Technology 20 (2022) 139–151. https://doi.org/10.3151/JACT.20.139.

[387] Y. Alrefaei, J.G. Dai, Effects of delayed addition of polycarboxylate ether on one-part alkali-activated fly ash/slag pastes: Adsorption, reaction kinetics, and rheology, Constr Build Mater 323 (2022) 126611. https://doi.org/10.1016/J.CONBUILDMAT.2022.126611.

[388] Y.K. Kong, K. Kurumisawa, Fresh properties and characteristic testing methods for alkali-activated materials: A review, Journal of Building Engineering 75 (2023) 106830. https://doi.org/10.1016/J.JOBE.2023.106830.

[389] C. Lu, Z. Zhang, J. Hu, Q. Yu, C. Shi, Relationship between rheological property and early age-microstructure building up of alkali-activated slag, Compos B Eng 247 (2022) 110271. https://doi.org/10.1016/J.COMPOSITESB.2022.110271.

[390] R. Shilton, S. Wang, N. Banthia, Use of polysaccharides as a rheology modifying admixture for alkali activated materials for 3D printing, Constr Build Mater 458 (2025) 139661. https://doi.org/10.1016/J.CONBUILDMAT.2024.139661.

[391] Y. Sun, S. Ghorbani, X. Dai, G. Ye, G. De Schutter, Evaluation of rheology and strength development of alkali-activated slag with different silicates sources, Cem Concr Compos 128 (2022) 104415. https://doi.org/10.1016/J.CEMCONCOMP.2022.104415.

[392] J. Liu, L. Guo, Y. Xi, L. Cheng, D. Chen, Study on the rheology, mechanical properties and microstructure of polypropylene fibers in different binder systems, Journal of Building Engineering 90 (2024) 109491. https://doi.org/10.1016/J.JOBE.2024.109491.

[393] L. del-Mazo-Barbara, M.P. Ginebra, Rheological characterisation of ceramic inks for 3D direct ink writing: A review, J Eur Ceram Soc 41 (2021) 18–33. https://doi.org/10.1016/J.JEURCERAMSOC.2021.08.031.

[394] M.A. S R Saadi, A. Maguire, N.T. Pottackal, M. Shajedul Hoque Thakur, M. Md Ikram, A. John Hart, P.M. Ajayan, M.M. Rahman, A. Maguire, N.T. Pottackal, M.S. H Thakur, P.M. Ajayan, M.M. Rahman, M. Md Ikram, A.J. Hart, Direct Ink Writing: A 3D Printing Technology for Diverse Materials, Advanced Materials 34 (2022) 2108855. https://doi.org/10.1002/ADMA.202108855.

[395] Provis, JL, Palomo, Shi, Advances in understanding alkali-activated materials, (n.d.). https://doi.org/10.1016/j.cemconres.2015.04.013.

[396] K.S. Sandhu, A.K. Siroha, S. Punia, L. Sangwan, M. Nehra, S.S. Purewal, Effect of degree of cross linking on physicochemical, rheological and morphological properties of Sorghum starch, Carbohydrate Polymer Technologies and Applications 2 (2021) 100073. https://doi.org/10.1016/J.CARPTA.2021.100073.

[397] G. Kimbell, M.A. Azad, 3D printing: Bioinspired materials for drug delivery, Bioinspired and Biomimetic Materials for Drug Delivery (2021) 295–318. https://doi.org/10.1016/B978-0-12-821352-0.00011-3.

[398] M.M.S. Quiambao, D.D. Laplana, M.I.D. Abobo, A.G. Jancon, S.D. Salvador, H.C. Siy, D.P.Jr. Penaloza, Rheological characterization of the curing process for a water-based epoxy added with polythiol crosslinking agent, Epitoanyag - Journal of Silicate Based and Composite Materials 71 (2019) 162–167. https://doi.org/10.14382/EPITOANYAG-JSBCM.2019.28.

[399] A. Pistone, C. Scolaro, C. Celesti, A. Visco, Study of Protective Layers Based on Crosslinked Glutaraldehyde/3-aminopropyltriethoxysilane, Polymers (Basel) 14 (2022). https://doi.org/10.3390/POLYM14040801.

[400] H. Ramli, N.F.A. Zainal, M. Hess, C.H. Chan, Basic principle and good practices of rheology for polymers for teachers and beginners, Chemistry Teacher International 4 (2022) 307–326. https://doi.org/10.1515/CTI-2022-0010.

[401] C. Lu, Z. Zhang, C. Shi, N. Li, D. Jiao, Q. Yuan, Rheology of alkali-activated materials: A review, Cem Concr Compos 121 (2021) 104061. https://doi.org/10.1016/J.CEMCONCOMP.2021.104061.

[402] S. Siddique, V. Gupta, S. Chaudhary, S. Park, J.G. Jang, Influence of the Precursor, Molarity and Temperature on the Rheology and Structural Buildup of Alkali-Activated Materials, Materials 2021, Vol. 14, Page 3590 14 (2021) 3590. https://doi.org/10.3390/MA14133590.

[403] G. Michlmayr, D. Or, Mechanisms for acoustic emissions generation during granular shearing, Granul Matter 16 (2014) 627–640. https://doi.org/10.1007/S10035-014-0516-2/FIGURES/11.

[404] S.E. Thomas, K.P. Ramaswamy, B.S. Thomas, A review on rheological behaviour of alkali activated materials and the influence of composition factors, Mater Today Proc (2023). https://doi.org/10.1016/J.MATPR.2023.03.277.

[405] A. Kashani, J.L. Provis, G.G. Qiao, J.S.J. Van Deventer, The interrelationship between surface chemistry and rheology in alkali activated slag paste, Constr Build Mater 65 (2014) 583–591. https://doi.org/10.1016/J.CONBUILDMAT.2014.04.127.

[406] H. Mundra, P. Panchmatia, M. Juenger, E. van Oort, Rheological properties of Class F fly-ash based alkali-activated materials (AAMs) for oil and gas well cementing applications, CEMENT 12 (2023) 100068. https://doi.org/10.1016/J.CEMENT.2023.100068.

[407] M.F. Alnahhal, T. Kim, A. Hajimohammadi, Distinctive rheological and temporal viscoelastic behaviour of alkali-activated fly ash/slag pastes: A comparative study with cement paste, Cem Concr Res 144 (2021) 106441. https://doi.org/10.1016/J.CEMCONRES.2021.106441.

[408] M.C. Caggiani, F. Salvemini, C. Finocchiaro, M. Fugazzotto, R. Occhipinti, S. Portale, S. Zafarana, P. Mazzoleni, G. Barone, Capillary water uptake in artificially weathered geopolymers for cultural heritage conservation: real-time neutron imaging investigation, The European Physical Journal Plus 2025 140:4 140 (2025) 1–14. https://doi.org/10.1140/EPJP/S13360-025-06282-4.

[409] L. Feng, S. Yi, S. Zhao, Q. Zhong, F. Ren, C. Liu, Y. Zhang, W. Wang, N. Xie, Z. Li, N. Cui, Recycling of Aluminosilicate-Based Solid Wastes through Alkali-Activation: Preparation, Characterization, and Challenges, Buildings 2024, Vol. 14, Page 226 14 (2024) 226. https://doi.org/10.3390/BUILDINGS14010226.

[410] X. Li, D. Wang, Q. Chen, C. Qi, Alkali activation of blast furnace slag using Bayer red mud as an alternative activator to prepare cemented paste backfill, Constr Build Mater 453 (2024) 139061. https://doi.org/10.1016/J.CONBUILDMAT.2024.139061.

[411] R. Xiao, X. Jiang, Y. Wang, Q. He, B. Huang, Experimental and Thermodynamic Study of Alkali-Activated Waste Glass and Calcium Sulfoaluminate Cement Blends: Shrinkage, Efflorescence Potential, and Phase Assemblages, Journal of Materials in Civil Engineering 33 (2021) 04021312. https://doi.org/10.1061/(ASCE)MT.1943-5533.0003941/ASSET/624663E4-C71E-4248-B162-836A4CE46F9B/ASSETS/IMAGES/LARGE/FIGURE13.JPG.

[412] S. Zhang, Y. Zuo, Z. Li, G. Ye, Isothermal Calorimetric Study on Heat Evolution and Apparent Activation Energy of Alkali-activated Slag/Fly ash Pastes, (n.d.).

[413] X. Liu, S. Li, Y. Ding, Z. Lu, D. Stephan, Y. Chen, Z. Wang, S. Cui, Investigation on admixtures applied to alkali-activated materials: A review, Journal of Building Engineering 64 (2023) 105694. https://doi.org/10.1016/J.JOBE.2022.105694.

[414] Z. Sun, A. Vollpracht, Isothermal calorimetry and in-situ XRD study of the NaOH activated fly ash, metakaolin and slag, Cem Concr Res 103 (2018) 110–122. https://doi.org/10.1016/J.CEMCONRES.2017.10.004.

[415] R. Mohamed, R. Abd Razak, M.M.A.B. Abdullah, S.Z.A. Abd Rahim, L. Yuan-Li, Subaer, A.V. Sandu, J.J. Wysłocki, Heat evolution of alkali-activated materials: A review on influence factors, Constr Build Mater 314 (2022) 125651. https://doi.org/10.1016/J.CONBUILDMAT.2021.125651.

[416] Y. Zhang, X. Zhu, B. Ma, L. Wang, J. Yan, D.C.W. Tsang, Insights into microstructural alterations in alkali-activated materials incorporating municipal solid waste incineration fly ash, Constr Build Mater 425 (2024) 136129. https://doi.org/10.1016/J.CONBUILDMAT.2024.136129.

[417] H. Gao, I. Munadhil, A. Al-damad, A. Siddika, T. Kim, S. Foster, A. Hajimohammadi, Enhancing the workability retention of one-part alkali activated binders by adjusting the chemistry of the activators, Cem Concr Compos 157 (2025) 105928. https://doi.org/10.1016/J.CEMCONCOMP.2025.105928.

[418] R. Davidovits, C. Pelegris, J. Davidovits, Testing Commercial Metakaolins for Geopolymer Formulations Geopolymer Institute Library Standardized Method in Testing Commercial Metakaolins for Geopolymer Formulations, (2019). https://doi.org/10.13140/RG.2.2.18109.10727/1.

[419] G. Franchin, L. Wahl, P. Colombo, Direct ink writing of ceramic matrix composite structures, Journal of the American Ceramic Society 100 (2017) 4397–4401. https://doi.org/10.1111/JACE.15045.